Experimental Study of Plasma Implosion Dynamics in a Two-Stage Wire Array Z-Pinch Configuration

Essa Khoory

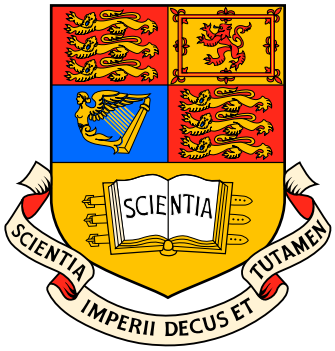

Imperial College London

Department of Physics

Plasma Physics Group

Submitted in partial fulfilment of the requirements for the degree of Doctor of Philosophy in Science and Diploma of Imperial College.

2013

Declaration

I hereby certify that the material in this thesis, which I submit for the degree of Doctor of Philosophy, is entirely original unless otherwise cited or acknowledged in the text.

The copyright of this thesis rests with the author and is made available under a Creative Commons Attribution Non-Commercial No Derivatives licence. Researchers are free to copy, distribute or transmit the thesis on the condition that they attribute it, that they do not use it for commercial purposes and that they do not alter, transform or build upon it. For any reuse or redistribution, researchers must make clear to others the licence terms of this work.

Essa Khoory

06 September 2013

Abstract

This thesis presents results from experiments of a two-stage wire array Z-pinch configuration carried out on the MAGPIE generator (~ 1.4MA in ~ 250ns) at Imperial College, London. This configuration preconditions the load wires (heating and expanding wires into columns of gas) before allowing the full current to rapidly switch into the load. The preconditioning effect of cylindrical Al wire array loads of different wire numbers and wire thicknesses were investigated from density analysis of laser interferometry. It was found that thicker wires expand to larger diameters than thinner wires in the preconditioning phase. The 30μm wire expanded to a diameter of 3.7±0.4mm while the 10μm wire expanded to a diameter of 1.6±0.4mm in ~ 170ns after current start.

Experiments were also conducted on a single Al wire load of different thicknesses. Again thicker wires expanded to a larger diameter. This uniform column of Al gas on axis showed a high degree of azimuthal symmetry. The fast current switch into the load drives a snowplough implosion with an implosion time of ~ 25-30ns with no apparent development of Rayleigh-Taylor instability. It was observed at stagnation that the expansion the m=1 MHD instability into a helical structure was responsible for the main X-ray pulse.

A cylindrical plasma 'shell' was formed by preconditioning an array of large wire number and a small inter-wire separation causing the expanding wires to merge before the current switch time. The shell imploded in a 0D manner with no ablation phase and no trailing mass left behind as in standards wire arrays. Implosion of the 'shell' was susceptible to R-T instability. Analysis of this instability growth estimated an initial effective perturbation of ~ 1-2μm on the preconditioned wires surface prior to implosion.

Acknowledgement

I wish to express my sincere appreciation to my supervisor Professor Sergey Lebedev for giving me the opportunity to get involved in such an interesting project and for his constant guidance and support throughout my PhD degree.

The experiments presented in this thesis would not have been possible without the continuous help and support from the MAGPIE team. The assistance of Dr. Simon Bland, Dr. Gareth Hall, Dr. Francisco Suzuki-Vidal, Dr. Adam Harvey-Thompson, Dr. George Swadling, Dr. Nicolas Niasse, Dr. Guy Burdiak, Dr. Louisa Pickworth, Phil de Grouchy, Lee Suttle, Matthew Bennett and Dr. Liang Sheng is hugely appreciated. It was such a pleasure to work with a team always ready to offer a hand when needed. Thank you guys very much!

I must thank Alan Finch, Paul Brown and his mechanical workshop team for producing most of the experimental hardware used in my experiments. I would also like to thank John Worley and Bandula Ratnasekara for fixing most of the electronics and high voltage components in MAGPIE.

I would like to thank Mohammed Tahlak, Taha Moqbel and Talha Khoory who have constantly encouraged and motivated me to continue my post-graduate education and obtain a PhD degree in Physics. Its finally done! ;)

I am highly grateful to Emirates Foundation for offering me a scholarship and the financial support needed to do a PhD at Imperial College, London. My deepest thanks also goes to Dr. Ali Shaheen from EIAST for his constant support and back-up to continue my doctoral post-graduate studies.

Finally, I am thoroughly indebted to my parents Tariq and Tahira and my wife Hind for their unconditional support, help and patience throughout my PhD degree course. It is to them that I dedicate this thesis.

Contents

1 Introduction **23**

1.1 Inertial confinement fusion 24

1.2 Review of wire array Z-pinch dynamics 27

1.2.1 0D implosion 28

1.2.2 Discrete wire mode dynamics 29

1.2.3 0D implosion of preconditioned wires 36

1.3 1D model of Z-pinch plasma implosion 42

1.3.1 0D implosion 44

1.3.2 Snowplough implosion 45

1.4 Growth of Rayleigh-Taylor instability 46

1.5 Thesis outline and authors contribution 48

2 MAGPIE Generator and Diagnostics **52**

2.1 The MAGPIE generator 52

2.1.1 Marx banks 53

2.1.2 Pulse forming lines 54

2.1.3 Trigatron switches 55

2.1.4 Transfer line and load section 56

2.2 MAGPIE diagnostics 58

2.2.1 B-dot probe 59

2.2.2 Rogowski groove 60

2.2.3 Optical framing camera 61

2.2.4 Time integrated pinhole camera 61

2.2.5 4-frame XUV micro-channel plate (MCP) camera 62

2.2.6 Optical streak camera 64

2.2.7 Diamond photo-conducting detectors (PCD) 65

2.2.8 Laser probing for density measurements 66

3 Investigation of the Preconditioning Effect & Current Switch Mechanism 78

3.1 Investigation of the preconditioning effect 79

3.1.1 Experimental setup 79

3.1.2 Initial current prepulse 82

3.1.3 Preconditioning of load wires 87

3.1.4 Summary and conclusion 106

3.2 Investigation of the current switch mechanism 107

3.2.1 Experimental setup 108

3.2.2 Results and analysis 109

3.2.3 Conclusion 112

4 Dynamics of a Single Wire Load 114

4.1 Experimental setup 114

4.2 Early stage dynamics before current switch 116

4.2.1 Initial current prepulse 116

4.2.2 Preconditioning of load wire 122

4.3 Implosion dynamics after current switch 140

4.3.1 Current switch 140

4.3.2 Implosion trajectory 147

4.3.3 Stagnation and X-ray production 160

5 Formation and Implosion of a Cylindrical Plasma Shell 171

5.1 Linear wire array experiments 172

5.1.1 Linear array load consisting of 2 wires 172

5.1.2 A linear array equivalent to a cylindrical 16×15µm 178

5.2 Formation of a cylindrical 'shell' 181

5.2.1 Experimental setup 181

5.2.2 Initial current prepulse 182

5.2.3 2D density analysis of 'shell' before current switch 183

5.3 Implosion dynamics of 'shell' after current switch 190

5.3.1 Development of Rayleigh-Taylor instability 196

5.3.2 Implosion trajectory 198
5.3.3 Stagnation and X-ray production 201

6 Conclusion 206

Bibliography 212

List of Figures

Figure 1.1: (Left) A picture and (Right) a structure of an ICF capsule to be used at the National Ignition Facility [1]. 24

Figure 1.2: Schematic diagram of a capsule implosion dynamics. 25

Figure 1.3: Schematic diagrams of different concepts to generate radiation for ICF capsule implosion. (a) An indirect laser drive which heats the inner wall of a hohlraum with a capsule embedded inside. (b) A double ended Z-pinch hohlraum, implosion of top and bottom wire array heats the central hohlraum where the fuel capsule is located [6]. (c) A Z-pinch dynamic hohlraum, where wires implode on a cylindrical foam containing the fuel capsule creating a radiating shock wave and act as the hohlraum wall [1]. 26

Figure 1.4: 1D simulations for (a) 10- and (b) 40-wire, 8.6mm radius implosions at 86, 11, 3 and 0 ns before stagnation. (c) Maximum total x-ray power from experiments versus inter-wire gap [17]. 28

Figure 1.5: Implosion trajectories measured from optical streak for 8, 16, 32 & 64 15μm Al wire arrays [19]. 29

Figure 1.6: X-ray radiographic image at ~70% of implosion time showing (above) edge wires of Al and W arrays and (below) the corresponding radial profiles of film optical density [19]. 30

Figure 1.7: Schematic of the core-corona plasma structure. Interaction of global magnetic field Bgl with the current forces the coronal plasma towards the array axis [23]. 31

Figure 1.8: End-on laser interferometric image of 8×20μm Ti wire array (16mm diameter) at t=92ns showing the inwards radial flow of coronal plasma from wire core positions [23]. 32

Figure 1.9: Side-on laser probing showing periodic structures in coronal plasma flow along the axial length for Al, Ti & W wire arrays [23]. 32

Figure 1.10: End-on XUV emission from 16mm diameter arrays of (left) 16×20μm Al at 134ns and (right) 16×13μm W at 134ns showing the formation a precursor at array axis [27]. 33

Figure 1.11: (Top) Radial density profile for a 32×15μm Al wire array calculated from the ablation model (integration of Eq(1.2)) at t0=230ns corresponding to 80% of implosion time. (Bottom) Radial profile of the accumulated mass by integrating the radial density plot [23]. 34

Figure 1.12: X-ray radiograph from the Z facility of an 11μm Cu wire array clearly showing the formation of gaps prior to implosion [28]. 35

Figure 1.13: (a) Implosion trajectory of a 32×15μm Al wire array from an experiment in MAGPIE along with a 0D implosion fit and a snowplough model fit for different fraction of initial piston mass at R0. (b) The corresponding X-ray pulse generated and detected by filtered PCDs [23]. 36

Figure 1.14: Schematic diagram of a two-stage wire array Z-pinch configuration [31]. 37

Figure 1.15: (a) Plot of total dI/dt (blue) and dI/dt in the load array (red). (b) Plot of dI/dt (red) and voltage (green) in the load array during the initial prepulse phase. Both (a) and (b) are for a 17mm diameter 8×15μm Al wire array load [31]. 38

Figure 1.16: (a) Interferometric image of an 8×15μm Al array taken during the preconditioning phase (after the prepulse and before the current switch) and the corresponding line density is shown in (b) [31]. 39

Figure 1.17: (a) Optical streak image of a radial slice looking at a 16mm diameter 8×10μm Al load array and (b) the corresponding implosion trajectory along with a 0D implosion model of a linearly rising current reaching a Max of 1.4MA in 90ns [32]. 40

Figure 1.18: XUV images showing the development of R-T instability during the implosion phase of an 8×15μm Al wire array load. Arrows show the initial position of wires [31]. 41

Figure 1.19: Schematic diagram of a structureless, perfectly conducting cylindrical plasma. 42

Figure 1.20: Cross-section diagram in r-z of a cylindrically imploding plasma, showing the growth of Rayleigh-Taylor instability after some time t. 46

Figure 1.21: Plot of G/$\sqrt{}$kr0 vs Convergence C for a cylindrically imploding shell with Π corresponding to peak current at stagnation for purely axis- symmetric perturbations [15]. 48

Figure 2.1: Block diagram showing the various stages in high pulsed power system. 52

Figure 2.2: A diagram showing the layout of various parts of the MAGPIE generator. 53

Figure 2.3: Diagram showing (left) the parallel charging of a Marx bank capacitors in a bi-polar configuration and (right) the series discharge initiated by a separate trigger pulse into one of the spark-gap switches causing a cascade effect and the self break-down of the the other switches. 54

Figure 2.4: Diagram showing the three electrodes in a trigatron switch [34]. 55

Figure 2.5: Diagram showing the diode-stack and the MITL which sits on top of the transfer line. B-dot probes for current measurements were placed at A, B and C [34]. 56

Figure 2.6: Final output current pulse at the load section from the MAGPIE generator [Reproduced from the MAGPIE website]. 57

Figure 2.7: Layout of various diagnostics around MAGPIE's load vacuum chamber. 58

Figure 2.9: Schematic cross-sectional diagram of a Rogowski groove mounted around a current return post. 60

Figure 2.11: (a) Schematic diagram of a 4-frame MCP pinhole camera setup in MAGPIE and (b) shows the micro-channel tubes of an MCP and the cascade effect of electrons. 63

Figure 2.12: Schematic diagram showing the basic components of an optical streak camera (reproduced from HAMAMATSU Guide to streak camera, 1999). 64

Figure 2.13: (a) Schematic cross-sectional diagram of a PCD and (b) transmission curves for the various filters used on a PCD. 65

Figure 2.14: Schematic diagram of a Mach-Zender interferometer setup. 67

Figure 2.15: Chordal length measurements in a cylindrical object with radius a. 76

Figure 3.1: A schematic diagram (a) and a photo (b) of a 2-stage wire array Z-pinch setup. The photo was taken prior to loading the array in MAGPIE. 79

Figure 3.2: A schematic diagram showing the two different paths of current flow in a 2-stage wire array Z-pinch setup. Green arrow represent current into the load while blue arrows represent current into the bottom inverse array. 81

Figure 3.3: Plot showing dI/dt and current signals in the load at an early stage of the experiment for a $2 \times 30\mu$m Al wire array. 83

Figure 3.4: Variation of Al resistivity and specific heat capacity with temperature [44]. 85

Figure 3.5: The rise in current and temperature of a 2×30μm Al wire array during the pre-pulse phase. 86

Figure 3.6: Plot showing a roughly constant dI/dt after the pre-pulse and before the current switch through a 2×30μm Al wire load. 88

Figure 3.7: Laser interferogram images of cylindrical Al wire array loads taken in the time between the pre-pulse and current switch. The wire array properties and timings for the following images are (a) 2×30μm at 177ns,(b) 4×20μm at 185ns, (c) 8×15μum at 128ns and (d) 16×10μm at 168ns. 89

Figure 3.8: Position of a fringe trace could vary within the boundaries of a fringe introducing an error of ~ $\pm$0.2 fringe-shift (or phase-shift). 91

Figure 3.9: Interferometric images from a 2×30μm load array at 177ns showing (a) the electrode end effect of the wire and (b) the effect of plasma (free electrons) around the wire boundary. In both regions the fringe pattern were not well defined due to a high density of atoms or electrons. 92

Figure 3.10: Example of a (a) background and (b) experimental interferogram image for a load array consisting of 2×30μm Al wires along with their corresponding fringe trace image (c) & (d) respectively. 93

Figure 3.11: 2D phase-shift map along with a line-out at 8mm from cathode for Al wire array loads of (a,b) 2×30μm at 177ns, (c,d) 4×20μm at 185ns, (e,f) 8×15μm at 128ns and (g,h) 16×10μm at 168ns. 94

Figure 3.12: A simple 2-layer cylindrical model for preconditioned wires consisting of an outer layer of plasma and an inner layer of neutral gas, along with a sketch of a basic fringe-shift line-out pattern showing the key turning points. 96

Figure 3.13: Fringe-shift line-out plot for a 2×30μm Al wire array after removing the effect of a plasma layer. Fringe-shift on wire edges show a significant amount of a negative shift, suggesting our model did not take into account all the plasma present. 98

Figure 3.14: A 3-layer model of a preconditioned wire consisting of an outer plasma layer an inner neutral layer and an intermediate layer in-between containing a mixture of plasma and neutrals. 99

Figure 3.15: Fringe shift line-out plot for the neutral atoms of a 2×30μm Al wire array after removing the effect of the plasma and mixture layer. The negative 'dip' at the edges lie within our error boundary of 0.25 fringe-shift and therefore we will ignore it. 99

Figure 3.16: Electron and neutral line-density plots for preconditioned Al wire array loads of (a) 2×30μm at 177ns, (b) 4×20μm at 185ns, (c) 8×15μm at 128ns and (d) 16×10μm at 168ns. 100

Figure 3.17: Table showing the average diameter of a preconditioned wire, the total calculated number of neutral atoms and electrons along with the real value for Al load array setups of 2×30μm, 4×20μm, 8×15μm and 16×10μm. 102

Figure 3.18: The percentage difference of the upper limit of the experimentally calculated value of total no. of atoms per length from the real value, for Al wire array loads of 2×30μm, 4×20μm, 8×15μm and 16×10μm. 103

Figure 3.19: A plot showing the variation of current per surface area and the total number of electrons per wire for Al wire array loads of 2×30μm, 4×20μm, 8×15μm and 16×10μm. 104

Figure 3.20: Plot showing the variation of a preconditioned wire temperature, expansion velocity and total number of atoms per length for different initial wire thickness. 106

Figure 3.21: (Left) Schematic diagram of a two-stage wire array load showing the two different paths of current. (Right) dI/dt signal of the generator (blue) and of the load section (red) for an 8×15μm Al wire array [31]. 108

Figure 3.22: Schematic of a static current-measuring diagnostic load, showing the two B-dot probes sitting at the bottom of the brass cylinder (green object). The field of view is a zoom-in of the region inside the dashed circle in Figure 3.21 with the array replaced by the current-measuring hardware. 109

Figure 3.23: dI/dt signals from the two B-dot probes of the current-measuring load and the total dI/dt of the generator from the MITL B-dot. Polarity of one of the load B-dot is inverted to account for the opposite direction of the probe's winding. 110

Figure 3.24: (a) Laser (λ=532nm) interferogram image at 175ns showing the presence of plasma in between the gap separating the load from the inverse array. (b) XUV images at 188ns (left) showing the presence of plasma in the gap and at 218ns (right) after the implosion of this plasma in the gap region re-opening the gap. 110

Figure 3.25: Schematic of a two-stage wire array configuration showing the possible current path formed by the exploding plasma at different times after the switch. 111

Figure 3.26: Current through the load obtained by integrating B-dot dI/dt signals, along with the total generator current. 112

Figure 4.1: A cross-section schematic diagram of a two-stage wire array Z-pinch configuration with a load consisting of a single wire on axis. 115

Figure 4.2: Plot showing the variation of (a) dI/dt and (b) current with time during the first 50ns after the start of the current pulse for a single 25μm, 40μm and 50μm Al wire load. 117

Figure 4.3: The rise in (a) current prepulse and (b) calculated temperature at an early stage of the experiment for a single Al wire load of 25μm, 40μm and 50μm thickness. The dashed vertical lines in (a) are the time at which the corresponding load wire reaches boiling point. 120

Figure 4.4: Plot of (a) dI/dt and (b) current into the load vs time for different load wire thicknesses. After the prepulse and before the current switch dI/dt
falls to a relatively low level but not zero. 122

Figure 4.5: Optical streak image showing the radial expansion before current switch of a single Al wire load of (a) 25μm, (b) 40μm and (c) 50μm initial thickness. 124

Figure 4.6: Laser (532nm) interferometric images for a single Al wire load of (a) 25μm at 211ns, (b) 40μm at 201ns and (c) 50μm at 210ns. 126

Figure 4.7: Laser (355nm) interferometric images for a single Al wire load of (a) 40μm at 201ns and (b) 50μm at 210ns. 126

Figure 4.8: A zoomed-in interferometric image showing fringe-shift around wire edges for a single Al wire load of (a) 25μm and (b) 50μm. 128

Figure 4.9: 2D fringe-shift maps from green interferometric images along with line-outs at different heights from cathode for single Al wire loads of (a,b) 25μm at 211ns, (c,d) 40μm at 201ns and (e,f) 50μm at 210ns. 129

Figure 4.10: (a) A schematic diagram of a perfectly circular preconditioned wire of radius 'a' and chordal laser path 2(a2-y2)1/2. (b) A wire model consisting of n equally spaced layers. 131

Figure 4.11: (a-c) Axially averaged line integrated phase-shift, (d-f) azimuthally averaged line integrated phase-shift along with its Abel inverted plot and (g-i) radial distribution of neutral and plasma density for a single Al wire load of (a,d,g) 25μm at 211ns, (b,e,h) 40μm at 201ns and (c,f,i) 50μm at 210ns. 133

Figure 4.12: A table showing the average diameter and the total number of neutral atoms and electrons per length for a single preconditioned Al wire load of 25μm, 40μm and 50μm initial thickness. 135

Figure 4.13: 2D phase-shift map from blue (λ=355nm) laser interferometric images along with line-outs at different heights from cathode for a single Al wire load of (a,b) 40μm at 201ns and (c,d) 50μm at 210ns. 136

Figure 4.14: Axially averaged line integrated phase-shift plots from green (λ=532nm) and blue (λ=355nm) interferometric images for a single Al wire load of (a) 40μm at 201ns and (b) 50μm at 210ns. 136

Figure 4.15: Atom and electron line density obtained by solving the green and blue line integrated phase-shifts simultaneously for a single Al wire load of (a) 40μm at 201ns and (b) 50μm at 210ns. 137

Figure 4.16: Plot of atom number density vs radius for a single preconditioned Al wire of (a) 40μm and (b) 50μm initial thickness. 138

Figure 4.17: Variation of MAGPIE's current with time for the three different experiments involving different load wire thicknesses (values shown in legend). The dashed lines show the switching time for each experiment taken from the optical streak image in Figure 4.6. 141

Figure 4.18: Variation of dI/dt and calculated current through a single 25μm Al wire load measured from a rogowski groove placed at one of the 4 return posts. 142

Figure 4.19: Interferometric images of a 50μm Al load wire from (a) a green (532nm) laser at 266ns and (b) a blue (355nm) laser at 286ns. The current switch was at ~ 270ns. 143

Figure 4.20: A 2D fringe-shift map of a 50μm Al load wire at (a) 4ns before current switch and (b) 16ns after current switch. 144

Figure 4.21: Averaged fringe-shift line-outs between the axial height 8.2 - 8.9mm for a 50μm Al wire load at 4ns before the switch (blue plot) and 16ns after the switch (red plot). 145

Figure 4.22: Variation of neutral and plasma number density with radius for a 50μm Al wire load at 4ns before the current switch (blue and red plot) and 16ns after the switch (black plot) obtained by Abel inverting (a) the left hand side and (b) the right hand side portion of the preconditioned wire fringe-shift line-out in Figure 4.21. 146

Figure 4.23: An optical streak camera image showing a radial slice of a 25μm Al wire at the centre of the load. The dashed green line shows the current switch time and the dashed red line shows roughly the 'region' of stagnation. 147

Figure 4.24: Images of a 25μm Al wire from an optical framing camera set at 10ns interval. Length scales at the corners of images are in mm. Images are from the shot s0312_12. 148

Figure 4.25: Optical streak image showing a radial slice of a 40μm Al wire at the centre of the load. The dashed green line shows the current switch time and the dashed red line shows the point of stagnation. 148

Figure 4.26: Images of a 40μm Al wire from an optical framing camera set at 10ns interval. Length scales at the corners of images are in mm. Images are from the shot s1026_11. 149

Figure 4.27: 4-Frame XUV images after current switch of a 40μm Al wire. Length scales at the corners of images are in mm. Images are from the shot s1026_11. 149

Figure 4.28: Laser (λ = 532nm) interferometric images after the current switch time of a 40μm Al wire. Length scales at the corners of images are in mm. Images taken from the shot s1026_11. 150

Figure 4.29: Optical streak image showing a radial slice of a 50μm Al wire at the centre of the load. The dashed green line shows the current switch time and the dashed red line shows the point of stagnation. 150

Figure 4.30: Load images taken after the current switch of a 50μm Al wire from: (a) an optical framing camera set at 10ns interval. (b) a 4-frame XUV camera, where the timings in blue in square brackets [ ] are measured after the current switch. Length scales at the corners of images are in mm. Images in (a) are from the shot s0227_12, while images in (b) are from two different shots (s0227_12 & s0228_12). 151

Figure 4.31: Implosion trajectory plots for a single Al wire load of (a) 25μm, (b) 40μm and (c) 50μm thickness. 153

Figure 4.32: Experimentally obtained density distribution from Abel inversion of interferogram analysis along with a curve-fit for (a) 25μm, (b) 40μm and (c) 50μm preconditioned Al wire load. All quantities are normalised and in dimensionless units. 157

Figure 4.33: Implosion trajectory plots from the snowplough model for different current functions along with an experimental data plot for single preconditioned aluminium wires of (a) 25μm, (b) 40μm and (c) 50μm initial thickness. 159

Figure 4.34: Temperatures of He- and H- like atoms at stagnation (assuming the formation of a Bennett pinch) for different initial thicknesses of a single Al wire load. 161

Figure 4.35: Development of sausage (m=0) and kink (m=1) MHD instabilities on the stagnated plasma column from a single Al wire load of (a) 25μm, (b) 40μm and (c) 50μm initial thickness. 162

Figure 4.36: X-ray signals from 6μm polycarbonate and 20μm Beryllium filtered PCD along with implosion trajectories for single Al wire loads of (a) 25μm, (b) 40μm and (c) 50μm initial thickness. 164

Figure 4.37: Post-stagnation images from optical framing camera for a 40μm Al wire showing the formation and expansion of a helical structure which is initially caused by the m=1 MHD instability. 167

Figure 4.38: Schematic showing how X-rays can be generated in an m=1 unstable plasma, when the Lorentz force does work in forcing the plasma helix to expand (Image reproduced from [30]). 167

Figure 4.39: Time integrated pinhole image of the stagnated plasma column for a 40μm Al wire load through (a) a 7μm Be filter and (b) a 6μm Al filter. 169

Figure 5.1: A schematic diagram and a photo of a 2-stage Z-pinch array setup with a load consisting of 2 Al wires few millimetres apart. 173

Figure 5.2: Laser (λ=532nm) interferometric image at 156ns of a linear array consisting of 2×30μm Al wires 4mm apart. 173

Figure 5.3: (a) A 2D fringe-shift map and (b) an averaged line-out between the axial position 6-8mm (specified by the region in the red box in (a)) taken at 156ns for a load consisting of 2×30μm Al wires 4mm apart. 174

Figure 5.4: Top-view schematic diagram of 2 preconditioned wires supported by a square disc at the cathode. Green arrow shows the direction of the laser beam for the interferometric image in Figure 5.3. 175

Figure 5.5: Minimum and maximum atom number line density in-between the preconditioned wires at 156ns for a load consisting of 2×30μm Al wires 4mm apart. 176

Figure 5.6: (a) Green (λ=532nm) and (b) blue (λ=355nm) laser interferometric images of a 7×15μm Al wire linear array before the current switch at 228ns. 178

Figure 5.7: 2D fringe-shift maps of a 7×15μm linear array from a (a) green (λ=532nm) and a (b) blue (λ=355nm) laser interferometric image at 228ns. (c) Axially averaged fringe-shift line-out between the height 6-8mm (black box in (a)&(b)). (d) Electron and atom number line density obtained by simultaneously solving the green and blue fringe-shift plots in (c). 179

Figure 5.8: (a) Current and (b) temperature variation of a 2×30μm and 16×15μm Al wire array load at the early stage of the experiment. 182

Figure 5.9: Laser interferometric images of a cylindrical Al wire array of (a,b) 16×10μm at 168ns [~100ns before the switch] and (c,d) 16×15μm at 247ns [~25ns before the switch]. Images (a & c) are taken with the green laser (λ=532nm) and images (b & d) are taken with the blue laser (λ=355nm). 183

Figure 5.10: 2D fringe-shift maps for a 16×10μm Al wire array at 168ns from a (a) green λ=532nm and (c) blue λ=355nm laser along with fringe-shift line- outs (b) and

(d) respectively between the axial height 6-8mm (the region inside the black box in the 2D maps). 184

Figure 5.11: (a) Averaged fringe-shift line-out from the blue and green laser between the axial region 6-8mm from the cathode, and (b) the averaged electron and atom line density obtained by simultaneously solving the two fringe-shift plots in (a) for a 16×10μm Al wire array at 168ns. 186

Figure 5.12: (a) 2D fringe-shift map from the green (λ=532nm) interferometric image along with (b) line-outs between the axial positions 7-8mm (as shown by the black box) for a 16×15μm wire array at 247ns. 188

Figure 5.13: The averaged neutral line density between the axial height 7-8mm of a 16×15μm Al wire array at 247ns. 189

Figure 5.14: dI/dt and current variation with time from a Rogowski groove for a cylindrical array load consisting of 16×15μm Al wire. 190

Figure 5.15: Images for a cylindrical array load consisting of 16×10μm Al wires from: (a) optical streak camera showing a radial slice at the centre of the load. (b) Optical framing camera with a 15ns inter-frame timing. All length scales are in mm. All images taken from the experiment s1021_11. 192

Figure 5.16: Images for a cylindrical array load consisting of 16×10μm Al wires from a 4-frame XUV camera with a 30ns inter-frame timing. All images taken from the same experiment (s1021_11). 193

Figure 5.17: Images for a cylindrical array load consisting of 16×15μm Al wires from an optical framing camera with a 10ns inter-frame timing. All length scales are in mm and all images are taken from the same experiment (s0313_12). 194

Figure 5.18: Images for a cylindrical array load consisting of 16×15μm Al wires from a 4-frame XUV camera with a 30ns inter-frame timing. All length scales are in mm. All images taken from the same experiment (s0313_12). 195

Figure 5.19: Theoretically calculated growth of R-T instability during initial linear stage vs radial convergence for an imploding shell with different initial perturbation $\xi 0$, along with the experimental values from an optical framing camera for a 16×15μm Al wire array load. 197

Figure 5.20: Implosion trajectory (radius vs time) plots for a 'shell' formed by preconditioning an Al wire array load of (a) 16×10μm and (b) 16×15μm. 199

Figure 5.21: Implosion trajectory plots from the thin-shell model for different current functions along with the experimental data of the optical framing camera for a (a) 16×10μm and (b) 16×15μm Al wire array load. 201

Figure 5.22: X-ray signals from a 6μm polycarbonate and 20μm Beryllium filteredPCD along with the implosion trajectory from optical framing camera for a 16×10μm Al wire array load. 202

Figure 5.23: (a) dI/dt and current signal from a Rogowski groove and (b) X- ray signal from a 6μm polycarbonate and 20μm Beryllium filtered PCDs for a 16×15μm Al wire array load taken from experiment s0320_12. 203

Figure 5.24: Time integrated pinhole image through a 7μm Be filter of the stagnated plasma column from a 16×15μm Al wire array. 205

Chapter 1

Introduction

Achieving a state of energy sustainability and mitigating global warming are major challenges currently facing every developed nation. Renewable energy sources such as wind and solar produce zero carbon but possess a low energy density per unit area and their energy production is subject to daily environmental and climate fluctuations. Hence, such sources of energy are not feasible and reliable to produce the base demand in major cities which have a high energy demand per unit area.

Nuclear fusion on the other hand, can tackle both those challenges. It has the potential to provide a constant supply of energy for millions of years with energy density per unit area equivalent to or higher than conventional gas and nuclear power plants. It does not produce any carbon dioxide or gases which contribute to global warming nor it produces any long-term radioactive wastes as by products. For those reasons, achieving a self sustained nuclear fusion reaction with a net positive energy output has been an active area of research in many countries for the past 50 years.

A nuclear fusion is a reaction where light atomic nuclei are 'fused' together under immense temperature and pressure to form a heavier nuclei, generating a large amount of energy through the conversion of a small fraction of mass ($E=mc^2$). This kind of reaction continuously takes place at the core of every star (including our sun) where such extreme conditions are sustained. There are two main streams of research to achieve such conditions: magnetic confinement fusion (MCF) and inertial confinement fusion (ICF), both of which try to utilise the Deuterium-Tritium (DT) nuclear fusion reaction (Eq (1.1)) due to its high cross section.

$$ {}^{2}_{1}D + {}^{3}_{1}T \rightarrow {}^{4}_{2}He(3.5MeV) + n(14.1MeV) \qquad (1.1) $$

In MCF a high temperature low density plasma is confined by magnetic fields in a torus shaped cavity for a long period of time (few seconds), while in ICF, a lower temperature and higher density plasma is confined by the inertial force of a spherically imploding pellet for a much shorter time (few nanoseconds).

1.1 Inertial confinement fusion

Inertial confinement fusion is a technique by which a nuclear fusion reaction is initiated by compressing and heating a spherical fuel target. A typical ICF capsule would look like the one in Figure 1.1.

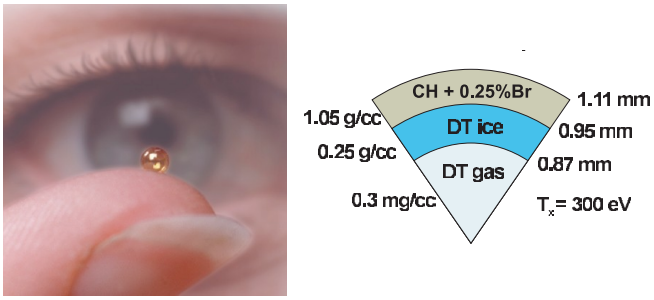

Figure 1.1: (Left) A picture and (Right) a structure of an ICF capsule to be used at the National Ignition Facility [1].

The capsule is composed of 3 distinct layers [1]. The inner most layer is a DT gas surrounded by thicker layer of frozen or liquid DT which forms the main fuel for the nuclear reaction. The outer most layer is a CH ablator containing 0.25% Bromine.

The implosion process of the capsule is achieved by illuminating the surface with a high intense radiation (usually from a laser or a Z-pinch machine) rapidly heating and exploding the ablator outwards (Stage 1 in Figure 1.2). By conservation of momentum, the rest of the capsule is forced inwards reaching a velocity of the order of 10^7 cms^{-1} with energy conversion efficiency ~ 5 - 15% [2]. As the capsule

implodes it does PdV work on the central DT gas increasing its pressure. However not all the kinetic energy is transferred to the central gas, an equal amount of PdV work is done on the cold fuel shell. Therefore - taking into account energy losses by radiation and other factors - to reach the desired potential energy, one needs more than double this amount as initial kinetic energy.

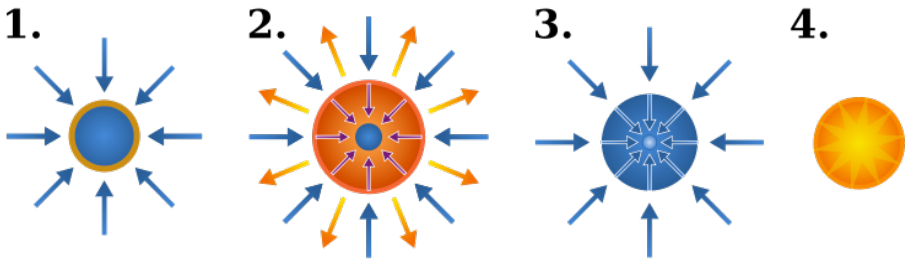

Figure 1.2: Schematic diagram of a capsule implosion dynamics.

The aim of the implosion is to heat and compress the central gas to achieve a 'hot-spot ignition'. Fusion initiates at the central hot-spot which contains 2-5% of the fuel, giving off a significant amount of highly energetic alpha particles. Due to the high density of the surrounding 'cold' fuel, those alpha particles move only a short distance before becoming thermalised, losing their energy to the main fuel as heat. This triggers more fusion reaction, giving off more alpha particles. This process spreads outwards from the central hot-spot, producing a self-sustained fusion burn known as *ignition*. To achieve ignition, one requires the implosion to be highly uniform (99%), with a spherical convergence ratio $C_r \geq 30$ and hot-spot temperature ≥ 5 keV [2, 3].

Lasers and Z-pinch machines have been used in different setups and arrangements to generate the required radiation to drive the capsule implosion. Figure 1.3 shows some of the popular concepts which have been investigated in the past literature. One approach which is currently being investigated at the National Ignition Facility (NIF) and is shown in Figure 1.3(a) is the indirect laser drive [4, 5]. It consists of a fusion capsule centred inside a gold can (~6mm long) known as a hohlraum. Laser beams entering from both ends of the hohlraum heat the inner wall which generates a 'super-hot' plasma that emits X-rays. Multiple absorption and re-emission by the hohlraum walls creates a cavity of intense thermal x-ray

around the capsule which heats the ablator and drives the capsule implosion. This approach has the advantage of creating a more symmetric implosion when compared to a direct laser drive, however the laser-capsule coupling efficiency is lower as the hohlraum takes a considerable amount of energy to heat up.

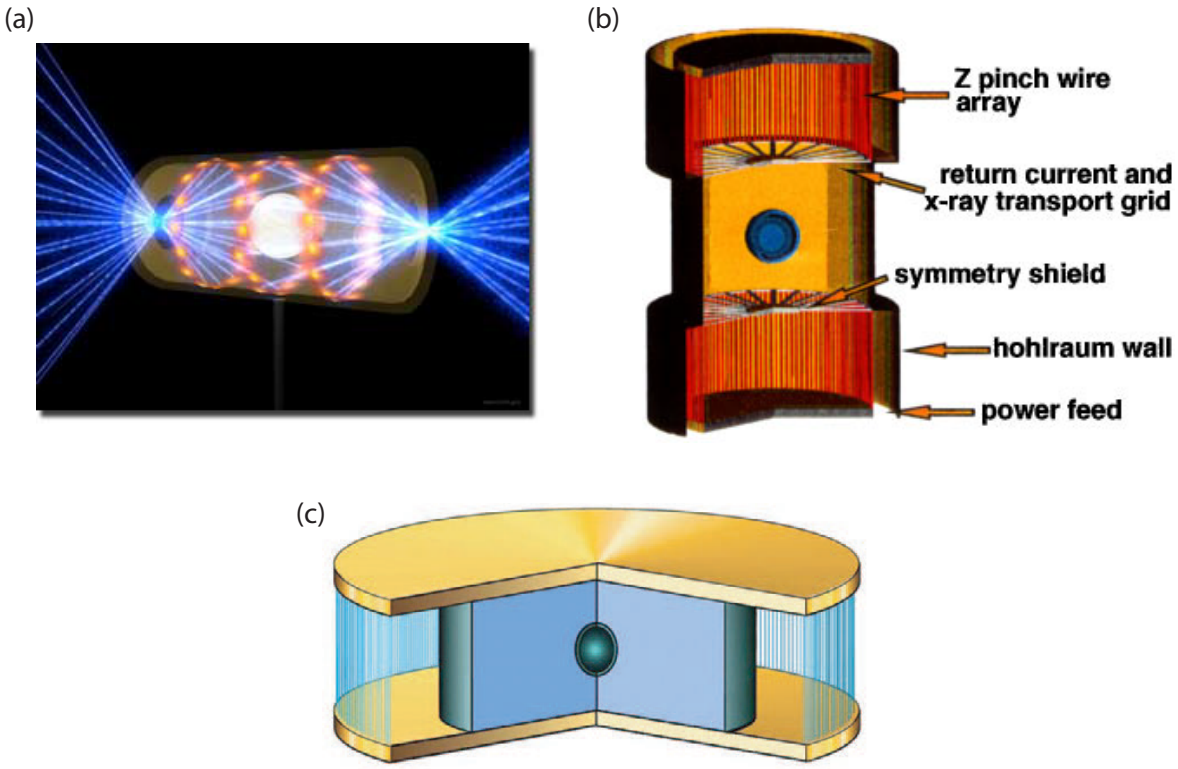

Figure 1.3: Schematic diagrams of different concepts to generate radiation for ICF capsule implosion. (a) An indirect laser drive which heats the inner wall of a hohlraum with a capsule embedded inside. (b) A double ended Z-pinch hohlraum, implosion of top and bottom wire array heats the central hohlraum where the fuel capsule is located [6]. (c) A Z-pinch dynamic hohlraum, where wires implode on a cylindrical foam containing the fuel capsule creating a radiating shock wave and act as the hohlraum wall [1].

The other two approaches shown in Figure 1.3(b)&(c) utilise a Z-pinch machine where a fast current pulse in the order of 1-20 MA passes through a cylindrical wire array configuration. This generates an azimuthal magnetic field and hence a JxB force acting radially inwards, causing the wires to implode. In a double-ended hohlraum concept [6] (Figure 1.3(b)) two cylindrically imploding wire arrays (10mm in length and 24mm in diameter) are positioned inside the hohlraum above and below the capsule cavity. The stagnation of the imploding wire arrays generate a huge X-ray pulse. The openings in the end of the wire array hohlraum allows radiation to pass into the central hohlraum while the symmetry shields prevent

direct illumination of capsule from the stagnating pinch. This radiation heats the inner wall of the central hohlraum and the capsule implodes by the thermalised X-ray radiation. Similar to laser indirect drive, this approach has the advantage of a high degree of radiation symmetry, but in the expense of energy coupling efficiency. The double-ended hohlraum has been tested at the Z facility at Sandia National Laboratory with a peak current of ~ 20MA at ~ 100ns generating a radiation temperature of ~ 70 eV and C_r ~ 10 [7].

In a dynamic hohlraum (Figure 1.3(c)), a high density cylindrical wire array impacts on a low density CH foam where the capsule is embedded inside at the centre [8, 9]. At impact velocity $\geq$ 20 cm/μs, a radiating shock wave propagates through the foam [10], while the wire array Z-pinch plasma acts as the hohlraum wall confines and thermalises the radiation. This concept did show an improved energy coupling efficiency (generating 200 eV radiation temperature at Z) over the double-ended hohlraum at the expense of radiation asymmetry between the poles and the equator causing the capsule to implode in a 'sausage' shape [10].

Z-pinch machines are highly efficient in converting electrical energy into radiation yield with a typical efficiency of ~ 15% [11]. On the other hand, lasers such as the one being used at NIF have a wall plug efficiency less than 0.5% [12]. In addition, Z-pinch machines benefit from being a much cheaper device to build if one considers the economic feasibility of a future fusion power plant. For a Z-pinch driven ICF one needs to understand - and hence control and tailor - the X-ray power generation from a wire array Z-pinch machine. Thus, we need to understand and investigate the wire array dynamics from the point of current start and up to stagnation.

1.2 Review of wire array Z-pinch dynamics

The physics of cylindrical wire array Z-pinches has been an active area of research for the past two decades [13-15]. This progress has been mainly driven by major improvements in pulsed-power technology reaching a record maximum current of ~

20MA in ~ 100ns at the Z facility in Sandia National Laboratory (USA). Application of this enhanced current pulse on a wire array Z-pinch generated X-ray power in excess of 300TW [16] making this machine the worlds most powerful laboratory X-ray source. In recent years, significant progress was made in understanding wire array Z-pinch dynamics due to the development of sophisticated diagnostic equipments and a boost in CPU power for simulating 3D MHD codes. In this section we give a brief chronological review on the physics of wire array Z-pinch dynamics.

1.2.1 0D implosion

During the 80s and late 90s it has been widely thought that at the start of the current pulse wires are first heated and expand into columns of gas, which at a small inter-wire separation those columns would merge into a uniform shell [15, 17]. The J×B force then accelerates the expanded wires or 'shell' uniformly towards the axis (example shown in Figure 1.4(a)&(b)). This type of implosion is commonly referred to as *0D implosion*.

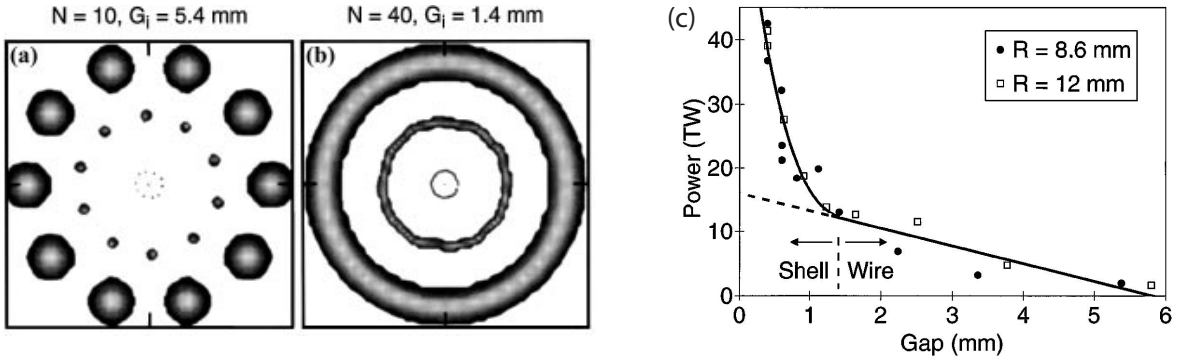

Figure 1.4: 1D simulations for (a) 10- and (b) 40-wire, 8.6mm radius implosions at 86, 11, 3 and 0 ns before stagnation. (c) Maximum total x-ray power from experiments versus inter-wire gap [17].

Computer simulations of the 0D model accurately predicted the implosion time observed in wire array Z-pinch experiments, giving support to this model. In addition, experiments and simulations conducted by Sanford et al. [17] and Deeney et al. [18] on Saturn (~ 7MA in ~ 35ns 10-90% rise time) have shown a dramatic improvement in X-ray power yield as the inter-wire gap was reduced (Figure 1.4 (c)). Specifically, a sharp increase in X-ray power was observed for inter-wire gap

G $<$ 1.4mm. This corresponds to wire number N $>$ 40 on a ~ 18mm diameter array. This improvement has been attributed to the formation a plasma 'shell' by the expansion of wires prior to implosion (Figure 1.4(b)).

To further support this model, 1D radial simulations [17] of a single solid wire have shown that for a current-per-wire equivalent to that of N $\leq$ 20 the expansion of individual wires is reversed by the self-constricting magnetic field before the array implodes on axis (Figure 1.4(a)). For the lower current-per-wire where N $>$ 40 the expanding wires merge forming a continuous plasma shell prior to implosion. This code highly depends on the resistivity model used and we will see in the next section how this model breaks down at the early stage of current start.

1.2.2 Discrete wire mode dynamics

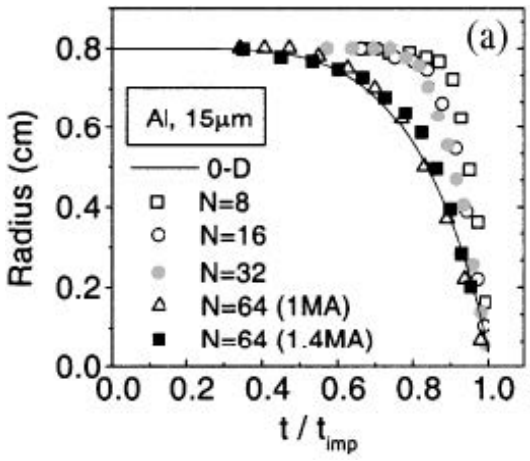

Figure 1.5: Implosion trajectories measured from optical streak for 8, 16, 32 & 64 15μm Al wire arrays [19].

Implosion trajectory (radius vs time) plots for Al wire array Z-pinch have shown that trajectories deviate from the 0D model as the array wire number N is decreased below a certain value. This is illustrated in Figure 1.5 from Lebedev et al [19], were implosions of 8, 16 and 32 Al wires on a 16mm diameter array had a different trajectory from the 0D model while the 64 wire array closely followed this model. It is believed that when the ratio of inter-wire separation to wire diameter is $\leq \pi$ the contribution of the 'private' magnetic flux of each wire to the array inductance is zero [19] and the array inductance becomes equal to that of a thin

shell. Hence the observed change in implosion trajectory for higher N (lower inter-wire separation) array. However for lower N array, the wires appear to be stationary for ~ 80% of the implosion time before it begins to implode. In this section we explore the dynamics of arrays in the discrete wire mode (ratio of inter-wire separation to wire diameter $> \pi$) which leads to this kind of implosion trajectory.

Core-corona structure

Single wire Z-pinch experiments conducted in the early 90s did not show a volumetric heating of the wire into gas/plasma [20]. Instead at the early stage of the current pulse the wire consisted of a heterogeneous structure with a dense cold core and a hot coronal plasma. Similar observations were then made in the late 90s for wire array Z-pinches where laser probing experiments have shown the core-corona structure in a wire array for current between 1 - 7 MA [21, 22].

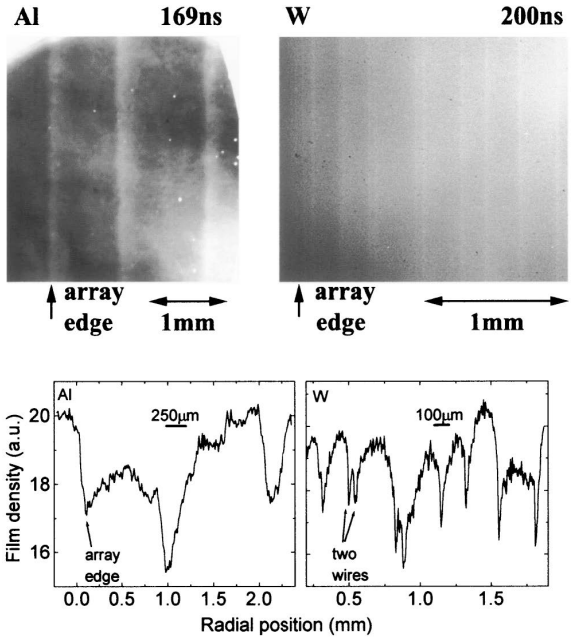

Figure 1.6: X-ray radiographic image at ~70% of implosion time showing (above) edge wires of Al and W arrays and (below) the corresponding radial profiles of film optical density [19].

Once this wire heterogeneous structure occurs the current switches from the resistive wire core to the less resistive coronal plasma causing a voltage breakdown and hence a fall in array resistivity (c.f wire expansion code Section 1.2.1). This

structure is maintained during the first 80% of the implosion time [23]. Figure 1.6 shows radiographic images obtained at ~ 70% of implosion time showing edge wires in Al and W arrays with the corresponding radial profile film optical density taken from [19]. Those images show that the characteristic core size are different for different wire materials (~ 0.25mm for Al and ~ 0.1mm for W). Those sizes were found to be the same for 16 and 64 wire array, hence core expansion is insensitive to the current in each wire [23, 24]. The images also show that the position of the core remains stationary for roughly 70-80% of the implosion time.

Ablation streams

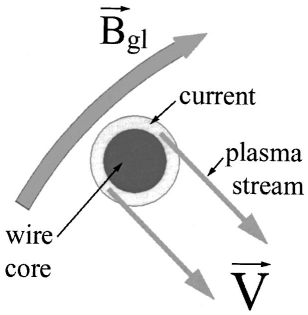

Figure 1.7: Schematic of the core-corona plasma structure. Interaction of global magnetic field B_{gl} with the current forces the coronal plasma towards the array axis [23].

The current carrying coronal plasma around each wire interacts with the global azimuthal magnetic field of the array and the resulting J×B force accelerates the coronal plasma radially inwards towards the array axis (Figure 1.7). This can be seen from end-on interferometric image (Figure 1.8) of an 8 wire Ti array. This image shows a high degree of azimuthal symmetry and indicates that the average ablation rate of material from individual wires in the array is the same. The inward velocity of the ablated plasma streams was measured from similar end-on images at different times to be constant at an average value ~ 1.5×10^7 cms^{-1} for different wire materials (Al, W, Ti & Ni). This constant ablation stream velocity results in the first coronal plasma arriving at the axis at ~ 50% of the implosion time [23].

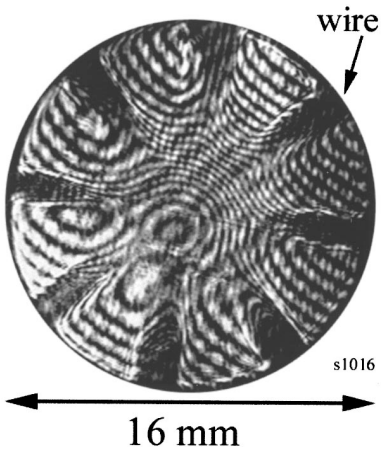

Figure 1.8: End-on laser interferometric image of 8×20μm Ti wire array (16mm diameter) at t=92ns showing the inwards radial flow of coronal plasma from wire core positions [23].

Side-on laser probing have shown that the ablation streams along the length of the wire is not uniform (Figure 1.9). It possess a quasi-periodic structure of high and low streams of material along the axial length of each wire. This is caused by an MHD instability in each wire similar to the global m=0 instability observed in a pinching plasma column. The structure of this instability is a 'sausage' like with periodic local regions along the axial length experiencing greater pinch (smaller diameter) generating a stronger magnetic field and hence greater magnetic pressure and heating. The instability in the wires of an array reaches a stable state as the coronal plasma is continuously swept away and does not participate in the instability growth feedback loop [25].

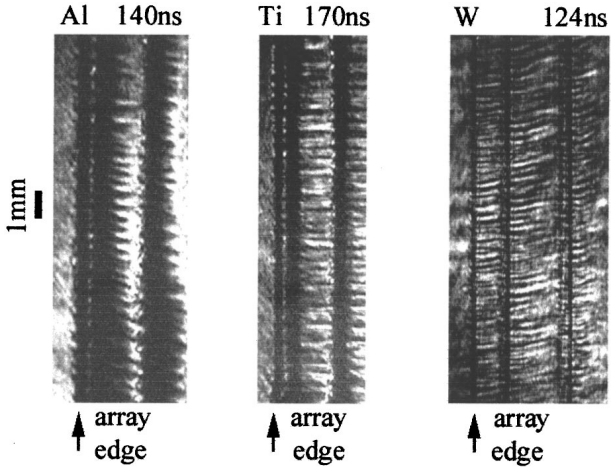

Figure 1.9: Side-on laser probing showing periodic structures in coronal plasma flow along the axial length for Al, Ti & W wire arrays [23].

The wavelength λ of instability around each wire and in plasma streams does not change throughout the ablation phase of a wire array (~ 80% of implosion time). This wavelength varies for different wire materials and is comparable to the size of the core where λ ~ 0.5mm for Al and ~ 0.25mm for W. This is a constant property of the material in a wire array Z-pinch and does not vary for different inter-wire separation and for different initial wire diameters. Quantitatively, the value of ka, where k is the wavenumber of instability and a the radius of the core, is roughly constant (ka ~ 1.6 for Al and ~ 1.3 for W). A constant wavelength up to 80% of implosion time suggests that the size of the region where the coronal plasma is generated does not change significantly. The large extent at which the instability structure is maintained in the inward radial direction [δR ~ (5-10)λ] indicates a force-free character of the plasma streams inside the array. Its worth noting that the maxima and minima of plasma streams are not correlated between different wires of the same array [23].

Redistribution of mass and formation of the precursor column

As the ablated coronal plasma streams arrive at the array axis, it assembles itself into a precursor column of plasma [26] (Figure 1.10). The diameter of this plasma column is practically constant in time (for a particular material) and is assumed to be in a dynamic pressure equilibrium with the incoming flux of coronal plasma [23, 27].

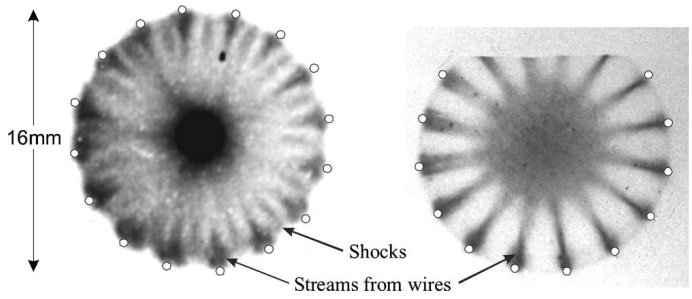

Figure 1.10: End-on XUV emission from 16mm diameter arrays of (left) 16×20μm Al at 134ns and (right) 16×13μm W at 134ns showing the formation a precursor at array axis [27].

To estimate the mass distribution m in the array during the first 80% of implosion time before the onset of implosion, a simple phenomenological model of ablation rate was developed by Lebedev et al [23]. This model assumes plasma leaving the

wire core are practically without current and travel at a constant velocity v_{abl}. Using the modified version of Newtons 2nd Law for a variable-mass system, the rate of mass ablated could be written as

$$v_{abl}\frac{dm}{dt} = -\frac{\mu_0 I^2}{4\pi R_0} \tag{1.2}$$

where I is the current through the array and R_0 is the array radius. By integrating this equation it has been possible to construct the radial mass distribution at some moment of time t_0. For a 16mm diameter 32×15μm Al wire array driven by current from the MAGPIE generator [I ~ I_0 SIN^2(πt/125ns)] and using the experimentally measured v_{abl} ~ 1.5×10^7 cms^{-1}, the radial mass density distribution at 80% of implosion time was calculated by Lebedev et al [23] and is shown in Figure 1.11. In this calculation the radius of the precursor was assumed to be 1 mm.

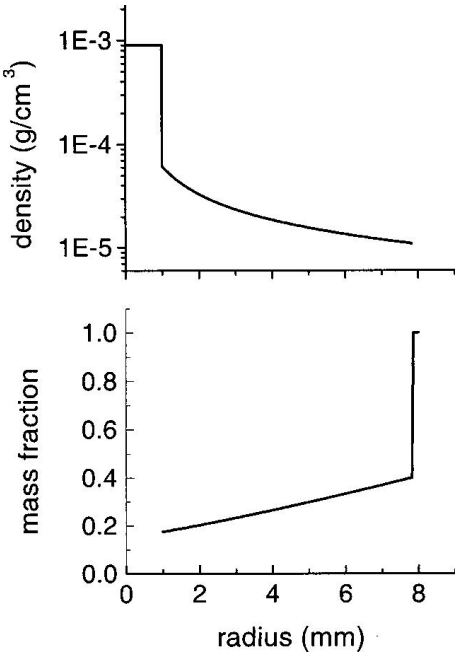

Figure 1.11: (Top) Radial density profile for a 32×15μm Al wire array calculated from the ablation model (integration of Eq(1.2)) at t_0=230ns corresponding to 80% of implosion time. (Bottom) Radial profile of the accumulated mass by integrating the radial density plot [23].

The accumulated mass fraction vs radius plot shows that at 80% of implosion time, just before the onset of implosion, ~ 17% of the mass is in the precursor, ~ 23% is between the edge of precursor and R_0 and the remaining ~ 60% are in the

wire cores at the initial array radius. This redistribution of mass from a 'shell-like' structure is the main reason why the implosions of wire arrays with large enough inter-wire separation deviates from a 0D implosion trajectory.

Snowplough implosion and stagnation

The removal of mass from wire cores into the array cavity appears to be nonuniform along the axial length. At 80% of implosion time, gaps appear in the wire core along the axial length (Figure 1.12). The average distance between the gaps for Al wire arrays is ~ 0.5mm [23], identical to wavelength of ablation streams in Al wire arrays. The ablation streams in Figure 1.12 appears to be correlated to the 'bulges' rather than the gaps, indicating a strong axial motion of plasma over a very short radial distance due to MHD activity.

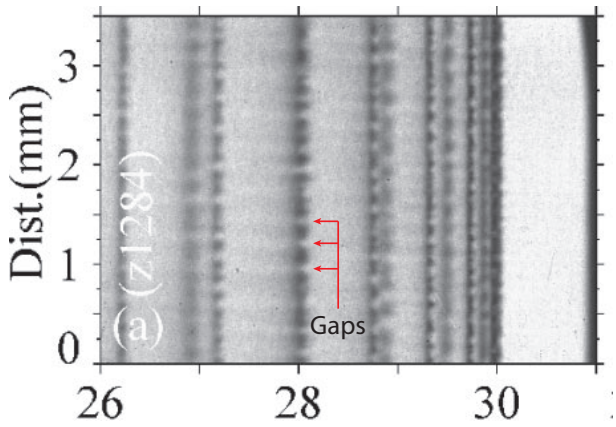

Figure 1.12: X-ray radiograph from the Z facility of an 11μm Cu wire array clearly showing the formation of gaps prior to implosion [28].

The formation of gaps along the wire length breaks up the current path along the wire and current switches to the plasma pre-fill. The actual radial position of this current sheath is not precisely known and will strongly affect how much mass from the wire cores at initial radial position participate in the implosion. As soon as the current switches to the plasma pre-fill it begins to implode. The imploding piston constantly accretes mass as it moves towards the array axis [29]. The implosion trajectory of a 32×15μm Al wire array along with a 0D model and a 1D snowplough model with different initial fraction of 'piston' mass at R_0 is shown in Figure 1.13(a). The snowplough implosion model was calculated using the radial mass distribution presented in Figure 1.11. This distribution does not take into

account the azimuthal and axial asymmetries from discrete wires and ablation instabilities.

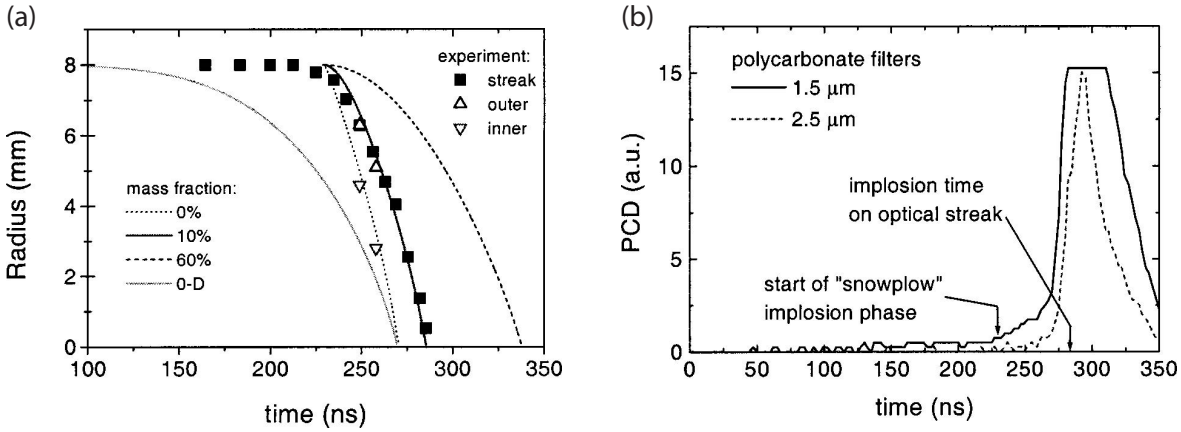

Figure 1.13: (a) Implosion trajectory of a 32×15μm Al wire array from an experiment in MAGPIE along with a 0D implosion fit and a snowplough model fit for different fraction of initial piston mass at R_0. (b) The corresponding X-ray pulse generated and detected by filtered PCDs [23].

The experimental data clearly deviates from a 0D implosion, and the best fit was a snowplough implosion model with an initial value of mass ~ 1/6 of the mass left in the wire core (10% of total array mass) at 80% of implosion time. This is a good indication that a significant amount of mass ~ 50 - 40% of the total array mass does not participate in the final implosion. At the start of implosion the X-ray pulse (Figure 1.13(b)) begin to rise gradually as the accreting piston which is in continuous collision with the pre-fill plasma radiates. The sharp rise in X-ray at ~270ns is when the current carrying piston impacts the precursor column. Later increase could be to do with further compression, ohmic heating and development of MHD instabilities of the plasma column on axis [30]. It is strongly believed that the trailing mass at the initial wire radius creates a secondary current path lowering the current into the 'piston' which drives the implosion and lowering the axial current at stagnation, thus reducing the total X-ray yield.

1.2.3 0D implosion of preconditioned wires

Mitigating the ablation process and hence snowplough implosion in wire array Z-pinches has been a challenge in the Z-pinch community for the past decade. Experiments conducted at the MAGPIE generator (Imperial College, London) in

2009 and 2010 - in which the author participated in - involving a two-stage wire array Z-pinch configuration [31, 32] have shown a dramatic change in implosion dynamics of wire arrays Z-pinch. The ablation phase was suppressed and wires expanded and imploded in a 0D manner similar to Figure 1.4(a). In this section we describe the experimental setup of such an array and the different dynamical processes involved from the very start of current pulse until the final stagnation.

Experimental setup of a two-stage wire array Z-pinch

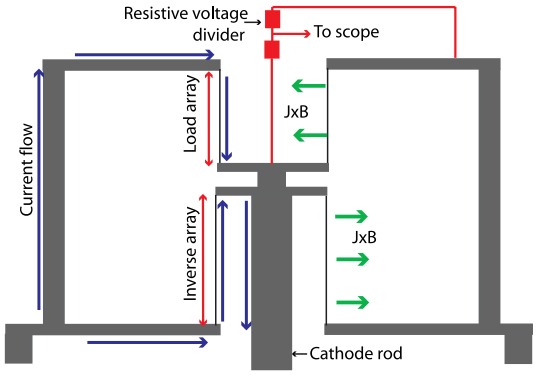

Figure 1.14: Schematic diagram of a two-stage wire array Z-pinch configuration [31].

This configuration consists of two cylindrical wire arrays, one placed on top of the other and connected as a parallel circuit providing two separate paths for the current (Figure 1.1.4). The bottom section is an inverse wire array where the magnetic field produced by the central cathode rod generates a J×B force pushing the ablated coronal plasma radially outward. The top section is a normal imploding load wire array with a J×B force acting radially inward. The heights of the inverse and load arrays were varied in the range 20-50 mm and 20-30 mm respectively.

Initial current prepulse into the load array

At the start of the current pulse the impedance of the two arrays is mainly governed by their resistance value and hence the current division. The resistance R of the arrays can be found using Eq(1.3).

$$R = \frac{\rho l}{nA} \tag{1.3}$$

Where n is the total number of wires in the array, ρ is the material resistivity, l is the wire length and A is the cross-sectional area of a wire. At this early stage the current in both arrays heats up the wires. This resistive current division stops when voltage breaks-down at the inverse array by the formation of plasma (highly conductive). The current now takes the least inductive root which is through the inverse wire array. In between the current start and voltage break down at the inverse array a ~ 25ns, ~ 5kA prepulse current was detected into the load (Figure 1.15). From the prepulse current and voltage measurements the average energy deposited into the load array is ~ 2-3 eV/atom [31].

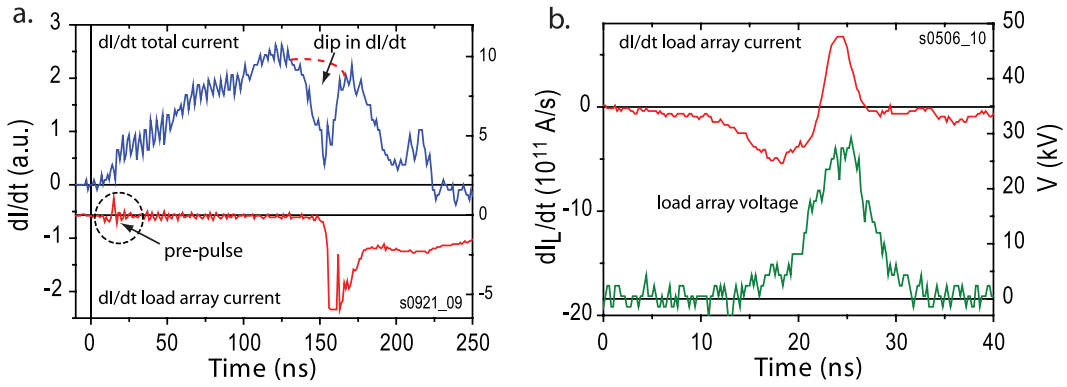

Figure 1.15: (a) Plot of total dI/dt (blue) and dI/dt in the load array (red). (b) Plot of dI/dt (red) and voltage (green) in the load array during the initial prepulse phase. Both (a) and (b) are for a 17mm diameter 8×15μm Al wire array load [31].

Preconditioning phase

The above figure of dI/dt into the load array shows that after the prepulse, dI/dt falls down to nearly zero. It cannot be clearly seen in this plot, but in other experiments including the ones conducted in this thesis shows that the value of dI/dt during this phase (i.e after the prepulse) does not fall down to zero. It stays roughly constant at a relatively low level. This is caused by the private magnetic flux escaping from the gaps in between the wires. As the current increases so does the magnetic flux and a changing magnetic flux generates a voltage (hence current) across the load. The inductance of an ideal cylindrical array L_{array} can be divided into two parts: the inductance caused by the global magnetic field L_{global}

and the inductance caused by the escaping magnetic fields in between the wires $L_{private}$ [33].

$$L_{array} = L_{global} + L_{private}$$
$$L_{array} = \frac{\mu_0 l}{2\pi}\ln\frac{R_{rp}}{R_a} + \frac{\mu_0 l}{2\pi}\frac{1}{N}\ln\frac{R_a}{NR_w} \quad (1.4)$$

Where l is the length of the array, N is the total number of wires, R_{rp} is the radial position of the return posts, R_a is the array radius and R_w is the wire radius. We can see from Eq(1.4) that as N becomes large, the contribution of $L_{private}$ to the total inductance becomes negligible and the array inductance approaches that of a 'cylindrical can' load ($L_{array} \rightarrow L_{global}$). For a 'cylindrical can' inverse array, $L_{private}$ = 0 and no voltage is generated at the load section.

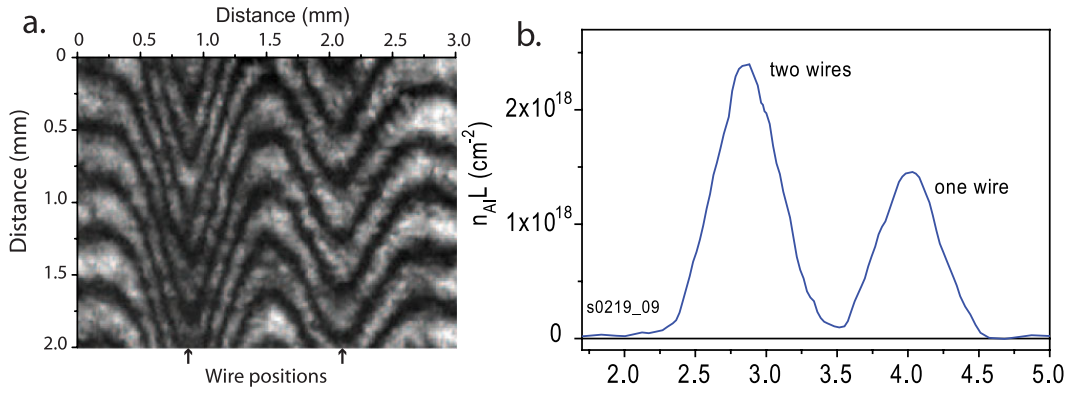

Figure 1.16: (a) Interferometric image of an 8×15μm Al array taken during the preconditioning phase (after the prepulse and before the current switch) and the corresponding line density is shown in (b) [31].

During this phase where very little current goes through the array, interferometric images show a drastic change in wire structure (Figure 1.16). By having a phase of nearly zero current for ~ 150ns after the prepulse current have deposited some energy into the wires; the wires managed to 'freely' expanded into columns of mainly neutral gas to ~ 1mm in diameter with no presence of a core and no detectable perturbations on the outer edges (another indication of low level current passing through). This expansion of wire is referred to as the *preconditioning effect*. Comparing the total number of atoms per length (integrating line density plot in Figure 1.16(b)) to the real number of atoms in solid wires suggests that ~ 70% of

the wire mass has been converted into Al gas. The remaining mass could be in the form of liquid droplets or clusters that are not detected by the interferometer [31].

Current switch and implosion of load array

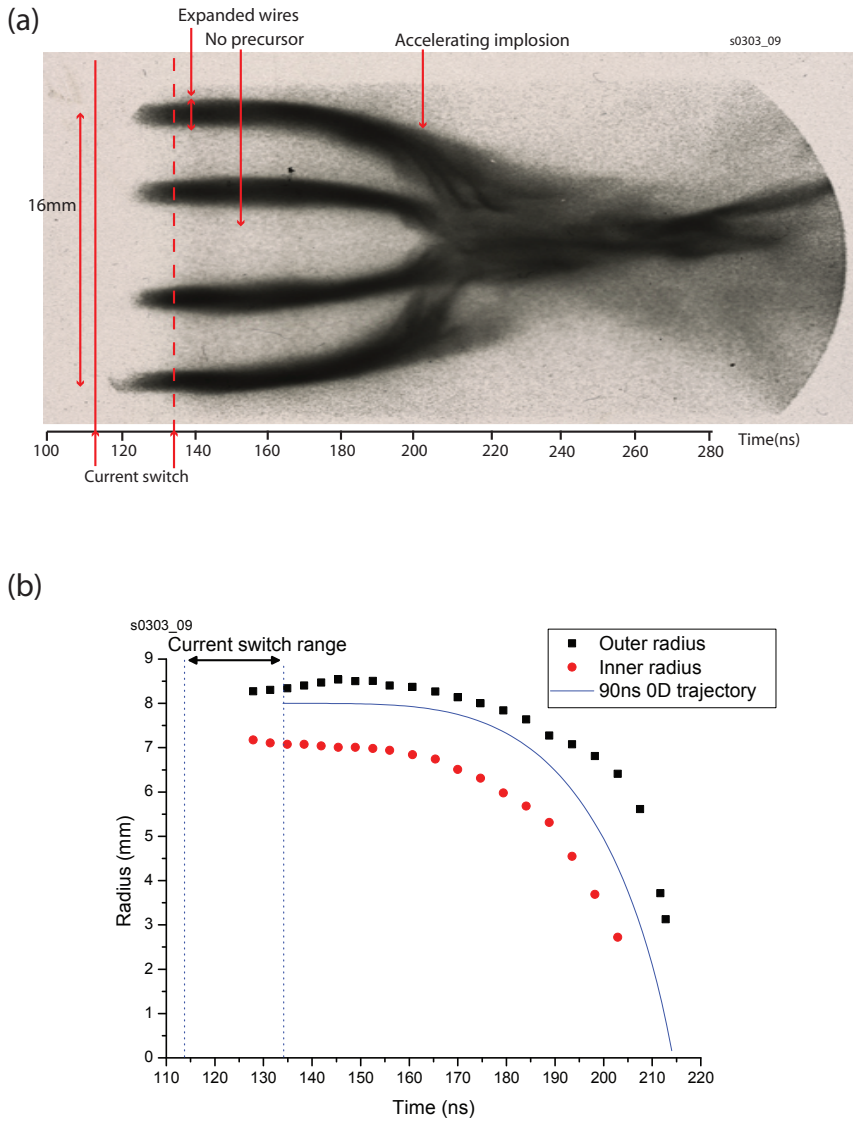

Figure 1.17: (a) Optical streak image of a radial slice looking at a 16mm diameter 8×10μm Al load array and (b) the corresponding implosion trajectory along with a 0D implosion model of a linearly rising current reaching a Max of 1.4MA in 90ns [32].

During the preconditioning phase the inverse wire array continuously ablate coronal plasma radially outwards in a similar fashion (with axial instability of ~ constant λ) [32] to standard imploding wire arrays discussed earlier (Section 1.2.2). Once gaps start to form in the cores along the length of the wires, the inverse

array begins to explode. This increases the impedance of current through this array and triggers a fast current switch into the *preconditioned* load array. This switch of current into the load can be seen as a fast rise in the load's dI/dt at ~ 150ns in Figure 1.15(a).

As the current switches into the load, it ionises the whole bulk of the wire (no core-corona structure). Optical streak camera image (Figure 1.17(a)) shows an accelerating implosion with no ablation, plasma pre-fill and precursor column. The J×B force acts upon all the mass at the initial array radius and implosion trajectory (Figure 1.17(b)) is consistent with a shell-like 0D implosion driven by linearly increasing current reaching a maximum of 1.4MA in 90ns [32].

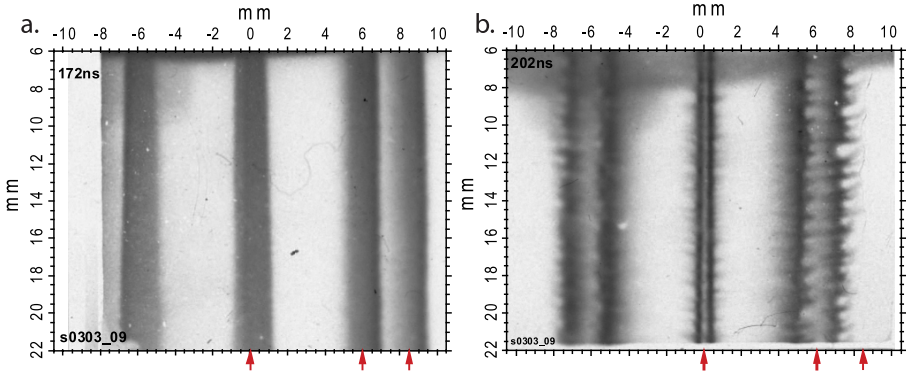

Figure 1.18: XUV images showing the development of R-T instability during the implosion phase of an 8×15μm Al wire array load. Arrows show the initial position of wires [31].

As soon as the wire array converges towards the axis, Rayleigh-Taylor (R-T) instability begins to develop along the length of the wires. XUV images (Figure 1.18) shows that by the time the wires have moved inwards by ~ 1.5mm, R-T instability of λ ~ 0.8mm has grown to an amplitude of ~ 0.4mm. By applying the theory of R-T instability growth during the linear stage in a converging 'thin-shell' [15] (Section 1.4 in this thesis), the initial amplitudes of those instabilities at the time of current switch was estimated to be ~ 0.8 - 1.5μm. This suggests that the current prepulse produces a low level of initial perturbation around the surface of individual wires [31].

The fact that all the mass participated in the implosion of the load array, and the lack of trailing mass at the initial radial position which maximises the current in the stagnated plasma did not generate a better X-ray pulse than a standard wire array. R-T instabilities develop much faster in a shell-like implosion than a snowplough implosion, due to the continuous accretion of mass in the 'piston' of the later implosion. It is thought that this is the main reason why the imploding array in a two-stage wire array Z-pinch generated a lower X-ray pulse. This is based on PCD results from few experiments using this configuration and further investigation is needed to assess X-ray production from different load wire arrangements.

1.3 1D model of Z-pinch plasma implosion

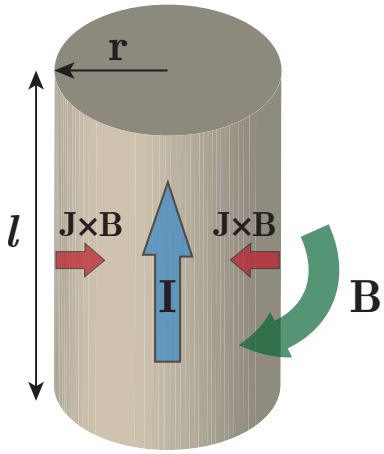

Figure 1.19: Schematic diagram of a structureless, perfectly conducting cylindrical plasma.

In this section we reproduce the analytical 1D model of a cylindrically converging plasma in the simplest possible system presented by Ryutov et al [15]. Starting from a structureless (no presence of instability), perfectly conducting cylindrical plasma (Figure 1.19), where the current I is localised on the surface and does not penetrate the cylindrical object. The current generates an azimuthal magnetic field **B** around the surface of the object. The interaction of the current density **J** and magnetic field **B** generates a **J×B** force density. Using Amperes Law and the appropriate vector identity, the **J×B** force density could be written as,

$$\mathbf{J}\times\mathbf{B}=\frac{1}{\mu_0}\left(\mathbf{B}\cdot\nabla\right)\mathbf{B}-\nabla\left(\frac{B^2}{2\mu_0}\right) \tag{1.5}$$

The first term in this equation corresponds to the curvature tension force and the second term is the magnetic pressure gradient. Considering an infinitesimal thin layer of current-carrying region as in our model, the pressure just outside this region is $B^2/2\mu_0$ while the pressure just inside this region is 0 (since there is not current penetrates into the cylindrical object). The pressure difference generates a radially inward force **F** on the surface of the object,

$$\mathbf{F}=-2\pi rl\times\frac{B^2}{2\mu_0} \tag{1.6}$$

where the first term on the right hand side is the area of the curved surface of the cylindrical object and the second term is the pressure difference. We can write B in terms of I by applying Ampere's Law on a perfectly conducting cylindrical object

$$\begin{aligned}&\oint B\cdot dl=\mu_0 I\\&\Rightarrow B=\frac{\mu_0 I}{2\pi r}\end{aligned} \tag{1.7}$$

In this section two types of implosion models are explored which are characterised by their initial mass density distribution:

- A 0D implosion model were all the array mass is concentrated in an annular shell located at the array radius (applicable to preconditioned wire array implosions).
- A snowplough implosion model were the array mass is smoothly distributed inside the array cavity and mass density only varies in the radial direction (applicable to standard wire array implosions).

1.3.1 0D implosion

This type of implosion applies to a thin annular cylindrical plasma. The J×B force accelerates the plasma shell radially inwards. The equation of radial motion for this system can be written as,

$$\frac{m_0}{2\pi r}\ddot{r} = -\frac{B^2}{2\mu_0} = -\frac{\mu_0 I^2}{8\pi^2 r^2} \tag{1.8}$$

where m_0 is the total mass per length of the imploding plasma, B=$B(t)$ and I=$I(t)$.

By quantifying I in units of the maximum current $I_{\max}$, the time t in units of the time it takes current to reach maximum value τ and r in units of the initial radius r_0, we can write Eq(1.8) in the following dimensionless variables,

$$\begin{aligned} \tilde{r} &= r/r_0 \\ \tilde{t} &= t/\tau \\ \tilde{I} &= I/I_{\max} \end{aligned} \tag{1.9}$$

Hence Eq(1.8) becomes,

$$\tilde{r}\ddot{\tilde{r}} = -\Pi\tilde{I}^2 \tag{1.10}$$

where,

$$\Pi = \frac{\mu_0 I_{\max}^2 \tau^2}{4\pi m_0 r_0^2} \tag{1.11}$$

is a dimensionless scaling parameter known as the 'pinch parameter'. Two implosions with the same functional dependence of current on time, i.e $\tilde{I}$=$\tilde{I}(t)$, occur in a similar fashion if their parameter Π is the same, for which their implosion time in units of τ would be the same. For the optimum efficiency in converting the stored electrical energy into kinetic energy of imploding plasma, one has to choose Π so that implosion time of the pinch (time of stagnation) coincides with the time of maximum current τ.

1.3.2 Snowplough implosion

This type of implosion applies for a cylindrical plasma where the mass smoothly varies in the radial direction (for simplicity we will assume no mass density variation in the z and θ direction). In this model the J×B force accelerates the current-carrying surface ('piston') radially inwards which continuously accretes all the mass it impacts between r_0 to r. We also assume no shock is formed ahead of the 'piston' which is a good approximation for implosions of high Z material with strong radiation losses. Starting from the modified version of Newton's 2nd Law for a variable-mass system,

$$F_{ext} + v_{rel}\frac{dm}{dt} = m\frac{dv}{dt} \tag{1.12}$$

where F_{ext} is the external force (J×B) acting on the 'piston', v_{rel} is the relative velocity of the incoming mass with respect to the centre of mass of the imploding piston, m is the instantaneous mass accreted on the piston and v is the velocity of the piston. By substituting Eq(1.6 & 1.7) into Eq(1.12), we obtain the equation of radial motion of the magnetic piston in a snowplough implosion,

$$\frac{m}{2\pi r}\ddot{r} - \rho(r)\dot{r}^2 = -\frac{\mu_0 I^2}{8\pi^2 r^2} \tag{1.13}$$

$$\dot{m} = -2\pi r\dot{r}\rho(r) \tag{1.14}$$

where m in this equation represents the instantaneous mass per length of the piston and $\rho(r)$ is the initial mass density distribution. Again we can write this equation of motion in dimensionless variables (Eq(1.9)), and therefore Eq (1.13 & 1.14) becomes,

$$\tilde{m}\ddot{\tilde{r}} - 2\tilde{r}\dot{\tilde{r}}^2\tilde{\rho}(\tilde{r}) = -\Pi\frac{\tilde{I}^2}{\tilde{r}} \tag{1.15}$$

$$\dot{\tilde{m}} = -2\tilde{r}\dot{\tilde{r}}\tilde{\rho}(\tilde{r}) \tag{1.16}$$

where

$$\tilde{m} = m/m_0$$
$$\tilde{\rho} = \rho/\rho_0, \rho_0 = m_0/\pi r_0^2 \tag{1.17}$$

Two snowplough implosions are identical if they have a similar Π and a similar initial density distribution dependence on r/r_0. We can see that by setting the initial density distribution to zero and the initial mass per length of the piston to the total mass per length m_0, then we obtain the the 0D implosion equation of motion shown in Eq(1.10).

1.4 Growth of Rayleigh-Taylor instability

Rayleigh-Taylor (R-T) instability is a common instability in fluid dynamics. It happens when a lighter (low density) fluid is accelerated into a heavier fluid (higher density). In the case of a magnetically driven radial implosion, the magnetic field around the plasma acts as the 'low density fluid' while the plasma is the 'higher density fluid'.

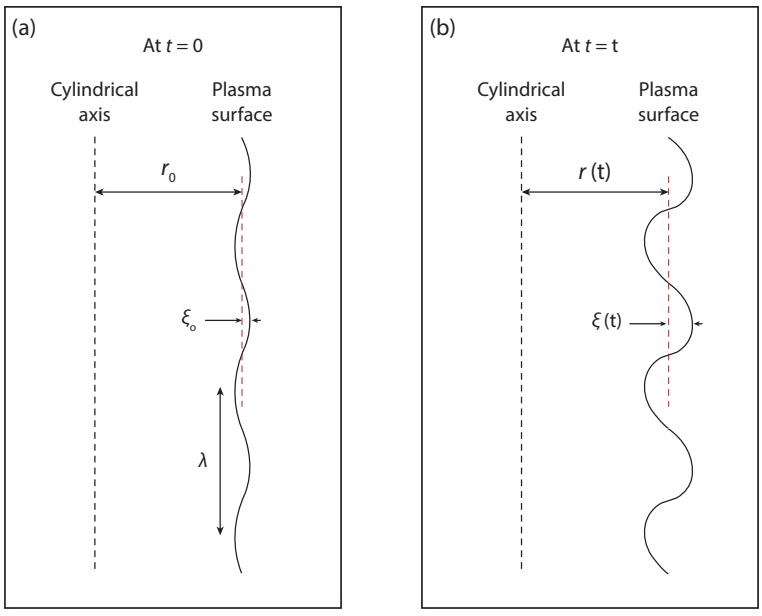

Figure 1.20: Cross-section diagram in r-z of a cylindrically imploding plasma, showing the growth of Rayleigh-Taylor instability after some time t.

For a cylindrically converging plasma shell (Figure 1.20), the initial linear stage of R-T instability growth from an initial perturbation ξ_o can be written as [15],

$$\xi(t) = \xi_o \exp\Big[G(t)\Big] \tag{1.18}$$

where the factor $G(t)$ depends on the growth rate Γ by the following equation,

$$G(t) = \int_0^t \Gamma(t')\,dt' \tag{1.19}$$

and Γ depends on the instability wave-vector k (=$2\pi/\lambda$) and acceleration a.

$$\Gamma = \sqrt{ka} \tag{1.20}$$

This linear approach breaks down when the amplitude ξ reaches ξ_{NL}, and happens at the instant of time when,

$$G(t) = \ln\left(\frac{\xi_{NL}}{\xi_o}\right) \tag{1.21}$$

The initial perturbations are quite small and a few order of magnitude less than ξ_{NL}. Hence, the logarithm in Eq(1.21) weakly depends on both ξ_{o} and ξ_{NL} and the value of G at this instant is ~ 4-5 [15].

Assuming the shell maintains its initial thickness as it implodes (as in the 0D implosion model), then the radial acceleration is determined by the 0D implosion equation of motion Eq(1.10). Therefore by substituting Eq(1.10) into Eq(1.20), the growth rate can be written as,

$$\Gamma = \sqrt{k(r_0\ddot{\tilde{r}})} = \sqrt{kr_0}\sqrt{\frac{\Pi}{\tilde{r}}\tilde{I}} \tag{1.22}$$

hence,

$$\frac{G}{\sqrt{kr_0}} = \sqrt{\frac{\Pi}{\tilde{r}}}\int_0^t \tilde{I}\,dt' \tag{1.23}$$

Eq(1.23) can be approximated to [31],

$$\frac{G}{\sqrt{kr_0}} \sim \sqrt{1-\tilde{r}} \times F \tag{1.24}$$

where F is the form factor which depends on the temporal profile of driving current, and varies between 1.63 - 1.83. Eq(1.24) shows that the growth rate weakly depends on the current temporal profile, but strongly depends on the radial position of the plasma shell. Therefore for a given F, we can estimate the value of G (hence the growth rate) just from the radial position of imploding plasma. To illustrate this dependence, a plot of $G/\sqrt{kr_0}$ vs radial convergence ($=r_0/r$) for a sine wave current with Π corresponding to peak current at stagnation [15] is shown in Figure 1.21.

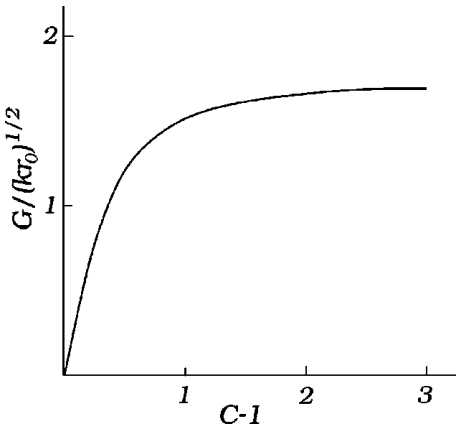

Figure 1.21: Plot of $G/\sqrt{kr_0}$ vs Convergence C for a cylindrically imploding shell with Π corresponding to peak current at stagnation for purely axis-symmetric perturbations [15].

For $k \sim 1/h$, where h is shell thickness and is equal to $0.1r_0$, nonlinear effects become important at a convergence equal to ~ 4 [15].

1.5 Thesis outline and authors contribution

In this research we further investigate the two-stage wire array Z-pinch configuration. Many aspects and properties of this configuration could be varied including wire material for both or one of the arrays, ratio of lengths of arrays,

wire number, wire thickness..etc, and variations in current prepulse, preconditioning effect or current switch properties could be measured. However one of the major aims of this investigation is to create and implode a cylindrical plasma shell load. The implosion of a shell in a 0D manner could have potential applications in Z-pinch ICF such as in a dynamic hohlraum. The idea is to precondition a load of large number of wires with a small inter-wire separation to achieve wire merging before the main current switch into the load. Experiments involving a two-stage wire array configuration were only performed on 8 wire loads of Al [31]. Therefore our initial investigation was to test if the preconditioned effect of this two-stage configuration was sensitive to variation in load wire number. We have investigated cylindrical array loads of 2, 4, 8 & 16 Al wires in this setup while keeping the load mass per length constant. The preconditioning effect was analysed from laser interferogram images presented in Chapter 3 Section 3.1.

The two-stage configuration is designed to rapidly switch the current into the load. Obtaining a direct measurement of current in the load is crucial for analysing the implosion dynamics. Attempts by Harvey-Thompson [32] to measure the current using Rogowski probes placed at one of the loads return posts and around the load itself were not successful. Therefore an experiment with a specially designed current-measuring load was conducted (Chapter 3, Section 3.2) in order to obtain a direct measurement of current at the load section after the switch. Those experiments have shown that the current switch is not simply due to resistive current division when the inverse array explodes, but a more complicated mechanism involving a plasma-flow switch takes place.

By showing that the preconditioning effect of the load wires in a two-stage wire array configuration is not sensitive to the number of wires from 2 up to 16 (keeping the mass per length constant), we thought of re-visiting the single wire Z-pinch but as a load in a two-stage configuration. Experiments were conducted of a single Al wire load on axis (Chapter 4) of different thicknesses (25, 40 & 50μm) and hence different mass per length. The preconditioning effect was analysed again from laser interferogram images however this time we used images from two different laser wavelengths in order to differentiate the free electrons from the

atoms. Implosion dynamics were investigated from images obtained by XUV, optical framing and optical streak camera. X-ray generation was analysed from filtered PCD signals and filtered time integrated camera.

The final part of this research (Chapter 5) was to create and implode a plasma shell by preconditioning a large number of wires with a small inter-wire separation. Before attempting to create a shell we did some preliminary experiment to explore any dynamics that could arise between preconditioned wires at close proximity. Experiments were also done on linear array loads to investigate the minimum inter-wire spacing needed to form a shell. This is because overlapping wires in a side-on image of a cylindrical array geometry makes it difficult to judge if adjacent wires have or have not merged. A shell was formed from a 16×10μm and a 16×15μm Al wire on an 8mm diameter cylindrical array. Again wire array density measurements before the switch was obtained from a two-wavelength laser interferometry analysis, while implosion trajectory data was obtained from XUV, optical framing and optical streak camera. X-ray pulse data at stagnation was obtained from filtered PCD signals and filtered time integrated pinhole camera.

All of the experiments presented in this thesis were carried out at the 1.4MA, 250ns MAGPIE generator at Imperial College London. The experiments were conducted with the help of a team of experienced post-doctoral researchers and PhD students were the author took the leading role in managing the experiments and building the array hardware for the results presented in this thesis. In the same way, the author was part of this team to assist other MAGPIE members conducting their experiments including the first ever experiments of a two-stage wire array Z-pinch published by Harvey et al. [31, 32]. The author has contributed throughout his PhD to the general operation and maintenance of the MAGPIE generator and diagnostic equipments.

All the data were analysed by the author with the help and advice from the MAGPIE team members. The MATLAB program used to interpolate the 'traced fringe images' and generate a 2D Map was developed by Dr. George Swaddling in which the author is highly appreciative for allowing him to use this program for

fringe-shift analysis. Implementation of the fringe traced images into this program to generate a 2D fringe-shift map and subsequent analysis was solely done by the author himself.

Chapter 2

MAGPIE Generator and Diagnostics

The Mega Ampere Generator for Plasma Implosion Experiments (MAGPIE) facility includes the 1.4MA in 250ns pulsed power generator along with various electrical and plasma diagnostic equipments. All results presented in the following chapters are from experiments conducted in this facility. This chapter describes the main features of the MAGPIE generator and the various diagnostic equipments used in our experiments.

2.1 The MAGPIE generator

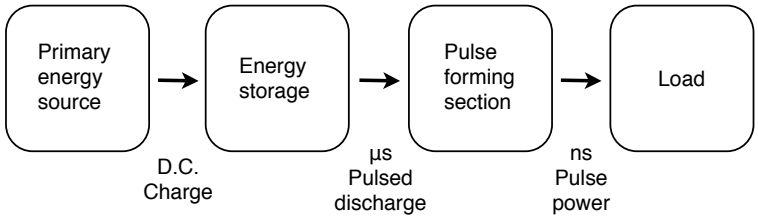

Figure 2.1: Block diagram showing the various stages in high pulsed power system.

The basic working principle of a pulsed power device is summarised in Figure 2.1. The first step is energy storage in a bank (such as a capacitor bank) from a primary source at a relatively low power level and a long time (~ few mins). This energy is then discharged over a µs time scale into a pulse forming section. This section rapidly compresses the pulse in time and by using fast (spark-gap) switches, a high power pulse in the range of 50-250ns is discharged into the load.

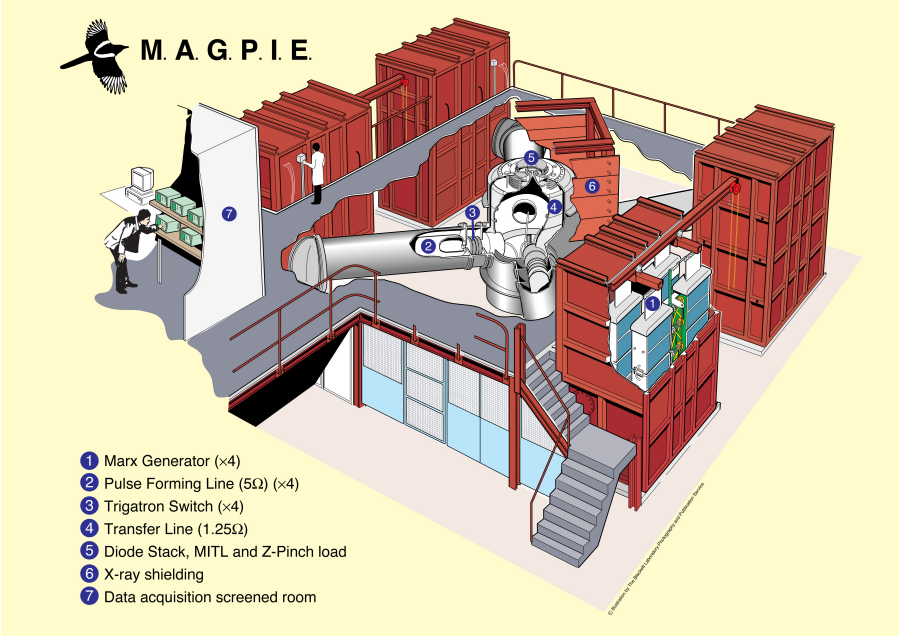

Figure 2.2: A diagram showing the layout of various parts of the MAGPIE generator.

The MAGPIE generator is a high impedance generator (1.25Ω at the load section), giving rise to a peak current pulse of 1.4MA in 250ns [34]. The layout of various components of this generator can be seen in Figure 2.2. The generator consists of 4 Marx bank capacitors inside oil-filled tanks located in the four corners of the lab. Each bank is connected to a pulse forming line (PFL) of 1m diameter × 3.3m long. The PFLs are all connected to a single transfer line (2m diameter × 2.17m tall) at the centre of the lab, which transmits the current pulse up into the load section. Data acquired from various diagnostics around the load chamber are recorded in the screened room. The following part of this section describes each of MAGPIE generator components in more detail.

2.1.1 Marx banks

The MAGPIE generator consists of 4 Marx banks. Each consists of 24 × 1.3μF high voltage capacitors. The capacitors are charged in parallel in a bi-polar configuration, where adjacent capacitors are charged with opposite polarities (Figure 2.3 left diagram). Those oppositely charged capacitors are connected together by spark-gap switches. Each Marx bank contains 12 of those switches which are filled with SF_6 gas. Once the capacitors are charged to the desired voltage V_{charge}, a trigger pulse from a separate smaller Marx, breaks-down the first

5 spark-gap switches leading to a cascade effect and the self breakdown of all other spark-gap switches. The Marx is discharged in series (Figure 2.3 right diagram) generating an output voltage $V_{Marx} = 24 \times V_{charge}$. In our experiments, each Marx was charged to $\pm$ 65kV generating an output voltage $V_{Marx} = 1.56$ MV.

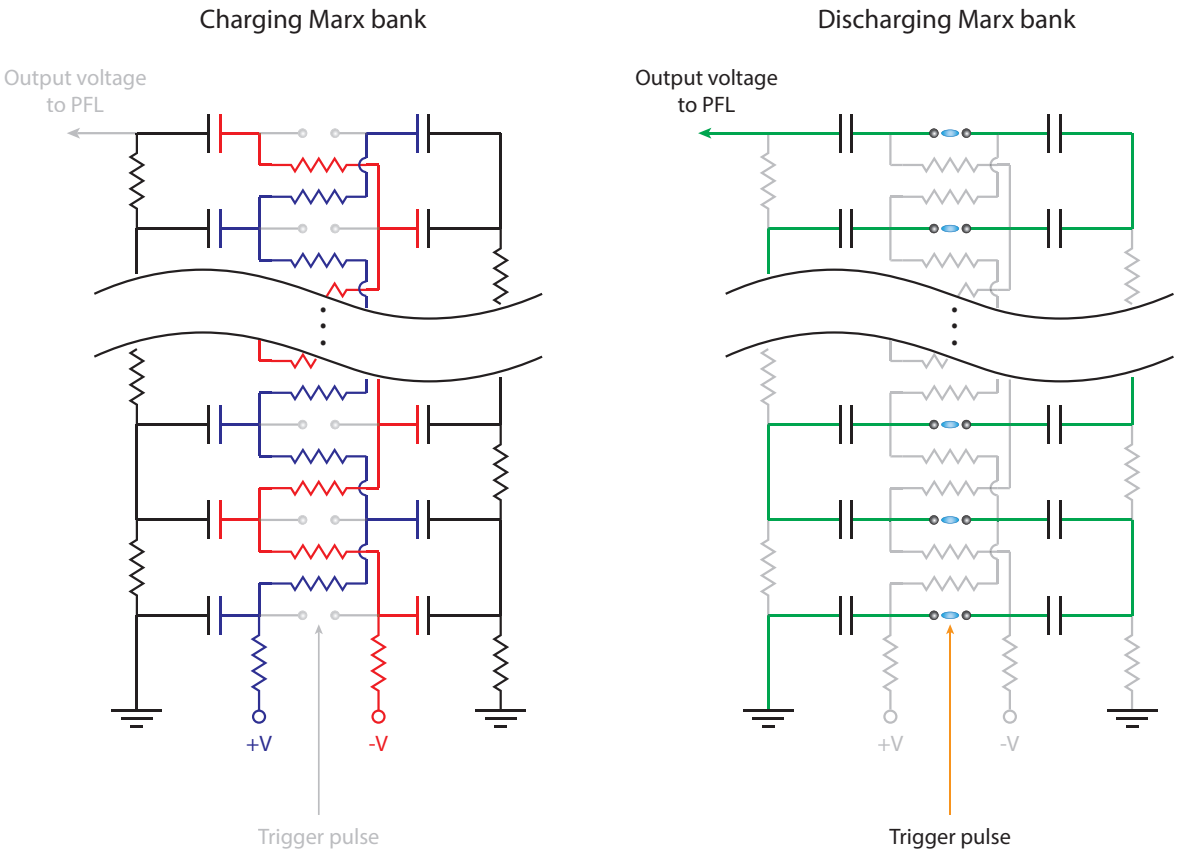

Figure 2.3: Diagram showing (left) the parallel charging of a Marx bank capacitors in a bi-polar configuration and (right) the series discharge initiated by a separate trigger pulse into one of the spark-gap switches causing a cascade effect and the self break-down of the the other switches.

2.1.2 Pulse forming lines

Each Marx bank discharges its voltage into a pulse forming line PFL. This is simply a coaxial transmission line filled with de-ionised water. The inner and outer radius are 0.25 and 0.53m respectively. The aim of the PFL is to compress the µs-timescale pulse from the Marx bank into a ns-timescale pulse. The time it takes to charge the PFL t_{charge} and voltage reached V_{PFL} is given by [34],

$$t_{\text{charge}} = \pi \sqrt{\frac{L_{Marx} C_{PFL} C_{Marx}}{C_{PFL} + C_{Marx}}} \tag{2.1}$$

$$V_{PFL} = \frac{2C_{Marx}V_{Marx}}{C_{PFL} + C_{Marx}} \tag{2.2}$$

where L_{Marx} and C_{Marx} are the inductance and capacitance of the Marx bank respectively, and C_{PFL} is the capacitance of the PFL. For effective voltage transfer $C_{Marx} \geq C_{PFL}$.

Once fully charged, the PFL discharges this voltage with an amplitude equal to half the charging voltage and a period equal to double the transit time τ. MAGPIE was originally designed for radiative collapse studies requiring a high impedance generator of ~ 1.25Ω and a pulse length of ~ 200ns. This means a PFL length equivalent to a transit time τ of ~ 100ns and an impedance Z of ~ 5Ω. The capacitance of the PFL can be calculated from values of τ and Z using the following equation [34],

$$C_{PFL} = \frac{\tau}{Z} m^{-1} \tag{2.3}$$

Hence the maximum voltage generated across the PFL (using Eq(2.2)) is ~ 2.28MV.

2.1.3 Trigatron switches

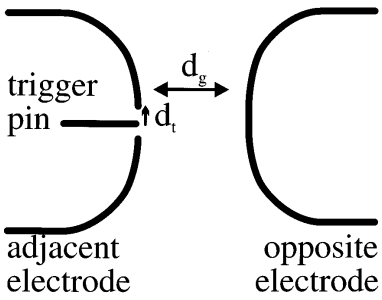

Figure 2.4: Diagram showing the three electrodes in a trigatron switch [34].

For the PFL to transfer a short ~ 200ns current pulse into the transfer line (hence the load) it needs a fast switching mechanism. This is achieved using oil-filled trigatron switches (Figure 2.4), with a trigger pin being concentric with one of the two main electrodes. A single unit is used to trigger all four switches

simultaneously, by sending a voltage pulse through the trigger pin. The discharge across the switch has two different routes [34]. One where a break-down happens between the trigger pin and the adjacent electrode generating UV and charged particle which then initiates the discharge across the main electrodes. The other route is the pin's voltage distorts the electric field between the two main electrodes causing a direct discharge between them. It has been suggested that the optimum operating regime for the switch is when both routes of break-down happen simultaneously. At this regime, a trigatron switch operating at voltages between 1 - 2 MV can be triggered by a voltage pulse as low as 2 - 4% of the operating voltage [34].

2.1.4 Transfer line and load section

All four PFLs discharge their current into a single coaxial transmission line (transfer line) positioned at 90° to the PFLs which transfers the combined pulse vertically upwards into the load section. It is filled with de-ionised water and possess an inner and outer radius of 0.83 and 1.0m respectively, producing an impedance of ~ 1.25Ω. The height of the transfer line is 2.17m corresponding to a transit time of ~ 65ns.

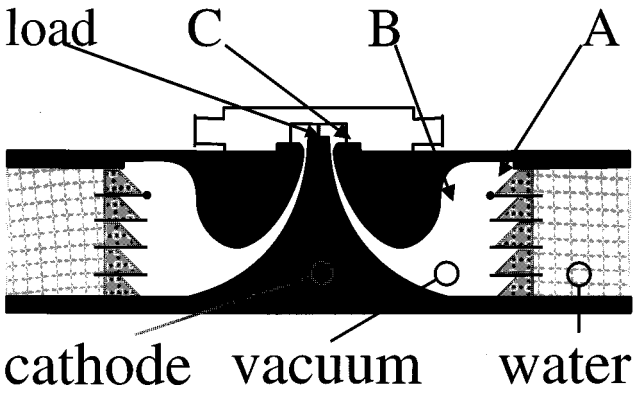

Figure 2.5: Diagram showing the diode-stack and the MITL which sits on top of the transfer line. B-dot probes for current measurements were placed at A, B and C [34].

The transfer line delivers current to the load via the magnetically insulated transmission line (MITL) shown in Figure 2.5. Both the load and the MITL are in vacuum while the transfer line is in water. The interface between the two medium

was a diode stack consisted of five Perspex insulator rings. The surface of the insulator facing the vacuum was machined at 45° with the normal pointing to the anode. This creates an E×B drift directing electrons away from the insulator surface and hence preventing an electron avalanche break-down. This is referred to as magnetic flash-over inhibition (MFI) and increases the voltage that can be held by the insulator.

The MITL focuses the current pulse into a ~ 4cm diameter load. At high voltages, electron emission form the current carrying surface can cause breakdown through the vacuum gap. However, the increase in magnetic field as the current moves up through the MITL ensures that the electron cyclotron orbit is less than the gap between the cathode and anode. The MITL has also been designed to prevent break-down of the diode stack from the Z-pinch UV radiation and to allow easy access of diagnostics. The final current pulse generated at the load section is shown in Figure 2.6.

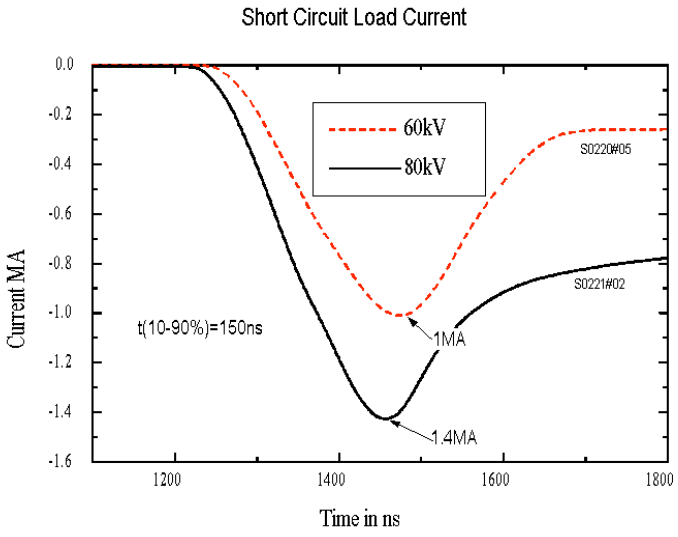

Figure 2.6: Final output current pulse at the load section from the MAGPIE generator [Reproduced from the MAGPIE website].

The high impedance property of the MAGPIE generator makes this final current relatively insensitive to the impedance of a dynamical plasma load, hence allowing for various array configurations such as coiled [35] and radial [36] wire array to be fired without significantly reducing current.

2.2 MAGPIE diagnostics

The MAGPIE generator produces a current pulse reaching a peak at 250ns on loads typically of the order of ~ few cm in dimension. The plasma dynamics would vary around the current pulse time scale and for an imploding plasma the length scale would shrink to the order of ~ few 100μm. Certain types of plasma dynamics (such as development of MHD instabilities) can happen at even smaller temporal and spatial scale. Therefore, in order to accurately assess and analyse such a 'compact' 'short-lived' plasma it is important to have diagnostic equipments of extremely high resolution in both temporal and spatial dimension.

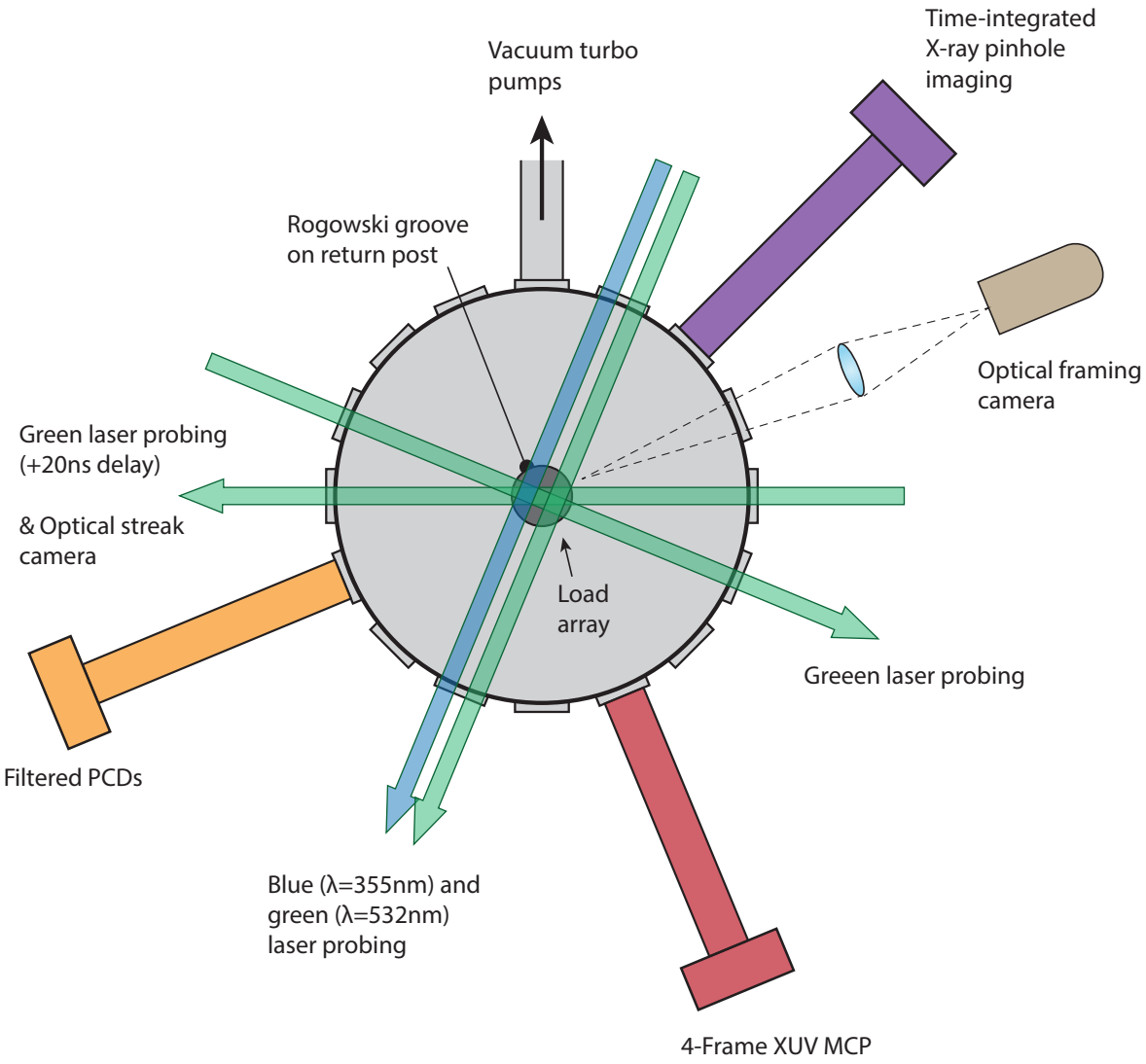

Figure 2.7: Layout of various diagnostics around MAGPIE's load vacuum chamber.

This section describes the various plasma diagnostic equipments (including current probes) available in the MAGPIE facility which were used to obtain the results presented in the following chapters. Figure 2.7 shows the layout of various diagnostic equipments around MAGPIE's load chamber.

2.2.1 B-dot probe

This probe is used to measure current at various points of the pulse power device. The B-dot data used in our experiments are taken from position B in Figure 2.5.

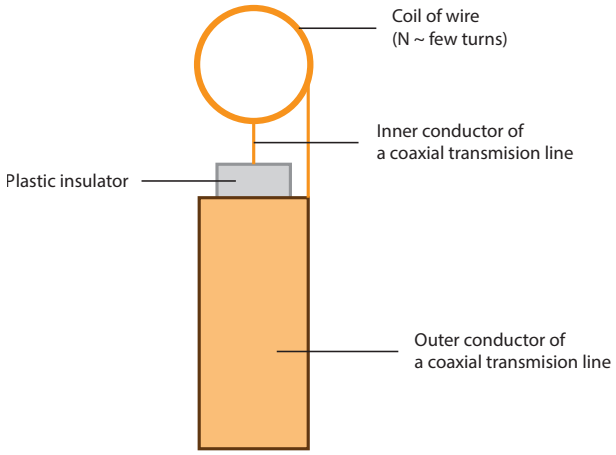

Figure 2.8: Diagram of a B-dot probe.

This probe consist of a coil of few turns with a diameter in the order of the size of the transmission line ~ 8mm. One end of the coiled wire is attached to the central conductor of the coaxial transmission line and the other end is attached to the outer conductor (Figure 2.8). A changing magnetic field B passing through the coil generates a voltage between the inner and outer conductor which is detected by oscilloscopes at the screened room. The rate of change in magnetic flux Φ through the coil is proportional to the voltage V generated as shown in Eq(2.4).

$$V = -\frac{d\Phi}{dt} \tag{2.4}$$

and assuming the magnetic field is constant in the space inside the coil,

$$\Phi(t) = N \times A \times B(t) \tag{2.5}$$

where A is the circular area of the coil. Then by integrating

$$B(t) = -\frac{1}{NA}\int V(t)\,dt \tag{2.6}$$

the magnetic field and hence current can be deduced from the B-dot voltage measurement at the scope. This probe has also been used in other Z-pinch experiments to measure the magnetic field at various points around the plasma [37]. In our experiments a proper geometric calibration has not been done for this probe due to its unaccessible location. However B-dot signals have been used to obtain a temporal profile of the current pulse.

2.2.2 Rogowski groove

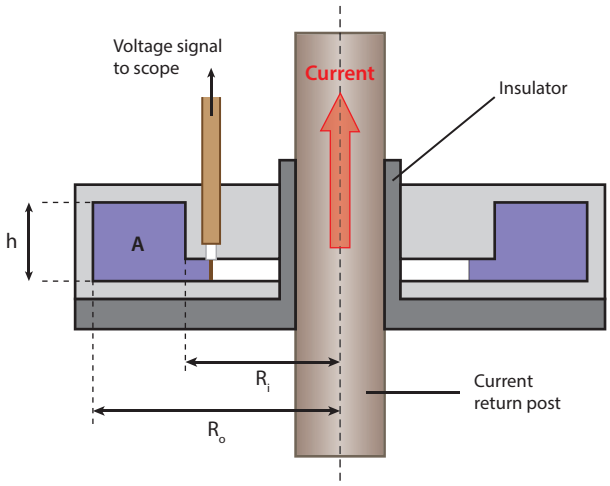

Figure 2.9: Schematic cross-sectional diagram of a Rogowski groove mounted around a current return post.

The Rogowski groove is used to measure current at the load section by placing it through one of the current return posts as shown in Figure 2.9. As current flows through the post it will generate an azimuthal magnetic field B_θ. Similar to the B-dot probe, the rate of change of magnetic flux Φ through area A is proportional to the voltage V generated across the top and bottom surface of the Rogowski groove. The coaxial transmission line detects this voltage and transmits the signal to the scope. Equations (2.7 & 2.8) show that the detected voltage signal is proportional to the rate of change of current through the return post.

$$\Phi = \oint \mathbf{B} \cdot d\mathbf{A} = \int_0^h \int_{R_i}^{R_o} \frac{\mu_0 I}{2\pi r} dr\, dz = \frac{\mu_0 I}{2\pi} h \ln\left(\frac{R_o}{R_i}\right) \tag{2.7}$$

$$V = -\frac{d\Phi}{dt} = -\left[\frac{\mu_0}{2\pi} h \ln\left(\frac{R_o}{R_i}\right)\right] \frac{dI}{dt} \tag{2.8}$$

Therefore the current through the load can be measured by integrating Eq(2.8) and multiplying by the appropriate number of return posts.

2.2.3 Optical framing camera

As soon as current flows through the load it begins to emit visible radiation. This optical self-emission of the load is focused into the aperture of a fast optical framing camera using a standard optical lens. The camera records the image digitally on frames with a 5ns exposer. This camera is able to record 12 frames per experiment at a minimum inter-frame timing of 10ns. 10 and 15ns inter-frame timings were set for our experiments to capture plasma implosion images after the current switches into the load.

2.2.4 Time integrated pinhole camera

A pinhole camera is the simplest form of camera where no focusing optics (such as lenses or mirrors) is required. It is usually used to image high energy radiations from XUV (10 - 100eV) to hard X-rays ($\geq$ 1keV) where optical components are either unavailable or extremely expensive. A setup of pinhole imaging system is shown in Figure 2.10.

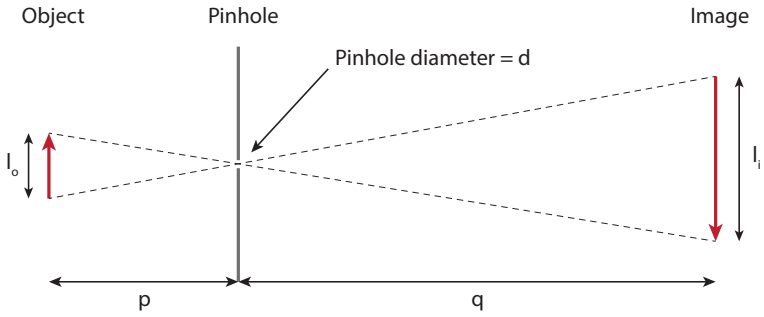

Figure 2.10: Schematic diagram showing the setup of a pinhole imaging system.

When the pinhole is placed at a distance p from the object and the detector placed at a distance q from the pinhole an image is created of length l_i at the detector of an object of length l_o. The magnification M of a pinhole imaging system is given by

$$M = \frac{q}{p} \tag{2.9}$$

The resolution of a pinhole camera is given by the geometrical and diffraction limit which can be calculated using equations 2.10 and 2.11 respectively.

$$\delta_{geo} = d\left(1 + \frac{1}{M}\right) \tag{2.10}$$

$$\delta_{diff} = 1.22\frac{\lambda p}{d} \tag{2.11}$$

The pinhole imaging system was used to image the plasma structure at stagnation which is characterised by intense hard X-ray emission for a very short period of time ~ 10-20ns. Two 20μm diameter pinholes were placed at 580mm from the load axis with Al and Be filters which only transmit hard X-rays. The imaging plate was placed at a position of 488mm form the pinhole, resulting in a magnification of 0.84. For photons of ~ 1 keV (λ ~ 1nm) this system will generate images with a resolution of ~ 45μm.

2.2.5 4-frame XUV micro-channel plate (MCP) camera

This is another pinhole camera system with 4 pinholes arranged in a 2×2 array. The detector is a micro-channel plate divided into 4 frames. Each pinhole images the load onto one of the 4 frames of the MCP photocathode (sensitive to XUV radiation 10 - 100eV) as shown in Figure 2.11(a). Electrons - generated via the photoelectric effect - reach the MCP which consists of a 2D array of ~ 12μm diameter silica tubes (Figure 2.11(b)). A ~ 1kV voltage applied across the MCP accelerates the photo-electrons which constantly collide with the tube walls generating more electrons resulting in a cascade amplification. The amplified electrons coming out from the back of the MCP are further accelerated by a ~ 4kV

potential before hitting the phosphor scintillator converting their kinetic energy into visible radiation. A Canon SLR camera placed at the other side of the scintillator captures those images.

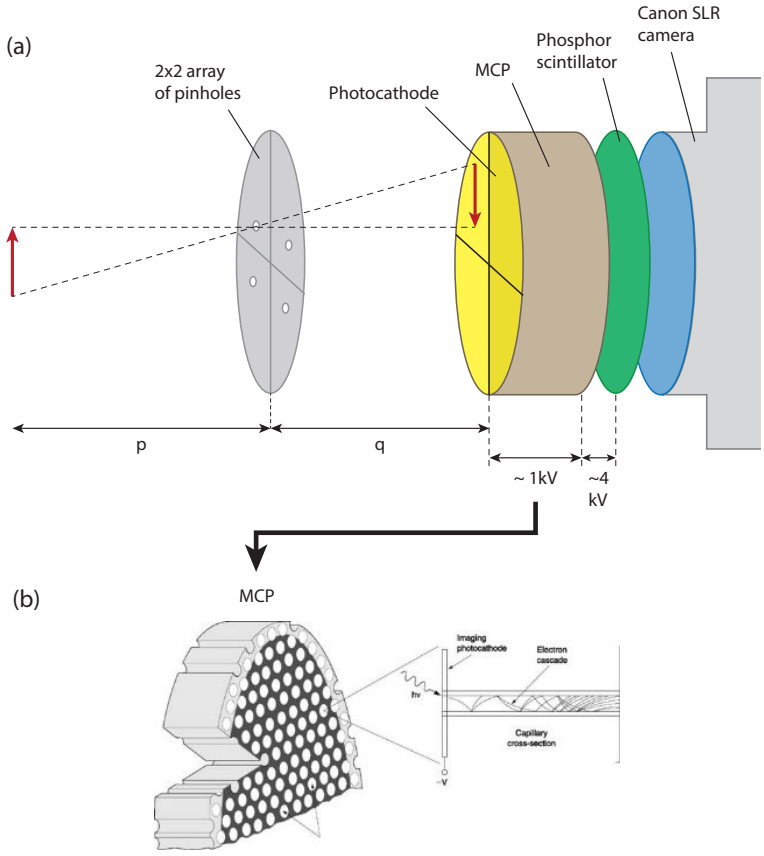

Figure 2.11: (a) Schematic diagram of a 4-frame MCP pinhole camera setup in MAGPIE and (b) shows the micro-channel tubes of an MCP and the cascade effect of electrons.

Each frame of the MCP is independently triggered, and therefore by varying the length of the voltage-supplying cable we were able to control the delay of this voltage pulse for each frame and hence obtain 4 images at different times. The delay between each frame was kept at a constant value of either 10 or 30ns per experiment and the image exposure is determined by the voltage pulse duration ~ 2ns. The sensitivity of the MCP strongly depends on the voltage pulse and is proportional to V^5 [38]. In our experiments, p was set to 560mm and q to 412mm producing an image with a magnification of ~ 0.74 and resolution of ~ 240μm.

2.2.6 Optical streak camera

This diagnostic is used to measure optical radiation emitted from the plasma vs time on one axis and position on the other axis. The streak camera setup in the MAGPIE facility shares the same optical path as one of the green laser probing beams. Therefore a broadband filter was used to restrict light arriving at the camera aperture to the red part of the spectrum (hence preventing any green laser light through).

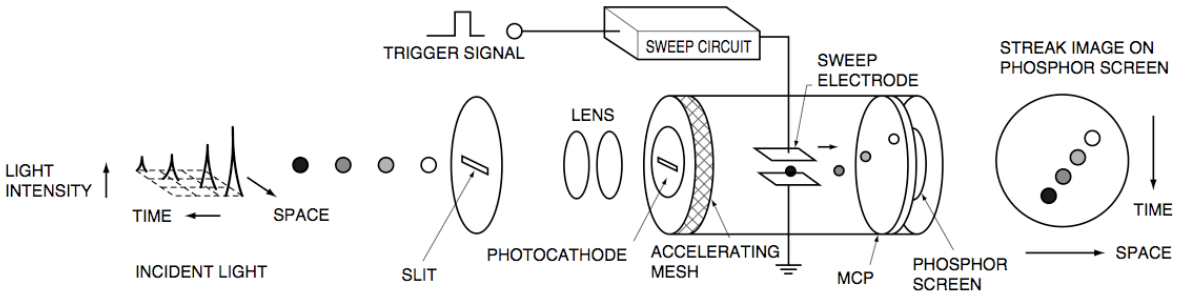

Figure 2.12: Schematic diagram showing the basic components of an optical streak camera (reproduced from HAMAMATSU Guide to streak camera, 1999).

The basic operation of an optical streak camera is as follows (Figure 2.12). Visible radiation emitted from the plasma is focused on a ~ 0.5mm horizontal slit (imaging a radial slice of the Z-pinch load). Radiation passing through the slit hit a photocathode which emits electrons in proportion to radiation intensity. Voltage across a mesh accelerates those electrons towards a pair of sweeping electrodes, were a linearly increasing voltage ramp with time deflects those electrons in the vertical direction (orthogonal to the slit position). Those deflected electrons go through a micro-channel plate amplifying their number in an avalanche process (as explained earlier in Section 2.2.5) before colliding into a phosphor scintillator converting their kinetic energy into optical radiation. This is recorded by an Ilford HP5 photographic film placed at the back of the camera. Electrons arriving at a later time are deflected at a greater angle and hence appears at a different position on the image. For a 300ns sweep duration over a 40mm diameter photocathode the streak camera will produce an image with a ~ 4ns temporal resolution [39].

2.2.7 Diamond photo-conducting detectors (PCD)

For a potential application of Z-pinch in ICF it is important to accurately characterise their X-ray generation. Diamond photo-conducting detectors (PCDs) have shown a high degree of durability, with an excellent time response and low leakage current when compared to other X-ray detectors such as XRD and *p-i-n* diodes. They also have a flat response to radiation energies from 10 eV up to ~ 6 keV [40].

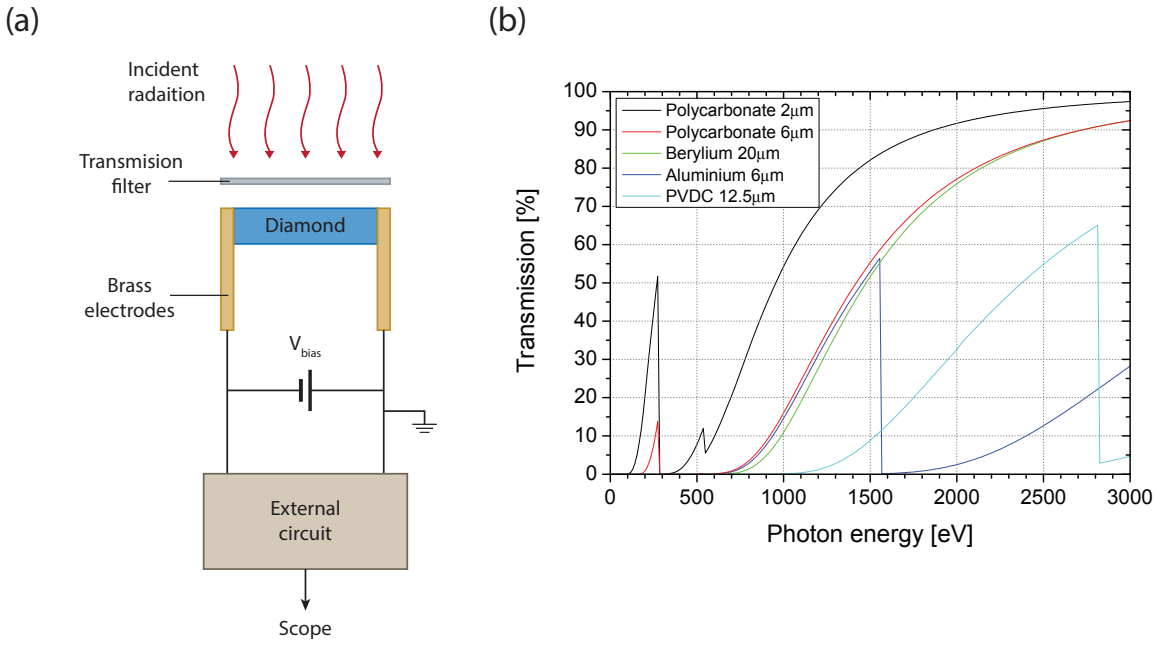

Figure 2.13: (a) Schematic cross-sectional diagram of a PCD and (b) transmission curves for the various filters used on a PCD.

A cross-sectional diagram showing the basic design of a PCD is shown in Figure 2.13(a). It consists of a diamond detector with an area of 3mm × 1mm and a depth of 0.5mm. It sits between two electrodes with an applied voltage V_{bias} ~ 350V. X-ray photons with energies greater than the band-gap ($h\nu \geq 5.5$eV) hitting the detector release an electron-hole pair with a recombination time ~ 200ps (however the temporal resolution is limited to 1ns by the scope). This decreases the resistance of the detector and hence a change in voltage across which is detected by an external circuit and transmitted to the scope.

To have a better analyses of the X-ray radiation spectrum, an array of five filtered PCDs were installed at a distance of 1010mm from the load axis. The transmission curves for the filters used is shown in Figure 2.13(b). All filters are highly transmissive to hard X-rays which can dominate all PCD signals. However an estimate of the soft X-ray yield in the range of 200-300 eV can be obtained by subtracting the Beryllium filtered PCD signal from the 6μm polycarbonate PCD signal.

2.2.8 Laser probing for density measurements

One of the major advantages of using electromagnetic (EM) waves as a probing tool is their non-perturbing nature. Given that the power is not great enough to affect the plasma dynamics, the changes in the wave properties such as intensity, phase and polarisation can be related to various plasma properties including density, temperature and field strength [41]. When a collimated coherent light source such as a laser is used, then the changes in the light properties can be measured to a high degree of temporal and spatial resolution.

The laser beam used for plasma diagnostics in the MAGPIE facility was generated from the 2nd and 3rd harmonics of a flash-lamp pumped Nd:YAG source. Resulting in a green (λ=532nm) and blue (λ=355nm) laser beams respectively, each with a pulse duration of ~ 0.5ns. All laser beams have been setup for side-on imaging as shown in Figure 2.7.

Laser interferometry

In our analysis we aim to calculate the particle density of our plasma which is composed of electrons, ions and neutrals. Each will have a unique refractive index which depends on the laser wavelength passing through the plasma. Therefore a collimated coherent EM wave passing through such a medium will experience a change in phase $\Delta\phi$ corresponding to the change in optical path length.

To measure $\Delta\phi$ we use a laser diagnostic technique called interferometry. Specifically we use a Mach-Zender Interferometer which is characterised by a single

pass of the laser beam through the plasma (Figure 2.14). In this technique a collimated laser beam is divided into two components. One passes through the plasma (probing beam) while the other is transmitted through vacuum unperturbed (reference beam). The two beams are then recombined and an interference fringe pattern is observed at the screen. This fringe pattern is then compared with the one prior to the formation of plasma and a change in fringe position is calculated in terms of numbers of fringes. We refer to this as the fringe shift *FS*.

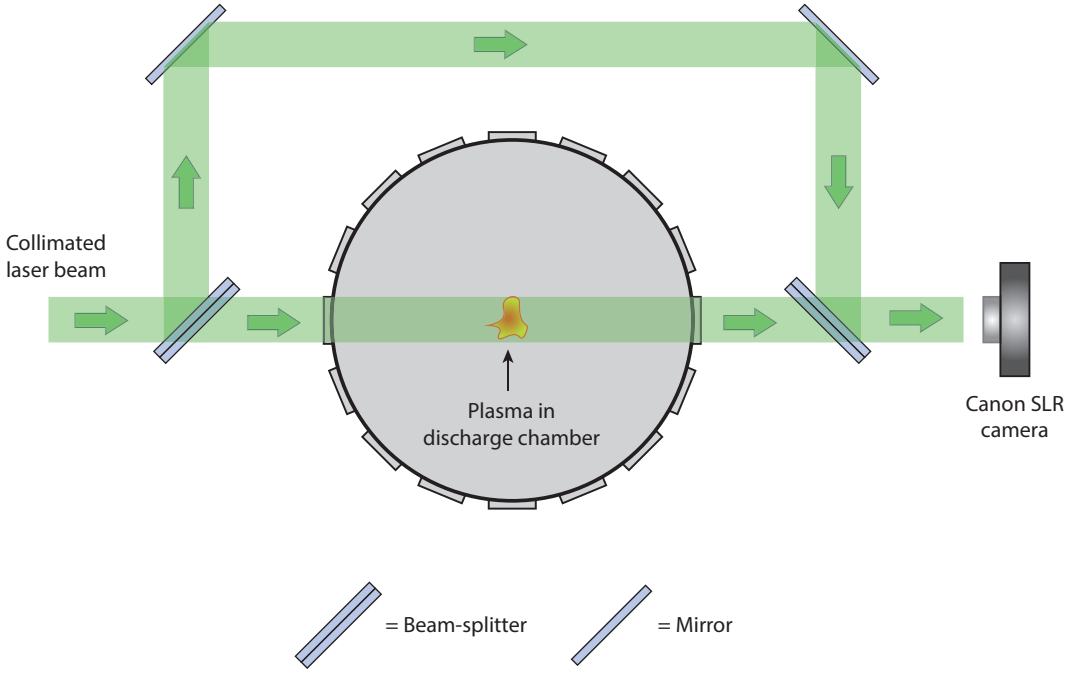

Figure 2.14: Schematic diagram of a Mach-Zender interferometer setup.

To understand how fringes arise and how we can relate *FS* to $\Delta\phi$, we need to understand what happens when we add two monochromatic beams together with a phase difference between them. Let us start by writing the wave's field equation for the probing and reference beam as

$$E_p = E_0 e^{i\left(\phi_p - \omega t\right)} \tag{2.12}$$

$$E_r = E_0 e^{i\left(\phi_r - \omega t\right)} \tag{2.13}$$

where ϕ_p and ϕ_r are the phase of the probing and reference beam respectively. We have assumed both waves have equal intensities (E_0) in order to simplify the mathematics in the following expression, however in practice, the probing beam will experience some degree of absorption as it passes through the plasma. When the two beams combine, the total electric field E_{tot} is then equal to

$$E_{tot} = E_p + E_r = E_0 e^{-i\omega t}\left[e^{i\phi_p} + e^{i\phi_r}\right] \tag{2.14}$$

However, detectors - in general - measure intensity which is proportional to $|E_{tot}|^2$ and this can be expressed as

$$\left|E_{tot}\right|^2 = 2E_0^{\,2}\left[1+\cos\left(\phi_p - \phi_r\right)\right] \tag{2.15}$$

From Eq(2.15) we can see that the intensity will depend on the phase difference between the probing and reference beam ($\Delta\phi = \phi_p - \phi_r$). This intensity varies in a sinusoidal manner w.r.t $\Delta\phi$, from 0 to $4E_0^2$. Therefore bright fringes results from a constructive interference of the 2 waves which corresponds to $\Delta\phi = n(2\pi)$, where n can be zero or any positive integer. On the other hand, dark fringes results from a destructive interference of the 2 waves which corresponds to $\Delta\phi = (1+2n)\pi$.

Hence, the fringe shift FS can be related to $\Delta\phi$ using Eq(2.16).

$$FS = \frac{\Delta\phi}{2\pi} \tag{2.16}$$

In the following sections we show how $\Delta\phi$ (hence FS) can be related to the free electron density and atom density (neutrals and ions) in a plasma. However we first need to understand how the refractive index of a plasma is related to the electron density and atom density.

Refractive index of free electrons

To attempt to relate the contribution of free electrons to the refractive index of a plasma we start by considering a simple model of a transverse electromagnetic

wave passing through a cold plasma (negligible thermal motion) of uniform properties throughout all space. We assume the wave's electric field (E-field) is the only field acting on the plasma. In addition, we only consider the electron motion since they possess a much lower mass than ions and therefore will experience a much greater acceleration. For this simplistic model we can apply the following Maxwell's equations.

$$\nabla \times \mathbf{E} = -\frac{\partial \mathbf{B}}{\partial t} \tag{2.17}$$

$$\nabla \times \mathbf{B} = \mu_0 \mathbf{j} + \frac{1}{c^2}\frac{\partial \mathbf{E}}{\partial t} \tag{2.18}$$

Where **E** and **B** are the electric and magnetic fields vectors respectively, and **j** is the current density vector. The constants μ_0 and c are the permeability of free space and speed of light in vacuum respectively.

By combining Eq(2.17) & Eq(2.18) and using the triple product identity, we obtain:

$$\nabla^2 \mathbf{E} - \nabla\left(\nabla \cdot \mathbf{E}\right) = \mu_0 \frac{\partial \mathbf{j}}{\partial t} + \frac{1}{c^2}\frac{\partial^2 \mathbf{E}}{\partial t^2} \tag{2.19}$$

Now we define our transverse wave to be traveling in the **z** direction and the electric field **E** pointing in the **x** direction. We can write,

$$\mathbf{E} = E_x e^{i\left(\mathbf{k}\cdot\mathbf{z} - \omega t\right)}\hat{\mathbf{x}} \tag{2.20}$$

where **k** and ω are the wave vector and angular frequency of the electromagnetic wave respectively.

As mentioned earlier, we are ignoring the motion of ions and any electron thermal motion. Therefore, the current density will only depend on the electrons

acceleration caused by **E** in Eq(2.20). Hence, we can write the electron equation of motion as,

$$-e\mathbf{E} = m_e \frac{\partial \mathbf{v}}{\partial t} \tag{2.21}$$

and the current density as,

$$\mathbf{j} = -n_e e\mathbf{v} \tag{2.22}$$

where e is the charge on a single electron, m_e is the electron mass and n_e is the electron density. By substituting Eq(2.20), (2.21) & (2.22) into Eq(2.19) and skipping few steps we obtain the dispersion relation of an electromagnetic wave in a plasma due to free electrons.

$$\omega^2 = \omega_p{}^2 + k^2c^2 \tag{2.23}$$

$$\omega_p = \left(\frac{n_e e^2}{\varepsilon_0 m_e}\right)^{\frac{1}{2}} \tag{2.24}$$

Where ω_p is defined as the plasma frequency and ε_0 in Eq(2.24) is the permittivity of free space. The refractive index η of any medium is defined as

$$\eta = \frac{c}{v_{phase}} = \frac{kc}{\omega} \tag{2.25}$$

where v_{phase} is the phase velocity of the EM wave in the medium.

Therefore Eq(2.23) can be re-arranged to show that the refractive index η_e of a plasma due to free electrons is

$$\eta_e = \sqrt{1 - \frac{\omega_p{}^2}{\omega^2}} = \sqrt{1 - \frac{n_e}{n_{cr}}} \tag{2.26}$$

where n_{cr} is the critical density of the probing beam defined as

$$n_{cr} = \frac{\varepsilon_0 m_e}{e^2}\omega^2 \tag{2.27}$$

Refractive index of ions and neutral atoms

We have seen how an EM wave passing through a plasma can interact with free electrons. The same EM wave can also interact with bound electrons within ions and neutral atoms. In classical mechanics, electrons are at equilibrium positions with their nucleus. Such electrons will experience elastic oscillations when exposed to electromagnetic radiation. The nature of these oscillations will depend on the 'natural' frequency of the electron ω_0, the frequency of the EM wave ω and a damping force which we will ignore for relatively low pressure gas. These factors will effect how the wave propagates through such medium and hence its refractive index. However, we know from quantum mechanics, electrons do not have a fixed equilibrium position within an atom. Instead they have a probabilistic distribution of positions in space. As a result, the electron in an atom of state i will not possess a single unique 'natural' frequency ω_{0i} but rather a probabilistic distribution of frequencies $\omega_{0i,j}$. Therefore the concept of an oscillator strength $f_{i,j}$ is introduced to give the probabilities for the possible frequencies $\omega_{0i,j}$. An equation relating the refractive index of atoms η_a to the above properties is stated below in Eq(2.28). The derivation of such equation is quite complex and can be found in journal reviews and text books [41, 42].

$$\eta_a = 1 + \frac{2\pi e^2}{m_e}\sum_{i,j}\frac{f_{i,j}n_i}{\left(\omega_{0i,j}^2 - \omega^2\right)} \tag{2.28}$$

For optical frequencies far from spectral lines Eq(2.28) can be approximated to

$$\eta_a \simeq 1 + 2\pi\alpha n_a \tag{2.29}$$

where α is the polarizibility of the specific atom, which is wavelength dependent, and n_a is the atom's number density.

Line density measurements from fringe shift

In real life no practical plasma satisfies the condition of possessing uniform EM properties throughout all space. As a result, wave field solutions with a phase component equal to $\mathbf{k}\cdot\mathbf{z}$ where $\mathbf{k}$ is constant through out space will not satisfy Maxwell's equations. However, if the plasma EM properties vary sufficiently slowly (variation of $\mathbf{k}$ in one wavelength is small), then we can divide the plasma into local regions of 'uniform' properties. For such regions, a well defined value for η and hence $\mathbf{k}$ exists. Therefore we can sum over all those regions and use the WKBJ approximation [42] to obtain the propagation of a wave of a given frequency through the plasma. Hence the field equation can be written as

$$E \simeq E_x e^{i\left(\int \mathbf{k}\cdot\mathbf{dl} - \omega t\right)} \tag{2.30}$$

In Eq(2.30) we see that the phase is now an integral sum of $\mathbf{k}\cdot\mathbf{dl}$, where $\mathbf{dl}$ is an infinitesimal length along the ray path and $\mathbf{k}$ is the solution of the homogenous plasma dispersion for the given 'uniform' infinitesimal region.

Comparing Eq(2.30) to Eq(2.12) & (2.13) we can write down an equation for the phase of the probing and reference beam in a laser interferometery setup.

$$\phi_p = \int k_p \, dl \tag{2.31}$$

$$\phi_r = \int k_r \, dl \tag{2.32}$$

Hence, the phase difference can be written as

$$\Delta\phi = \phi_p - \phi_r = \int (k_p - k_r)\, dl \tag{2.33}$$

Since we are interested in the phase difference and not the actual phase, and assuming both beams travel equal lengths, then the difference is only in the part of the path that lies in the plasma. Therefore, we limit our integral in that region only, for which we will assume that the reference beam travels in vacuum while the

probing beam passes through the plasma. Using the general definition of a refractive index in Eq(2.25) we re-write Eq(2.33) as

$$\Delta\phi = \frac{\omega}{c}\int (\eta_{p} - 1)\, dl \tag{2.34}$$

where η_p is the plasma refractive index. We have shown in the previous sections how the refractive index of free electrons and atoms are related to their number density. Hence we can now show how their line integrated number density can be related to the phase difference.

For a plasma consisting just of free electrons ($\eta_p = \eta_e$), we can sub Eq(2.26) into Eq(2.34) and obtain the change in phase due to free electrons $\Delta\phi_e$.

$$\Delta\phi_{e} = \frac{\omega}{c}\int (\sqrt{1 - \frac{n_{e}}{n_{cr}}} - 1) dl \tag{2.35}$$

For $n_e \ll n_{cr}$, we can use the binomial expansion to approximate Eq(2.35) to,

$$\Delta\phi_{e} \simeq -\frac{\omega}{2cn_{cr}}\int n_{e}\, dl \tag{2.36}$$

and by using Eq(2.16) & (2.27) the fringe shift due to free electrons is

$$FS_{e} = -\frac{e^{2}}{8\pi^{2}c^{2}\varepsilon_{0}m_{e}}\lambda\int n_{e}\, dl = -\frac{r_{e}}{2\pi}\lambda\int n_{e}\, dl \tag{2.37}$$

where λ is the wavelength of the EM wave, and r_e is the classical electron radius. For λ measured in cm we can write

$$FS_{e} = -4.46\times10^{-14}\lambda_{cm}\int n_{e}\, dl \tag{2.38}$$

Similarly, for a plasma consisting of just atoms ($\eta_p = \eta_a$), we can sub Eq(2.29) into Eq(2.34) and obtain the change in phase due to bound electrons in ions and neutrals.

$$\Delta\phi_{a} = 2\pi\alpha\frac{\omega}{c}\int n_{a}\,dl \tag{2.39}$$

Hence, the fringe shift caused by atoms is

$$FS_{a} = \frac{2\pi\alpha}{\lambda}\int n_{a}\,dl \tag{2.40}$$

We note that the negative sign in Eq(2.37) suggests that the fringe shift caused by free electrons is in opposite direction to the one caused by atoms. In real-life, a plasma would consist of both free electrons and atoms and therefore the measured fringe shift would be the total effect of both species. We can write this as

$$FS = FS_{e} + FS_{a}$$

$$FS = -\frac{r_{e}}{2\pi}\lambda\int n_{e}\,dl + \frac{2\pi\alpha}{\lambda}\int n_{a}\,dl \tag{2.41}$$

For a plasma which consists of equal densities of plasma and atoms, the contribution of FS_a is relatively small, at the order of ~ 3-4% FS_e and hence it can be neglected. However in experiments, such as the ones conducted in this thesis which involves a 2-stage Z-pinch configuration, there exists a long period of minimal ionisation, and the contribution of neutral atoms to the total fringe shift becomes significant. For those kinds of plasmas its important to differentiate the contribution of atoms and electrons from the total fringe shift.

Extraction of electron and atom line density from FS measurements

In order to calculate the line density of atoms and electrons in a plasma from fringe shift measurements, we need to apply a two-wavelength interferometry, and solve the two fringe shift equations simultaneously [41, 43]. We start by re-writing Eq(2.41) for the two different laser wavelengths we have used in our experiment (green at λ=532nm and blue at λ=355nm).

$$FS_{G} = -\frac{r_{e}}{2\pi}\lambda_{G}\int n_{e}\,dl + \frac{2\pi\alpha_{G}}{\lambda_{G}}\int n_{a}\,dl \tag{2.42}$$

$$FS_B = -\frac{r_e}{2\pi}\lambda_B \int n_e \, dl + \frac{2\pi\alpha_B}{\lambda_B}\int n_a \, dl \qquad (2.43)$$

Where the G and B subscripts refer to the green and blue wavelengths respectively. We sub $-\frac{r_e}{2\pi}\int n_e \, dl$ from Eq(2.42) into Eq(2.43), and re-arranging to get an equation for the atom line density.

$$\int n_a \, dl = \frac{1}{2\pi}\left[\frac{\lambda_G FS_B - \lambda_B FS_G}{\alpha_B\left(\lambda_G/\lambda_B\right) - \alpha_G\left(\lambda_B/\lambda_G\right)}\right] \qquad (2.44)$$

By substituting Eq(2.44) into either Eq(2.42) or (2.43) we get the equation for the electron line density.

$$\int n_e \, dl = \frac{2\pi}{r_e}\left[\frac{\alpha_G\lambda_B FS_B - \alpha_B\lambda_G FS_G}{\alpha_B\lambda_G^2 - \alpha_G\lambda_B^2}\right] \qquad (2.45)$$

Therefore from fringe shift measurements of two different wavelengths at the same point in space and time, we can distinguish the electron and atom line density within a plasma.

In general, laser transmission diagnostic techniques such as interferometry can only measure the line integrated value of a particular quantity along the laser path. However, in cases where the plasma has a reasonable degree of cylindrical symmetry, one can take advantage of this to compute the local values from the line integrals using a mathematical technique called *Abel inversion*.

Abel inversion

Let us start by considering a cylindrically symmetric quantity $f(r)$, which only varies radially and is constant in the **z** and **θ** axis. From the diagram shown in Figure 2.15 we can calculate the line integrals F of f at y using

$$F\left(y\right)=\int_{-\sqrt{\left(a^2-y^2\right)}}^{+\sqrt{\left(a^2-y^2\right)}} f\left(r\right)dx \tag{2.46}$$

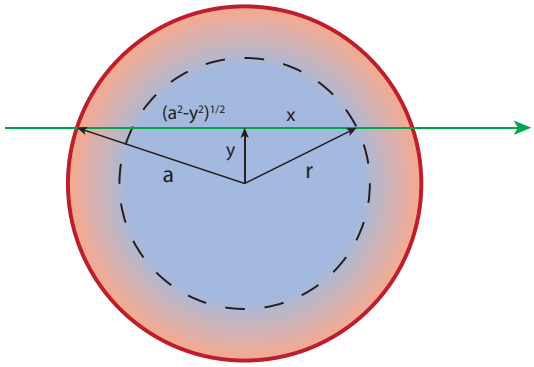

Figure 2.15: Chordal length measurements in a cylindrical object with radius a.

We can change this into an r integral to obtain - what is referred to as - the Abel transform of f.

$$F\left(y\right)=2\int_{y}^{a} f\left(r\right)\frac{rdr}{\left(r^2-y^2\right)^{1/2}} \tag{2.47}$$

The Abel transform allows us to calculate the quantity $F(y)$ from an integral sum of $f(r)$. Given that $f(a)=0$, the inverse Abel transform [42] is defined as,

$$f\left(r\right)=-\frac{1}{\pi}\int_{r}^{a}\frac{dF}{dy}\frac{dy}{\left(y^2-r^2\right)^{1/2}} \tag{2.48}$$

which allows us to calculate the quantity $f(r)$ from its line integrals $F(y)$. In practical situations, the value of F is measured at finite numbers of y. Therefore, to calculate f, one has to approximate Eq(2.48) to a summation and solve the integral numerically. This approximation can be written as,

$$f\left(r\right)\simeq-\frac{1}{\pi}\sum_{r+\Delta y}^{a}\frac{F_{y+\Delta y}-F_{y}}{\sqrt{y^2-r^2}} \tag{2.49}$$

Where the lower integral limit has been changed from $y = r$ to $y = r+\Delta y$ to prevent the denominator $\sqrt{y^2 - r^2}$ from becoming zero. For data with a limited number of $F(y)$, we can apply an interpolation method to allow us to obtain a smoother distribution of $f(r)$.

Chapter 3

Investigation of the Preconditioning Effect & Current Switch Mechanism

Previous experiments using a 2-stage wire array Z-pinch configuration were only performed using a 1MA current pulse on loads consisting of 8 Al wires [31, 32]. In the first section of this chapter we investigate the preconditioning effect of such configuration using a higher current pulse of 1.4MA on loads with different wire numbers, while keeping the load material and total mass constant. This has been analysed using line density measurements from interferogram images before the main current switches into the load. We have investigated cylindrical load arrays of 2, 4, 8 and 16 aluminium wires.

In the second section, we investigate the dynamics and mechanism of current switching in a 2-stage Z-pinch configuration. The load array was replaced with a static current-measuring diagnostic incorporating B-dot probes. dI/dt signals from those probe and plasma images from laser interferometry and XUV camera have strongly suggested that probably a more dynamical mechanism of current switching takes place than what we have originally thought.

3.1 Investigation of the preconditioning effect

3.1.1 Experimental setup

All of our experiments were performed on the MAGPIE generator (1.4MA in 250ns) which is described in detail in Chapter 2 Section 2.1, and diagnostics were arranged as shown in Figure 2.7 in Chapter 2. A cross section schematic diagram of the 2-stage wire array setup is shown below in Figure 3.1 along with a photo. The photo was taken prior to loading the array in MAGPIE and therefore we see 2 cylindrical brass spacers holding the 'cathode holder' in position while the array is being built. Those spacers are taken off after loading the array, and hence we do not see them in the schematic diagram (Figure 3.1(a)) which shows the array hardware resting on MAGPIE's anode and cathode.

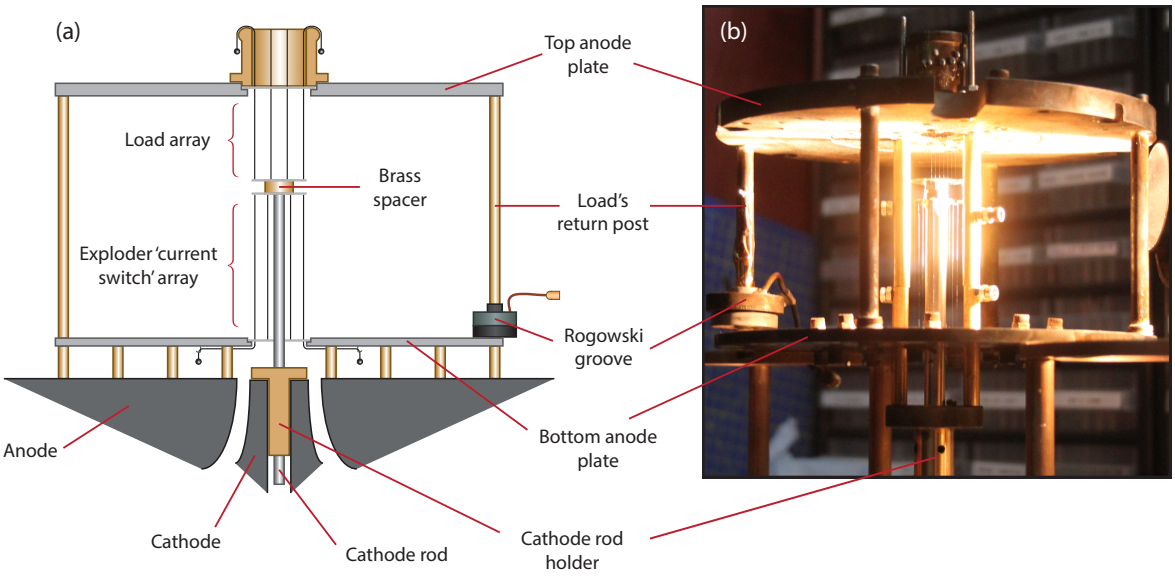

Figure 3.1: A schematic diagram (a) and a photo (b) of a 2-stage wire array Z-pinch setup. The photo was taken prior to loading the array in MAGPIE.

We can see in Figure 3.1, that our setup is made up of 2 distinct cylindrical wire arrays sandwiched between two 170mm diameter stainless steel anode plates. The top anode plate is attached to the bottom plate by 4 brass return posts, 6mm diameter × 75mm long each. A minimum number of return posts is used in order to keep as much open space as possible around the array for diagnostic equipments. On the other hand, the bottom plate is connected to MAGPIE's anode by 16 brass return posts, 10mm diameter × 10mm long each. The large

number of short return posts minimises the total inductance of the inverse array and ensures an equal distribution of current around the bottom plate. At the centre, a brass cathode holder - which sits on MAGPIE cathode - holds the 8mm diameter stainless steel cathode rod in place. This rod supports both top and bottom arrays which are separated by a brass spacer 5mm thick. Both the cathode rod and the spacer are replaced by a new one for every experiment.

The current switch array (bottom array) setup was kept constant through out all our experiments described in this thesis. This array is simply an inverse array consisting of 8 × 15μm thick aluminium (5056 alloy) wires. The array diameter and length were set to 16mm and 55mm respectively. The wires were arranged in a cylindrical fashion equidistant from each other using notched disks placed on the top and bottom end of the array. At the top end, wires were glued on the disk using a fast-setting epoxy. While at the bottom end, the wires would pass through the notched disk and placed underneath the bottom anode plate. There the wire are left hanging on hooks with lead weights attached to their ends to keep the array wires taut and straight. The distance between the two notched disks is the array length (55mm).

The load array (top array) setup was simply a classical cylindrical wire array. The properties of this array is what we varied in our experiment. In particular, we are interested in investigating the array dynamics before the current switch for different wire numbers while keeping the total array mass constant. Therefore we have assembled arrays of 2 × 30μm, 4 × 20μm, 8 × 15μm and 16 × 10μm aluminium (5056 alloy) wires, keeping a roughly constant array mass per length of 40μg/cm. The array diameter was kept constant to 16mm, except for the 16 wire array where it was reduced to half this value (8mm), since this experiment could also be used as a step towards forming a plasma shell (discussed in more details in Chapter 5). The wires were arranged in place using notched disks, connecting the top end of the cathode rod to the anode at the top. The wires were glued at the bottom disk, while the other weighted ends were left hanging above the top anode plate as shown in Figure 3.1 to keep the array wires taut and straight. The array

length was kept constant throughout these experiments at 15mm (distance between the two notched disks of the top array).

Looking at the two wire arrays as a whole system we can see that they are connected in parallel to a high voltage source, and therefore the current can have two different routes from anode to cathode. Those are labelled as green and blue arrows in Figure 3.2. One route is for the current to go through the inverse array wires (bottom array) and down into the cathode (blue arrows) . While the other route is for it to go up the return posts into the top anode plate, through the load and down into the cathode (green arrows). This division of current will depend on the impedance ratio of both arrays, hence their inductance (including mutual inductance of both arrays) and resistance. The Rogowski groove is placed on one of the 4 long return posts so that it only measure the current through the load. The total current was measured by Rogowski groove placed on one of the 16 shorter posts at the bottom of the array hardware and also by the B-dot probe in the MITL.

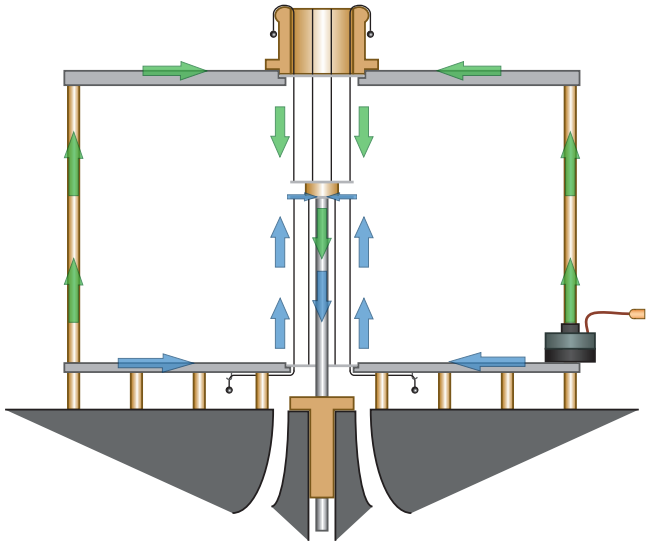

Figure 3.2: A schematic diagram showing the two different paths of current flow in a 2-stage wire array Z-pinch setup. Green arrow represent current into the load while blue arrows represent current into the bottom inverse array.

3.1.2 Initial current prepulse

At the instant of the start of the current pulse, before the formation of any plasma, the impedance of the both arrays is dominated by their resistance values R. That is, the resistance of the wires contained in each array. This can be calculated for each array using Eq (3.1).

$$R = \frac{\rho l}{nA} \tag{3.1}$$

Where n is the total number of wires in the array, ρ is the material resistivity, l is the wire length and A is the cross-sectional area of a single wire. This current division will vary as we progress in time, since energy deposited by the current will heat up the wires increasing its resistance. When enough heat has been deposited to form sufficient amount of plasma, resistive current division becomes negligible due to the high conductivity of plasma. At that point, the current division ratio of the two arrays will be governed by the local inductance $L_{private}$ of the inverse array. The inductance of a cylindrical array load is given by [33]

$$\begin{aligned} L_{array} &= L_{global} + L_{private} \\ L_{array} &= \frac{\mu_0 l}{2\pi} \ln \frac{R_{rp}}{R_a} + \frac{\mu_0 l}{2\pi} \frac{1}{N} \ln \frac{R_a}{N R_w} \end{aligned} \tag{3.2}$$

Where l is the length of the array, N is the total number of wires, R_{rp} is the radial position of the return posts, R_a is the array radius and R_w is the wire radius. We can see from Eq(3.2) that as N becomes large, the contribution of $L_{private}$ to the total inductance becomes negligible and the array inductance approaches that of a 'cylindrical can' load ($L_{array} \rightarrow L_{global}$). For a 'cylindrical can' bottom aray, $L_{private} = 0$ and no voltage is generated at the load section.

Therefore we expect an initial current pulse into the load at the start of our experiment due to the resistive division. After the formation of plasma in the inverse array, the current in the load falls down to a relatively low level. This has been observed from the Rogowski signals in all four load setups described above.

The main features of this pulse has been consistent for all experiments. In Figure 3.3 we present an example of this signal from an experiment done on a 2 × 30μm load array.

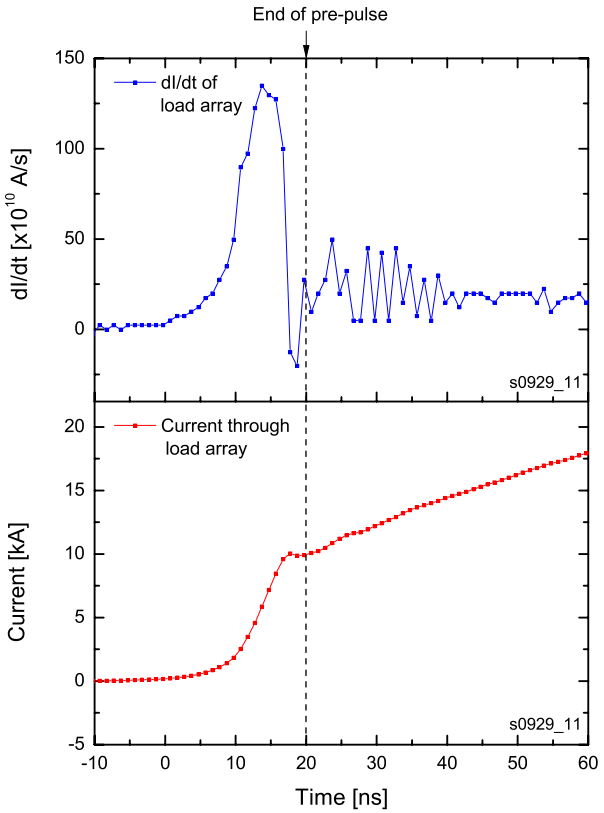

Figure 3.3: Plot showing dI/dt and current signals in the load at an early stage of the experiment for a 2 × 30μm Al wire array.

As described earlier in Chapter 2, a Rogowski groove measures dI/dt through the post that it is placed on. By taking into account the total number of posts (×4) driving current into the load and signal attenuators placed at the Rogowski's output, we present the variation of dI/dt with time in the load array (Figure 3.3 blue plot). By integrating this plot, we also present the variation of current through the load (Figure 3.3 red plot).

We can see that soon after the current start, dI/dt in the load goes up steeply then down to nearly zero in around 20ns. This change corresponds to a current pulse reaching a peak of 10kA in 18ns. Due to the fast nature of the pre-pulse and limited temporal resolution (1ns) of our scope, there has only been a limited number of data points recorded to define the pulse shape. The pre-pulse current

ends when plasma forms at the bottom array. The voltage breakdown in the bottom array, abruptly changes the flow of current into the load. That change happens too fast for our Rogowski to measure accurately, and therefore we cannot precisely tell to what value the current falls down after the pre-pulse peak. However what we know for sure is that dI/dt after the pre-pulse does not fall down to zero, rather it stays at a constant but relatively low level for some time. This corresponds to a steadily increasing current into the load. In the next section we explore this phase of the experiment in more detail. For now we will focus on the pre-pulse period, which we have defined in Figure 3.3 as the time between current start and the point when dI/dt falls down to 'nearly' zero.

The temperature variation of the load wires during the pre-pulse period can be calculated from the current values. Assuming all electrical power is dissipated as heat into the load wires, we can use Eq (3.4 & 3.5) in an iterative process to calculate the change in temperature with time.

$$\Delta Q = \int I^2\left(t\right) R\left(T\right) dt \tag{3.4}$$

$$\Delta T = \frac{\Delta Q}{mc\left(T\right)} \tag{3.5}$$

Where ΔQ is the energy deposited into the wires, R is the resistance of the wire array, ΔT is the change in temperature, m is the total mass and c is the specific heat capacity. Both R and c are dependent on temperature, and those values change for every new iteration. The variation of aluminium resistivity and specific heat capacity with temperature [44] is shown in Figure 3.4.

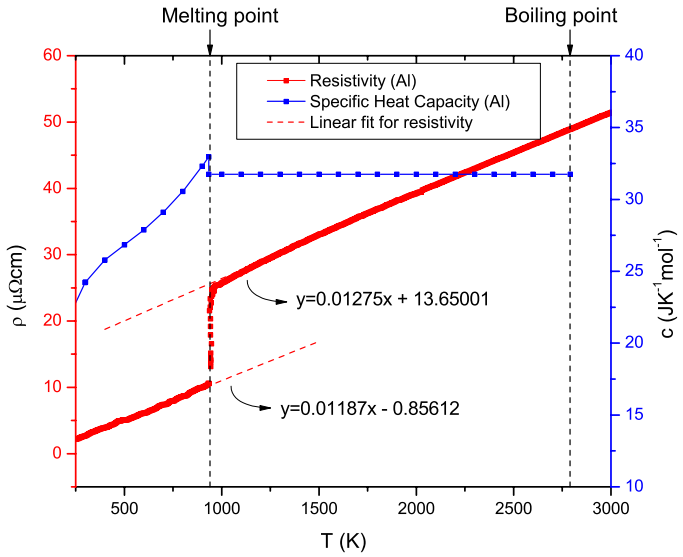

Figure 3.4: Variation of Al resistivity and specific heat capacity with temperature [44].

We see that aluminium resistivity varies linearly from room temperature (276K) to its melting point (934K), it then jumps up to 24μΩcm as it turns into liquid. Again at that phase it varies linearly up to its boiling point (2790K). We used the two linear relationships presented in Figure 3.4 to calculate our resistance value as the wires heat up. The specific heat capacity on the other hand, varies over a smaller range with increasing temperature. Therefore, prior to melting, we have approximated this variation as an average constant value of 28.7JK^{-1}mol^{-1}. After melting, the specific heat capacity settles to a constant value of 31.8JK^{-1}mol^{-1} up to boiling point. In between the change in phase (solid to liquid), the temperature remains constant while the bonds are broken up. The change in latent heat enthalpy ΔH required for this process is 10.7kJmol^{-1}. During this phase, the resistivity is assumed to be a constant mid point value between solid and liquid at melting point temperature. While the value for specific heat capacity is assumed to be the same as in liquid form (31.8JK^{-1}mol^{-1}).

As mentioned earlier, we have a limited number of current data points (17 points) during the pre-pulse phase. In order to compute a reasonably accurate summation for the integral in Eq(3.4), we have linearly interpolated the current values in between the data points using the 'interp1' function in matlab. The temperature calculations were then done on the new interpolated values, which are presented in Figure 3.5.

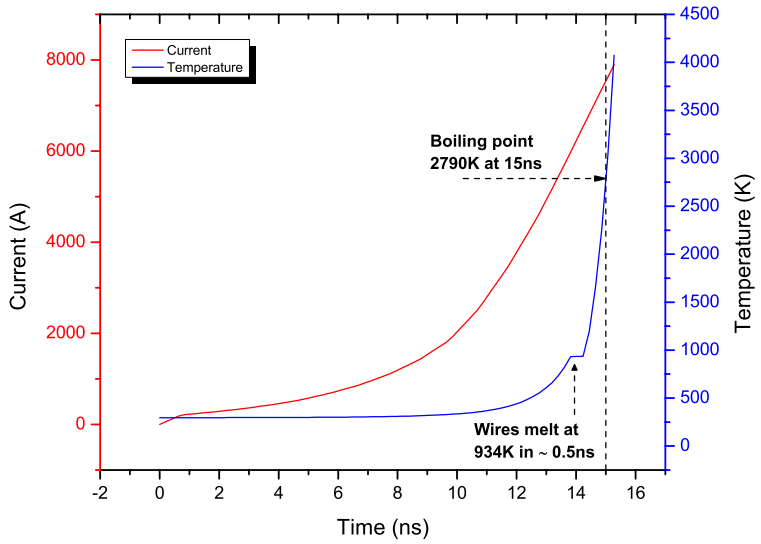

Figure 3.5: The rise in current and temperature of a 2×30μm Al wire array during the pre-pulse phase.

At the start of the current pulse when the rise time and wire resistance are low, the change in wire temperature is slow. As the current rises and more energy is deposited into the wires, its temperature and hence resistance goes up. The rise of resistance ensures that the current is equally distributed among the wires. In addition, it further increases the amount of energy deposited into the wires. This results in the temperatures rising faster as time progresses. At 13.8ns, the wires melt at a temperature of 934K. The temperature then stays constant for a brief amount time of roughly ~ 0.5ns, during which the current's energy is used to break the structural bonds of the solid aluminium. Afterwards, the temperature steeply rises due to the sudden increase in resistivity from solid to liquid aluminium, and in roughly 1ns the wires reach boiling point. We will ignore temperature calculations beyond this point as no accurate resistivity data is available for gaseous Al, and our measurements of dI/dt is not sufficiently accurate.

While our top array heats up and solid wires change into gas, similar heating happens to the bottom inverse array. The duration of heating this array into a conducting plasma determines the pre-pulse phase duration. Our load wires reach boiling point at 15ns while the pre-pulse current ends at roughly 20ns. During this 5ns period, dI/dt in Figure 3.3 falls down sharply, and the Rogowski groove cannot

measure this change in current accurately. We cannot tell if this change happens because of the formation of gaseous Al or coincidentally plasma formed at the bottom array during this period. However previous experiments [32] have shown that the end of the pre-pulse is predominantly related to the formation of plasma on the inverse array wires.

We know that enough energy has been deposited into the load to convert it to gas just before plasma has formed at the bottom inverse array. As plasma is highly conductive, the current now takes the least inductive route, which is the path into the bottom inverse array. As a result, very little current goes into load during this time period. The absence of sufficient current allows the heated wires in the load array to 'freely' expand as there is no (or very low) magnetic pressure present.

3.1.3 Preconditioning of load wires

As discussed in the previous section, the pre-pulse has deposited enough energy into the load array to convert solid wires into gas. This happens before plasma forms in the bottom array which marks the end of the pre-pulse (resistive division) phase. After which, the highly conductive plasma ensures that current flows into the lower inductance inverse array until it fully explodes. Therefore, during this period we expect a relatively low current into the load. In this section we examine the load dynamics between the end of the pre-pulse and before current switch.

Let us begin by examining the current through the load during this period of time. Figure 3.6 shows the variation of dI/dt and current for the first 250ns through a 2×30μm Al wire array load. We see that dI/dt after the pre-pulse current and before the switch does not fall down to zero, rather it stays roughly constant at a relatively low level, which corresponds to a steadily increasing current into the load during this period of time. This has been consistent for all our experiments on loads of a 2-stage wire array Z-pinch setup.

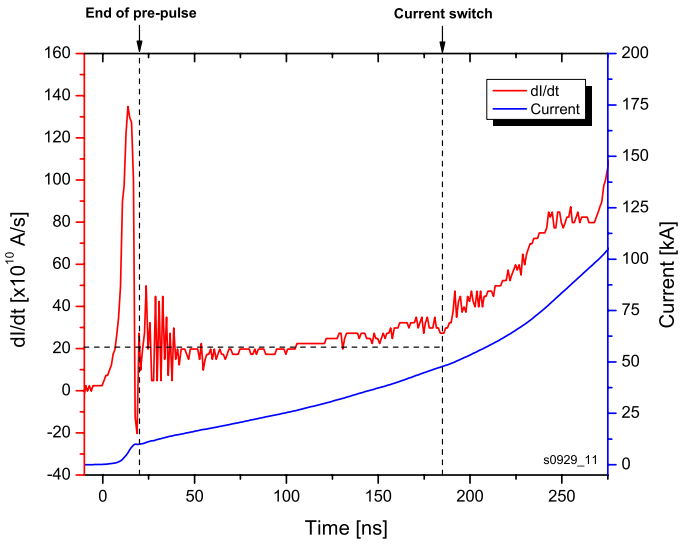

Figure 3.6: Plot showing a roughly constant dI/dt after the pre-pulse and before the current switch through a 2×30μm Al wire load.

As explained in Chapter 1, the small voltage across the load array which drives the current is induced by a changing magnetic flux escaping from the gaps between the wires of the inverse array. As dI/dt increases through this array so is the rate of change of the magnetic flux and hence the voltage, causing current to increase with time into the load. In addition, as inverse wires ablate, the current path takes the form of the ablation streams moving radially outwards along the vertical axis [45]. Those streams grow larger with time which increases the resistance of the inverse array, hence contributing to the steadily increasing current into the load after the pre-pulse and before the main current switch. We cannot accurately tell how much current is going through the load due to the ambiguity of the current level soon after the pre-pulse. In addition, the Rogowski groove used in our experiments has a low sensitivity, and therefore a small dI/dt for a low current level cannot be accurately quantified. However, it is safe to state that the current through the load during this period is small, at the level of a few percent of the total current.

To determine if such a small current has an effect on the load array dynamics, we need to look into laser interferometric images in the time frame between the current pre-pulse and current switch. Such images were obtained for all our load setups experimented in this investigation (2,4,8 & 16 wire arrays) using the 2nd harmonic (532nm) of a Nd:YAG laser (Figure 3.7). This figure shows

interferometric images of wire arrays for 2×30μm at 177ns, 4×20μm at 185ns, 8×15μm at 128ns and 16×10μm at168ns.

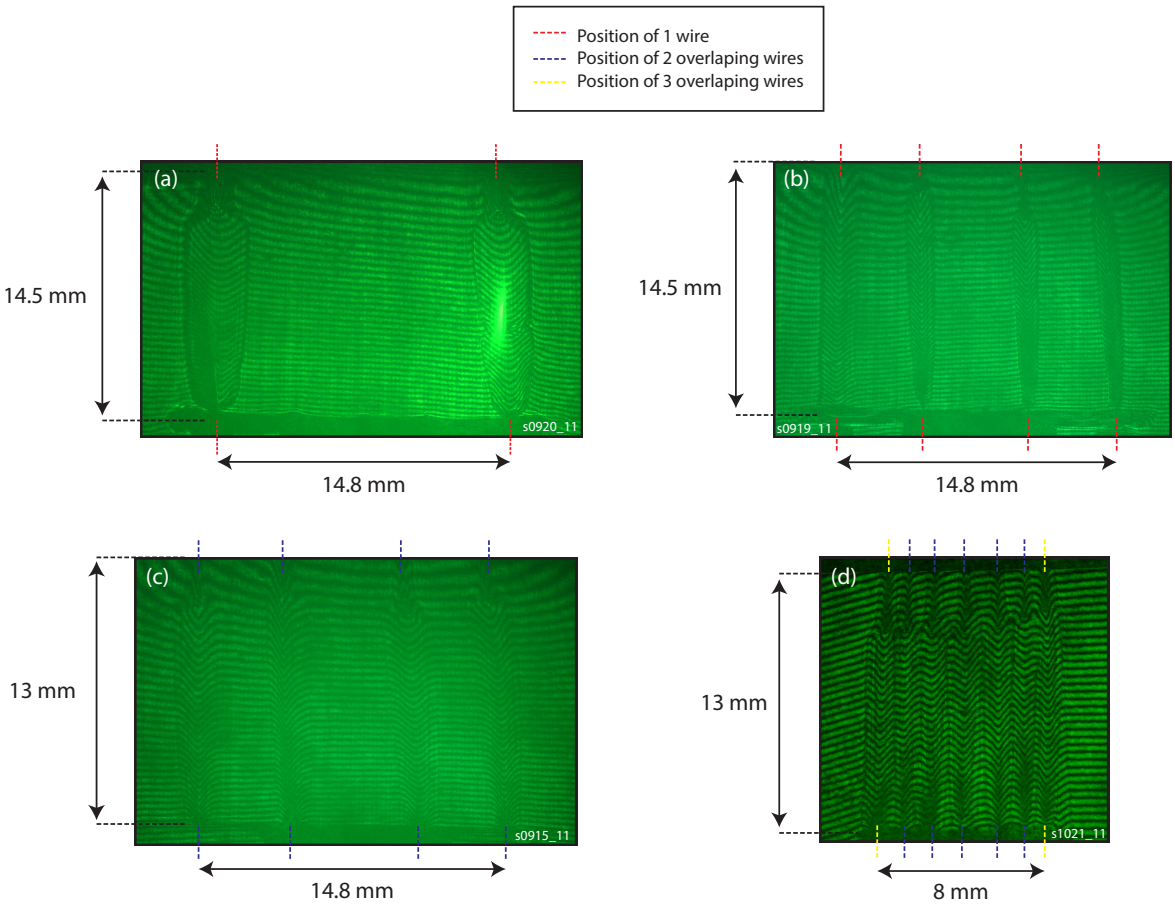

Figure 3.7: Laser interferogram images of cylindrical Al wire array loads taken in the time between the pre-pulse and current switch. The wire array properties and timings for the following images are (a) 2×30μm at 177ns, (b) 4×20μm at 185ns, (c) 8×15μum at 128ns and (d) 16×10μm at 168ns.

As expected from earlier Z-pinch experiments of a 2-stage wire array [31], the absence of dense wire cores is clear from the above images. Fringes can be seen all the way across the wires over a significant portion of its length. By diverting most of the current to the bottom array, the heated wires at the top array have expanded radially outwards to form a relatively uniform column of Al gas. We refer to this as the preconditioning effect of the wires. Qualitatively, we can see that wires with larger initial thickness have expanded to a greater diameter. The 30μm wires have expanded to an average diameter of ~ 3.5mm, while the 20μm wires have expanded to an average diameter of ~ 2.3mm. Measuring the diameter

of a single wire for the 15 & 10μm array in Figure 3.7(c)&(d) has proven to be difficult due to wires overlapping in their corresponding images (however we did measure the preconditioned wire diameter of the 10 and 15μm wire from line density plots which is shown in a later section in this chapter). In addition, images taken at a later time (before the main current switch) will possess a larger diameter since more time is given for the wires to expand. However, the 20μm wire array image was taken at slightly later time than the 30μm wire array, and we still see that the latter has expanded to a significantly larger diameter. Hence, we can confidently say that wires with larger thickness expand to greater diameters. Close to the electrodes we notice that the wires have not expanded as much as the central region. This electrode end effect has been previously observed on standard Z-pinch arrays [46], and it has been suggested that the electric field at the electrodes cause an early formation of plasma in this region, thus reducing energy deposition in the wires and this is seen as 'pinching' of wire ends. By averaging measurements taken from non-overlapping wires in Figure 3.7, the width of those regions are roughly ~ 35% of the central region width, while their lengths are at ~ 15% of the loads array length.

In the above images we note that the height shown is not the actual array height, since part of the array is blocked by the top anode plate. This can be seen in Figure 3.1(a) were the top disc of the load array sits at 1.5mm above the bottom surface of the top anode plate. As more experiments were done using the same hardware, we have noticed the loads return posts buries itself deeper into the bottom anode plate holes and hence not maintaining the correct array height. This has been adjusted from time to time by placing several washers at the bottom of each post to correct the overall height. This is the reason why there is a slight change in the load's height in our images for different experiments. The width shown in Figure 3.7(a)(b)&(c) is slightly shorter than the array diameter of 16mm. This is because those images were taken at an angle to show an open axis instead of edge-wires. While the image for the 16 wire (Figure 3.7(d)) was taken at an angle to show edge-wires and hence the width matches the array diameter of 8mm.

We also note that the bright streak on the RHS wire in Figure 3.7(a) is caused by the emission from a laser - used for Thomson scattering measurements - striking the wire. This happens after the interferogram image was taken, however it is recorded in our image since the CCD camera shutter is left open during the whole duration of our experiment. Prior to firing the experiment, the same laser was used to strike the RHS solid wire at the same axial position, which has been done several times for alignment purposes. This could have induced a slight perturbation in the solid wire causing the pinch effect observed in Figure 3.7(a).

In order to obtain density measurements from interferogram images in Figure 3.7, the fringe positions are compared with their corresponding ones in the pre-shot interferogram images (background images) and the change in fringe position is recorded. This quantity is proportional to the phase shift introduced by the expanded wires. We have noticed that around the edges of thicker wires there has been an opposite shift in fringe position compared to its central region. As explained earlier in Chapter 2 Section 2.2.8, the phase-shifts of free electrons and atoms are in opposite directions, which suggests some presence of plasma around the wire boundaries.

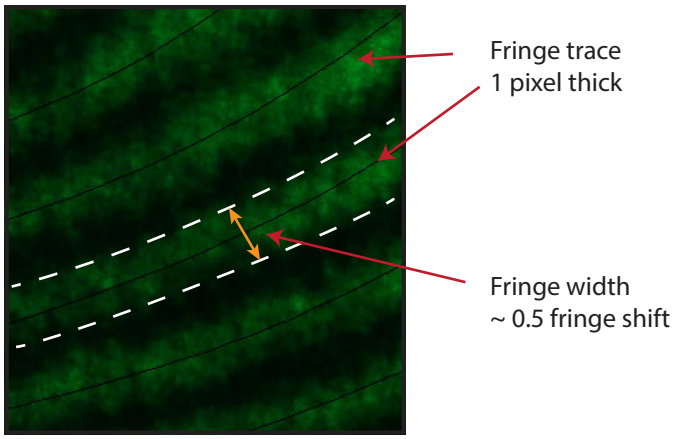

Figure 3.8: Position of a fringe trace could vary within the boundaries of a fringe introducing an error of ~ ± 0.2 fringe-shift (or phase-shift).

To obtain a 2D map of phase-shift, fringe paths in images in Figure 3.7 were all traced manually along with the background image using Adobe Photoshop. The traced fringe lines (lines of constant phase) were then put into a MATLAB

program (developed by Dr. George Swadling) which interpolates the phase value in between the lines using a 2D linear function. The interpolated fringe map of the experimental image is subtracted from the interpolated background image to generate a 2D map of phase-shift. Given that we have correctly traced the fringes, a maximum error of ± 0.2 of a fringe-shift is introduced by our tracing method. This is because the traced line (1 pixel thick) is much thinner than the width of a fringe (Figure 3.8), and its position could vary within the boundaries of a single fringe.

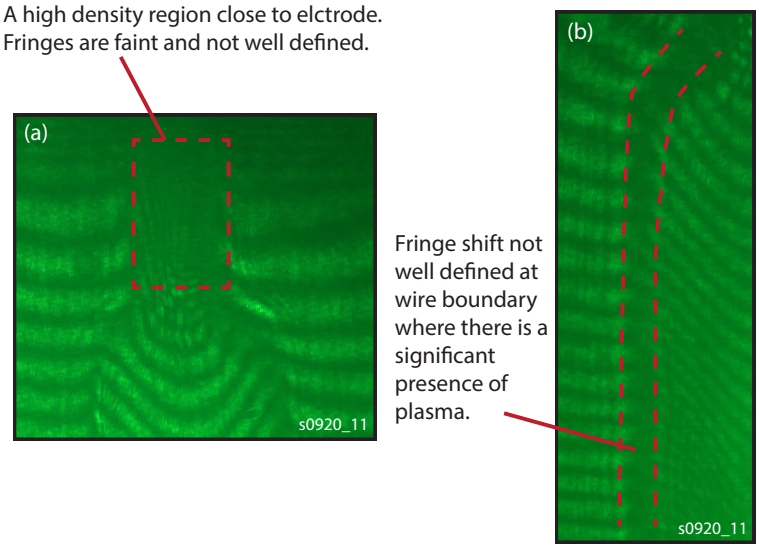

Figure 3.9: Interferometric images from a 2×30μm load array at 177ns showing (a) the electrode end effect of the wire and (b) the effect of plasma (free electrons) around the wire boundary. In both regions the fringe pattern were not well defined due to a high density of atoms or electrons.

We were able to trace a significant portion of the array length, however two regions remained quite challenging to accurately trace. The first was near the electrodes where we observe a 'pinching' effect (Figure 3.9(a)) caused by the electrode's electric fields. As a result, the particle density at those regions are significantly higher than the rest of the array blocking most of the laser light through. We have ignored this region in most of our density analysis and focused on the central region as we have later found that by changing the geometry of the electrode hardware it was possible to suppress those end-effects. The other region was at the wires boundary (Figure 3.9(b)) where in some cases a significant amount of plasma was present causing a large shift in fringe position over a very

small distance. Given the limited resolution of our CCD camera and strong deflection of probing beam on the density gradient, this region was not always accurately resolved. This results in an ambiguity when connecting fringes outside the wires to the ones inside the wires. In such cases, we would look for the best fringe that we could confidently trace through the whole array and set this as our reference point for fringe numbering.

Figure 3.10 shows an example of a traced image for a 2×30μm array (before and during the shot) which is used by MATLAB to interpolate then subtract one form the other in order to generate a 2D map of phase-shift. Regions which were difficult to trace have been blocked by a grey area. In all our experiments, a slight angle has been introduced between the two interfering beam to get a background image of horizontal fringes.

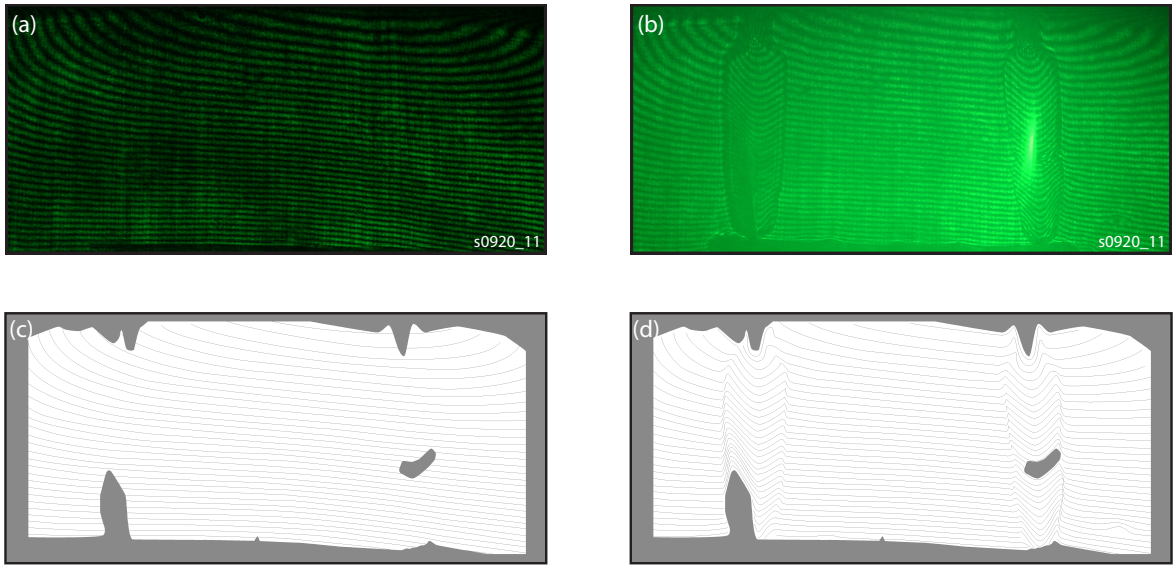

Figure 3.10: Example of a (a) background and (b) experimental interferogram image for a load array consisting of 2×30μm Al wires along with their corresponding fringe trace image (c) & (d) respectively.

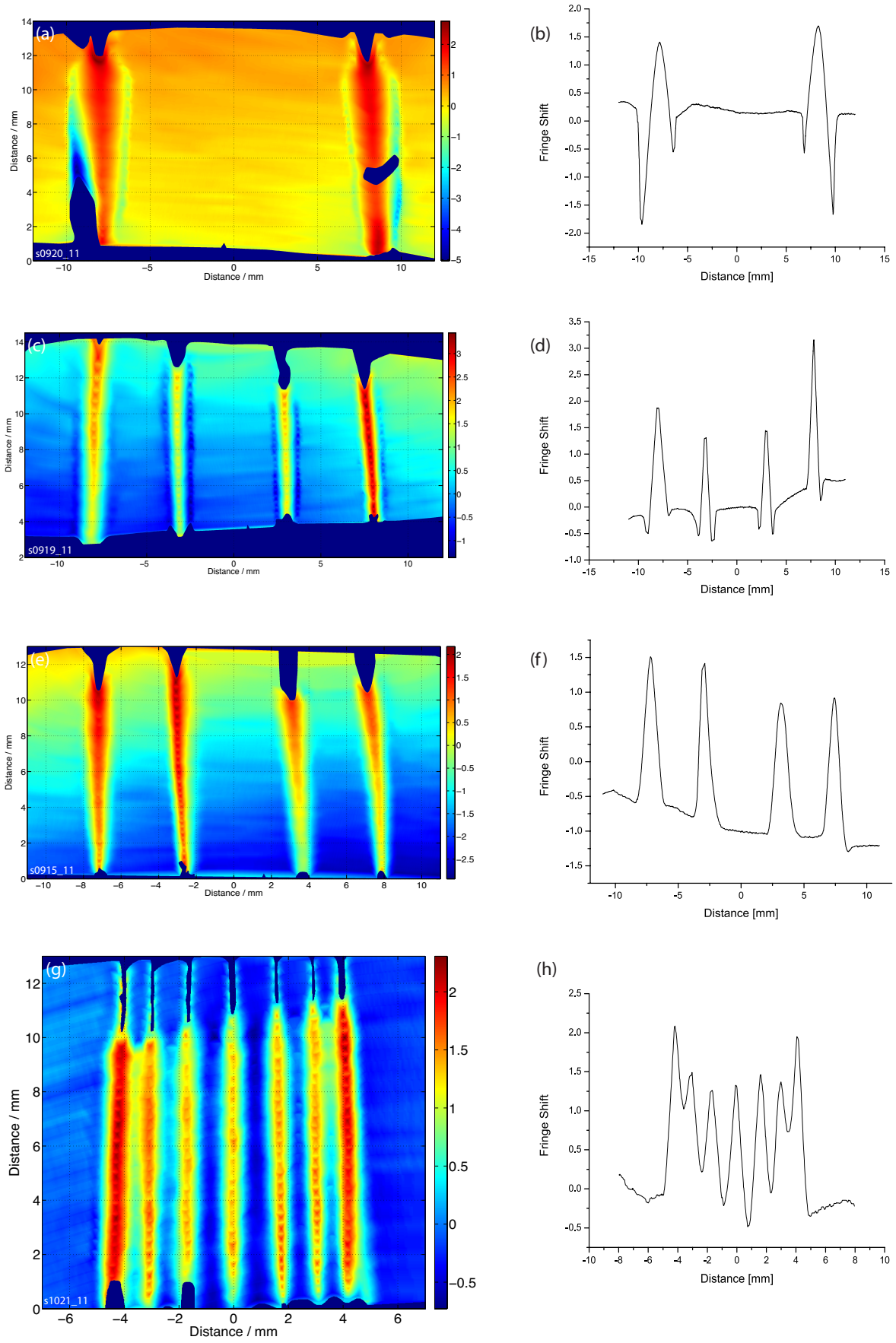

Figure 3.11: 2D phase-shift map along with a line-out at 8mm from cathode for Al wire array loads of (a,b) 2×30μm at 177ns, (c,d) 4×20μm at 185ns, (e,f) 8×15μm at 128ns and (g,h) 16×10μm at 168ns.

Figure 3.11 shows the 2D phase-shift maps for the images presented in Figure 3.7 along with a line-out plot in the central region of the load at a height of 8mm from the cathode. Both positive and negative phase-shifts are observed in our 2D maps. At the central region of each wire we see a positive shift (red), which corresponds to the dominance of neutral Al. While around the edges of thicker wires we see a negative shift (blue), and this corresponds to the presence of plasma (free electrons). This is also evident from the line-outs of the 2×30μm and 4×20μm arrays. We note that we can see - in both 2D maps and line-outs - a gradual change in phase-shift in areas where we do not expect a presence of neutrals or plasmas. For example if we look at at Figure 3.11(e) we notice a change in phase-shift from ~ 0.5 at the top-left corner to ~ -2.5 at the bottom-right corner. This is also reflected on the horizontal line-out plot in Figure 3.11(f) were there is a change in the phase-shift of ~ 1 at the two ends of the plot were we do not expect the presence of a significant amount particles. This gradual change in phase-shift over the entire space of our 2D maps is not real. It is due to the high sensitivity of fringe positions to slightest movement of our mirrors and cameras. Given that the background image is usually taken 30-20mins before the experimental image, we would expect a slight overall change in fringe positions.

We have corrected this error for every wire in an array separately by shifting each wire by a constant value for the end point to be at a roughly zero fringe-shift. In cases where the two end points of a wire line-out are not in line horizontally, we would draw a straight line between those two points and apply a shift based on the gradient of the straight line.

To obtain line density plots from phase-shift line-outs we first need to separate the effect of free electrons from bound electrons in atoms (neutral & ions). Ideally, one would measure the phase-shift using two different laser wavelengths then solve them simultaneously to differentiate the effect of electrons from atoms (Chapter 2, Section 2.2.8). As these were preliminary experiments, such a system has not been setup on MAGPIE at that time. However we can estimate the effect of each (plasma and neutrals) by considering a simple cylindrical model for each wire, consisting of two layers. An outer plasma layer and an inner neutral layer. Figure

3.12 shows a simple schematic diagram of such a model along with a sketch of a phase-shift line-out pattern for a single wire, showing the key turning points. Where a is the thickness of the plasma layer, R is the radius of the neutral layer and P is the maximum phase-shift due to the plasma line density. As can be seen from the diagram we have differentiated those properties for left and right side with an L or R subscript. This is because such properties when measured on both ends from line-outs in Figure 3.11 do not match. Hence, those properties vary with distance in x-direction across each wire in the array.

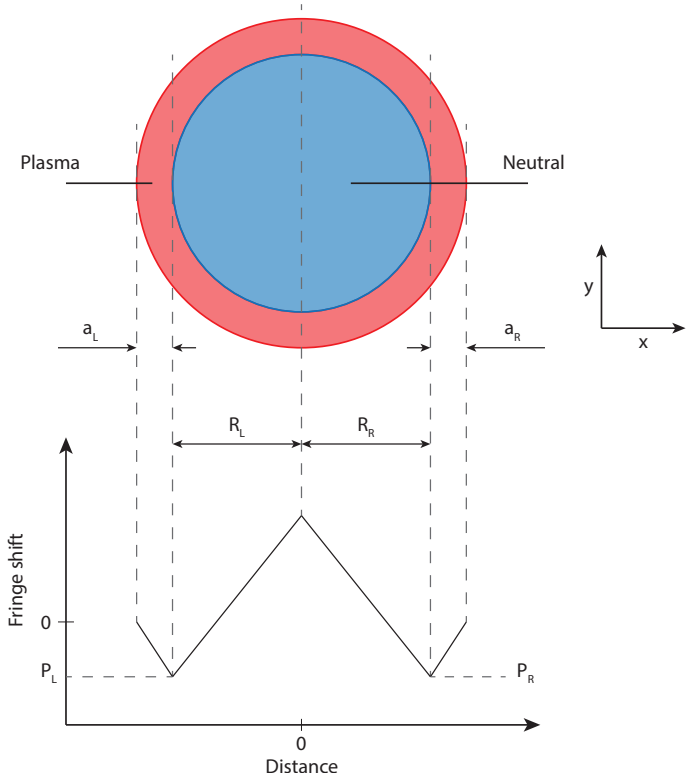

Figure 3.12: A simple 2-layer cylindrical model for preconditioned wires consisting of an outer layer of plasma and an inner layer of neutral gas, along with a sketch of a basic fringe-shift line-out pattern showing the key turning points.

In order to compute the effect of plasma fringe-shift on our total fringe-shift line-outs we need to calculate the average plasma density ρ_p in the plasma layer. Based on the above model, the value of P is proportional to the electron line density. Therefore we can calculate ρ_p for each side (left and right) using the following equation.

$$\rho_p = \frac{P}{2\sqrt{\left(R+a\right)^2 - R^2}} \tag{3.6}$$

Where the denominator in Eq(3.6) is the length of the chord in the y direction through the plasma layer. The average plasma density ρ_p also varies from left to right. One way to go ahead and solve this problem is to assume that a, R and ρ_p are constants for each side of the wire. Then by multiplying the average plasma density to the chordal length of the plasma layer at each point in x, we can estimate the plasma fringe-shift line-out FS_p along the distance in x (Eq(3.7)). The neutral fringe-shift line-out FS_n can then be calculated by subtracting FS_p from the original experimental fringe-shift line-out FS_{exp}. This approach will result in a discontinuity at the peak since we are using different constant values of a, R and ρ_p for each side. A better approach is to assume that a, R and ρ_p vary linearly with distance in the x-direction between the two extreme values in the left and right side. This will generate an 'egg-shaped' object rather than the perfect circular one shown in Figure 3.12, and a more realistic line density plots for plasma and neutrals.

$$FS_p = \rho_p \times 2\left[\sqrt{\left(R+a\right)^2 - x^2} - \sqrt{R^2 - x^2}\right] \tag{3.7}$$

$$FS_n = FS_{\exp} - FS_p \tag{3.8}$$

We applied this method for the 2×30μm and 4×20μm arrays as their fringe-shift line-outs in Figure 3.11 show a significant amount of plasma present at the wire edges. For arrays of thinner wires (8×15μm and 16×10μm), the negative fringe-shift at wire edges is within the boundaries of our error of 0.2. Therefore, for those wire arrays, we will assume the presence of plasma is negligible, and the measured fringe-shift is totally due to neutral Al atoms.

After taking into account the plasma effect on the 2×30μm array, the plot generated for FS_n in the range $-R_L$ to $+R_R$ (Figure 3.13) still shows some negative phase-shift at the edges. Therefore our 2-layer model in Figure 3.12 did not take

into account the effect of all the plasma present in our wire. One reason to explain this, is the fact that at the boundary between plasma and neutral there is an abrupt change. A more realistic approach is to introduce a third intermediate layer at the boundary which contains a mixture of plasma and neutrals (Figure 3.14).

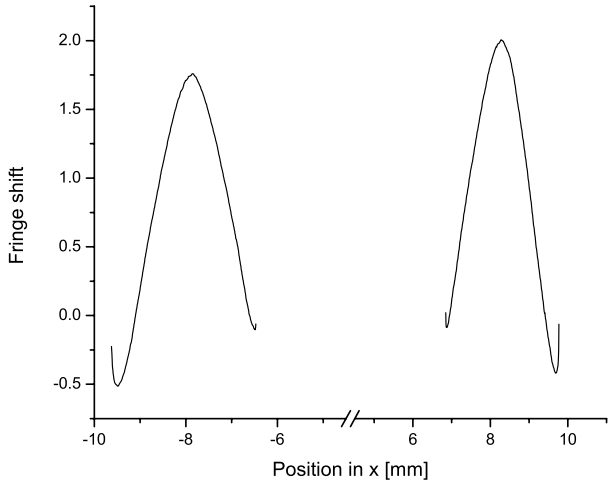

Figure 3.13: Fringe-shift line-out plot for a 2×30μm Al wire array after removing the effect of a plasma layer. Fringe-shift on wire edges show a significant amount of a negative shift, suggesting our model did not take into account all the plasma present.

The thickness of this boundary b (~ 25% of a) is the distance between R and the point where the fringe-shift reaches its minimum in Figure 3.13. This has been measured separately for the left and right side and again we have assumed a linear variation of this quantity between the two sides. We will not be able to resolve the amount of plasma and neutrals in that layer, but we can compute its effect in a similar manner to the plasma layer in Figure 3.12 using Eq(3.6 & 3.7) in order to obtain a more realistic neutral fringe-shift line-out. Therefore, for the 2×30μm array,

$$FS_n = FS_{\exp} - FS_p - FS_m \tag{3.9}$$

where FS_m is the fringe-shift line-out of the intermediate mixture layer. Figure 3.15 shows the new FS_n line-out between -(R_L-b_L) to +(R_R-b_R) when both the plasma and the mixture layer are taken into account. We still see some negative fringe-shift at the wire boundaries, and we can introduce a second intermediate mixture

layer and repeat the process again, but this value lies within our error limits of ± 0.2 and therefore we will ignore it.

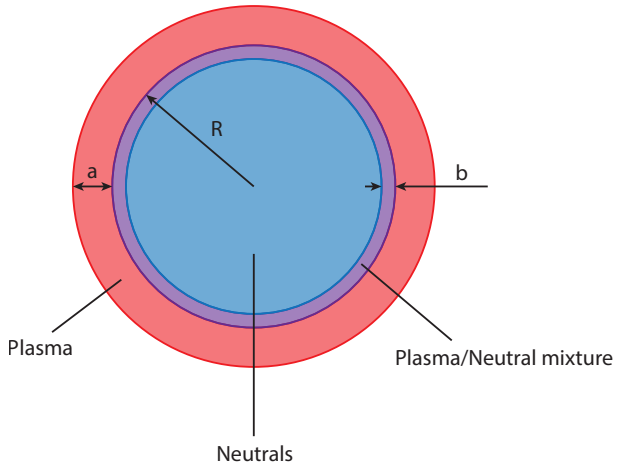

Figure 3.14: A 3-layer model of a preconditioned wire consisting of an outer plasma layer an inner neutral layer and an intermediate layer in-between containing a mixture of plasma and neutrals.

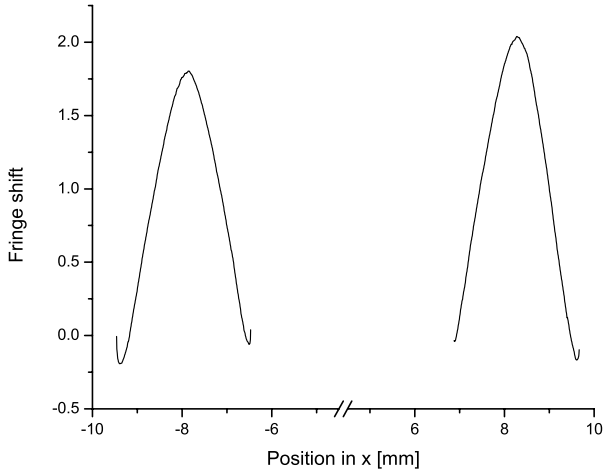

Figure 3.15: Fringe shift line-out plot for the neutral atoms of a 2×30µm Al wire array after removing the effect of the plasma and mixture layer. The negative 'dip' at the edges lie within our error boundary of 0.25 fringe-shift and therefore we will ignore it.

As discussed earlier in Chapter 2 Section 2.2.8, the phase-shift caused by a particular species is proportional to its number density, therefore we can obtain line-density plots from our phase-shift line-outs. To calculate the neutral and electron line density we used Eq(3.10 & 3.11).

$$\int n_e \, dl = -\frac{FS_e}{(4.46 \times 10^{-14}) \cdot \lambda_{[cm]}} \tag{3.10}$$

$$\int n_n \, dl = \frac{\lambda}{2\pi\alpha} FS_n \tag{3.11}$$

Where the e and n subscripts refer to the electron and neutral species respectively, n is the number density and α is the wavelength dependent polarizibility of Al atom. The value for α at λ=532nm is taken from [47] to be 10.8×10^{-24} cm^3. Figure 3.16 shows the line-density plots of neutral atoms and free electrons (where appropriate) for preconditioned Al wire array loads of 2×30μm at 177ns, 4×20μm at 185ns, 8×15μm at 128ns and 16×10μm at 168ns.

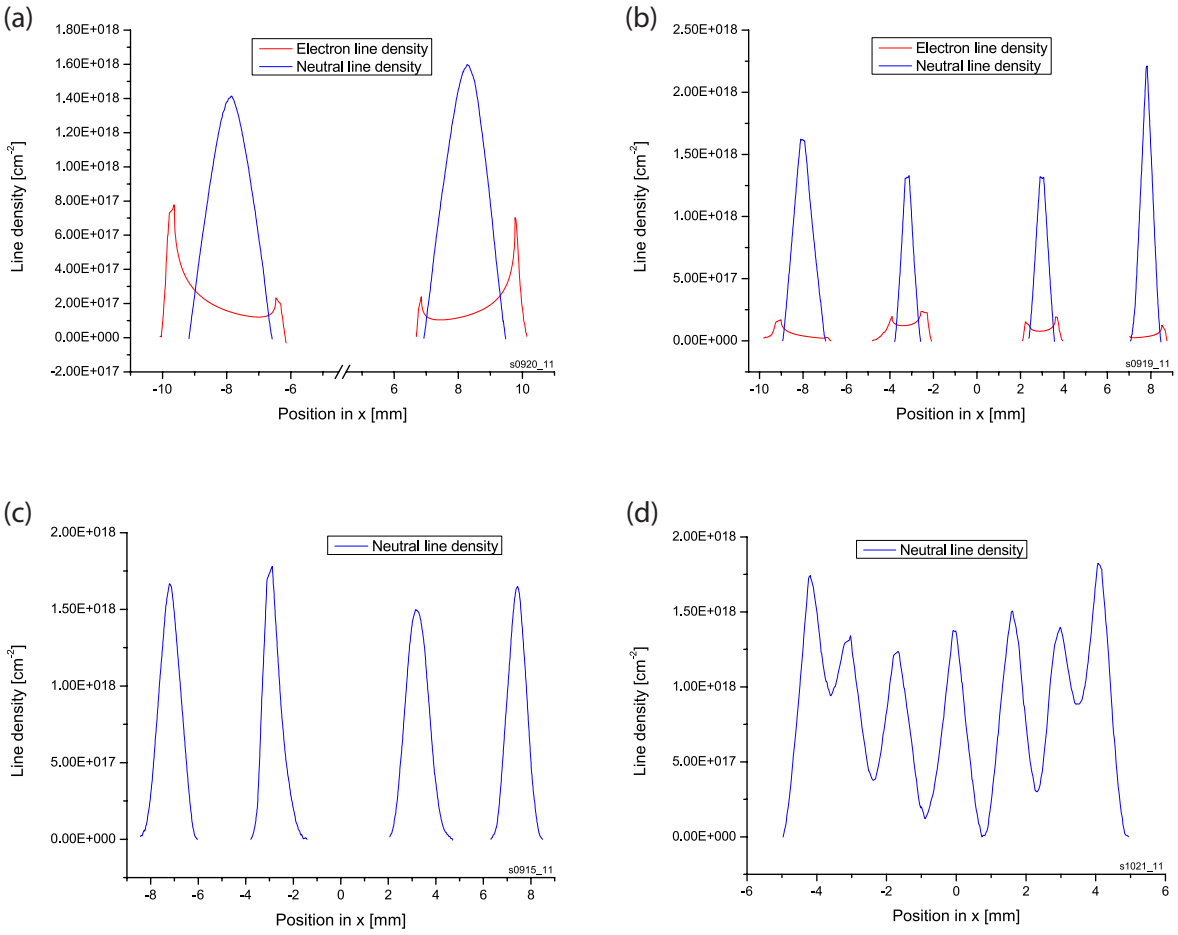

Figure 3.16: Electron and neutral line-density plots for preconditioned Al wire array loads of (a) 2×30μm at 177ns, (b) 4×20μm at 185ns, (c) 8×15μm at 128ns and (d) 16×10μm at 168ns.

Qualitatively, we can seen that thicker wires have expanded to larger diameters. We can also see that the presence of electron is greater for thicker wire arrays than thinner ones. In addition, the electron density is higher at the outer edges of each wire than their inner edges. This is because the inductance at the outer edges is lower and therefore carrying more current. The peak line-density for neutrals doesn't seem to vary much for the different initial wire thicknesses. From first impression, it seems that wires expand to keep a roughly constant peak line density at ~ 1 - 1.5×10^{18}cm^{-2}.

For the 2×30μm and 4×20μm array we have measured the preconditioned wire diameter between the two points where plasma starts to form for each wire. For the 8×15μm array, we managed to resolve the diameter of a single wire at two locations by zooming into the interferometric image (Figure 3.7(c)), where a faint vertical line appears at the place where the wires start to overlap. However its been difficult to resolve the diameter of 1 wire for the 16×10μm array, so we have simply taken the width of the 2 overlapping wires at the centre (x position = 0 in Figure 3.16(d)). Since we see one peak at that position, and the peak width is much smaller than half the total width, then the overlapping mismatch is roughly in the range of ~25% or less of the total width. This will be taken as our error for this value. In general, the error was calculated either from the standard deviation formula if enough measurements were available or by taking the range if only 2 measurements were available.

The total number of neutral atoms and electrons per length of load array can be calculated by integrating the plots shown in Figure 3.16. This is compared with the true value of total number of atoms per length in the solid wires of the array prior to the experiment (calculated using Eq(3.12)).

$$N_{tot} = n_{wire} \times \left(\frac{\rho_m}{A_r} N_A \right) \times \pi r^2 \tag{3.12}$$

Where N_{tot} is the total number of atoms per length, n_{wire} is total number of wires in the array, ρ_m is the mass density, A_r is the relative atomic mass, N_a is Avogadro's constant and r is the radius of the solid wire.

Load array setup	Time of measurement (ns)	Average diameter of a preconditioned wire (mm)	Experimental total number of neutral atoms per length (cm^{-1})	Experimental total number of electrons per length (cm^{-1})	Real total number of atoms per length (cm^{-1})
2×30μm	177	3.7±0.4	$4.52\pm0.71\times10^{17}$	$1.56\pm0.55\times10^{17}$	8.52×10^{17}
4×20μm	185	2.3±0.3	$4.73\pm0.58\times10^{17}$	$7.60\pm5.1\times10^{16}$	7.57×10^{17}
8×15μm	128	2.0±0.4	$6.64\pm0.94\times10^{17}$		8.52×10^{17}
16×10μm	168	1.6±0.4	$8.47\pm1.94\times10^{17}$		7.57×10^{17}

Figure 3.17: Table showing the average diameter of a preconditioned wire, the total calculated number of neutral atoms and electrons along with the real value for Al load array setups of 2×30μm, 4×20μm, 8×15μm and 16×10μm.

Figure 3.17 shows a table of such quantities for the the four different load array setups. The experimentally calculated total number of neutrals decreases when increasing the initial wire thickness of the array. On the other hand, the experimentally calculated total number of electrons N_e increases when increasing the wire thickness. The calculated total number of neutrals deviate significantly from the real value for increasing initial wire thickness. This is expected, since more plasma is present around thicker wires, and therefore more portion of the neutral atoms have turned into ions. Since $N_i \leq N_e$ we can calculate the upper limit for the total number of ions N_i by assuming that every ion has been singly ionised (Z=1, $N_i = N_e$). Therefore, the experimental total number of atoms (ions +neutrals) per length for the 2×30μm and 4×20μm array becomes $6.08\pm0.90\times10^{17}$ cm^{-1} and $5.49\pm0.77\times10^{17}$ cm^{-1} respectively. The real total atom number value still lies outside the error limits, and the same applies for the 8×15μm array. The 16×10μm array is the only one in which the real total number of atoms lie within the error limits of the experimentally calculated value. Figure 3.18 shows the percentage deviation of the real value from the upper limits of the experimentally calculated value of the total number of atoms per length for the four different array setups. As the number of wires in the array increases, the experimental value of total number of atoms gets closer to the real value. The reason for this could be to do with the mechanism in which the heat energy is transferred to the atoms

within the array. Thinner wires have a greater surface area to volume ratio than thicker wires. Therefore they are more efficient in delivering the energy internally to all the atoms. This minimises the chance of having liquid droplets or clusters [48] which have not been heated to boiling temperature within the preconditioned wire. Such droplets and clusters are not sensitive and therefore undetectable by our interferometry system.

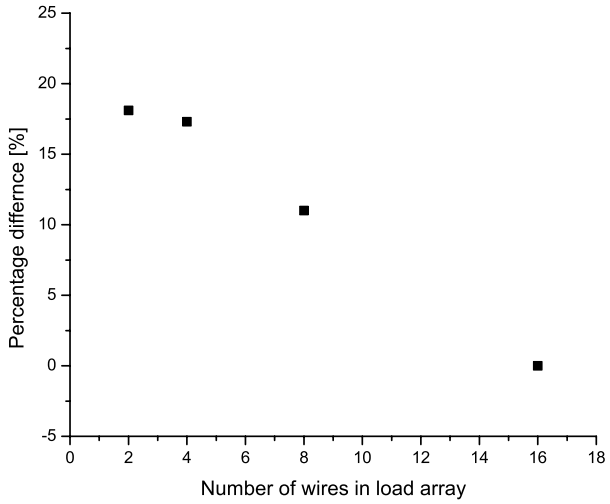

Figure 3.18: The percentage difference of the upper limit of the experimentally calculated value of total no. of atoms per length from the real value, for Al wire array loads of 2×30μm, 4×20μm, 8×15μm and 16×10μm.

Another reason could be to do with our model under-estimating the amount of plasma density around the wire, where we have assumed that this density varies linearly with position in the x-axis. A good example where this could have been true is when estimating the plasma distribution for the two inner wires in Figure 3.16(b) for the 4×20μm array. The image for this array was taken from side-on interferometer camera at a different angle, which had an open-axis view to the 4 wire array. We have mentioned earlier that plasma distribution is greater on the outer edges of each wire than their inner edges. We can see this in both wires in Figure 3.16(a) and the outer wires in Figure 3.16(b). However we cannot see this effect in the two inner wires in Figure 3.16(b) because their outer and inner edges are at the centre of the wire in the image. This means the plasma density around the centre is greater than what we have assumed. As a result, the neutral line-density and the total number of ions for those two wires have been under-estimated.

We have seen that the presence of free electrons is greater for thicker wires. One way to explain this is to look into the current per surface area of wires for the different load setups. For simplicity, we will assume that the current into the load during this phase is constant for all arrays (in reality this is not true since our images were taken at different times and the machine current profile varies slightly from one shot to another). As we are not interested in the actual values of current per surface area, but rather its profile with changing number of wires in an array, we have used arbitrary units (a.u) for this quantity. We plotted in Figure 3.19 the current per surface area along with the experimental values of total number of electrons per wire.

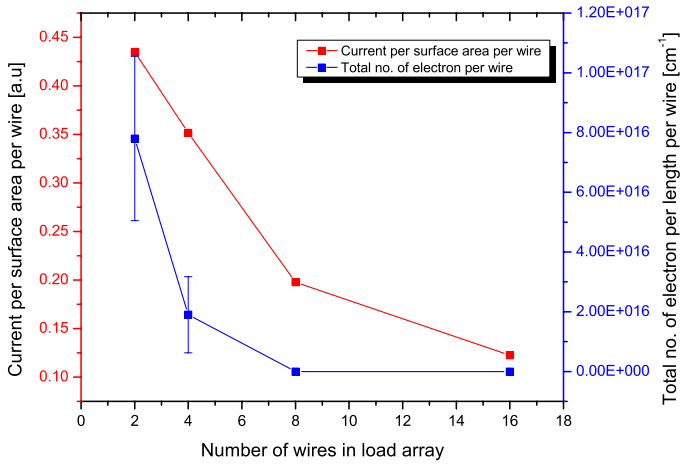

Figure 3.19: A plot showing the variation of current per surface area and the total number of electrons per wire for Al wire array loads of 2×30μm, 4×20μm, 8×15μm and 16×10μm.

We see that there is a correlation between the two plots. Arrays of larger wire numbers have less current per surface area per wire and therefore the presence of electron around the preconditioned wires is hardly detectable. While on the other hand, arrays consisting of fewer wires possess larger current per surface area per wire and hence the total number of electrons per wire is larger.

During the pre-pulse phase energy has been given to the atoms in each wires in the form of heat which causes the wire to expand radially outward. This phase is dominated by a resistive current division between the two arrays. Since the machine (MAGPIE) charging parameters and the inverse array properties have

been kept constant, the current in the load $I_L \propto 1/R_L$, where R_L is the resistance of the load. The loads material (hence resistivity ρ) and the length l have been kept constant, therefore from Eq(3.1) $R_L \propto 1/nA$. Hence, $I_L \propto nA$. The energy deposited into the load is $E_L = I_L^2 \times R_L \times \Delta t$. We will assume the duration of the pre-pulse Δt for all arrays has been constant, as this is governed by the properties of the inverse array which was kept constant. As a result, $E_L \propto nA$. From Eq(3.12), the total number of atoms per length in the load $N_{tot} \propto nA$. Therefore, the average energy per atom $E_{atom} = E_L/N_{tot} \propto 1$. This means that the average energy given to each atom is constant for all our load array setups.

From our results we have measurements of preconditioned wire diameter and the corresponding time of measurement. Assuming that wires begin to expand soon after they reach boiling point (~15ns), and their expansion is linear, we can calculate the linear expansion rate V_{exp} for wires with different initial thicknesses. For a monatomic gas expanding in a vacuum, $V_{exp} \sim 3 \cdot C_{sound}$, where C_{sound} is the gas sound speed defined as [49],

$$C_{sound}[cm/s] = 10^6 \sqrt{\frac{T[eV]}{A_r}} \tag{3.13}$$

T is the average temperature of the expanding gas and A_r is the relative atomic mass. From the above equation we can estimate the average temperature of the expanding wire. Figure 3.20 shows a plots for the expansion velocity and temperature for wires of different initial thicknesses.

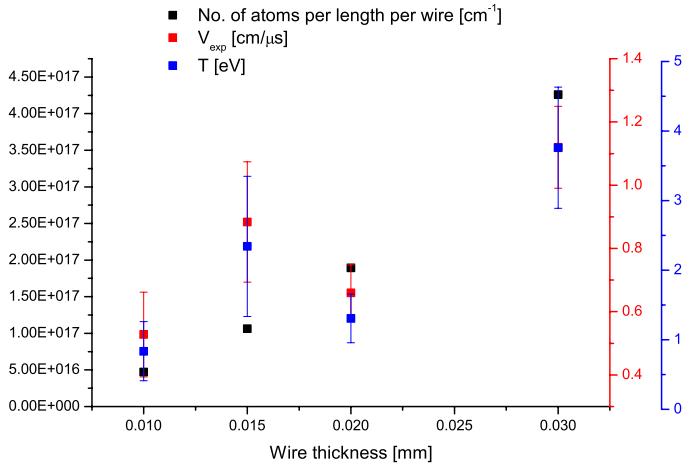

Figure 3.20: Plot showing the variation of a preconditioned wire temperature, expansion velocity and total number of atoms per length for different initial wire thickness.

We can see from the above figure that as the initial wire thickness increases so does its expansion velocity and hence its average temperature. We can understand this by looking into the amount of undetected mass by the interferometry in Figure 3.18. We have shown that the energy transferred per atom is constant in all load setups. Therefore, one possible explanation for this observation is that thicker wires are less efficient in transferring their heat energy equally to all atoms due to the lower surface area to volume ratio, therefore less gaseous mass is detected from interferometric analysis suggesting a greater presence of liquid droplets and clusters [48] (particles of low energy) hence the detected expanding gas contains more energy per atoms and therefore greater temperature.

The average temperature in our load array varied between a minimum and a maximum of 0.5 - 4.5eV for different wire thicknesses. This value represents the initial wire temperature at the start of expansion. As the wire expands it cools down and the average temperature after a given time would be lower than the values stated in Figure 3.20. This temperature is not sufficient to ionise the bulk of Al atoms, as most of the atoms are in a neutral gaseous state.

3.1.4 Summary and conclusion

Initial experiments of a 2-stage wire array Z-pinch configuration were previously only performed for loads of 8 wires on a 1MA pulsed power device. We have

demonstrated that by varying the load wire number but keeping the overall array mass constant at 40μg/cm and increasing the peak current to 1.4MA, we were able to trigger an early pre-pulse current into the load - similar to previous experiments [31] - which heated solid wires into gas. When plasma formed at the inverse array, most of the current diverted to that array (bottom array) due to inductive division, and the load gaseous wires were allowed to expand before the main current switch (*preconditioning of wires*). This period was roughly ~ 200ns, during which line-density plots were obtained from interferometric images showing that thicker wires have expanded to larger diameters than thiner wires. Where, the 30μm wire expanded to a diameter of 3.7±0.4mm while the 10μm wire expanded to a diameter of 1.6±0.4mm. In addition such plots showed that thicker wires had a significant amount of plasma around them (for the 30μm wire, $N_i \leq 0.18N_{tot}$), whereas this was hardly detectable in thinner wires. The expansion rate and temperatures of thicker wires were also greater, the average effective temperature of a 30μm wire at the start of expansion reached 4.5eV. This value becomes lower as the wire expands and not large enough to overcome the first ionisation potential as the expanding gaseous wires in all the arrays investigated were mostly in a neutral state.

In the next two chapters we investigate the preconditioning effect and the implosion dynamics after current switch for the 2 extreme conditions when varying the load wire number in a 2-stage wire array Z-pinch configuration. This is:

- A single wire on axis.
- A cylindrical array consisting of large wire number with a small inter-wire separation to form a plasma shell of preconditioned wires.

3.2 Investigation of the current switch mechanism

Earlier experiments conducted on the MAGPIE generator of a two-stage wire array Z-pinch configuration showed that the current through the load's wire array is sufficient to drive an accelerating implosion. It has been estimated from 0D implosion trajectory fittings that a linearly rising current reaching a peak of ~

1MA in ~ 90ns is needed to drive the observed implosions of an 8×10μm and 8×15μm Al wire array [31]. Attempts to directly measure the current through the load after the switch and during the implosion time were not successful. Rogowski probes positioned around a return post of the load array shows the signal rises sharply at the start of the switch before saturating at a low level (Figure 3.21 (Right)). This could indicate a break-down of the Rogowski probe due to a large dI/dt generating a large voltage. Another possibility could be the current takes a different route from the one shown in Figure (3.21 (Left)). The next section describes the experimental setup in which we attempt to directly measure the current in the load section.

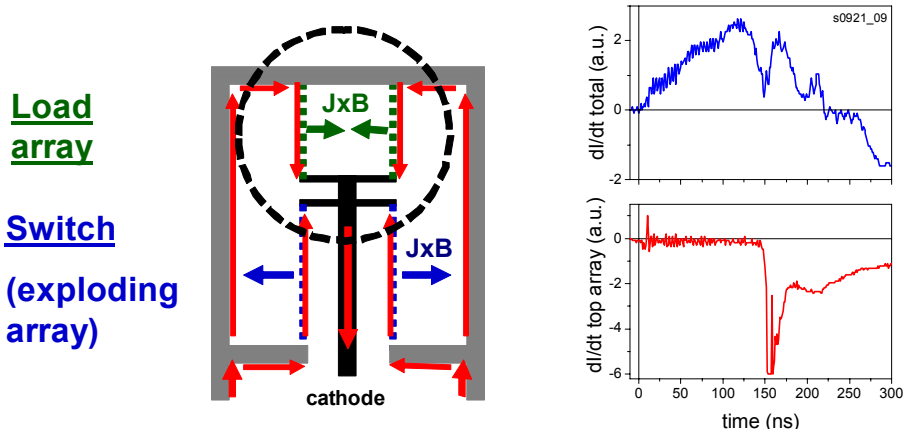

Figure 3.21: (Left) Schematic diagram of a two-stage wire array load showing the two different paths of current. (Right) dI/dt signal of the generator (blue) and of the load section (red) for an 8×15μm Al wire array [31].

3.2.1 Experimental setup

The setup for this experiment was identical to the setup described in Section 3.1.1, however the wire array load was replaced by a static current-measuring diagnostic (Figure 3.22). This is simply a brass cylinder (20mm in diameter × 25mm in length) with two B-dot probes inserted inside and positioned at equal radius of mm. The probes sit at the bottom of the brass cylinder and shielded with 5μm NiCr foil to allow penetration of the magnetic field. The two probes were wound in opposite direction to distinguish between the two signals and to measure the contribution of capacitive coupling to the measured signal. The two probes were calibrated in the same two-stage configuration setup but without the inverse array.

In this case all the current from the generator flows through the load section. This well known current profile of the machine was used to calibrate the B-dot probes.

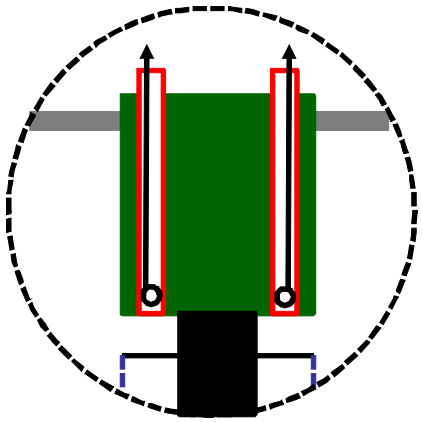

Figure 3.22: Schematic of a static current-measuring diagnostic load, showing the two B-dot probes sitting at the bottom of the brass cylinder (green object). The field of view is a zoom-in of the region inside the dashed circle in Figure 3.21 with the array replaced by the current-measuring hardware.

3.2.2 Results and analysis

The B-dot signals from the above setup is shown in Figure 3.23. The polarity of one of the B-dot signals was inverted to account for the opposite direction of probe winding. The signal from the two probes are in good agreement with each other and suggest the contribution from capacitive coupling is small. At the start of the current pulse a short (~ 15-20ns) prepulse current is detected in the load section by both B-dot probes. This prepulse is the result of resistive current division at the start of the experiment. The duration of this prepulse was exactly the same ($\pm$ 1-2ns) as for wire array loads (Section 3.1.2). Hence strongly suggests that the duration of the prepulse is determined by the formation of plasma at the inverse array rather than the increase in load wire resistance.

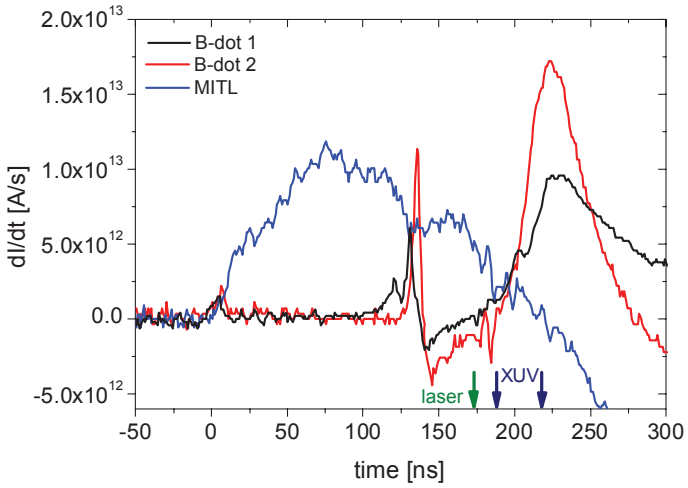

Figure 3.23: dI/dt signals from the two B-dot probes of the current-measuring load and the total dI/dt of the generator from the MITL B-dot. Polarity of one of the load B-dot is inverted to account for the opposite direction of the probe's winding.

At ~ 125ns we see a fast rise in dI/dt signal in both B-dot probes which indicates the beginning of current switch into the load. This switch usually coincides with formation of gaps in inverse array wires [32] triggering the onset of array explosion. The increase in resistance and inductance of the exploding array causes a significant portion of current to switch to the load. However at ~140ns the signal falls down to almost zero before rising again at ~ 200ns. To understand this behaviour in dI/dt signal, we have performed laser probing and XUV imaging of the current-measuring load at the period corresponding to ~ 'zero' dI/dt after the switch (The probing times are indicated by arrows in Figure 3.23).

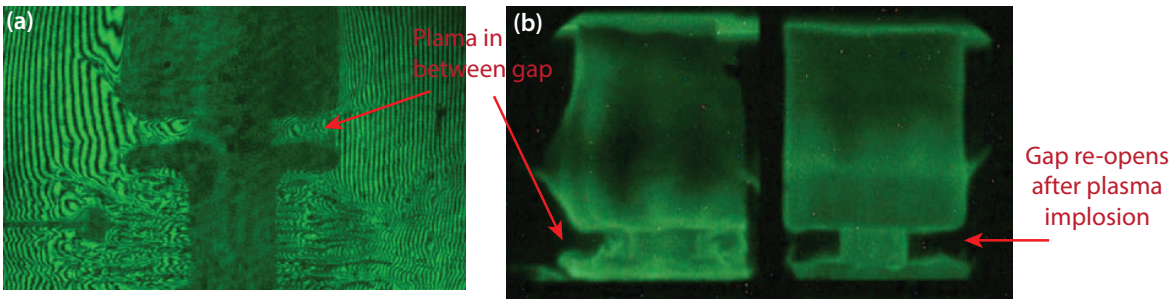

Figure 3.24: (a) Laser (λ=532nm) interferogram image at 175ns showing the presence of plasma in between the gap separating the load from the inverse array. (b) XUV images at 188ns (left) showing the presence of plasma in the gap and at 218ns (right) after the implosion of this plasma in the gap region re-opening the gap.

Both laser interferogram and XUV (at 188ns) images (Figure 3.24) show the presence of plasma in the gap between the load and the top electrode of the inverse array. This means that current could flow through this plasma across the gap into the cathode rod instead of flowing through the bottom surface of the load where the B-dots are located. As a result, the B-dot probes do not detect any change in current until this plasma implodes as seen in a later XUV image at 218ns (Figure 3.24(b)) and the gap is 're-opened'.

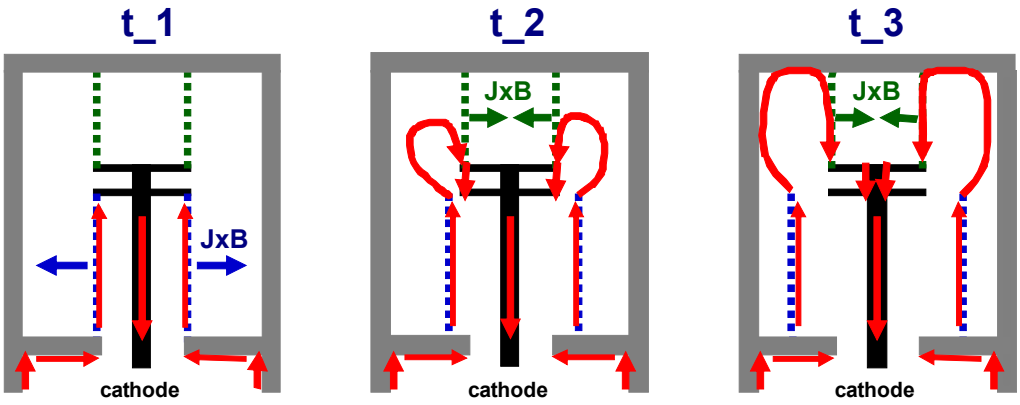

Figure 3.25: Schematic of a two-stage wire array configuration showing the possible current path formed by the exploding plasma at different times after the switch.

These observation suggest the following interpretation of current switching into the load (Figure 3.25). As gaps form along the inverse array which triggers the final explosion, both the inductance and resistance of this array increases significantly driving a great portion of the current into the load leading to the start of the current switch. As the explosion of the inverse array progresses, the plasma 'bubble' formed at the top electrode of this array expand upwards and closes the gap as shown in Figure 3.25 (t_2). The new current path formed does not go through the region were the B-dots are located and hence no signal is detected during this time. The current through the plasma in between the gap causes it to implode after some time (t_3) and 're-opening' the gap allowing the B-dots to measure dI/dt signal again. The new plasma return current path (Figure 3.25 at t_3) does not necessarily expand all the way to the return post and thus creating a secondary return current path for current in the load. The current will be divided between this new path and the return posts. This could be another

explanation for the break-down and decay in the Rogowski probe signal observed by Harvey-Thompson [32] (Figure 3.21).

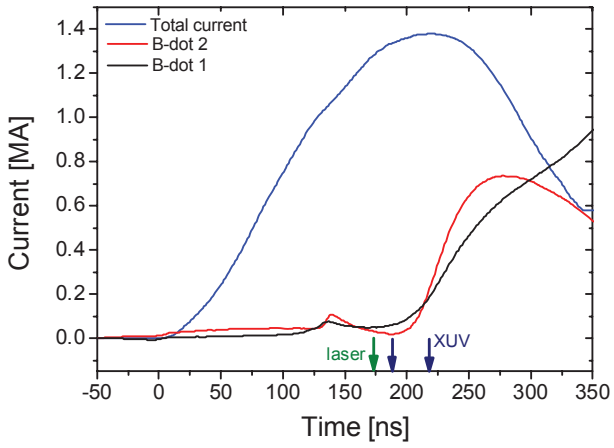

Figure 3.26: Current through the load obtained by integrating B-dot dI/dt signals, along with the total generator current.

By integrating the dI/dt signals we were able to plot the variation of current in the load with time which is shown in Figure 3.26 along with the total current of the generator. This a lower estimate of current in the load since the the B-dot probes were shielded for some time (~ 20ns) by the plasma in the gap and were not able to measure dI/dt for this period. The measured current peak in the load by the B-dot probes is ~ 700kA however the real peak value is most probably much higher.

3.2.3 Conclusion

This interpretation of current switch mechanism still needs to be supported by additional experiments, but it does appear to be very plausible. This current switch mechanism has a huge implication if one considers scaling this switching approach to Z conditions (~ 20MA in ~ 90ns). Since the switching does not entirely rely on the increase of resistance of the exploding array, but also relies on the flow of plasma 'bubble' from the top of the inverse array to the load (acting as a plasma-flow switch) and the re-opening of the gap by plasma implosion. Assuming the switching relies more on the latter, then it will have a more favourable scaling with increasing generator current causing a faster implosion of plasma in the gap and hence a more rapid current switch. One possible negative effect of the plasma-flow switch mechanism is the fact that switching is not axially

uniform in time. It starts from the bottom of the load reaching the top part as the exploding plasma further expands outwards leading to a 'zippering' effect. This effect has been observed in wire array ionisation after the switch [32], but the duration of this is much smaller than the implosion time and did not effect the implosion trajectory in the axial direction.

Chapter 4

Dynamics of a Single Wire Load

In the previous chapter we saw that cylindrical array loads in a two-stage wire array Z-pinch configuration can be preconditioned (expansion of individual wires into columns of gas) before the main current switch regardless of the number of wires. We have investigated cylindrical arrays of 2, 4, 8 and 16 wires. Z-pinch experiments involving a single wire on axis have been investigated decades ago [50, 51] but never in a two-stage configuration. In this chapter we investigate the preconditioning effect and implosion dynamics of an axial single wire load in a two-stage Z-pinch configuration. The preconditioning effect was analysed from line density measurements of interferogram images before the main current switch, while the implosion dynamics were analysed from optical and XUV images after the switch. We have investigated single wire loads of 25μm, 40μm and 50μm Al.

4.1 Experimental setup

Again, those experiments were conducted on the MAGPIE pulsed power generator (1.4MA in 250ns) which is described in detail in Chapter 2. The diagnostics were arranged as shown in Figure 2.7 (Chapter 2). The two-stage wire array Z-pinch setup was identical to previous experiments in Chapter 3 (Figure 3.1), however instead of having a cylindrical wire array load, the load was simply a single wire on axis. Figure 4.1 shows a cross-section schematic diagram of a two-stage wire array Z-pinch configuration with a load consisting a single axial wire.

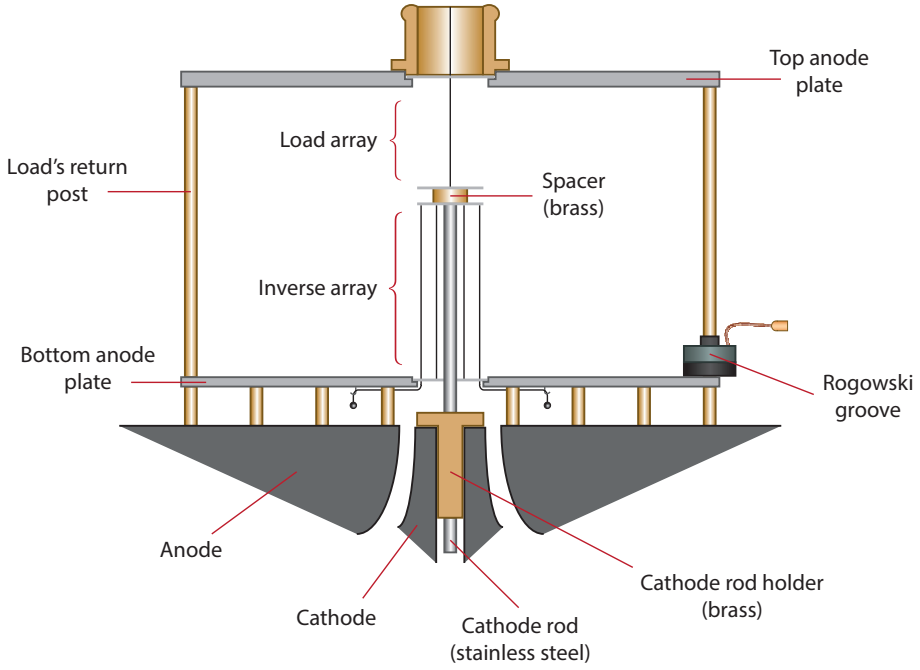

Figure 4.1: A cross-section schematic diagram of a two-stage wire array Z-pinch configuration with a load consisting of a single wire on axis.

This configuration consists of two wire array sections sandwiched between two 170mm diameter stainless steel anode plate. The top anode plate is attached to the bottom plate by 4 brass return posts, 6mm diameter × 75mm long each. A minimum number of return posts is used in order to keep as much open space as possible around the array for diagnostic equipments. On the other hand, the bottom plate is connected to MAGPIE's anode by 16 brass return posts, 10mm diameter × 10mm long each. The large number of short return posts minimises the total inductance of the inverse array and ensures an equal distribution of current around the bottom plate. At the centre, a brass cathode holder - which sits on MAGPIE cathode - holds the 8mm diameter stainless steel cathode rod in place. This rod supports both top and bottom arrays which are separated by a brass spacer 5mm thick. Both the cathode rod and the spacer are replaced by a new one for every experiment.

The inverse array (bottom array) properties were kept constant through out all our experiments described in this thesis. This array consists of 8×15μm thick aluminium (5056 alloy) wires. The array diameter and length were set to 16mm and 55mm respectively. The wires were arranged in a cylindrical fashion equidistant from each other using notched disks placed on the top and bottom end

of the array. At the top end, wires were glued on the disk using a fast-setting epoxy. While at the bottom end, the wires would pass through the notched disk and placed underneath the bottom anode plate. There the wire are left hanging on hooks with lead weights attached to their ends to keep the array wires taut and straight. The distance between the two notched disks is the array length (55mm).

The load array (top array) setup was simply a single wire on axis, where special notched discs were used at both ends to keep the wire held straight in position. No epoxy was used to attach the wire to the discs, instead a small lead weight was attached to the end of the wire and tucked underneath the notch of the bottom disc. This secured the wire in place at the bottom end. While, heavier weights were attached on the other (top) end of the wire and left hanging above the top anode plate (this can be seen clearer in Figure 3.1 Chapter 3). This ensures the wires are kept taut and straight before the start of the current pulse. The array length was kept constant throughout these experiments at 15mm, however the wire thickness (hence, total array mass) was varied. Experiments were conducted for loads consisting of a 25μm, 40μm and 50μm Al wire.

4.2 Early stage dynamics before current switch

4.2.1 Initial current prepulse

As discussed earlier in Chapter 3, the current has two paths from anode to cathode. One path is through the inverse array while the other path is into the load array and through the cathode rod. The current division is determined by the impedance ratio of both routes. This mainly depends on the resistance and the global and local inductance of each array.

At the start of the current pulse the two arrays consist of solid resistive wires. The impedance due to its resistance is much larger than the inductive impedance and therefore, the current division is governed by the resistance ratio of the two arrays. As time progresses, ohmic heating raises the temperature of the wires and further increases their resistance until the point solid wires melt then vaporise into plasma.

At that point the resistance falls down due to the high conductivity of plasma and the current division is now governed by the inductance ratio of the two arrays. Since current takes the least inductive route which is the path into the inverse array, we expect very little current to go through the load during this phase, until the inverse wires fully explode. Therefore at the start of the current pulse, the initial resistive division would trigger a prepulse current into the load. This prepulse current has been observed experimentally from Rogowski groove signals for a single 25µm, 40µm, and 50µm Al wire load.

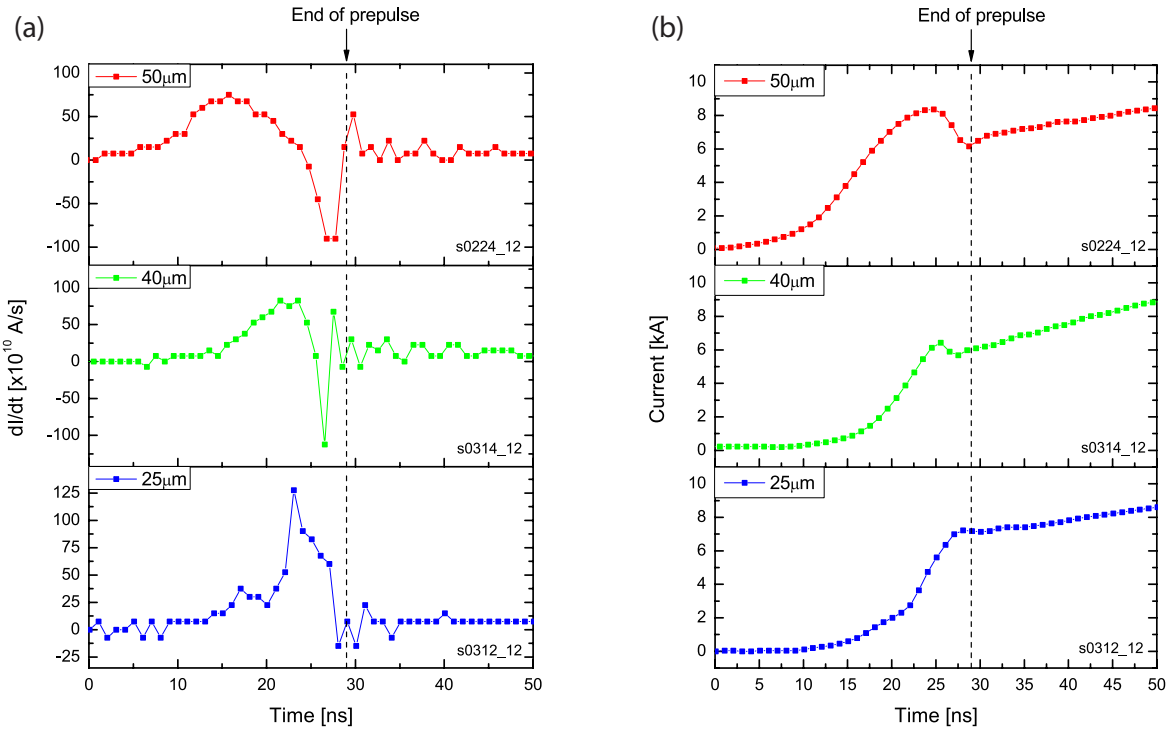

Figure 4.2: Plot showing the variation of (a) dI/dt and (b) current with time during the first 50ns after the start of the current pulse for a single 25µm, 40µm and 50µm Al wire load.

The Rogowski groove measure dI/dt through one of the 4 posts delivering current into the load. By taking into account the number of posts and multiplying by appropriate attenuation and coefficient factors, the actual variation of dI/dt into the load is presented in Figure 4.2(a) for different load wire thickness. By integrating dI/dt, we also present in Figure 4.2(b) the variation of current into the load for different wire thickness.

In all three single wire load experiments we see a steep increase in dI/dt soon after current start, which then falls down sharply to nearly zero at around 29ns. This change corresponds to a fast rising current into the load reaching a peak of 6-8kA in 25-27ns. The prepulse ends when voltage breaks down at the inverse array due to the formation of plasma. This abruptly changes the flow of current in the load section, which can be seen in Figure 4.2(a) as a sudden dip of dI/dt signal just before the 'end of prepulse' mark. We can see from both plots that the end of prepulse is constant (±1ns) for different load wire thickness, indicating that the duration of this pulse is controlled by the properties of the inverse array which we kept constant throughout this entire investigation.

Due to the short duration of the pulse and limited temporal resolution of our scope, there has only been a limited number of data points recorded to define the pulse shape. Specifically, at the point when voltage break down occurs at the inverse array, only 5 data point were recorded for the 50μm wire, 3 data points for the 40μm wire and 1 data point for the 25μm wire. In all cases, the amount of recorded data points are not enough to accurately quantify the current at the end of prepulse. However we can clearly see that this change happens over a larger period as the load wire gets thicker (hence, the larger amount of data points recorded for thicker wires). One reason to explain this is that thicker wires are less resistive and therefore at the start of the current pulse a greater fraction of the current goes through loads consisting of thicker wires. We will assume that this current division is maintained throughout the ohmic heating process until plasma forms at the inverse array. At that point, resistive current division becomes negligible and current takes the least inductive route (through the inverse array). The voltage across the load is now solely generated by the change in local inductance of the inverse array. Given that the there isn't a great variation in load resistance for different wire thicknesses after the prepulse (assuming wires reached boiling point), the current through the load at that instant should be constant for all wire thickness. Hence, as the load wire gets thicker, the difference between the prepulse current peak and the current value at voltage breakdown should get larger. This is clearly seen in Figure 4.2(b).

The temperature of the load wire during the prepulse phase can be calculated from current measurements and hence the state of the wire at voltage breakdown. Assuming a volumetric ohmic heating by the prepulse, we can use the following equations Eq(4.1 & 4.2) in an iterative loop to calculate the change in temperature with time.

$$\Delta Q = \int I^2(t) R(T)\, dt \tag{4.1}$$

$$\Delta T = \frac{\Delta Q}{mc(T)} \tag{4.2}$$

Where ΔQ is the energy deposited into the wire, R is the wire resistance, I is the current into the load, ΔT is the change in temperature, m is the total wire mass in the load and c is the specific heat capacity of the wire material. Both R and c are temperature dependent, and those values change at every new iteration. The variation of Al resistivity and specific heat capacity with temperature has been presented earlier in Chapter 3 Figure 3.4. Solid and liquid aluminium resistivity varies linearly with temperature, each possess a unique linear relationship. While the specific heat capacity does not vary much with temperature and is assumed to be a constant value of $28.7 JK^{-1}mol^{-1}$ for solid and $31.8 JK^{-1}mol^{-1}$ for liquid aluminium. In order to compute a reasonably accurate summation for the integral in Eq(4.1), we have linearly interpolated the current values in between the data points during the prepulse phase. The temperature values were then obtained from the interpolated current profile. Temperatures beyond boiling point were ignored as no reliable resistivity data is available for gaseous Al, and measurements of dI/dt are not sufficiently accurate at that time. Figure 4.3 shows the rise in wire temperature during the prepulse phase for a single Al wire load of 25μm, 40μm and 50μm thickness.

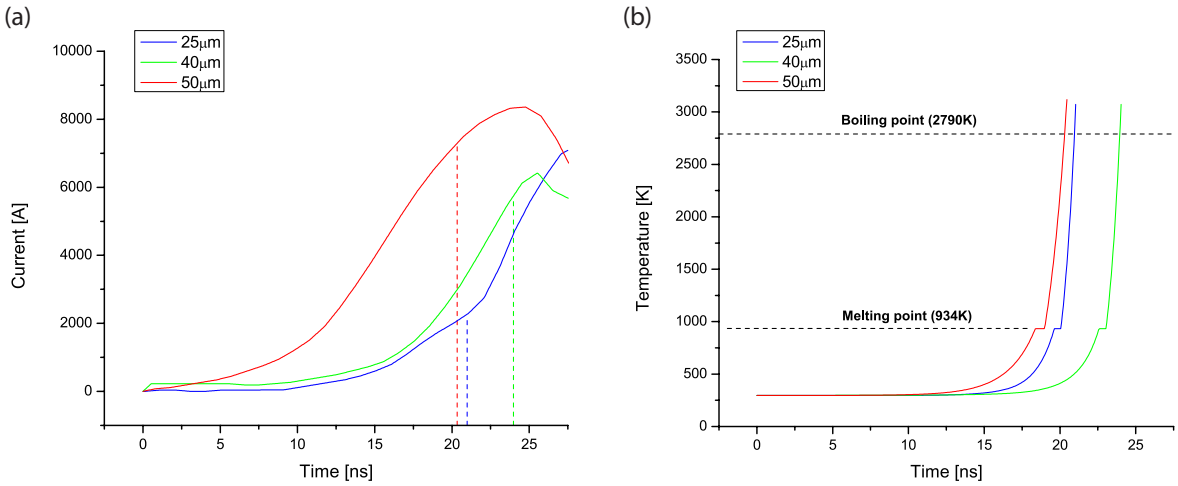

Figure 4.3: The rise in (a) current prepulse and (b) calculated temperature at an early stage of the experiment for a single Al wire load of 25μm, 40μm and 50μm thickness. The dashed vertical lines in (a) are the time at which the corresponding load wire reaches boiling point.

For all three load wire thicknesses, the prepulse current increases the wires temperature. The increase in temperature causes an increase in wire resistance, and hence more energy deposited (Eq(4.1)) into the wire increasing the temperature even further. The effect is an increase in the rate of temperature rise as time progresses. This rise abruptly stops for a brief time of ~ 0.5ns when the temperature reaches melting point (934K). During which the the energy deposited breaks the structural bonds of solid aluminium. Afterwards, the temperature steeply rises due to the sudden increase in resistivity of liquid Al, and in roughly 1ns the wires reach boiling point (2790K).

For the initial resistive stage we can model our 2-stage Z-pinch setup as two resistors connected in parallel. Since the machine parameters were not changed, we can assume that the voltage profile generated across the circuit during the prepulse phase is constant for all three experiments. Therefore the current though the load section is totally dependent on the resistance of the load. As we kept the load material and length constant while we varied the wire thickness, the change in current through the load ΔI_L between the three experiments is proportional to the change in cross-sectional area ΔA of the load wire ($\Delta I_L \propto \Delta A$). The change in the rate of energy deposition (i.e change in power) into the load ΔP_L between the three experiments is $\Delta I_L^2 \cdot \Delta R_L$. Hence $\Delta P_L \propto \Delta A$. Thicker wires contain more atoms,

and the change in the number of atoms in the load ΔN_{atom} between the three experiments is proportional to the change in cross-sectional area of the wire ($\Delta N_{atom} \propto \Delta A$). Hence, the change in power per atom ΔP_{atom} as we vary the load wire thickness is $\Delta P_L/\Delta N_{atom} = 1$. This means, the rate in energy increase per atom is constant and independent of the load wire thickness, suggesting that the temperature profile during this phase of the experiment should not vary with load wire thickness. In Figure 4.3(a) we can see that the thickest and thinest wire (50μm & 25μm respectively) reach boiling point at roughly the same time of 20-21ns, and their temperature profile in Figure 4.3(b) closely match in time. The 40μm wire reaches boiling point at a later time (24ns) and the temperature profile is shifted later in time. Those variations are due to the fact that the current and voltage profile of our machine fluctuates from one experiment to the other, which depends on the timings at which the 4 Marx banks and line gap switches are triggered. Therefore, affecting the overall superposition of current signals that reaches the load.

As the load wire heats up and vaporises into gas, similar heating happens to the bottom inverse array. In all three single wire load experiments, the wires did reach boiling point before the prepulse current reaches its peak value. Hence, the prepulse current continues to increase even when solid wires change into gas. This can be clearly seen in Figure 4.3(a) where the prepulse current of the 25μm wire continues to increase even further for 7ns after reaching boiling point. This strongly suggests that the end of the prepulse is not caused by the formation of gas at the load, rather by the formation of plasma at the inverse array.

The formation of plasma at the inverse array marks the end of the resistive current division, hence the end of the prepulse phase. Due to the high conductivity of plasma, current now takes the least inductive route which is the path into the inverse array. During this time and until the inverse array fully explodes, very little current goes into the load. This lack of significant current for some period of time, drastically affects the wire structure before the main current fully switches into the load.

4.2.2 Preconditioning of load wire

In all three experiments where we varied the load wire thickness (25μm, 40μm & 50μm), the prepulse current managed to deposit enough energy to vaporise the load wire. The prepulse phase ends when plasma forms at the inverse array, and current takes the least inductive route (into the inverse array). During the time when inverse array wires ablate, very little current goes into the load. Figure 4.4 shows a plot of dI/dt and current into the load during this phase of the experiments which is marked between the 'end of prepulse' time and 'current switch' time.

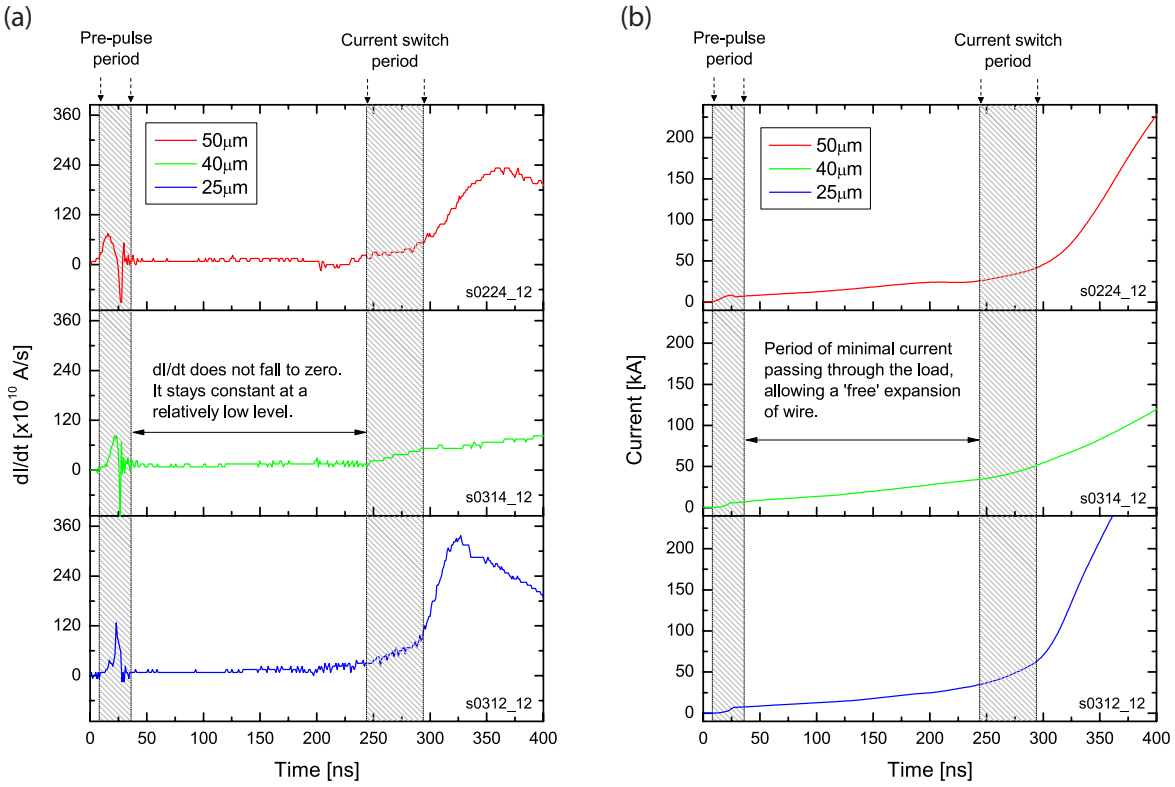

Figure 4.4: Plot of (a) dI/dt and (b) current into the load vs time for different load wire thicknesses. After the prepulse and before the current switch dI/dt falls to a relatively low level but not zero.

After the prepulse phase, dI/dt into the the load for all wire thicknesses does not fall down to zero. rather it stays at a relatively low level of ~ $10{\times}10^{10}$A/s. This corresponds to a steadily increasing current into the load. The small voltage across the load is generated by a changing magnetic flux escaping from the gaps between the wires of the inverse array. As dI/dt gets larger with time, so is the rate of

change of magnetic flux, and hence an increase in load current with time. In addition, the current through the inverse array follows the outer path of the ablation streams which gets larger as time progresses, increasing the resistance of this array, and consequently driving more current into the load. We cannot accurately quantify the amount of current rising into the load during this phase for two reasons. One - which has been explained earlier - is the fact that the prepulse dI/dt profile is not well defined when voltage breakdown happens at the inverse array. Secondly, the Rogowski groove used has a low sensitivity, which cannot accurately measure a low level dI/dt through a post which carries a small current. However, we can safely state that there is a relatively low level of current that goes into the load during this phase and it is at the order of a few percent of the total current.

From earlier results of cylindrical Al wire array loads (Chapter 3), this low level current had no dynamical effect on the load wires after the prepulse phase and before the current switch. The wires thermally expanded during this phase into columns of Al gas, and we referred to this as *preconditioning of wire*. This expansion is observed for all single wire loads from optical streak images (Figure 4.5) and interferometric images of a 2nd (532nm green) and 3rd (355nm blue) harmonics of a Nd:YAG laser (Figure 4.6 & 4.7). All images were taken at the period before the current switch and after the prepulse. Optical streak image for all three wire thicknesses clearly shows a linear expansion of the heated wire until the point of current switch. During the expansion phase, interferometric images show fringes all the way across the wire over a large portion of its axial length. This suggests that the solid wire has turned into an expanding gas unaffected by the low level of current through it.

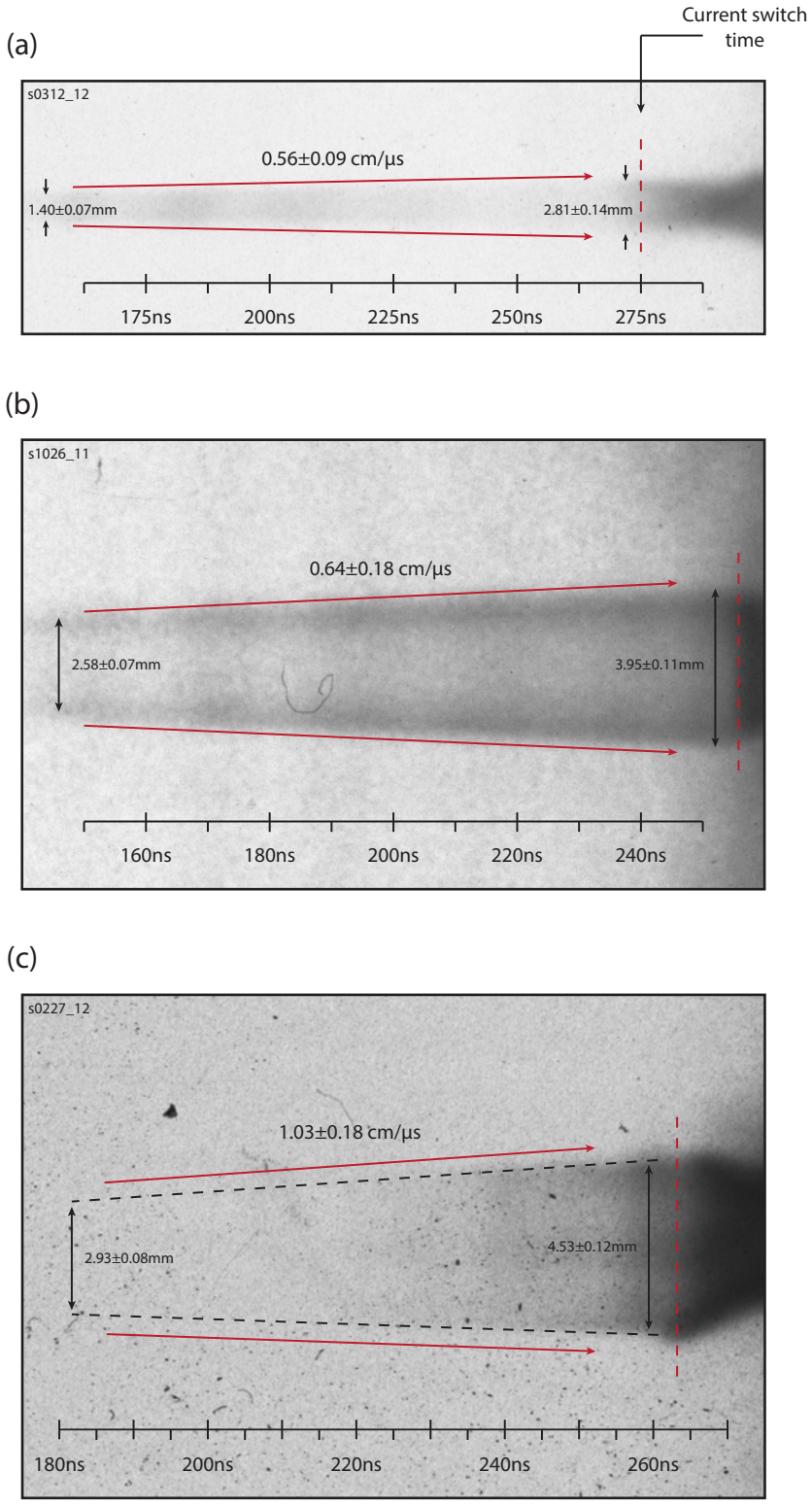

Figure 4.5: Optical streak image showing the radial expansion before current switch of a single Al wire load of (a) 25μm, (b) 40μm and (c) 50μm initial thickness.

The optical streak images show a side-on radial 'slice' at the centre of the load section. We see that wires with larger initial thickness have expanded to larger diameter before the current switch. The 25μm wire expanded to only 2.8mm before the switch while the 40μm and 50μm wires managed to expand further to 4.0mm

and 4.5mm respectively before the switch. This is due to the higher expansion velocity seen in thicker wires. Where the expansion velocity was 0.56±0.09 cm/μs for the 25μm, 0.64±0.18 cm/μs for the 40μm and 1.03±0.18 cm/μs for the 50μm. Another possibility could be that the initial expansion soon after the prepulse is not linear and varies for different wire thicknesses. From the expansion velocity we can calculate the average temperature of the expanding gas in vacuum using equation (3.13) in Chapter 3. The calculated temperature for the 25μm, 40μm and 50μm are 0.94±0.30 eV, 1.23±0.69 eV and 3.17±1.11 eV respectively. Those temperature are below the 1st ionisation potential of Al atom (~ 6 eV), suggesting that the expanding wires are mainly composed of neutrals rather than plasma. Those observations where thicker wires expand to larger diameters and possess a greater expansion velocity and temperature is consistent with the ones seen in Chapter 3 for cylindrical load arrays. As has been explained in the previous chapter, thicker wires are less efficient in transferring their heat energy equally to all atoms due to the lower surface area to volume ratio, therefore less gaseous mass is detected from interferometric analysis suggesting a greater presence of liquid droplets and clusters (particles of low energy) hence the detected expanding gas contains more energy per atoms and therefore greater temperature. If this is also true for a single wire case, we should see an increase in the percentage of unaccounted mass from interferometric analysis as wires get thicker.

We note that the 50μm image was not bright enough at earlier times and we have extrapolated a straight line from the brighter region before the current switch (dashed black line in Figure 4.5(c)) assuming a linear expansion. In all three streak images the time of current switch did not vary much and was around 260-275ns. The current switches to the load when the inverse array fully explodes. Since we kept the properties of this array constant throughout all our experiments, the time of current switch should be constant for all. The slight variations could be due to random errors in measurements when building this array and/or due to small variations in wire thickness. However the most probable reason - which has been explained earlier - is the fact that the current profile of the machine fluctuates from one experiments to the other.

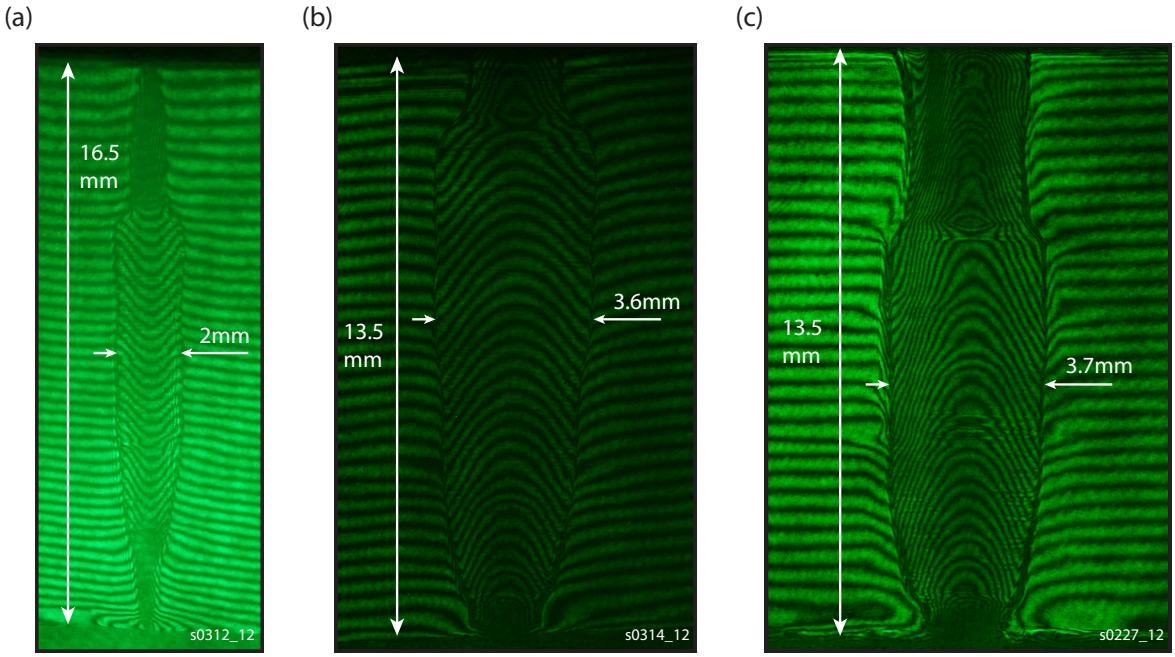

Figure 4.6: Laser (532nm) interferometric images for a single Al wire load of (a) 25µm at 211ns, (b) 40µm at 201ns and (c) 50µm at 210ns.

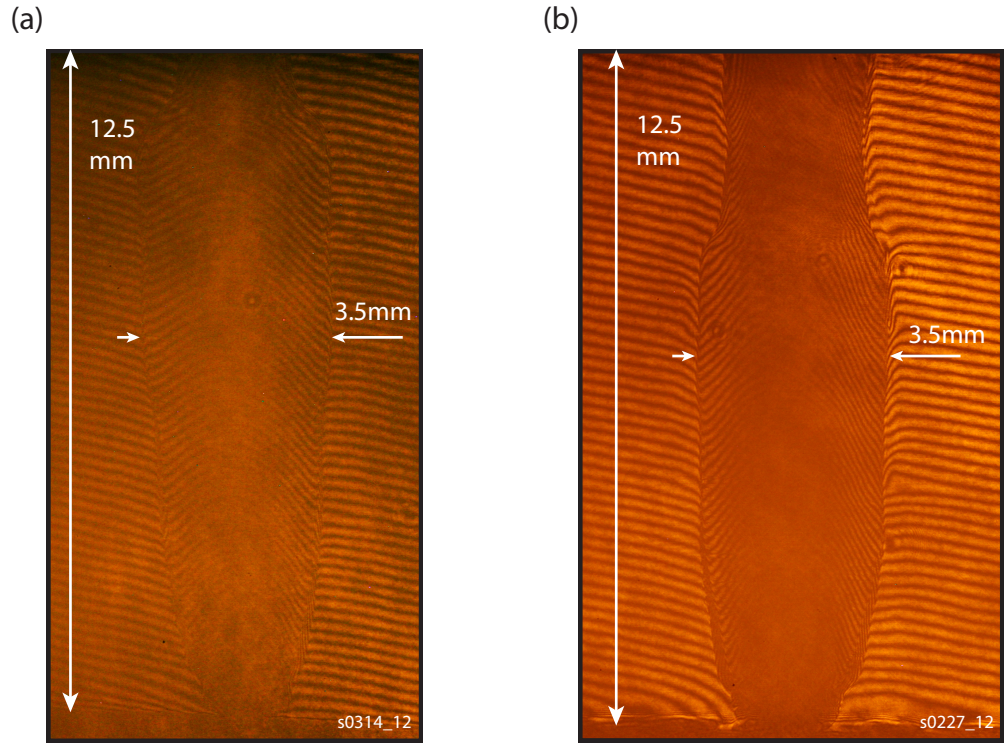

Figure 4.7: Laser (355nm) interferometric images for a single Al wire load of (a) 40µm at 201ns and (b) 50µm at 210ns.

Looking at interferometric images (Figure 4.6 & 4.7), all single wire loads managed to precondition before the main current switch. Wires have expanded to ~ 100 times their initial diameter, no evidence of a wire core as fringes can be traced all

the way across the wire, and boundaries appear to be smooth with no presence of instability suggesting a very low level of current passing through. Comparing the 25μm with the 40μm and 50μm we can clearly see that thicker wires have expanded to larger diameters. Where the 25μm wire expanded to ~ 2mm and the 40μm & 50μm expanded to ~ 3.5mm. In all wires, we clearly see the electrode-end effect close to the anode. Those are regions where the wire did not fully expand, and it is believed that the electrode electric field plays a major role in causing this effect [46]. Recent experiments conducted by G.N. Hall have shown that it is possible to mitigate the electrode-end effect by modifying the electrode shape. Therefore, we will ignore this region in our density analysis as it is a feature caused by external effects that can be mitigated. We note that the wire length for the 25μm load is slightly larger than the intended setup length (15mm) by ~ 2mm. This was unintentional and most probably an error in measurement when building the array hardware. The green (λ=532nm) and blue (λ=355nm) interferometric images were taken at the same instant in time from the same viewing angle. Therefore, we can apply the two-wavelength interferometric analysis for density measurements to differentiate neutrals from electrons (Chapter 2 Section 2.2.8) for the 40μm and 50μm single wires loads. The blue SLR camera did not work for the 25μm load experiment and therefore no blue interferometric image is presented for this load thickness.

By zooming around the edges of preconditioned wires in the above interferometric images we see that fringes at wire edges are shifting in opposite direction to the central bulk of wire. Figure 4.8 shows an example of such effect from a green laser image of a 25μm wire and blue laser image of a 50μm wire. This opposite shift suggests that there is a considerable presence of plasma around the edges of wires. This has also been observed in cylindrical wire array loads of a two-stage Z-pinch setup (Chapter 3). This plasma carries the low level current through the load during this phase of the experiment. We note that the edge plasma causes a large fringe shift within a small space on the image making it sometimes difficult to trace fringes around wire edges.

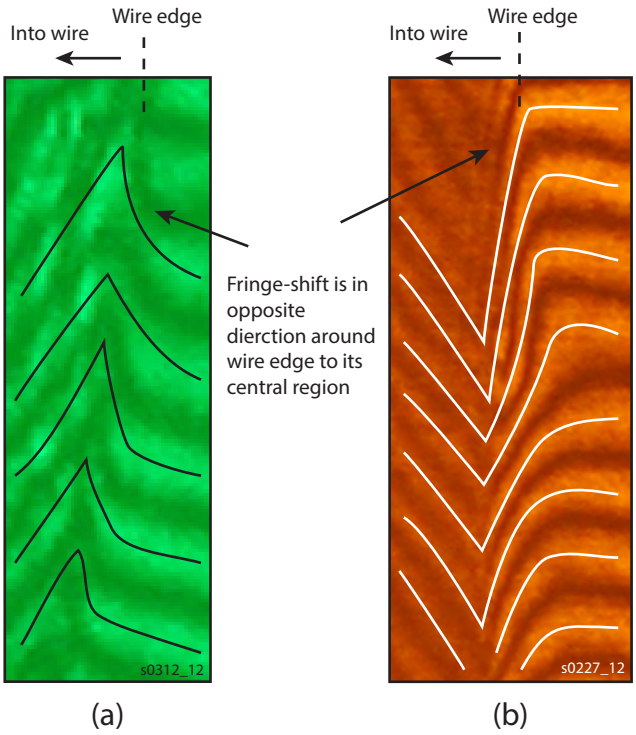

Figure 4.8: A zoomed-in interferometric image showing fringe-shift around wire edges for a single Al wire load of (a) 25μm and (b) 50μm.

Fringes of the above images in Figure 4.6 and 4.7 were manually traced using Adobe Photoshop and the traced image along with the background were fed into a MATLAB program to interpolate the data in between the fringes. Then the experimental and background interpolated data were subtracted from each other to generate a 2D fringe-shift map. Figure 4.9 shows such 2D map from green interferometric images for single Al wires of 25μm, 40μm and 50μm along with fringe-shift line-outs at different heights from the cathode. All preconditioned wires, regardless of thickness, show a positive fringe-shift in the central region and a negative shift around the edges which can be seen on both 2D maps and line-outs. This change in direction of fringe-shift means that the central region is dominated by neutral atoms while the edges posses a significant amount of plasma, causing the change in fringe-shift direction.

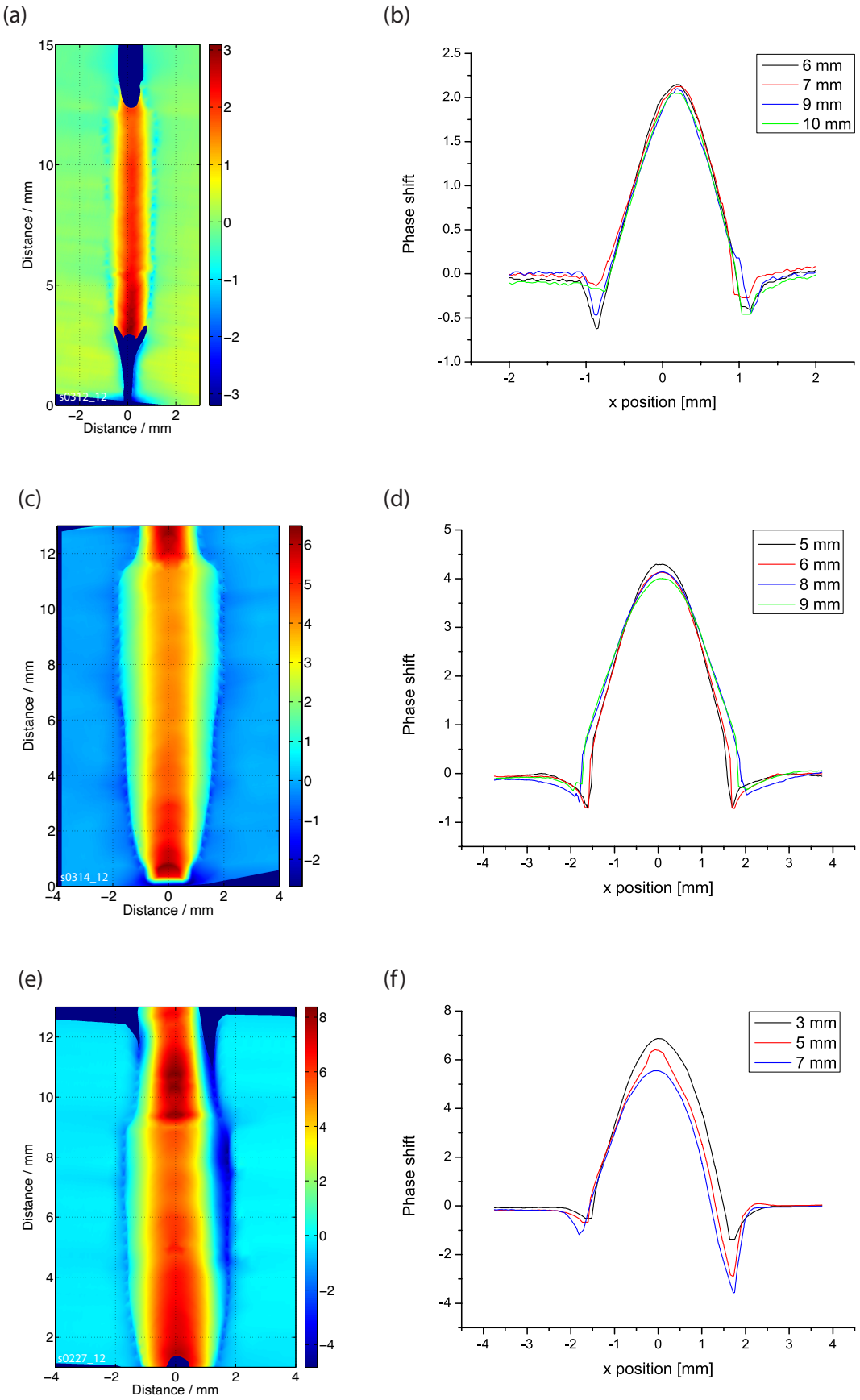

Figure 4.9: 2D fringe-shift maps from green interferometric images along with line-outs at different heights from cathode for single Al wire loads of (a,b) 25µm at 211ns, (c,d) 40µm at 201ns and (e,f) 50µm at 210ns.

As we increase the wire thickness from 25μm to 40μm we generate a preconditioned wire with a larger diameter, however an increase in thickness from 40μm to 50μm does not change the diameter of the preconditioned wire, which stays roughly constant at 3.5mm. On the other hand, as we increase the wire thickness from 25μm to 40μm then to 50μm the fringe-shift peak at the centre of the wire increases from ~ 2.25 to ~ 4.5 to ~ 7 respectively. We can see this clearly in Figure 4.9(b,d,e). This is expected as thicker wires contain more mass and hence more atoms per axial length.

Looking at the fringe-shift line-outs at different heights (6-10mm) for the 25μm wire (Figure 4.9(b)), we see that the line-outs closely overlap at the central region while the edges minimum fringe-shift vary between ~ 0.2 - 0.6. This could be due to axial variations in plasma distribution around the wire, or an effect from the interpolation method used in MATLAB. Looking at the 40μm fringe-shift 2D map (Figure 4.9(c)), we see that between the heights 7-11mm the wire diameter remains reasonably constant at ~ 3.8mm, this diameter then decreases gradually as we get closer to the cathode. This can also be seen at the corresponding line-outs in Figure 4.9(d), were the 8 and 9mm line-outs closely overlap and the 5 and 6mm line-outs posses a slightly smaller diameter. We also note that the edge plasma are relatively equal in both left and right side and gets slightly larger as we move closer to the cathode. On the other hand, the 50μm fringe-shift line-outs (Figure 4.9(f)) shows an unequal distribution of plasma between left and right side and an increase in plasma density as we move away from the cathode. There isn't any physical explanation why there is an opposite effect when we vary the thickness by 10μm, most likely this is just a random effect that varies from one shot to the other. The increase in plasma around the right side of the wire as we move towards the anode lowers the central positive fringe-shift down, as plasma has an opposite fringe-shift effect to neutrals.

In the previous chapter, wires in a cylindrical array did not have equal dimension when measured from the left and right side independently. This is expected as more current goes through the outer edges due to its lower inductance. In order to differentiate the plasma from the neutrals fringe-shift, we modelled our

preconditioned wires as elliptical objects with varying radius consisting of two layers: an outer plasma layer and an inner neutral layer (Chapter 3, Figure 3.12). For a load consisting of a single wire on axis, we do not expect current to take a preferred side and therefore current and hence plasma should be equally distributed around the wire circumference. Therefore we can model our wires as a perfect circular object as in Figure 4.10(a), where the green arrow represents the laser ray through the wire, and the chordal laser path through the wire is $2\times(a^2\text{-}y^2)^{1/2}$. This will allow us to apply an Abel Inversion technique (c.f Chapter 2, Section 2.2.8) to convert path integral phase-shift F into phase-shift caused by the density at radius r using Eq(4.3).

$$f(r) = -\frac{1}{\pi}\int_r^a \frac{dF}{dy}\frac{dy}{(y^2 - r^2)^{1/2}} \tag{4.3}$$

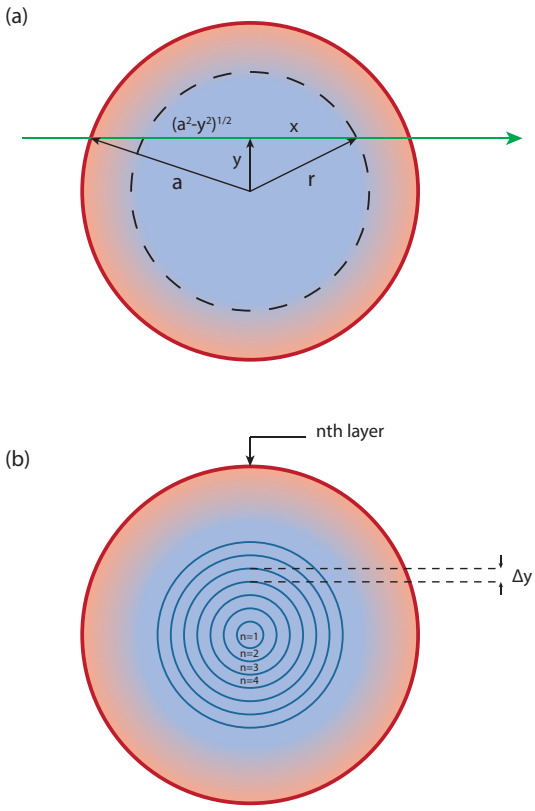

Figure 4.10: (a) A schematic diagram of a perfectly circular preconditioned wire of radius 'a' and chordal laser path $2(a^2\text{-}y^2)^{1/2}$.

(b) A wire model consisting of n equally spaced layers.

We note that in all our phase-shift plots (Figure 4.9), the 'x position' will be represented as 'y' for this part of the analysis (i.e the x and y coordinates will be swapped). Since F is measured at a finite number of y values and the values in between the real data were linearly interpolated with a constant Δy, the integral in Eq(4.3) was approximated to a sum (Eq(4.4)) and solved numerically in MATLAB. By doing this, we have approximated our wire as an n-layer model (Figure 4.10(b)) each with a unique phase-shift corresponding to a unique density. Positive values of $f(r)$ will be attributed to neutrals and negative values to plasma. This approach is much more realistic in differentiating neutral density from plasma than the 2-layer model we used in Chapter 3.

$$f(r) \simeq -\frac{1}{\pi} \sum_{r+\Delta y}^{a} \frac{F_{y+\Delta y} - F_{y}}{\sqrt{y^2 - r^2}} \tag{4.4}$$

From the line integrated phase-shift plots at different heights (Figure 4.9) we can see that the radius measured from the left and right side is roughly constant for all wire thickness. However, the plasma distribution on the left and right side of the wire does vary (with the exception of the 40μm wire). This could be due to the current taking random paths which averages out if we look at a time-averaged image, or it could be due to a slight tilt in the wire causing the current to flow more thorough one side than the other. However we will assume in all cases that the preconditioned wire properties only varies with radius and should be constant azimuthally and axially. Therefore we have averaged the phase-shift plots at different heights around an axial region where the wire diameter does not vary by much (Figure 4.11(a-c)). Then this axially averaged phase-shift plot was divided into a left and right region with the central peak set to zero. The two (left and right) plots where averaged to obtain a phase-shift line integrated plot which is averaged in the axial and azimuthal direction and only varies in the y direction (Figure 4.11(d-f)). Then Abel Inversion was applied to this averaged phase-shift line integrated plot with n = 10,000 layers to generate a neutral and plasma density distribution plot that varies with radius (Figure 4.11(g-i)).

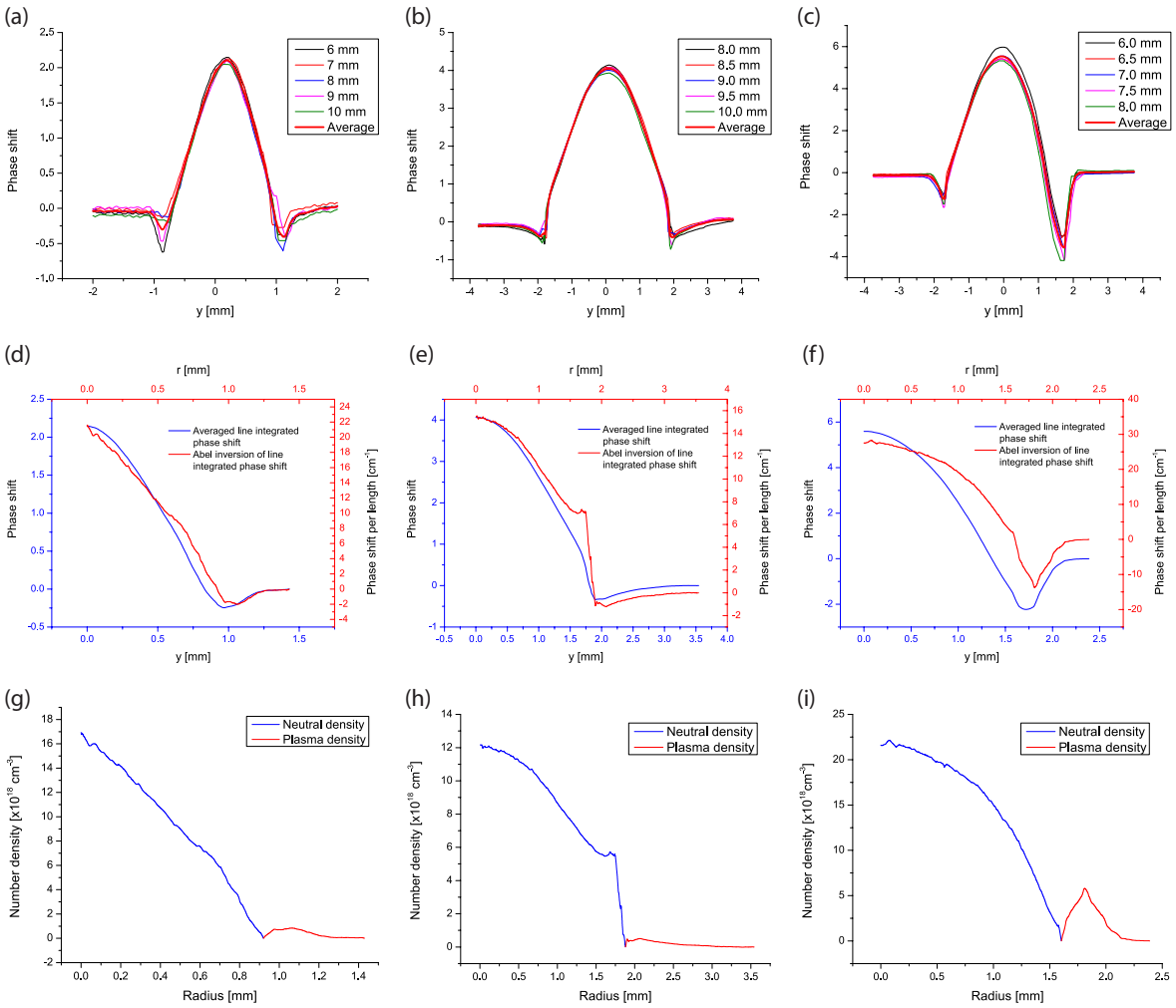

Figure 4.11: (a-c) Axially averaged line integrated phase-shift, (d-f) azimuthally averaged line integrated phase-shift along with its Abel inverted plot and (g-i) radial distribution of neutral and plasma density for a single Al wire load of (a,d,g) 25µm at 211ns, (b,e,h) 40µm at 201ns and (c,f,i) 50µm at 210ns.

By axially averaging line integrated phase-shift plots (Figure 4.11(a-c)) we managed to obtain a roughly equal plasma distribution on the left and right side for the 25µm and 40µm wire. However, the 50µm shows a significant difference in the azimuthal distribution of outer plasma which as explained earlier could be due to a tilt in the load hardware setup. As we increase the wire's initial thickness, it expands to a larger diameter and the averaged line integrated phase-shift peak gets larger. By averaging the left and right side (Figure 4.11(d-f)) we loose some of the outer plasma peak 'sharpness'. This can be clearly seen for the 25µm and 50µm when we compare (a) with (d) and (c) with (f) in Figure 4.11. This is because we aligned the two sides by setting their central peak to zero which creates a slight mismatch on the outer negative peak.

The neutral density distribution obtained from Abel inversion shows a different profile for the different wire thicknesses used. The 25μm wire shows approximately a linear profile in neutral density, reaching a maximum of ~ 17×10^{18}cm^{-3} at r = 0mm and reaches zero at r = 0.92mm. The 40μm wire neutral density shows two different profiles. First, its a curve which falls down with a decreasing gradient from a peak value of 12×10^{18}cm^{-3} at r = 0mm to 5.5×10^{18}cm^{-3} r = 1.62mm. Then the density jumps up slightly by ~ 0.3×10^{18}cm^{-3} before falling down sharply and linearly to zero at r = 1.88mm. The 50μm neutral density profile is a curve all the way through, which falls down form a peak value of ~ 22×10^{18}cm^{-3} at r ~ 0mm with a decreasing gradient until it reaches zero at r = 1.60mm. We can see that there is a transitions from a linear profile to a curve as we increase the wire initial thickness from 25μm to 50μm, and at 40μm we see a profile which is composed of both linear and curve.

The plasma density distribution, on the other hand, is quite flat and featureless for the 25 & 40μm wire, possessing a radial width of ~ 0.3mm and ~ 0.7mm respectively and a maximum value $< 0.8\times10^{18}$cm^{-3}. However, the 50μm has a significant amount of outer plasma and its density distribution reaches a peak of 5.8×10^{18}cm^{-3} at r = 1.81mm which decays to zero at r = 2.1mm. We note that all interferogram were taken at least 50ns before the main current switches to the load and therefore the effect of an increasing electric field just before the current switch time is not the cause for this increase in plasma around the 50μm wire.

To validate the neutral and plasma distribution plots we have used Eq (4.5) to calculate the total number of atoms per axial length N_{tot} in the preconditioned wire,

$$N_{tot} = 2\pi \int_{r_1}^{r_2} \rho \cdot r \, dr \qquad (4.5)$$

where ρ is the number density of either neutral or plasma. Then we compared this to the real value of N_{tot} in a solid wire. The results are shown in the table in Figure 4.12.

Initial wire thickness (μm)	Time of measurement (ns)	Average diameter of preconditioned wire (mm)	Total number of neutral atoms per length in preconditioned wire ($\times 10^{17}$ cm^{-1})	Total number of electrons per length in preconditioned wire ($\times 10^{16}$ cm^{-1})	Total number of atoms per length in a solid wire ($\times 10^{17}$ cm^{-1})
25	211	2.11±0.10	1.78	1.26	2.96
40	201	3.81±0.15	7.83	4.05	7.57
50	210	3.62±0.20	9.68	18.45	11.83

Figure 4.12: A table showing the average diameter and the total number of neutral atoms and electrons per length for a single preconditioned Al wire load of 25μm, 40μm and 50μm initial thickness.

If we assume a Z=1 ionisation then the total number of atoms in the 25μm preconditioned wire is 1.91×10^{17}cm^{-1} which is 35% less than the real value. Most likely the reason for this is an incorrect fringe trace due to the high gradient of particles at the wire boundaries and poor focus from the camera. Our initial trace and calculations generated a total atom number value which is 55% less than the real. Then by shifting the trace up by one fringe we managed to account for an extra 20% of atoms. Therefore in order to account for nearly all atoms we need to shift our fringe trace up again by 1 or 2 fringe-shift. On the other hand, the 40μm and 50μm preconditioned wires possess a total atom number of 8.24×10^{17}cm^{-1} and 11.53×10^{17}cm^{-1}, which is 8.9% greater than and 2.5% less than the real value respectively. Those percentage differences are much smaller than the 25μm wire and is more likely due to the higher magnification and focus of the camera system used for those experiments, hence a better judgment on fringe trace around wire boundaries.

Another approach to differentiate atom (neutrals and ions) line density from from free electrons is to simultaneously solve the fringe-shift equation for two different laser wavelengths (Chapter 2 Section 2.2.8). The blue (355nm) image for the 40μm and 50μm (Figure 4.7) were taken at the same instant in time from the same viewing angle as their green (532nm) image. Therefore we can simultaneously solve the blue and green line integrated phase-shift plot at a specific height to get the atom and electron line density plots. Figure 4.13 shows 2D fringe-shift maps from blue interferometric images along with an averaged line-out over the same height range as their green image for the 40μm and 50μm wire. This height averaged line integrated fringe-shift plot is compared with the green plot in Figure 4.14.

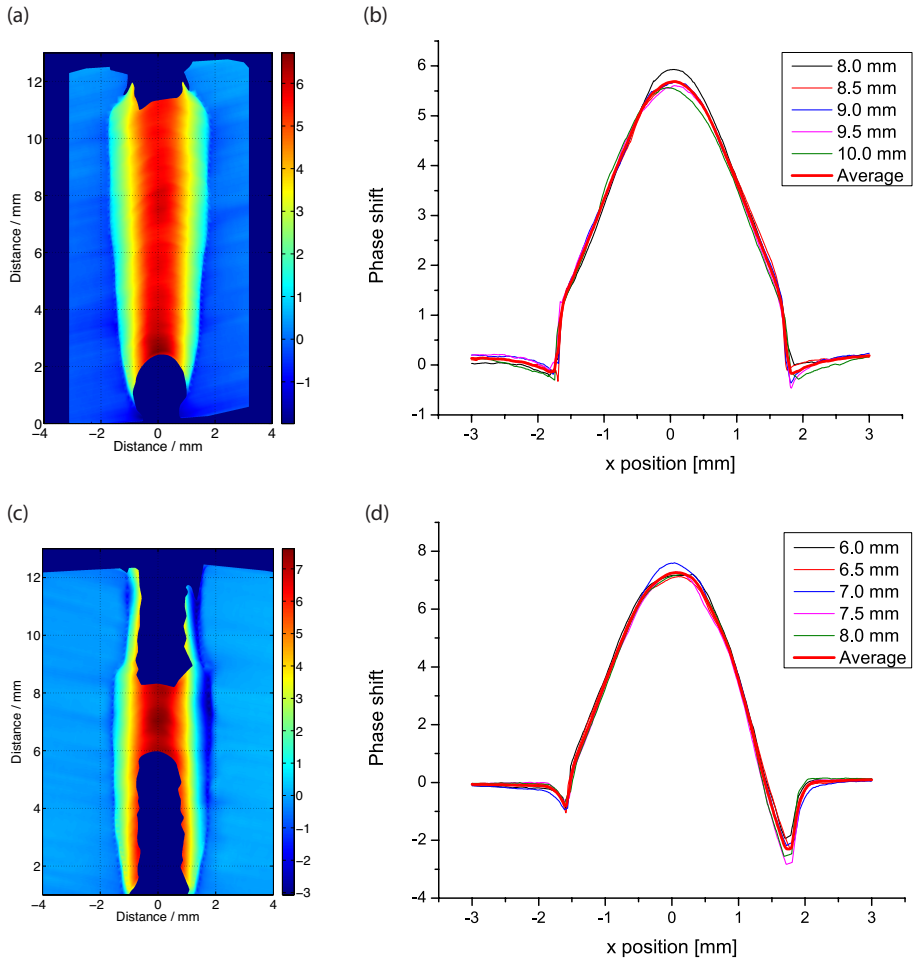

Figure 4.13: 2D phase-shift map from blue (λ=355nm) laser interferometric images along with line-outs at different heights from cathode for a single Al wire load of (a,b) 40μm at 201ns and (c,d) 50μm at 210ns.

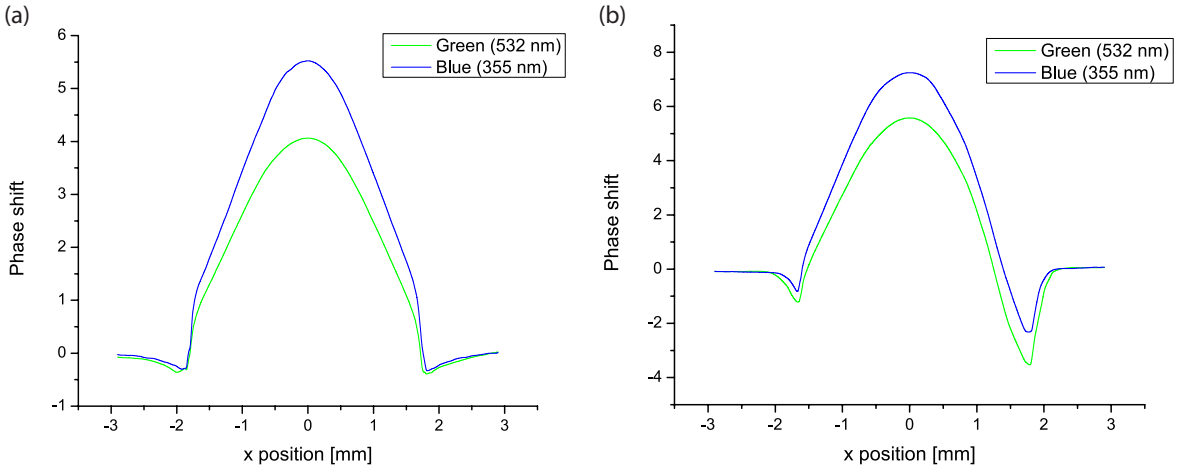

Figure 4.14: Axially averaged line integrated phase-shift plots from green (λ=532nm) and blue (λ=355nm) interferometric images for a single Al wire load of (a) 40μm at 201ns and (b) 50μm at 210ns.

We clearly see that the blue line integrated phase shift plot resembles the same shape as the green plot for both 40μm and 50μm wire. The blue plot possess a larger positive phase-shift value around the central peak reaching a maximum of 5.5 and 7.2 for the 40μm and 50μm respectively. However, it has a smaller negative phase-shift value around the edges which can be clearly seen in the 50μm plot (Figure 4.14(a)). That is because, electromagnetic waves of shorter wavelengths are more sensitive to bound electrons in atoms and less sensitive to free electrons in plasmas.

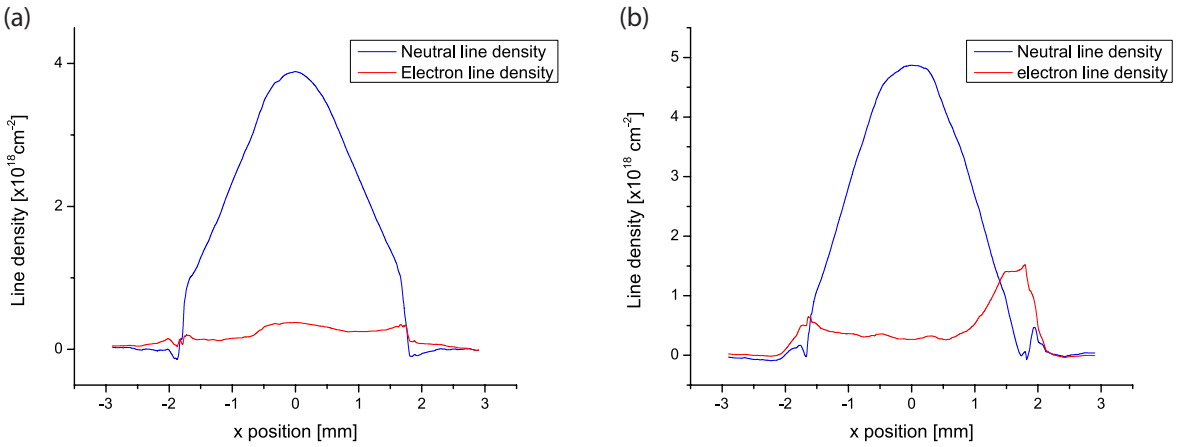

Figure 4.15: Atom and electron line density obtained by solving the green and blue line integrated phase-shifts simultaneously for a single Al wire load of (a) 40μm at 201ns and (b) 50μm at 210ns.

The atom and electron line density shown in Figure 4.15 were obtained by simultaneously solving the blue and green line integrated phase-shift plots in figure 4.14. The values for the wavelength dependant polarizibility α were taken to be $10.8\times10^{-24}cm^3$ and $8.9\times10^{-24}cm^3$ for the green (λ=532nm) and blue (λ=355nm) wavelengths respectively [47]. Both the 40μm and 50μm plot shows a dominating atom line density over electron line density by ~ 10 times around the central region, which is a proof of a low ionisation and hence low temperatures, indicating that most of the atoms around the centre are in a neutral state. Around the wire edges of the 50μm wire (Figure 4.15(b)) electrons dominates reaching a factor of ~ 3 times the atoms on both sides which is a strong indication of a Z=3 ionisation. However the 40μm wire does not show a strong presence of plasma around the wire edges, and stays roughly flat across the wire at a level of ~ $0.2\times10^{18}cm^{-1}$. The electron and atom line density around the 40μm wire edge cannot be accurately

quantified due to the close overlap of the green and blue phase-shift plots in Figure 4.14(a) which also generates a negative atom line density between -2mm and -1.8mm in Figure 4.15(a). Thats because there is a low presence of plasma around the edges and the fringe thickness is quite large when compared to the small fringe-shift caused by this low level of plasma.

By integrating the plots in Figure 4.15, we were able to obtain the total number of atoms and electrons per axial length from a different method. The 40μm preconditioned wire contained 8.99×10^{17}cm^{-1} atoms and 1.06×10^{17}cm^{-1} electrons, while the 50μm wire contained 10.39×10^{17}cm^{-1} atoms and 2.20×10^{17}cm^{-1} electrons. The 40μm preconditioned wire contained 18.8% more atoms than the real value in a solid wire while the 50μm wire contained 12.2% less atoms than the real value. Those differences are much greater than the ones calculated using the Abel Inversion technique. The reason for this, is the large errors in $\alpha(\lambda=532\text{nm})$ and $\alpha(\lambda=355\text{nm})$, which are 10% and 25% respectively [47]. Therefore by varying the those values within their specified error limits we might be able to get a value closer to the real one. Another reason could be in our previous assumption of ionisation Z=1, and therefore we have over-estimated the total number of ions around the wire, which - for the 50μm case - will generate a similar percentage difference (13%) if we assumed Z=3.

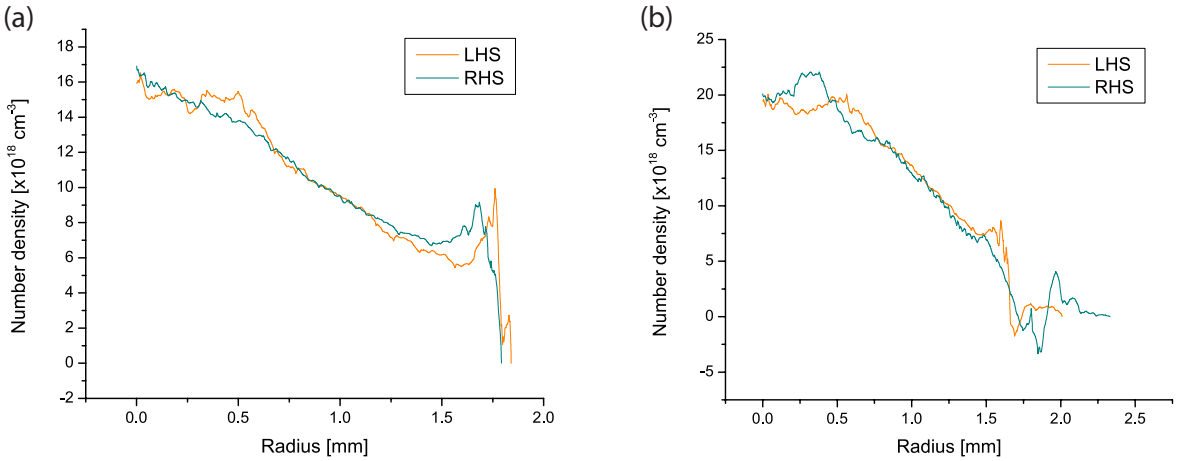

Figure 4.16: Plot of atom number density vs radius for a single preconditioned Al wire of (a) 40μm and (b) 50μm initial thickness.

To judge the axial symmetry of the preconditioned wires, we have Abel inverted the atom line density from the left and right side to generate two independent plots of atom density vs radius (Figure 4.16) for each wire thickness. Both (40 & 50μm wire) show a very close overlap of the left and right side between r=0.75mm and r=1.5mm, with a slight mismatch around the edges and close to the centre, an indication of a good azimuthal symmetry. Comparing the 40μm plot to the one generated directly by Abel inversion of the green phase-shift plot (Figure 4.11(h)) we see it resembles a similar pattern at the outer edges where the density shoots up steeply at r ~ 1.75mm but then the one in Figure 4.16(a) increase linearly reaching a peak of ~ 16×10^{18}cm^{-3} at r=0mm while the other plot in Figure 4.11(a) increases with a decreasing gradient as r tends to zero reaching a peak of only 12×10^{18}cm^{-3}. The larger peak in Figure 4.16(a) is a reflection of the exaggerated total atom number calculated from the two-wavelength interferometry method. The 50μm plot of number density vs radius (Figure 4.16(b)) shows negative values around the wire edges. Again that is because we have region of a decreasing atom line density at r=1.9 - 1.7mm (Figure 4.15(b)). Most likely this is not real and its a slight error in the phase-shift values around that region. However around the centre, the 50μm plot in Figure 4.16(b) reaches a similar peak value of ~ 22×10^{18}cm^{-3} to the plot in Figure 4.11(i). Overall, we can confidently say that there is a good azimuthal symmetry in the 40μm and 50μm preconditioned wire.

So far we have seen that a two-stage Z-pinch configuration managed to *precondition* a single wire load on axis of different initial thicknesses. This Z-pinch setup delivered an initial current prepulse into the load wire at the early stage of the experiment reaching a peak of ~ 7kA in ~ 25ns, causing the wires to reach temperatures beyond boiling point. After which the wires thermally expanded for ~ 250ns with minimal current going through them. The wires managed to expanded to ~ 2-4mm in diameter (depending on the initial thickness), forming a column of Al gas at the axis. In the following section we explore the implosion dynamics when switching a fast current pulse of the order of ~ 1MA into this column of Al gas.

4.3 Implosion dynamics after current switch

During the time when the load wire expands, the inverse array continuously explodes material radially outwards in a periodic fashion along the axial length. This ends when enough material has been depleted to form gaps along the wires of the inverse array, and hence breaking the current path. At this stage, the current rapidly switches into the the preconditioned load wire. In the following sections we investigate the change in neutral and electron density distribution at the point of current switch from laser interferometric images, the implosion trajectory after current switch from optical streak, XUV and optical framing images and X-ray production at stagnation from PCD signals and filtered time-integrated images.

4.3.1 Current switch

The current switches to the load when enough material has depleted from the inverse array forming gaps along the wires and hence breaking the current path through the bottom array. At that point the current has only one path which is through the load. The time of the current switch is controlled by the inverse array parameters such as array diameter, wire thickness...etc. Since we kept those parameters constant, we do not expect the time of the switch to vary. However, in reality, there will be some variation due to human error when building the array. In addition to this variation, the current profile tends to vary from one shot to the other, even though we kept the machines parameter constant. This is due to the discharge/switching time of various parts of the pulsed power device not being consistent. Before we start analysing and comparing the implosion dynamics and X-ray production for the three different load setup (25μm, 40μm & 50μm) we need to check at what temporal point of the current pulse did the switching happen. Figure 4.17 shows the current profile in arbitrary units measured using a B-dot probe at the MITL just before the load for all three load wire thicknesses along with their switching time (dashed line) measured from the optical streak in Figure 4.5. We clearly see that the switching time happens at ~ 15ns after the peak current time for all wire thicknesses. Both the 25μm and 40μm wires have a similar current magnitude at the point of the switch while the 50μm wire switches at a

current value which is 10% higher. Overall we can say that the current variation at the switch is not too significant between the three experiments and should not have a major contribution in altering the implosion dynamics.

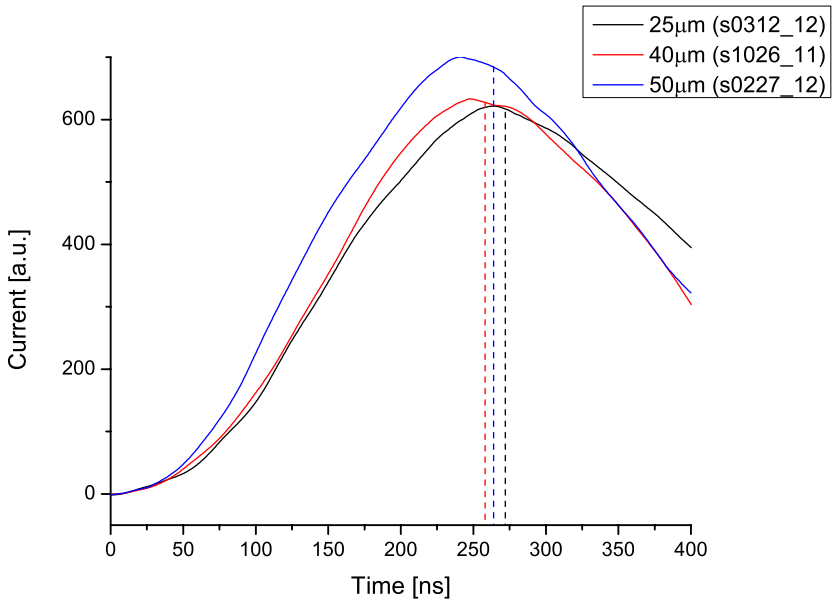

Figure 4.17: Variation of MAGPIE's current with time for the three different experiments involving different load wire thicknesses (values shown in legend). The dashed lines show the switching time for each experiment taken from the optical streak image in Figure 4.5.

The MAGPIE machines generates a current peak of ~ 1.4MA in ~ 250ns. A fast switch mechanism similar to our 2-stage Z-pinch setup would generate a high dI/dt at the point of the switch. Unfortunately, the large dI/dt (~ 3.5×10^{12} A/s) generates a large voltage of the the order of ~ 1kV at the load's Rogowski which causes it to break-down. This break-down has been observed in all our 2-stage Z-pinch experiments and Figure 4.18 shows an example of such a break-down from a single wire load experiment of 25µm. At the beginning of the switch at ~ 225ns dI/dt slowly increases from 0.25×10^{12} A/s to 0.75×10^{12} A/s within 60ns, it then rapidly increases reaching a maximum value of ~ 3.4×10^{12} A/s within ~ 30ns, at that point it breaks-down and gradually decays back to zero. The start time of this fast switch is what we have been measuring from optical streak images. It is thought that the initial slow increase of dI/dt marks the start of the inverse array explosion and by the time it fully explodes the current fully switches to the load causing the rapid increase in dI/dt. The calculated current shown in Figure 4.18 is

highly underestimated due to the fact the Rogowski breaks-down early after the switch and we know from Figure 4.17 that the switching happens at roughly the time of current peak and hence the current through the load should be at the order of ~ 1MA. In the next section we attempt to indirectly measure the current profile through the load by analysing the implosion trajectories.

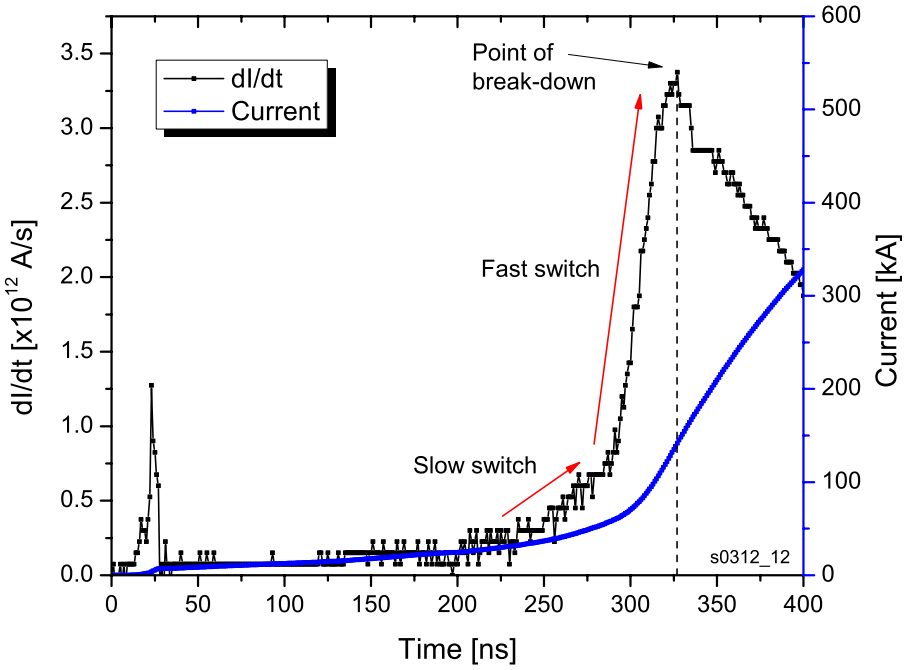

Figure 4.18: Variation of dI/dt and calculated current through a single 25μm Al wire load measured from a Rogowski groove placed at one of the 4 return posts.

At the time of current switch, we expect the fast-rising current to ionise the neutral gas and significantly increase the number of free electrons in and around the wire over a short period of time. To investigate this change in electron number density we have to look again at interferometric images at around the current switch time. Green (532nm) interferometric images were completely blacked-out around the wire soon after the switch due to their high sensitivity to free electron. Therefore blue (355nm) laser images were used to analyse electron density after the switch as it can probe deeper into a plasma. Even such laser images had a short window after the switch where fringes can be seen, after which the rising electron density blocked almost all the laser light passing through the wire. In addition to this, the machines current profile varies slightly from one shot to the other which makes it difficult to precisely predict the timing of current switch. For

this reason we have only managed to obtain laser interferometric images around the current switch time for one experiment which consisted of a 50μm wire load. Figure 4.19 shows such images of a green laser (λ=532nm) at 4ns before the switch and a blue laser (λ=355nm) at 16ns after the switch from the same experiment.

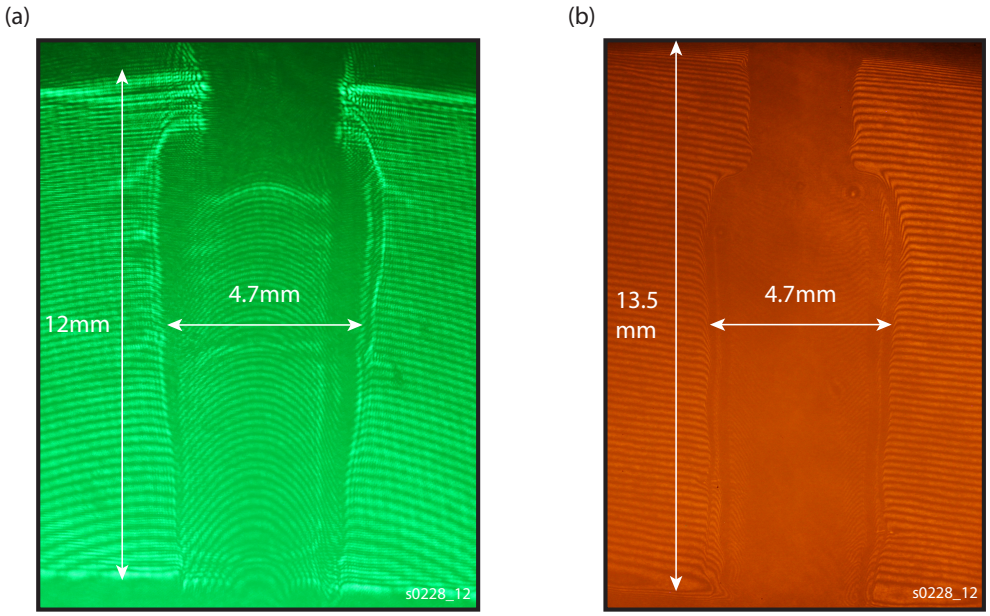

Figure 4.19: Interferometric images of a 50μm Al load wire from (a) a green (532nm) laser at 266ns and (b) a blue (355nm) laser at 286ns. The current switch was at ~ 270ns.

Even at 4ns before the main current switch, the effect of free electrons in significantly blocking the laser light of the green interferometric image can be clearly seen around the edges of the preconditioned wire (Figure 4.19(a)). This increase in electron presence before the switch time could be due to the increase in current through the load caused by the increase in resistance of the inverse array as more material is ablated. However at the central region, fringe shifts in the opposite direction to the edges, a strong indication of the presence of neutrals. At 16ns after the switch (Figure 4.19(b)), fringes can hardly be seen in the blue interferometric image. However by zooming in using Adobe Photoshop we were able to faintly identify the fringes. We note that the wire diameter did not change at all after 16ns have passed into current switching.

In order to obtain an unbiased comparison in the change in fringe-shift and hence particle density across the wire, fringes of both images were traced around the

same axial region. This was the top area below the 'end-effect' as this was the only common region in both images were fringes can be identified all the way across the wire. The traced images were put in a MATLAB program to interpolate the data and generate a 2D fringe-shift map (Figure 4.20).

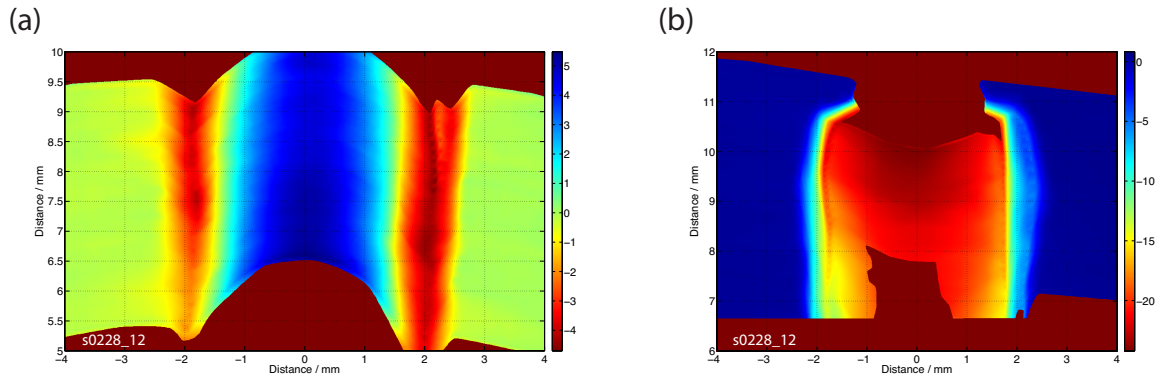

Figure 4.20: A 2D fringe-shift map of a 50μm Al load wire at (a) 4ns before current switch and (b) 16ns after current switch.

The blue colour in the 2D fringe-shift map is attributed to a positive fringe shift and hence neutrals while the red colour is attributed to a negative fringe shift and hence plasma (free electrons). We clearly see that there is some plasma present around the wire edges at the 4ns before the switch but the neutrals still dominate the central region. This pattern has been observed in all preconditioned wires before the switch (Section 4.2.2). This shows that wire structure does not change much until the time of the switch. At 16ns after the switch, the central region in the 2D image in Figure 4.20(b) turns completely red reaching values of ~ -20 fringe shift, which is an effect of a strong presence of free electrons generated from plasma. To analyse and compare the change in fringe-shift across the wire before and after the switch we have obtained line-outs between the heights of 8.2 - 8.9mm at 0.1mm interval. This was the overlapping range of heights (axial position) between the 2 images in Figure 4.20. Those line-outs hardly varied within the specified range, therefore an average fringe-shift line-out was obtained for each image in this axial range (8.2 - 8.9mm) which is shown in Figure 4.21.

At 4ns before the current switches into the load, the fringe-shift line-out of the preconditioned wire resembles similar features to the ones analysed in section 4.2.2

with negative shifts on the side and a positive shift around the centre. Comparing this plot to the one in Figure 4.11(c) which is of a 50μm wire at 54ns before the switch we see that the averaged negative peak values on the sides of the wire have grown larger by roughly ~ 50%, the central peak maximum shrunk by ~ 13% and the wire became wider in diameter by ~ 15%. The larger edge peaks and smaller central peak is the effect of an increase in the number of free electrons around the wire. This is consistent with the 'linear' increase in current during this preconditioning phase of the experiment (Figure 4.5(b)). At 16ns after the switch (Figure 4.21, red plot), the fringe-shift is completely on the negative side, and we see two different features in this plot. The first one is a steep increase in fringe-shift around the wire sides from 0 to ~ -18 within a space of ~ 0.8mm. Then it abruptly stops before it starts to increase again gradually with a decreasing gradient up to the peak of -22 at x=0mm. We note that the wire width does not change during the 20ns time space between the two plots in Figure 4.21.

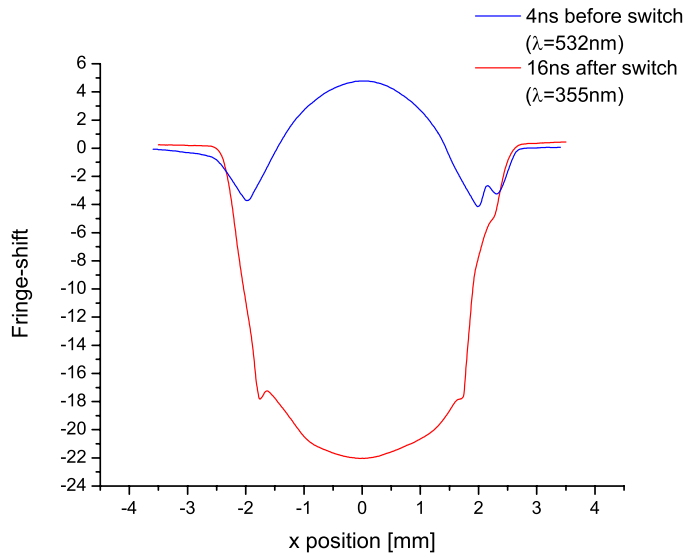

Figure 4.21: Averaged fringe-shift line-outs between the axial height 8.2 - 8.9mm for a 50μm Al wire load at 4ns before the switch (blue plot) and 16ns after the switch (red plot).

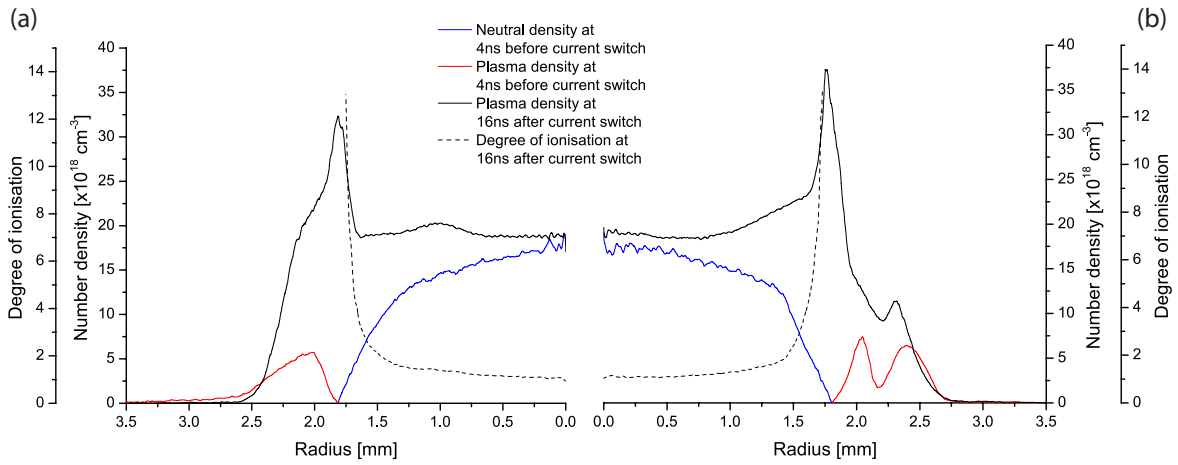

Figure 4.22: Variation of neutral and plasma number density with radius for a 50μm Al wire load at 4ns before the current switch (blue and red plot) and 16ns after the switch (black plot) obtained by Abel inverting (a) the left hand side and (b) the right hand side portion of the preconditioned wire fringe-shift line-out in Figure 4.21.

By Abel inverting both plots in Figure 4.21 and assigning positive values to neutrals and negative values to plasma, we managed to obtain the number density distribution with radius for neutrals and plasma at 4ns before the switch and 16ns after the switch (Figure 4.22). At 4ns before the switch, the neutral distribution is very similar to the one obtained at an earlier time from a different experiment (Figure 4.11(i)), however possessing a smaller peak of ~ 18×10^{18}cm^{-3} but a slightly larger radius of ~ 1.8mm, a consequence of further 50ns thermal expansion. The plasma distribution on the left hand side (LHS) also possess a similar feature to Figure 4.11(i), however the right hand side (RHS) plasma distribution shows a double peak which can also be seen in the original fringe-shift data in Figure 4.21. Most probably the second peak observed at the RHS edge is the plasma flow from the inverse array reaching the load section and initiating the 'flow-switch' (this switching mechanism is described in more detail in Chapter 3, Section 3.2)

At 16ns after the current switch, the electron density peak on both sides increase from an averaged value ~ 6×10^{18}cm^{-3} to ~ 35×10^{18}cm^{-3}, and have shifted inwards slight by ~ 0.25mm. The electron distribution falls down sharply after the peak to a constant value of ~ 18×10^{18}cm^{-3}. A strong indication that current switch happens around the outer edges first before moving inwards. The minimal change in

diameter after 16ns have passed from current switch suggests that there is a phase of heating and ionisation before the load begins to implode.

By assuming the atom density distribution does not vary after 16ns into current switch we can obtain an estimate of the degree of ionisation vs radius by calculating the ratio of electron density at 16ns after the switch to neutral density at 4ns before the switch. This ratio is proportional to temperature and is shown as a dashed plot in Figure 4.22. Throughout the central region the ionisation stays at a roughly constant level of 1, it then sharply rises reaching values of ~ 5-6 close to the plasma peaks on the wire sides.

4.3.2 Implosion trajectory

As the current switches into the load, the preconditioned wire is further heated and ionised, significantly increasing the density of free electrons and hence allowing more current to pass through. Implosion starts when enough current passes through and the J×B force overcomes the thermal expansion. To investigate the implosion trajectory of a single preconditioned wire, we have obtained images from an optical streak camera, optical framing camera, 4-frame MCP XUV camera and in some cases laser images after the current switch time. Those images are presented in Figures 4.23 - 4.30 for a 25μm, 40μm and 50μm Al wire loads.

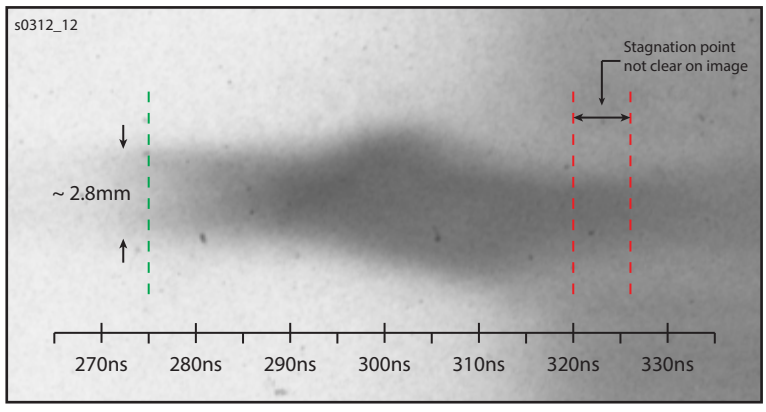

Figure 4.23: An optical streak camera image showing a radial slice of a 25μm Al wire at the centre of the load. The dashed green line shows the current switch time and the dashed red line shows roughly the 'region' of stagnation.

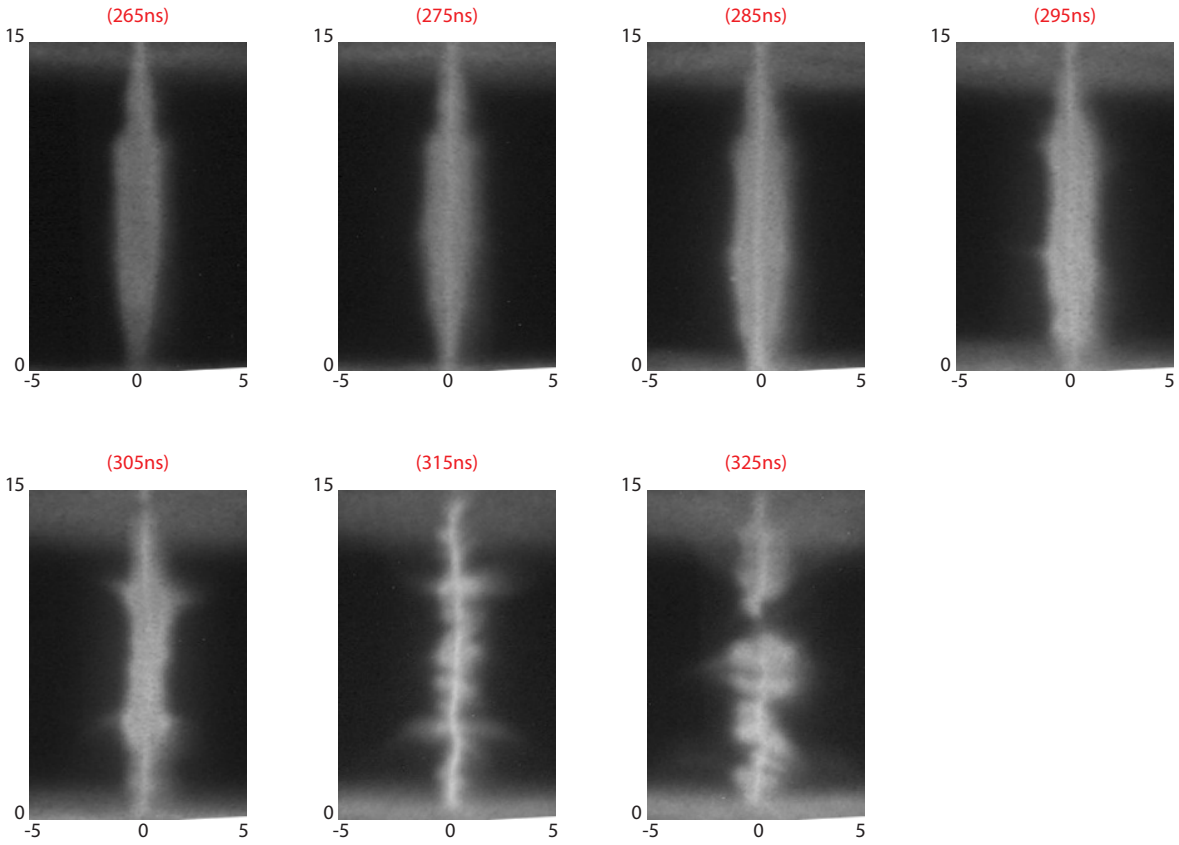

Figure 4.24: Images of a 25μm Al wire from an optical framing camera set at 10ns interval. Length scales at the corners of images are in mm. Images are from the shot s0312_12.

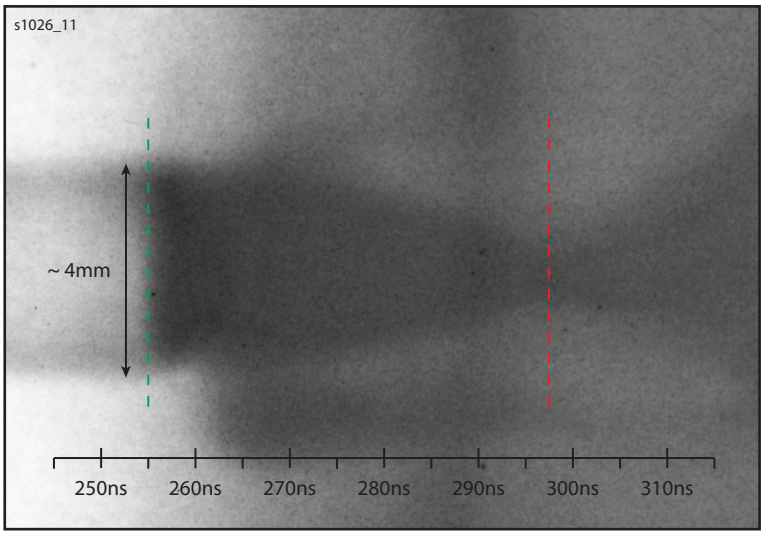

Figure 4.25: Optical streak image showing a radial slice of a 40μm Al wire at the centre of the load. The dashed green line shows the current switch time and the dashed red line shows the point of stagnation.

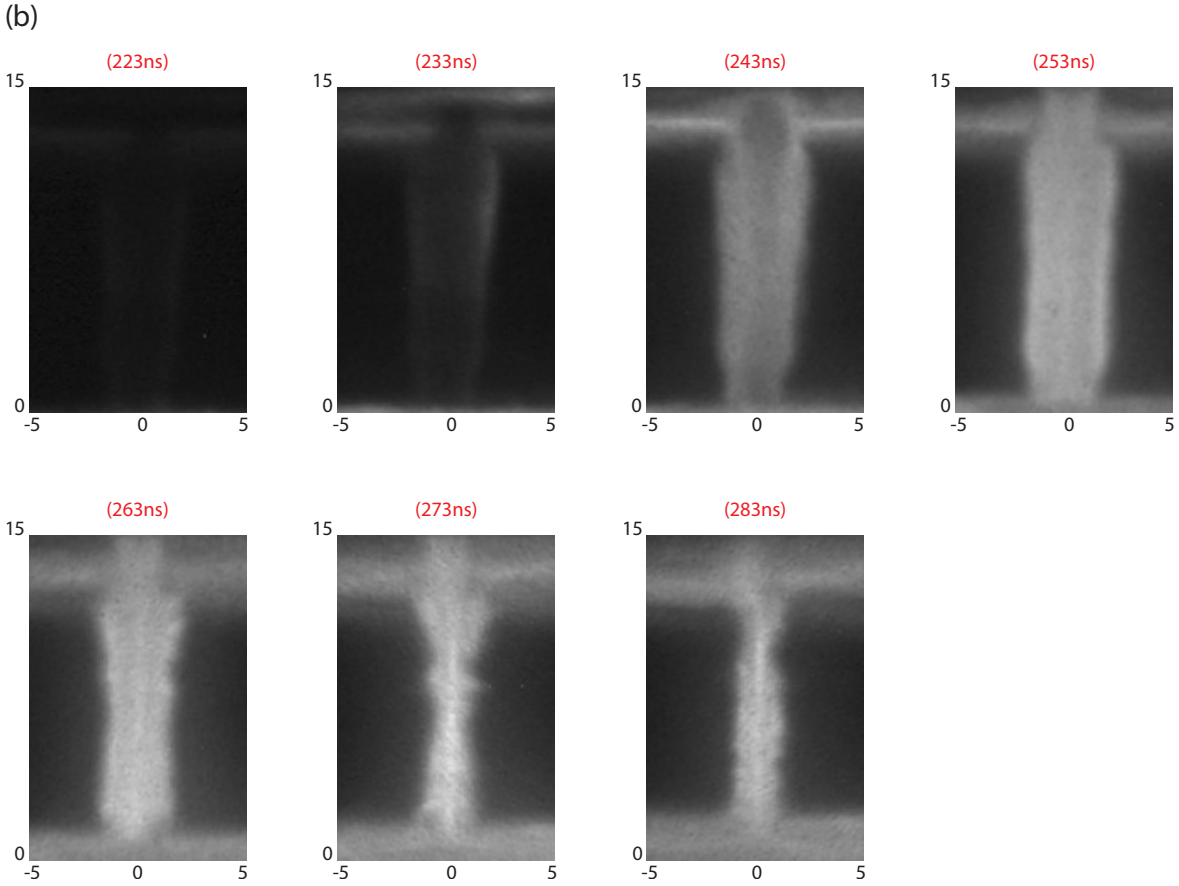

Figure 4.26: Images of a 40μm Al wire from an optical framing camera set at 10ns interval. Length scales at the corners of images are in mm. Images are from the shot s1026_11.

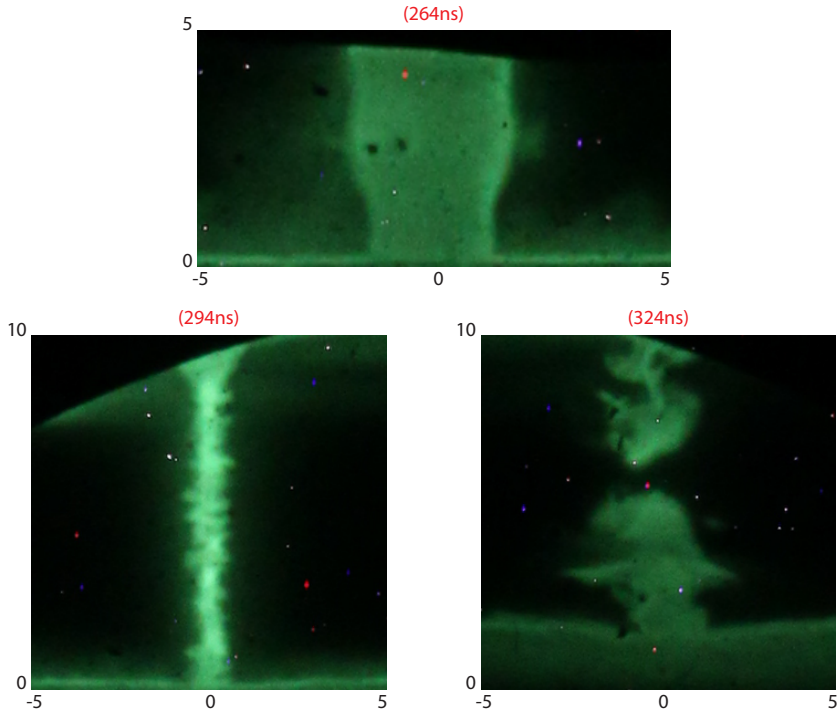

Figure 4.27: 4-Frame XUV images after current switch of a 40μm Al wire. Length scales at the corners of images are in mm. Images are from the shot s1026_11.

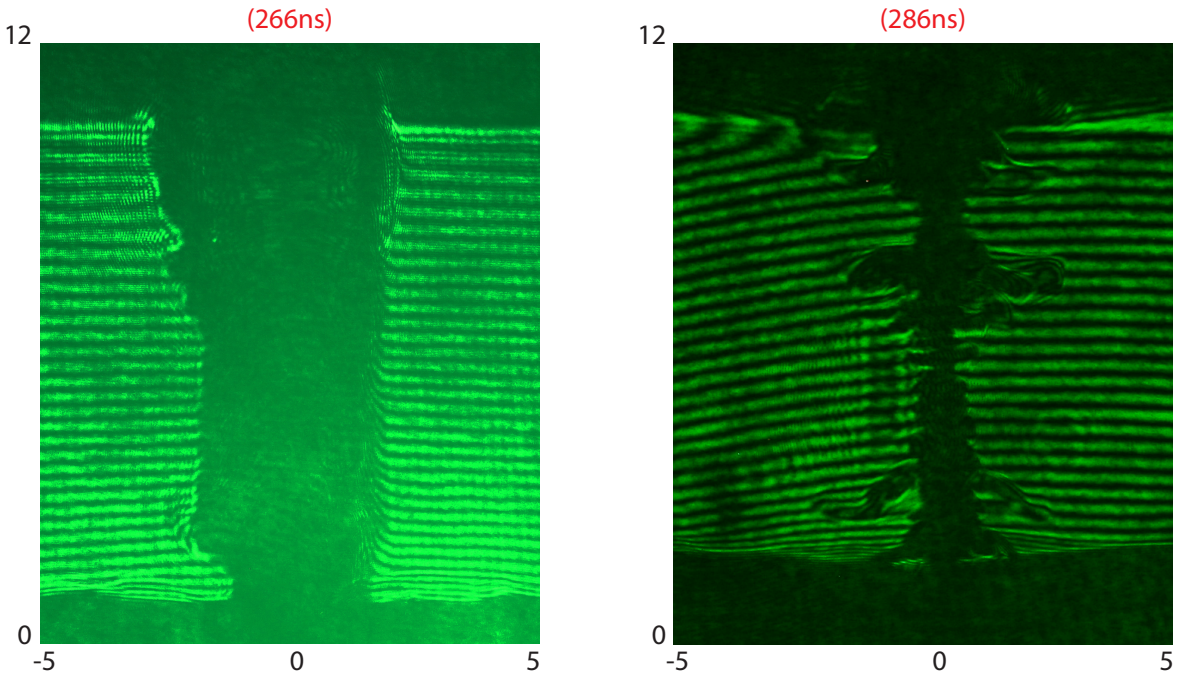

Figure 4.28: Laser ($\lambda = 532$nm) interferometric images after the current switch time of a 40μm Al wire. Length scales at the corners of images are in mm. Images taken from the shot s1026_11.

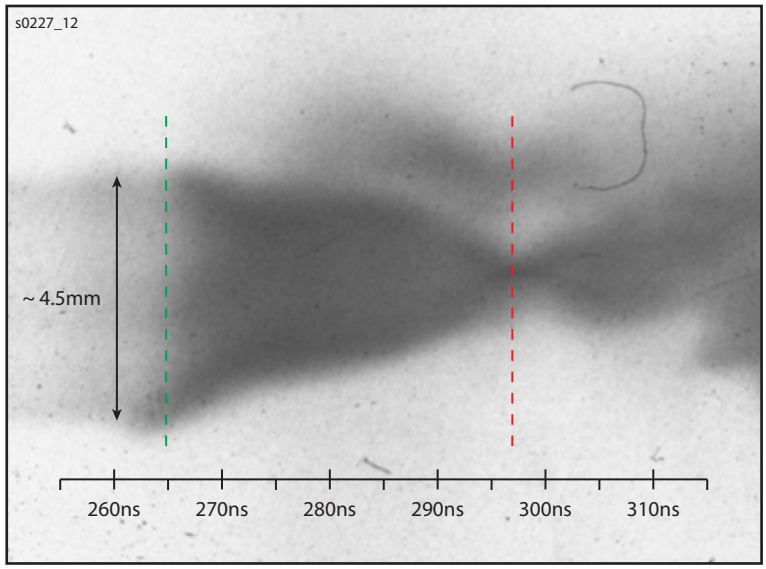

Figure 4.29: Optical streak image showing a radial slice of a 50μm Al wire at the centre of the load. The dashed green line shows the current switch time and the dashed red line shows the point of stagnation.

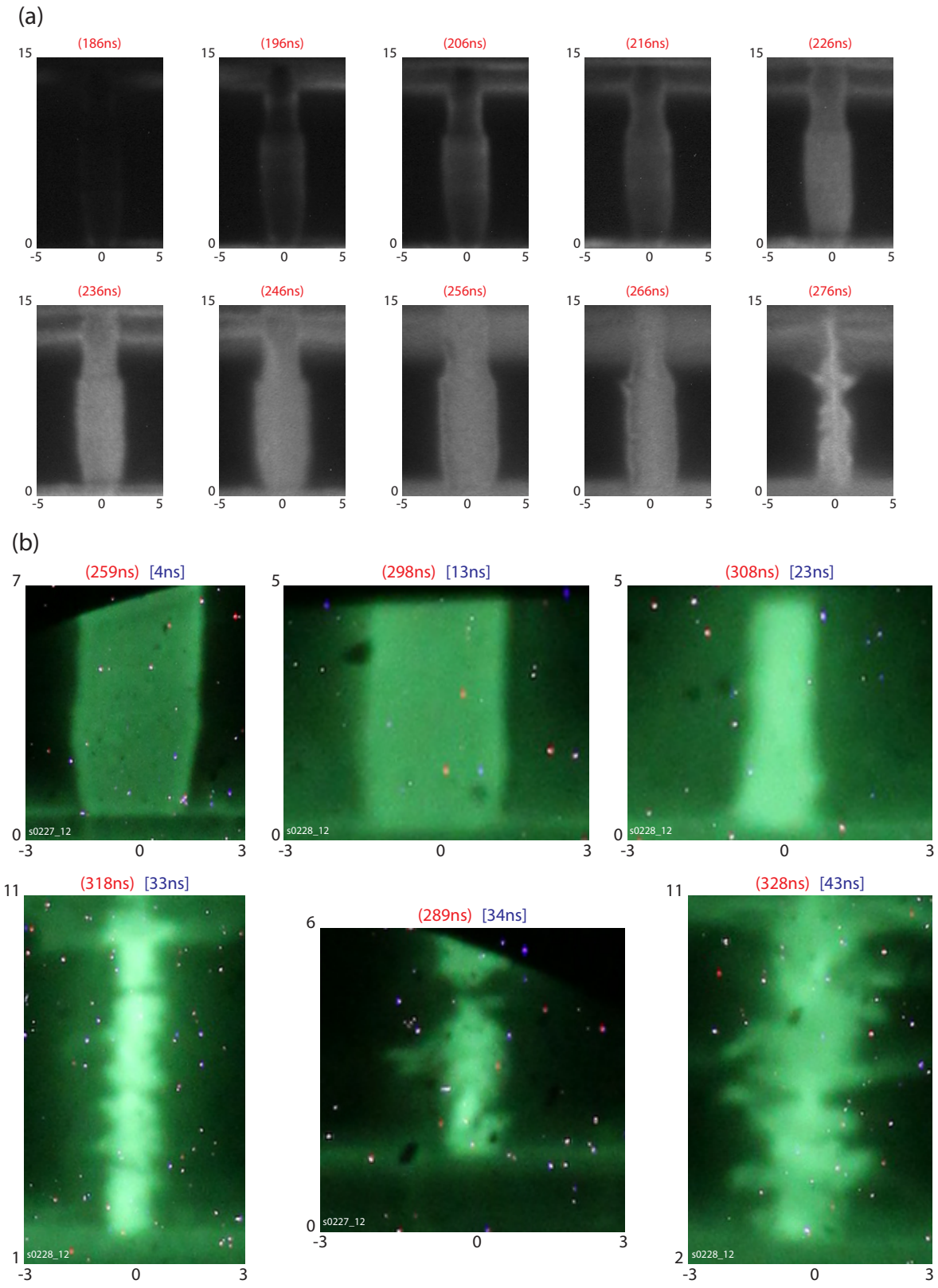

Figure 4.30: Load images taken after the current switch of a 50μm Al wire from: (a) an optical framing camera set at 10ns interval. (b) a 4-frame XUV camera, where the timings in blue in square brackets [ ] are measured after the current switch. Length scales at the corners of images are in mm. Images in (a) are from the shot s0227_12, while images in (b) are from two different shots (s0227_12 & s0228_12).

From the above figures we see that soon after current switches into the load, there is a period of heating and ionisation before the start of implosion. This period is ~ 20ns for the 25μm and 40μm wire and ~ 40ns for the 50μm measured from the optical framing images (Figure 4.24, 4.26 & 4.30(a)). It is expected that such a period should get larger as the wire thickness increases, since the total number of atoms to be ionised is larger. During this phase, the preconditioned wire experiences a thermal expansion before it begins to implode. The degree of this expansion is larger for thinner wires as they possess a lower mass per unit length. This expansion can be clearly seen in the optical streak image and optical framing image of a 25μm wire (Figure 4.23 & 4.24). After this phase, all preconditioned wires undergo implosion.

During the implosion phase, we do not observe any Rayleigh-Taylor instabilities. However there are some local non-periodic perturbations along the length of the imploding preconditioned wire, which grows larger as the implosion progresses. Those perturbation can be seen in images obtained from the optical framing camera. For example the 40μm image at 263ns in Figure 4.26 shows a small region on the RHS edge of the wire imploding slightly earlier than the rest. This small perturbation grows much larger in the next frame (273ns). The 50μm image at 266ns in Figure 4.30(a) also shows a small region on the LHS edge of the wire imploding earlier, which grows larger in the next frame (276ns) as the wire implodes. Other than few local perturbations, the implosion in general is quite uniform with no gross instabilities present. We can see this clearly in XUV images of 50μm wire (Figure 4.30(b)), were the wire diameter has shrunk by more than a 1/2 within 23ns after current switch and the compressed wire still maintains a straight smooth boundary. A strong indication of the absence of Rayleigh-Taylor instability. At stagnation, plasma MHD instabilities of the form m=0 or m=1 are clearly seen for all wire thicknesses. This is discussed later in the next section. The implosion time for all three thicknesses is ~ 20-30ns.

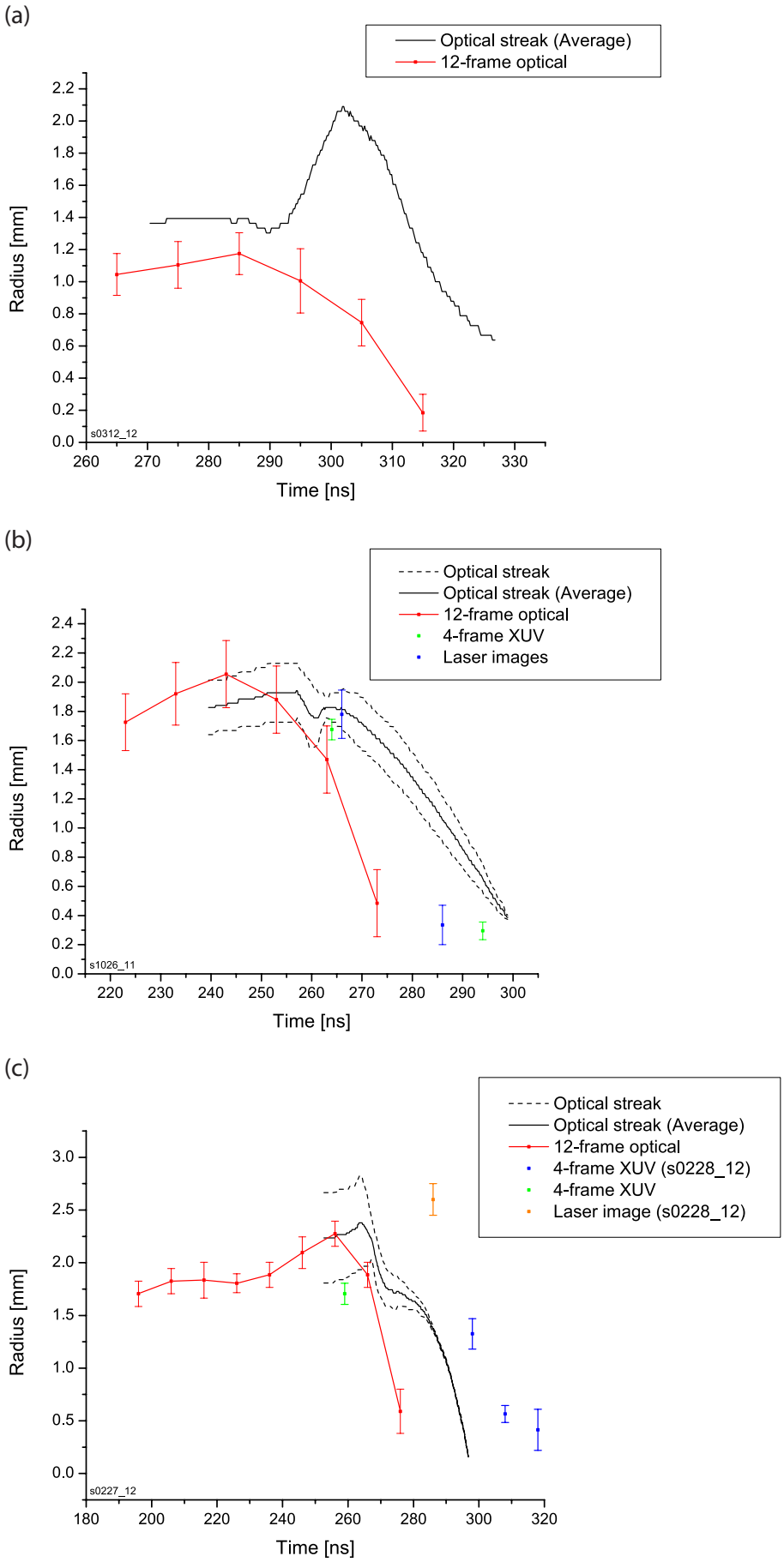

Figure 4.31: Implosion trajectory plots for a single Al wire load of (a) 25µm, (b) 40µm and (c) 50µm thickness.

To have a clearer view of the implosion trajectory we have plotted a 'radius vs time' graph after the switch (Figure 4.31) from all images presented in Figure 4.23 - 4.30. The mismatch in timings between the optical streak and optical framing camera in all three graphs in Figure 4.31 is most likely due to an error in calculating the delay times on the optical framing camera. Even though the implosion trajectory of the 25μm is not very clear from the streak image we made an attempt to plot it. This is due to the fact such a diagnostic looks at a radial slice at a particular axial height, where the development of instabilities can affect the implosion profile. However the optical framing which images the full height of the load shows a better representation of the implosion. The images from this camera shows an accelerating mass towards the axis. The implosion time for this load is ~ 30ns.

Looking at the 40μm plots (Figure 4.31(b)), we see a different implosion profile from the optical streak and optical framing camera The former shows a linear constant velocity implosion while the latter shows an accelerating implosion. One reason for this could be to do with the fact that we have assumed a linear time variation when calibrating the streak images, which might have a slightly different variation with time. To back up this argument, laser images show an implosion time which matches the optical framing (accelerating implosion). The 4-frame XUV has been setup to takes an image every 30ns for this experiment. It shows an implosion time of $\leq$ 30ns, and most probably the image at 294ns could be some time after the mass has stagnated and time is given for MHD instabilities to develop around the stagnated material. In addition to all this, the 50μm load - which possess a greater mass per length - shows an accelerating implosion (Figure 4.31(c)) from both optical streak and optical framing camera. Given that the current at the time of the switch for this experiment was not significantly higher than the 40μm experiment (~ 10%), one would expect a lower mass per length load to accelerate rather than implode at a constant velocity. Hence backing our argument that the optical framing shows a better representation of the implosion trajectory profile of the 40m wire, with an implosion time of ~ 30ns.

The 50μm wire load shows a fast acceleration reaching an average velocity of ~ 10cm/μs before stagnation. This has been observed from two independent experiments involving a 50μm wire load. The implosion time for this wire is ~ 20-25ns, which is faster than the thinner wires. This could be due to the slightly higher current at the time of the switch. Another explanation which is more likely is to do with the fact that dI/dt at the switch is not high enough for the current to reach its maximum value just before stagnation. Most likely wires stagnate before the current reaches it peak. Wires of larger mass require more time to heat and ionise and hence giving more time of the current to increase further. Therefore at the start of implosion (after ionising the bulk), heavy wires will have a greater value of current than lighter wires, producing a faster implosion.

At the start of the current switch, both the 50μm and 40μm load shows an initial implosion of the outer edges which stagnates at ~ 85% of the initial wire radius for ~ 6-7ns before the main implosion starts. This is the low density plasma seen at the outer edges of the preconditioned wires (Section 6.2.2) imploding into the bulk of the wire. The imploding 'piston' experiences a sudden increase in mass and hence reducing the velocity.

As mentioned earlier, one can obtain an estimate of the current temporal profile in the load from implosion trajectories. We can model implosions of a single preconditioned wire on axis using the snowplough model discussed in Chapter 1 Section 1.3.2. The implosion is modelled as a cylindrical piston driven by the J×B force constantly accreting mass as it move towards the axis. The equation of motion for such a system using dimensionless parameters is

$$m\ddot{r} - 2r\dot{r}\rho(r) = -\Pi\frac{I^2}{r} \tag{4.6}$$

$$\dot{m} = -2r\dot{r}\rho(r) \tag{4.7}$$

where r is the radius, m is the mass of imploding piston, I is the current driving the implosion, $\rho(r)$ is the radial density distribution and Π is the 'pinch parameter' defined as,

$$\Pi = \frac{\mu_0 I_{\max}^2 \tau^2}{4\pi m_0 r_0^2} \tag{4.8}$$

$I_{\max}$ is the peak current at the point of stagnation, τ is the implosion time, m_0 is the total mass per length of the load and r_0 is the initial radius at the start of implosion. Π is dimensionless, but the parameters defining it are in SI units.

In order to solve this differential equation we need the density distribution of the preconditioned wire at the time of current switch. We will assume this distribution profile does not vary significantly from the ones measured at ~ 50ns before the switch in Figure 4.11(g),(h)&(i) for the 25μm, 40μm and 50μm Al wire load respectively. All density distributions were normalised by dividing by the average density ρ_0 defined in Eq(4.9).

$$\rho_0 = \frac{m_0}{\pi r_0^2} \tag{4.9}$$

Then a curve-fit was applied on those distributions and the curve equation was used in the snowplough model (Eq 4.6 & 4.7). Figure 4.32 shows the experimentally obtained density distribution along with the curve fit used in normalised dimensionless units. Assuming the density profile maintains its normalised shape through the preconditioning phase up to the current switch time, and by using the appropriate values for m_0 and r_0 one can obtain the actual density distribution before the switch. The values used for m_0 for the snowplough model (Eq 4.8) are the real values in a solid wire rather than the experimentally calculated values which for the 25um case had an error of ~ 35%. While the m_0 value used to normalise the density distribution (Eq 4.9) is proportional to the total number of neutral and plasma ions experimentally calculated by integrating the density distribution.

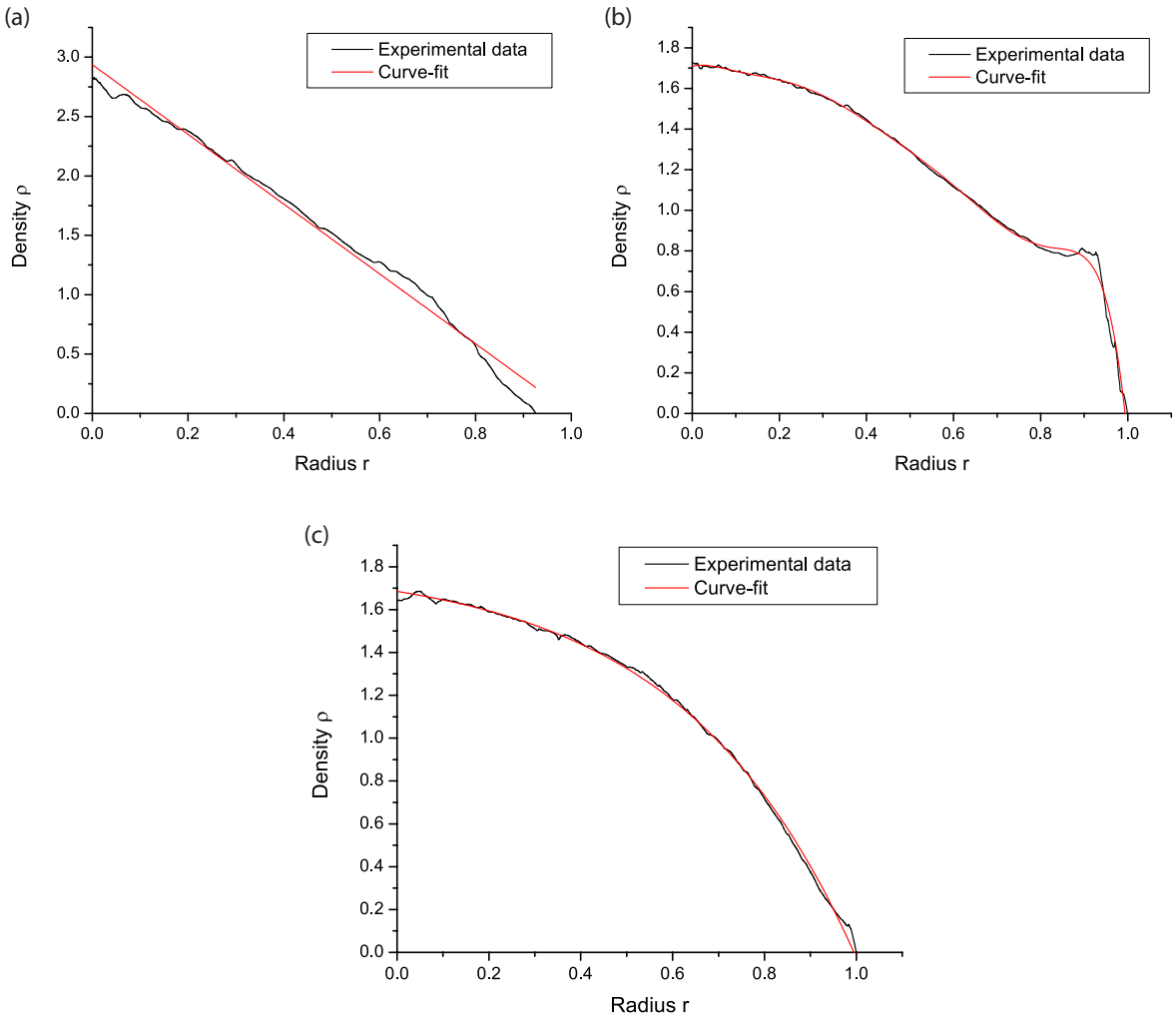

Figure 4.32: Experimentally obtained density distribution from Abel inversion of interferogram analysis along with a curve-fit for (a) 25μm, (b) 40μm and (c) 50μm preconditioned Al wire load. All quantities are normalised and in dimensionless units.

In order to numerically solve the snowplough differential equations (4.6) and (4.7), we have re-written them as three separate 1st order differential equations (Eq 4.10), where y_1 is radial position of the imploding piston, y_2 is the velocity of the piston and y_3 is the accreted mass on the piston. The solver 'ode45' was used in MATLAB to solve those sets of ordinary differential equations.

$$\begin{aligned} \frac{dy_1}{dt} &= y_2 \\ \frac{dy_2}{dt} &= \frac{1}{y_3}\left[2y_1y_2^2\rho(y_1) - \Pi\frac{I^2(t)}{y_1}\right] \\ \frac{dy_3}{dt} &= -2y_1y_2\rho(y_1) \end{aligned} \tag{4.10}$$

The initial condition (at $t = 0$) used to solve those equations are

$$\begin{aligned} y_1 &= 1 \\ y_2 &= 0 \\ y_3 &= \begin{cases} 0.04 \Rightarrow 25\mu m \\ 0.05 \Rightarrow 40\mu m \\ 0.09 \Rightarrow 50\mu m \end{cases} \end{aligned} \tag{4.11}$$

We have assumed that the implosion starts at the point when the neutral bulk begins to implode. At that time, we will assume that the imploding piston had swept the outer plasma. Therefore the initial values for the mass of the imploding 'piston' (y_3) were chosen based on the amount of plasma present around the preconditioned wire. We have assumed a Z=1 ionisation for the 25μm and 40μm wires while a Z=2 ionisation for the 50μm wire due to a higher presence of plasma and the density analysis from Figure 4.15 shows $n_e/n_a \sim 3$ at the outer peaks.

The snowplough equation was solved for different functions of current $I(t)$ and the corresponding implosion trajectory was compared with the one observed experimentally. Five different current functions were used to solve the snowplough implosion. A step function of constant current, a linearly increasing current, a parabolic function, a $\sin^2$ function and a square-root function. The implosion trajectories generated from those functions along with the ones experimentally observed are shown in Figure 4.33. Experimental data from the optical framing camera was used for the 25μm and 40μm load wire thickness for reasons explained earlier. While the optical streak data was used to present the experimental trajectory for the 50μm.

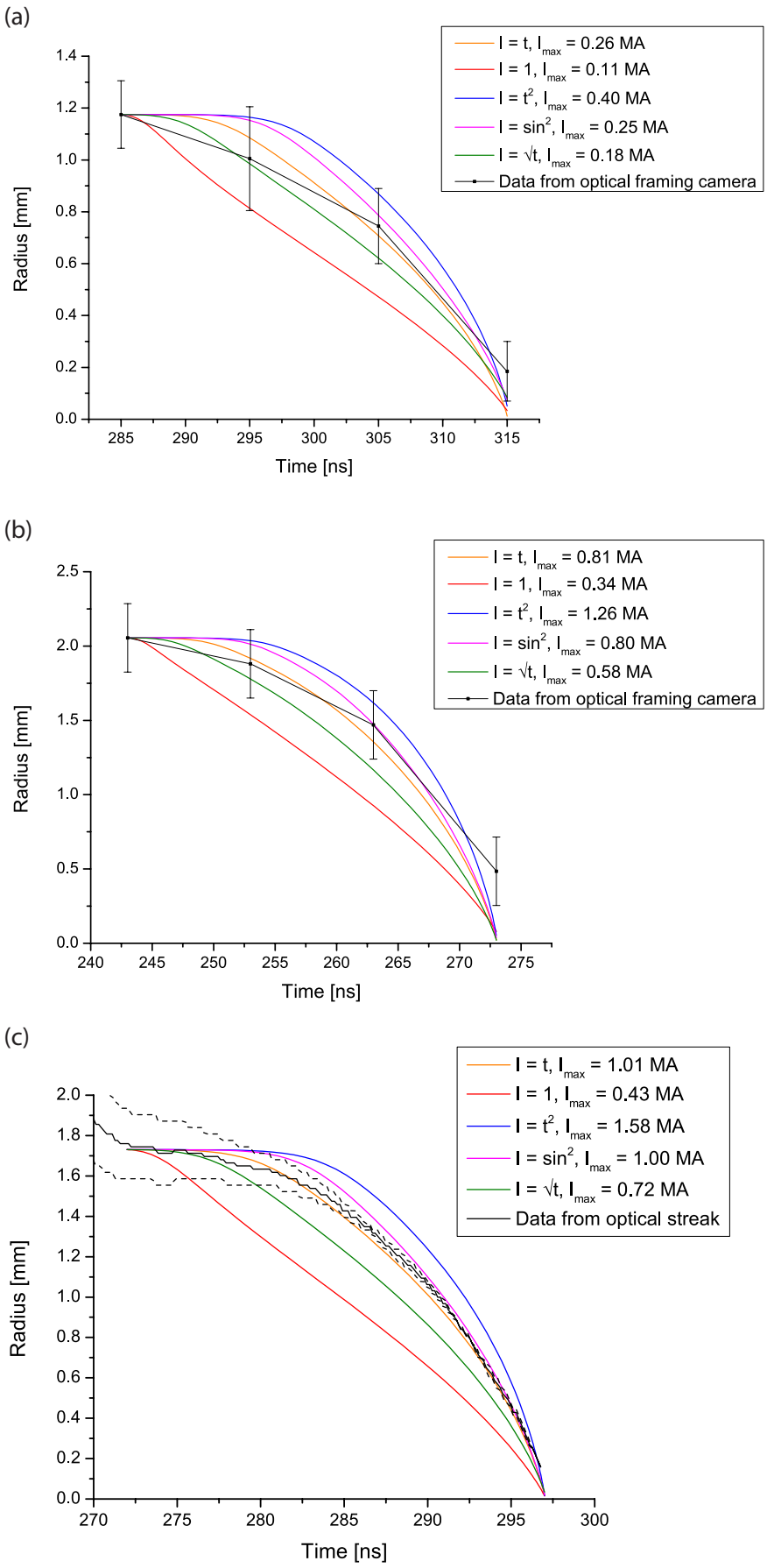

Figure 4.33: Implosion trajectory plots from the snowplough model for different current functions along with experimental data plot for single preconditioned aluminium wires of (a) 25µm, (b) 40µm and (c) 50µm initial thickness.

A quick inspection of the above figure shows that the most probable current profile is either a linear or a $\sin^2$ function for all initial wire thicknesses (25μm, 40μm, and 50μm). However, the maximum current reached which is also the current at the point of stagnation increases significantly as the wires become thicker. This is ~ 0.25 MA for the 25μm wire, ~ 0.80 MA for the 40μm wire and ~ 1.0 MA for the 50μm wire. The implosion time for the 25μm and 40μm was 30ns while it was slightly shorter for the 50μm wire (25ns). It appears as if the average dI/dt during implosion increases with increasing wire thickness, which is not entirely true. In the snowplough model we have assumed that current starts at the onset of implosion, however from experimental data we have seen that implosion starts some time after the current switch. During this phase the current is heating and ionising the neutral gas. Loads of thicker wires possess more mass per length and therefore require more time to heat. This can be seen clearly in the optical framing images of the 50μm wire (Figure 4.30(b)). Therefore by the time implosion starts, the current would have reached a higher value for thicker wires. This also means that the maximum current at stagnation obtained from the snowplough implosion is an overestimated value.

4.3.3 Stagnation and X-ray production

As the preconditioned wire implodes its temperature is constantly increasing due to factors such as increasing current (ohmic heating) and decreasing volume (PdV). This increases the thermal outward pressure of the imploding wire which counteracts the J×B force driving the implosion. The implosion stagnates when the imploding 'piston' collides on axis and the kinetic energy is thermalised. In between the point of stagnation and the development of MHD instabilities we will assume that for a short period of time a quasi-steady state is achieved where Eq 4.12 holds.

$$\nabla\left(P_i + P_e\right) = \mathbf{J} \times \mathbf{B} \tag{4.12}$$

Where P is the pinch pressure and the subscripts i and e refer to ions and electrons respectively. From which we can derive the Bennett relation (Eq 4.13) to estimate the average temperature of ions and electrons from current measurements.

$$8\pi N k_B \left(Z T_e + T_i \right) = \mu_0 I^2 \tag{4.13}$$

Where N is the total number of atoms per length, Z is the degree of ionisation, T is the average temperature and I is the current through the pinch. We will assume that $T_e = T_i = T$, and the Bennett pinch current is the estimated current at stagnation ($I_{\max}$) from the snowplough implosion fit in Figure 4.33. We note that those current values are an overestimate and hence giving us an upper limit to pinch temperature. Figure 4.34 shows the values of $(Z{+}1)\,T$, He-like atoms and H-like atoms temperature for a stagnated plasma of preconditioned singles Al wires of 25μm, 40μm and 50μm initial thickness.

Wire thickness [μm]	(Z+1)T [eV]	Temp. of He-like Al (Z=11) [eV]	Temp. of H-like Al (Z=12) [eV]
25	659	55	51
40	2638	220	203
50	2638	220	203

Figure 4.34: Temperatures of He- and H- like atoms at stagnation (assuming the formation of a Bennett pinch) for different initial thicknesses of a single Al wire load.

Comparing the 25μm and 40μm temperatures we clearly see that by increasing the load's mass per length by ~ 150% we managed to get a pinch temperature ~ 4 times larger. Again we stress that this factor is an overestimate and most likely it is < 4. The increase in mass, increases the heating and ionisation time allowing for current to reach higher values and since $(Z{+}1)\,T \propto I^2$ we expect higher temperatures. However by increasing the mass per length further by ~ 50% (50μm wire) we do not see an increase in temperature, which stays the same at 220 eV for the He-like atoms. Thats because the current does not increase significantly (most probably it is reaching its peak value) and the increase in the I^2 term is balanced by the increase in N. Hence, one would expect the temperature to fall for wires greater than 50μm thickness. This suggests that there is an optimum mass per length value for a single preconditioned wire to generate the maximum possible temperature at stagnation which most likely lies between 40μm and 50μm thickness.

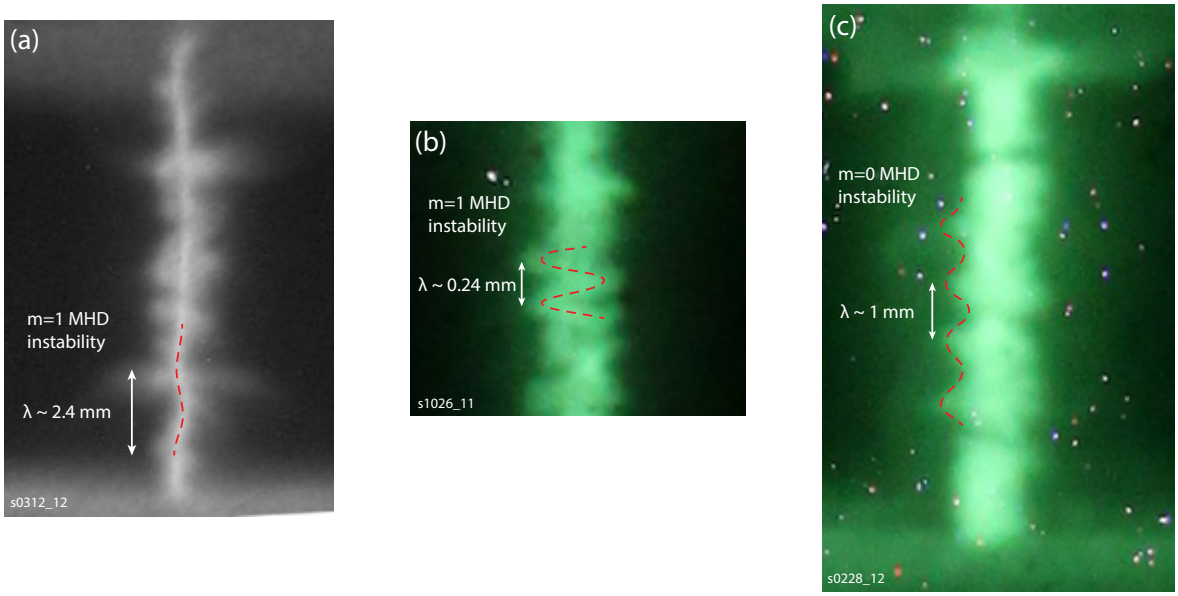

Figure 4.35: Development of *sausage* (m=0) and *kink* (m=1) MHD instabilities on the stagnated plasma column from a single Al wire load of (a) 25μm, (b) 40μm and (c) 50μm initial thickness.

As soon as the plasma stagnates on axis, *sausage* (m=0) and *kink* (m=1) MHD instabilities begin to develop which can be clearly seen in Figure 4.35. For the 25μm and 40μm images we did not observe a *sausage* instability which could be due to lack of image resolution. However we were able to observe the *kink* instability in certain regions along the the axial length possessing a λ ~ 2.4mm and 0.24mm for the 25μm and 40μm wires respectively (Figure 4.35(a)&(b)). The absence of m=0 instability could also be due to the fact that the radius of the pinch is quite small (or the average particle density is low). This means that there is a greater chance for current to penetrate radially into the wire and hence significantly lowering the growth rate for this mode of instability [52]. On the other hand the *kink* (m=1) mode is always unstable irrespective of radial distribution of current [52]. The stagnated pinch of the 50μm wire clearly shows the m=0 instability mode (λ ~ 1mm), which is expected for a greater radii (or denser) pinch and therefore less current penetration and greater growth rate.

To calculate the instability growth rate we have assumed an incompressible plasma with a constant density ρ. This is a valid assumption as compressibility has little influence on the growth rate for current confined on the surface of the plasma

column [52]. However this is not true for the m=0 instability mode with a $kr_0 < 1$. We have calculated the instability growth rate γ from wavelengths measurements using Eq(4.14) obtained from Pereira et al [52].

$$\gamma = \frac{C_A}{r_0}\Gamma \tag{4.14}$$

Where r_0 is the pinch radius, Γ is a dimensionless factor obtained from plots in Pereira et al [52] and C_A is the Alfven velocity defined as

$$C_A = \frac{B}{\sqrt{\mu_0 \rho}} \tag{4.15}$$

The instability growth rate for the 25μm, 40μm and 50μm Al wires are 1.58×10^8 s^{-1}, 8.22×10^8 s^{-1} and 3.41×10^8 s^{-1} respectively. This corresponds to an e-fold increase in the amplitude of instability within 6ns, 1ns, and 3ns respectively. Those values are consistent with images obtained from framing cameras (optical & XUV) 10ns after stagnation (i.e 10ns after the images in Figure 4.35) which shows the plasma is expanding or breaking up (Figure 4.24, 4.27 & 4.30(b)). We note that the calculated growth rate for the 40μm and 50μm wire are overestimated values due to the fact that we have assumed current is confined on the surface. This value could be 30% lower for the 40μm wire, and ~ 20 times lower for the 50μm wire if we assumed the current is 99% penetrable. On the other hand, the growth rate of the m=1 instability of the 25μm wire is not affected by radial current distribution due to the fact that $kr_0 < 1$ at stagnation [52].

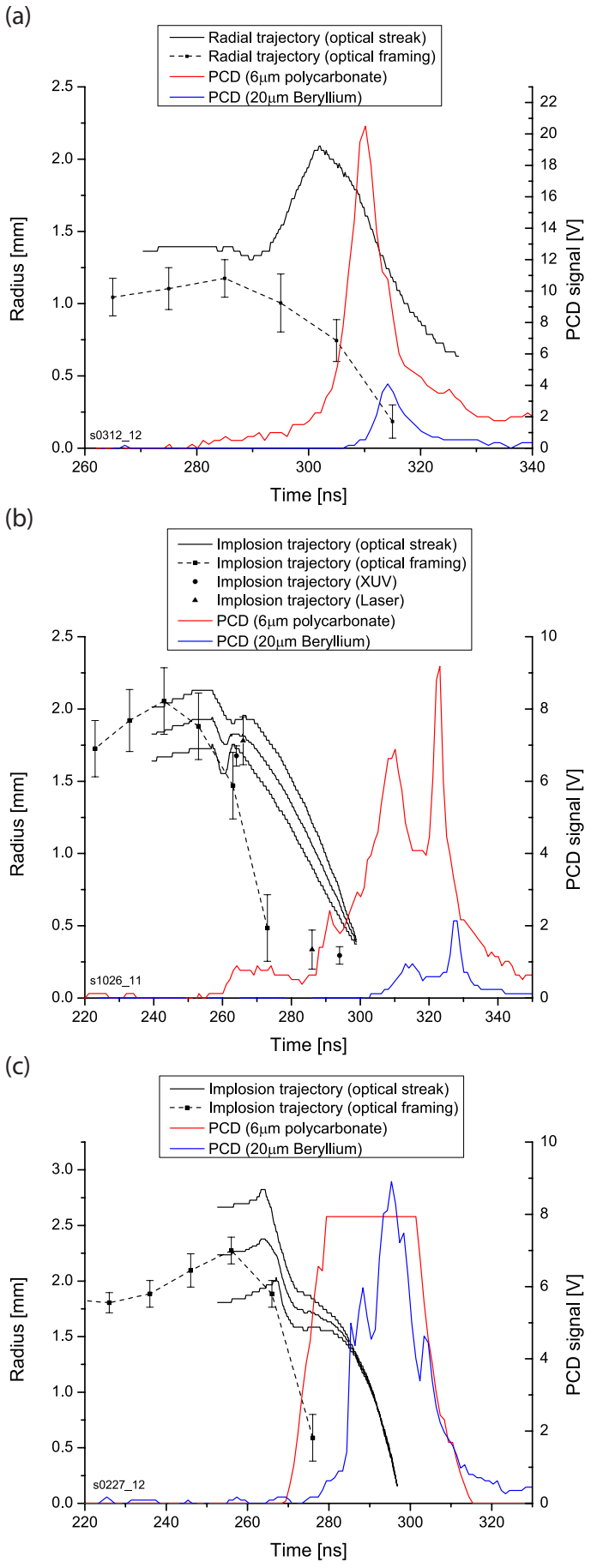

Figure 4.36: X-ray signals from filtered PCD along with implosion trajectories for single Al wire loads of (a) 25μm, (b) 40μm and (c) 50μm initial thickness.

As the imploding plasma stagnates, the kinetic energy it contained just before stagnation and the dynamics involved in the development of instabilities after stagnation all contribute to the final X-ray pulse. Chittenden et al [30] identifies four sources of energy which contribute to the total X-ray pulse. The kinetic energy of the imploding piston, the compression of the stagnated plasma by the Lorentz force (PdV), ohmic heating and formation of the *kink* m=1 instability. Simulations of a 16mm diameter 16 × Al wire array containing roughly twice the mass per length of a 40μm single wire shows that the kinetic energy only contributes to 28% of the total X-ray energy [30]. We expect this percentage to be much lower for our single wire experiments where the wire diameter at current switch is much smaller than 16mm and the effect of snowplough is larger, preventing the imploding piston from reaching high velocities. Figure 4.36 shows X-ray pulses from filtered PCDs of a 6μm poly-carbonated (soft + hard X-rays) and 20μm Beryllium (hard X-rays) for different load wire thickness. By subtracting the latter from the former one can obtain a % estimate of the soft X-ray yield.

As soon as the current switches into the 25μm wire load at ~ 275ns, we see a steady increase in soft X-ray radiation (6μm polycarbonate PCD signal in Figure 4.36(a)) which is due to the heating and ionisation of the neutral gas. The gaseous wire abruptly expands between 290-300ns due to the rapid heating by the fast current switch. This heating is reflected in the radiation emitted which is now increasing at a larger gradient. This expansion soon stops when the J×B force overtakes the thermal expansion, which marks the onset of the compression phase. The compression and ohmic heating of the wire causes a steep rise in the soft X-ray power reaching a peak 10 times its starting value (2V - 20V) in ~ 7ns. The optical streak image did not clearly present the implosion of this wire and therefore we will ignore its trajectory data after the expansion peak at 300ns. The optical framing images on the other hand shows the radial variation, but every 10ns, and could have missed the actual stagnation point which could have happened soon after the 305ns frame. If we assume that the stagnation happens few ns after the 305ns frame and adjusting slightly for the timing delay error this will coincide with the soft X-ray peak and will allow some time for the observed

instabilities to form in the next frame. Therefore the implosion time would become shorter to ~ 20ns, which means a larger current at stagnation from the one predicted in Figure 4.33(a). After stagnation, the hard X-ray signal (20μm Be PCD signal in Figure 4.36(a)) rises to 8 times its starting value (0.5V - 4V) in 4ns. This is most likely due to the formation of MHD instabilities after stagnation. By integrating the two PCD plots and comparing their areas we managed to estimate that the soft X-ray makes up ~ 86% of the polycarbonate PCD signal.

The 40μm wire shows a different X-ray signal profile comprising of several peaks. At 260ns the polycarbonte PCD signal (soft X-ray) rises from 0V to 1V as the outer plasma implode on the neutral bulk of the wire. Afterwards the soft X-ray signal stays at a relatively low level for ~ 20ns as the bulk of the wire is heated and ionised. This includes the first half of the implosion phase (i.e from r_0 to $r_0/2$). For reasons explained earlier, the final part of the implosion phase and specifically the point of stagnation will not be taken from optical streak or optical framing images. Instead laser and XUV diagnostics which provide much more accurate timings have captured images (Figure 4.27 & 4.28) at roughly the time of stagnations (± few ns). Laser image at 286ns shows some parts of the wire have stagnated while other are still imploding along the axial length. XUV image at 294ns shows the wire has fully stagnated and the m=1 instability begins to form. This means that the actual point of stagnation lies between those images. During the final half of the implosion (i.e $r_0/2$ to 0), the X-ray begins to rise reaching a peak of ~ 2.4V in ~ 5ns. This peak lies in between the laser and XUV images and most likely this corresponds to the point of stagnation (291ns). The loss of kinetic energy at stagnation and some degree of PdV compression are most likely the major sources of X-rays at this point in time.

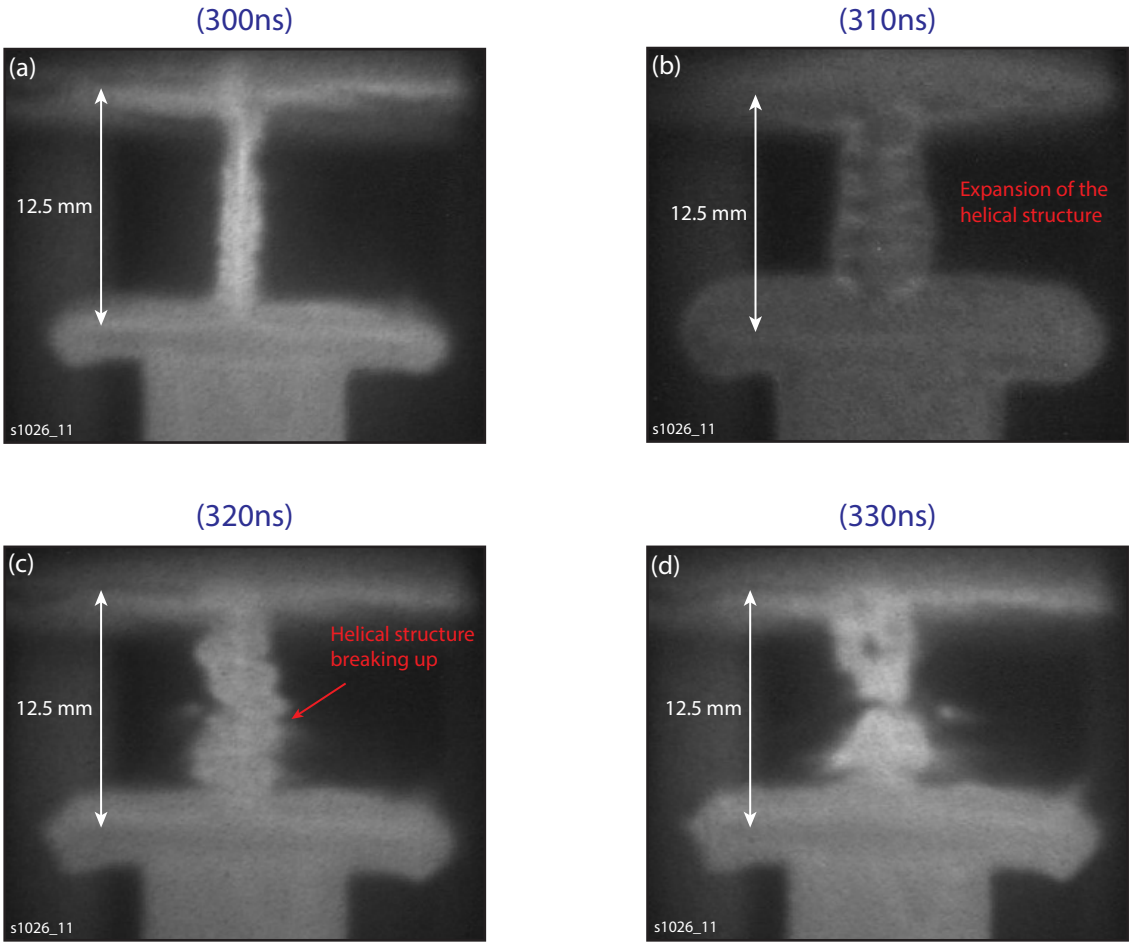

Figure 4.37: Post-stagnation images from optical framing camera for a 40μm Al wire showing the formation and expansion of a helical structure which is initially caused by the m=1 MHD instability.

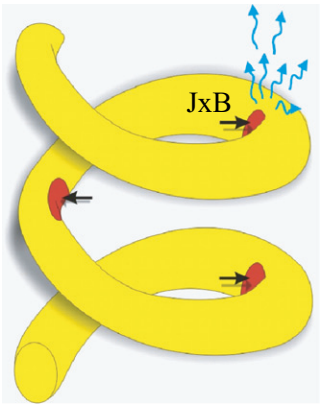

Figure 4.38: Schematic showing how X-rays can be generated in an m=1 unstable plasma, when the Lorentz force does work in forcing the plasma helix to expand (Image reproduced from [30]).

If we adjust our optical framing images to this stagnation time, then we clearly see that the m=1 instability which has been observed soon after stagnation in the XUV image (Figure 4.35(b)) has caused the plasma to form into a helical shape

expanding to a diameter ~ 4.8mm in 10ns (Figure 4.37). This corresponds to an average velocity of ~ $1.6\pm0.5\times10^5$ ms^{-1}. This post-stagnation process has been predicted by Chittenden et al [30] where simulations done on a 16x15μm Al wire array shows that the formation the m=1 instability at stagnation causes the current to take a helical path. This generates a magnetic field which is larger on the inside of the helix resulting in a Lorentz force pushing the helix outward (Figure 4.38). Those simulations show that the compression from the inside-out is shock-like and the speed of the expansion is supersonic reaching an average velocity of 2×10^5 ms^{-1}. A close agreement to the experimental value, which lies within its error boundaries. In addition to the expansion, the process of forming a helical current path increases the total effective length of the pinch and hence increases the contribution of ohmic heating. Simulations have shown that the helical evolution of the m=1 MHD instability is the dominant heat source at peak power. Experimentally, the expansion of the helix (Figure 4.37(b)) coincides with the rise of soft and hard x-ray power in our experiment where the 6μm polycarbonate PCD reaches a peak of ~ 7V at 310ns. The source of the second X-ray peak observed from both PCDs, and peaks at 323ns in the 6μm polycarbonate PCD plot is most likely to do with the break up of the helical structure (Figure 4.37(c)) creating a high voltage locally and hence driving an electron beam which generates mainly hard X-rays.

Looking at the 50μm X-ray plots in Figure 4.36(c), we see that the soft X-ray starts to rise as soon as the outer plasma impacts on the inner neutral mass and continues to rise as the current heats and ionises the neutral atoms. Soon the 6μm polycarbonate PCD signal saturates, this is due to fact that we increased the scope sensitivity for this experiment assuming that a thicker wire would generate less X-rays. However we managed to obtain the full profile of hard X-rays generated from Be filtered PCD. Based on thinner wire experimental results (Figure 4.36(a)&(b)), we will assume the polycarbonate PCD has a similar profile. Again we will rely on timings from XUV images presented in Figure 4.30(b). XUV image from the same shot as the X-ray pulse show that the plasma has stagnated and is breaking up at 289ns (8ns before the stagnation point on the streak). Again, there could have been an error in our streak timings. We will assume that the actual point of

stagnation happens few ns before and this corresponds to the first X-ray peak observed at 285ns reaching 5V on the Be filtered PCD. This peak is higher than the 40m wire as we have an accelerating imploding 'piston' and the estimated current at the point of stagnation is larger. Soon after, sausage m=0 instabilities grow - this has been observed from XUV images of a different shot (s0228_12) - and could be the source of the second X-ray peak at 288ns reaching 6V. Then at 289ns XUV image shows that the plasma is breaking up which would create a large voltage at that point, generating an electron beam. This could be the source of the max peak of hard X-rays observed on the Be filtered PCD which rises sharply at 290ns (soon after plasma breaking up) reaching a maximum of 9V in 5ns.

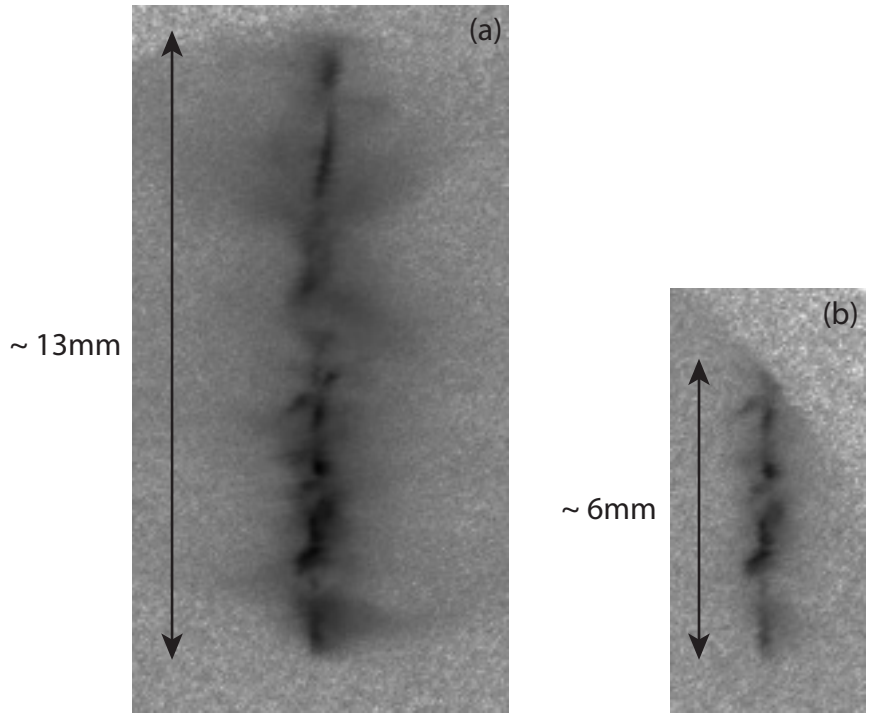

Figure 4.39: Time integrated pinhole image of the stagnated plasma column for a 40μm Al wire load through (a) a 7μm Be filter and (b) a 6μm Al filter.

Time integrated pinhole images of the stagnated plasma column was obtained for the 40μm wire through a 7μm Be filter and a 6μm Al filter. This is presented in Figure 4.39. Those images show that X-ray generation is much more uniform through the axial length than standard single wire Z-pinch [50, 51]. High energy radiation is emitted from the localised dark regions known as 'hot-spots'. This image has more similarity to standard wire array experiments of a snowplough

implosion than a standard single wire experiment. There isn't an obvious pattern (like a constant λ) in the distribution of the hot-spots but we can clearly see that the bottom half of the array (closer to cathode) is more energetic containing more of those 'spots' and are darker in colour than the top anode half. The generation of those hot-spots are directly related to the formation of MHD instabilities after stagnation.

Chapter 5

Formation and Implosion of a Cylindrical Plasma Shell

Preliminary experiments of a 2-stage wire array Z-pinch configuration have shown that the preconditioning effect is independent on the number of wires of a cylindrical array load (Chapter 3). In this chapter we utilise this fact to create a cylindrical plasma 'shell' by preconditioning a cylindrical array of large wire number and a small inter-wire separation. The aim is to get the expanding wires to merge before the main current switches into the load section. Before we attempt to build such an array, we need to investigate few things:

- We know during the preconditioning (wire expansion) phase, there is a gradual increase of a relatively low level current into the load section. At a small inter-wire separation, does the effect of merging and recombination of local magnetic fields between adjacent wires becomes large enough in changing the wire dynamics during this phase of the experiment?
- What is the minimum separation needed between wires prior to firing the experiment to achieve merging of preconditioned wires before the current switch?

To answer those questions, we need to analyse the mass distribution during the preconditioning phase from interferometric images. The geometry of our 2-stage Z-pinch array hardware prevents the use of end-on laser probing, and therefore side-on laser interferometry is our only option for spatial density analysis. For a cylindrical array we have the problem of overlapping wires in a side-on image. This results in an ambiguity when judging whether adjacent wires did or did not merge.

To overcome this problem we have conducted some initial experiments involving loads of linear wire arrays were the wires are arranged on a single plane (z-x plane). Such arrays also benefit from the fact that all wires can be in focus in a single image, and the inter-wire separation can be adjusted without increasing the wire number.

The first section of this chapter examines the spatial density distribution of neutrals and plasma in a linear array load from laser interferometric images. This analysis allowed us to obtain the initial conditions needed for a 2-stage Z-pinch configuration load to form a cylindrical plasma shell. The second part of this chapter analyses the spatial density distribution of the 'shell' before the current switch and implosion dynamics of the 'shell' after the current switch.

5.1 Linear wire array experiments

5.1.1 Linear array load consisting of 2 wires

Experimental setup

To understand if the interaction of the wires local magnetic fields with each other at close proximity will have an effect on the mass distribution during the preconditioning phase, we have assembled a 2-stage Z-pinch array with a load consisting of 2x30μm Al wires (Figure 5.1). The total array mass is slightly larger than the 40μm Al single wire load. The inter-wire separation was set to 4mm using specially designed notched discs for a square array. The aim is to create preconditioned wires with boundaries (edges) separated by a gap of $\leq$ 1mm (from Chapter 3 Section 3.1.3, expansion of such wires was roughly 3-3.5mm at 177ns). The length of the load section was kept constant at 15mm. The properties of the inverse (bottom) array were kept constant throughout all experiments described in this thesis. A detailed description of the assembly of a 2-stage Z-pinch array and the properties of the inverse array can be found in Chapter 3 Section 3.1 or Chapter 4 Section 4.1.

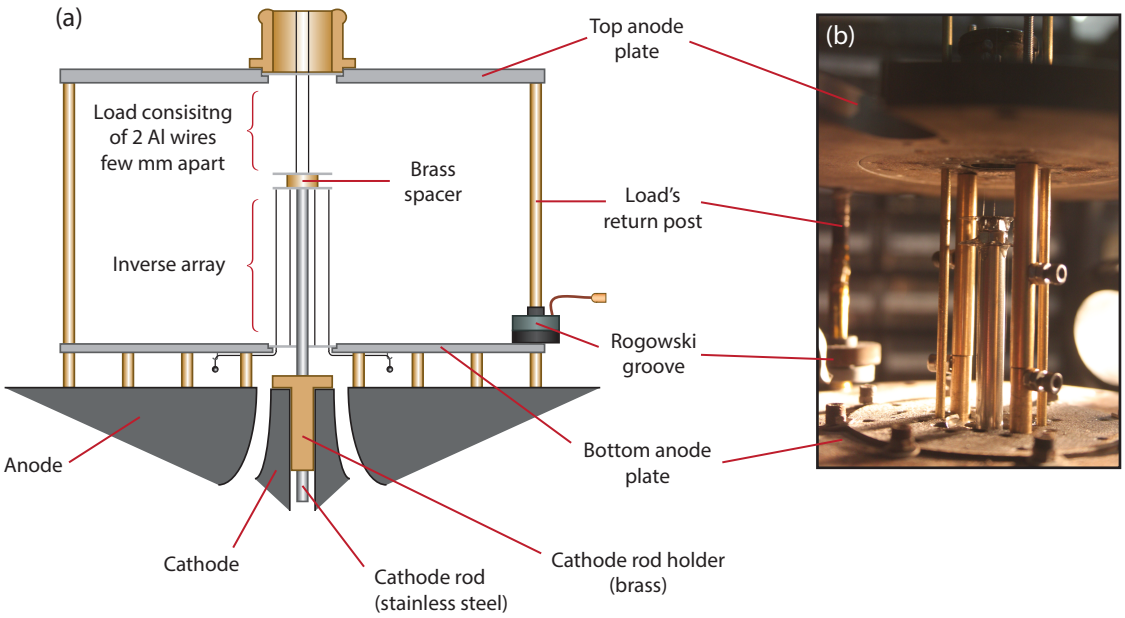

Figure 5.1: A schematic diagram and a photo of a 2-stage Z-pinch array setup with a load consisting of 2 Al wires few millimetres apart.

2D density analysis during the preconditioning phase

At the start of the current pulse, a prepulse into the load section has been observed from dI/dt measurements from the Rogowski groove. As in the previous experiments, this prepulse managed to heat the wires beyond boiling point. This is evident from laser interferometric image taken at 156ns (Figure 5.2) which shows the solid wires have expanded into columns of mainly neutral gas.

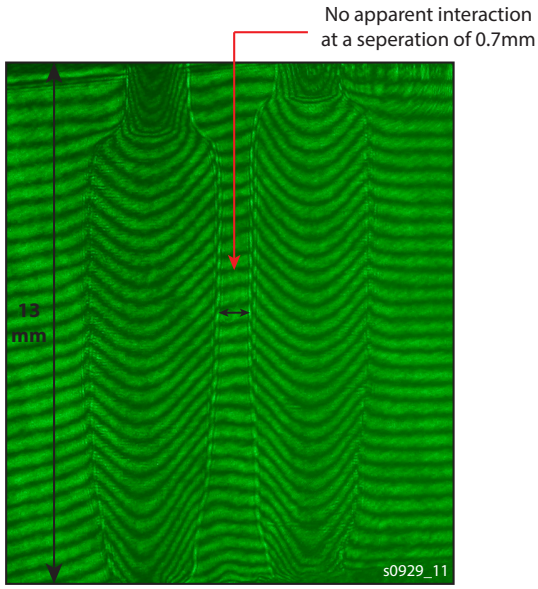

Figure 5.2: Laser (λ=532nm) interferometric image at 156ns of a linear array consisting of 2×30μm Al wires 4mm apart.

The interference patterns around and within the wire are very similar to previous experiments of cylindrical array and single wire loads (Chapter 3 & 4), where the fringe-shift around the wire boundaries are in opposite direction (due to the presence of plasma) to the main neutral bulk of the preconditioned wire. In between the wires, the separation varies in the axial direction, reaching a minimum of ~ 0.7mm. The fringe position between the 2 wires appear to be unchanged when compared to the background/reference image, which could suggest a very little presence of particles in this region. To quantitatively analyse the number of particles in this region, we have traced the fringe lines in Figure 5.2 an its corresponding reference image, then used a linear 2D interpolation code (MAGIC) in MATLAB to generate a 2D fringe-shift map along with an averaged line-out at the central axial region 6-8mm (Figure 5.3).

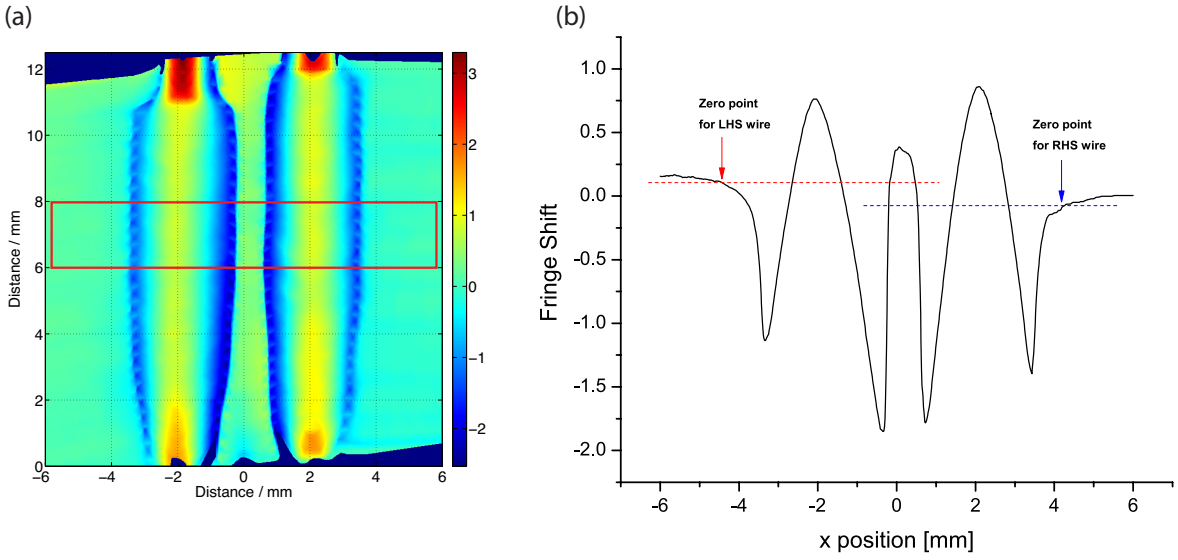

Figure 5.3: (a) A 2D fringe-shift map and (b) an averaged line-out between the axial position 6-8mm (specified by the region in the red box in (a)) taken at 156ns for a load consisting of 2×30μm Al wires 4mm apart.

The 2D fringe-shift map in Figure 5.3(a), looks more or less the same when compared to other similar experiments involving a cylindrical array load or a single wire load. Where plasma (negative fringe-shift) dominates the edges while neutrals (positive fringe-shift) dominate the central region of each preconditioned wire. We also notice that along the length of the load in the gap between the wires there are yellow patches corresponding to a +1 fringe-shift suggesting that there some

neutral atoms present in this region. As mentioned in previous chapter, we will ignore the regions close to the electrode and focus our analysis at the central axial region (those end-effect can be mitigated by modifying the shape of the electrodes). Hence we have taken line-outs every 0.5mm in the axial region 6-8mm (red box in Figure 5.3(a)). Those line-outs did not vary much and therefore an averaged line-out in this region was computed which is presented in Figure 5.3(b).

The overall shape of the averaged line-out looks similar to other preconditioned wires investigated in earlier chapter. If we compare this plot to the one obtained for a 2×30μm 16mm diameter cylindrical array load (Chapter 3, Section 3.1.3, Figure 3.11(b)), we notice that the negative fringe-shift peaks on the edges are higher (more plasma) while the positive central peak is lower for the linear array plot (Figure 5.3(b)). This is because the linear array (x,z) plane was not aligned with the cathode axis. The notched disc used to create linear array is originally designed for square arrays. Which means the linear arrays we have created by using only one side of this disc is offset from the cathode axis by ~ 10mm. Hence the current will take the path through the outer edges of the preconditioned wire in order to minimise inductance.

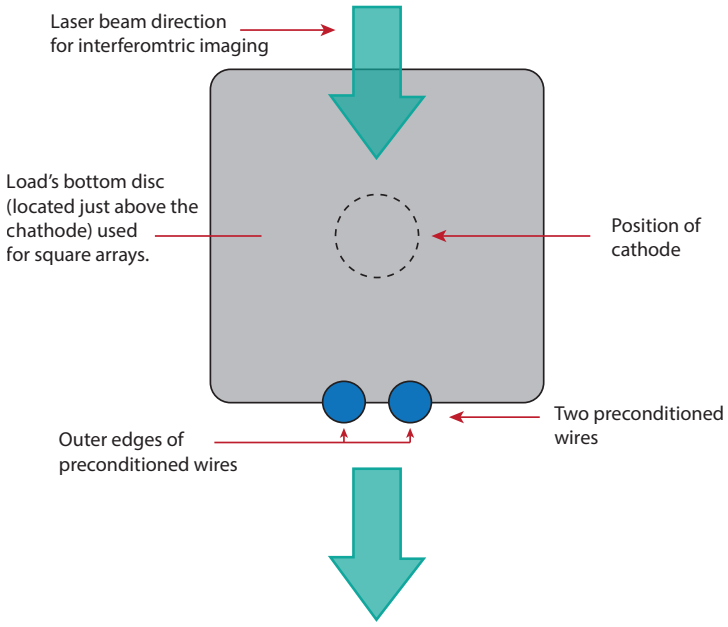

Figure 5.4: Top-view schematic diagram of 2 preconditioned wires supported by a square disc at the cathode. Green arrow shows the direction of the laser beam for the interferometric image in Figure 5.2.

The interferogram images are taken face-on (Figure 5.4) with the outer edge being at the centre of each wire hence a lower fringe-shift central peak observed. This also explains why the difference between the negative fringe-shift peaks on the left and right side for each wire is not as large as the cylindrical 2×30μm array. We note that in the linear array fringe-shift plot, we see ~ 30-60% more plasma on the edges closer to the gap. If we assume a constant current azimuthally, then those edges will possess a magnetic field which is ~ 68% lower than their counterpart edge for a gap = 0.7mm.

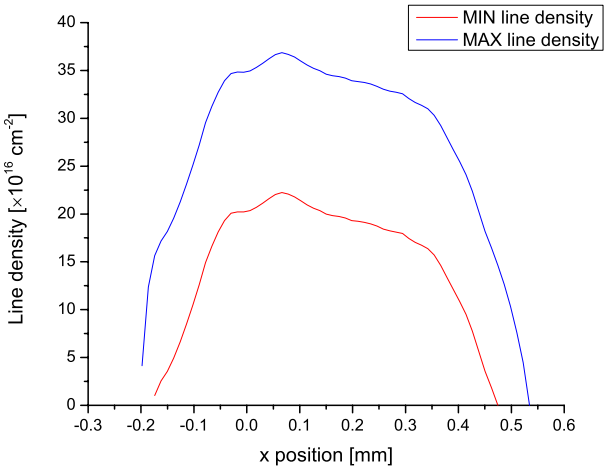

Figure 5.5: Minimum and maximum atom number line density in-between the preconditioned wires at 156ns for a load consisting of 2×30μm Al wires 4mm apart.

In order to measure the particle line density in the gap, we had to set a zero-reference line in Figure 5.3(b). The position of this zero line is not consistent when when we set it from the left side and right side of the plot (red and blue dashed line respectively). This is due to the fact that the fringes are very sensitive to the mirror positions and angle, and tends to move slightly between the time the reference and shot images are taken (~ 20 mins). By having two zero-reference lines, we have plotted the minimum and maximum atom number line density in the gap (Figure 5.5). Those plots show that there is a modest increase in particle line density inside the gap. We have calculated the minimum and maximum total number of atoms per length in the gap to be 1.01×10^{16} cm^{-1} and 2.04×10^{16} cm^{-1} respectively. This corresponds to 1.2 - 2.4% of the total number of atoms per

length in the load. This is a small percentage and therefore to form a shell the expanding wires need to physically merge before the switching time.

To create a shell using a cylindrical wire array with small inter-wire separation, while keeping the array mass at a minimum value, we need to reduce the diameter. The minimum size of notched-discs available were 8mm in diameter, any smaller than this and it will be very difficult to assemble wires on it and a radius smaller than 4mm would be to short to diagnose and assess the implosion trajectory or the formation of instabilities. Therefore, to attempt to create a shell we have chosen our cylindrical array to be of 8mm diameter.

The preconditioning of an 8mm diameter array consisting of 16×10μm Al wires was investigated in Chapter 3. At 168ns, the wires have expanded to ~ 1.6±0.4mm. By taking the lower limit of this estimated value, we see that wires did not manage to merge (a gap of ~ 0.4mm was present between the wires at this time). However if we assume the wires maintain the same linear expansion (~ 7.5μm/ns), then the edges would have merged before the current switch (~265ns). To be assured a shell has formed before the current switch, we have two options; either we increase the wire number from 16 to 32 (hence halving the inter-wire separation) or we increase the wire thickness from 10 to 15um (as seen in Chapter 3, thicker wires expand to larger diameters). The latter is more preferable as it is easier and less time consuming to assemble fewer thicker wires than a large number of thinner (more delicate) wires. In both cases we will roughly double the mass per length of the load above the limits investigated in this thesis so far.

Before attempting to build a cylindrical wire array of a small diameter (which is highly time consuming), we will first investigate a linear array of wires arranged to create a similar inter-wire spacing when assembled in a cylindrical geometry of 8mm diameter. As been explained earlier, those linear arrays allow a better assessment of the merging of wires before the switch - as there are no overlapping wires - from side-on interferometric images. We will first begin investigating a linear array with an inter-wire spacing equivalent to a cylindrical 16×15μm wire array.

5.1.2 A linear array equivalent to a cylindrical 16×15μm

Experimental setup

The inter-wire spacing in an 8mm cylindrical array of 16 wires is 1.57mm. To create a linear array of the same inter-wire spacing on a square disc we have assembled 7×15μm Al wires on one side of the disc, making use of the whole length of the notched square side (10mm). We have assembled the maximum possible number of wires in order to have a load mass per length closer to the equivalent cylindrical array (16×15μm). The rest of the array setup was identical to the previous experiment of a 2 wire linear array (Figure 5.1).

Density analysis at the preconditioning phase

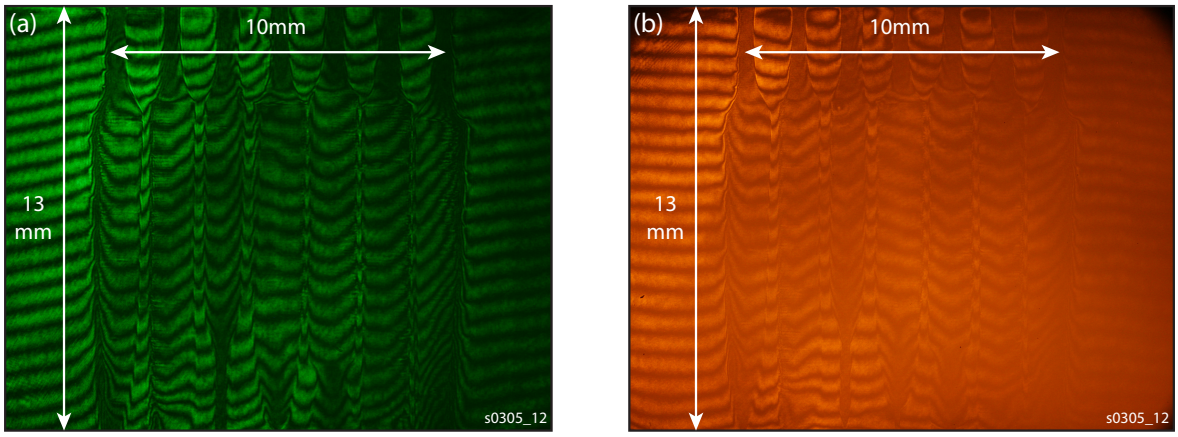

Figure 5.6: (a) Green (λ=532nm) and (b) blue (λ=355nm) laser interferometric images of a 7×15μm Al wire linear array before the current switch at 228ns.

Laser interferometric images (Figure 5.6) taken before the current switch at 228ns clearly show that the wires did *precondition*. Focusing around the central region, away from the end effects we see that the wires did not merge. The gap between the wires varies from a maximum of 0.4mm to a minimum of 0.1mm. The wires closer to the centre (x=0) possess a similar interferometric pattern observed in previous experiments, which is the presence of some plasma around the wire edges while the neutral dominates the bulk of the wire. However the fringes at the outer edges of the first and last wire (at x = ±5mm) shows a sharp rise in plasma which then gradually falls down as we move into the wire towards the other edge (due to the presence of neutrals). The neutral peak is not clear within those two wires

when compared to the central wires due to the high presence of plasma around the outermost edges. To differentiate the free electron and atom (ions + neutrals) distribution, we have traced the fringes and obtained an interpolated 2D fringe-shift map of both green and blue laser interferometric image (Figure 5.7(a)&(b)). An averaged fringe-shift line-out (Figure 5.7(c)) was obtained between the axial height 6-8mm (shown as a black box on the 2D fringe-shift map images). The two averaged fringe-shift line-outs were solved simultaneously to obtain the averaged electron and atom line density between the axial height 6-8mm (Figure 5.7(d)).

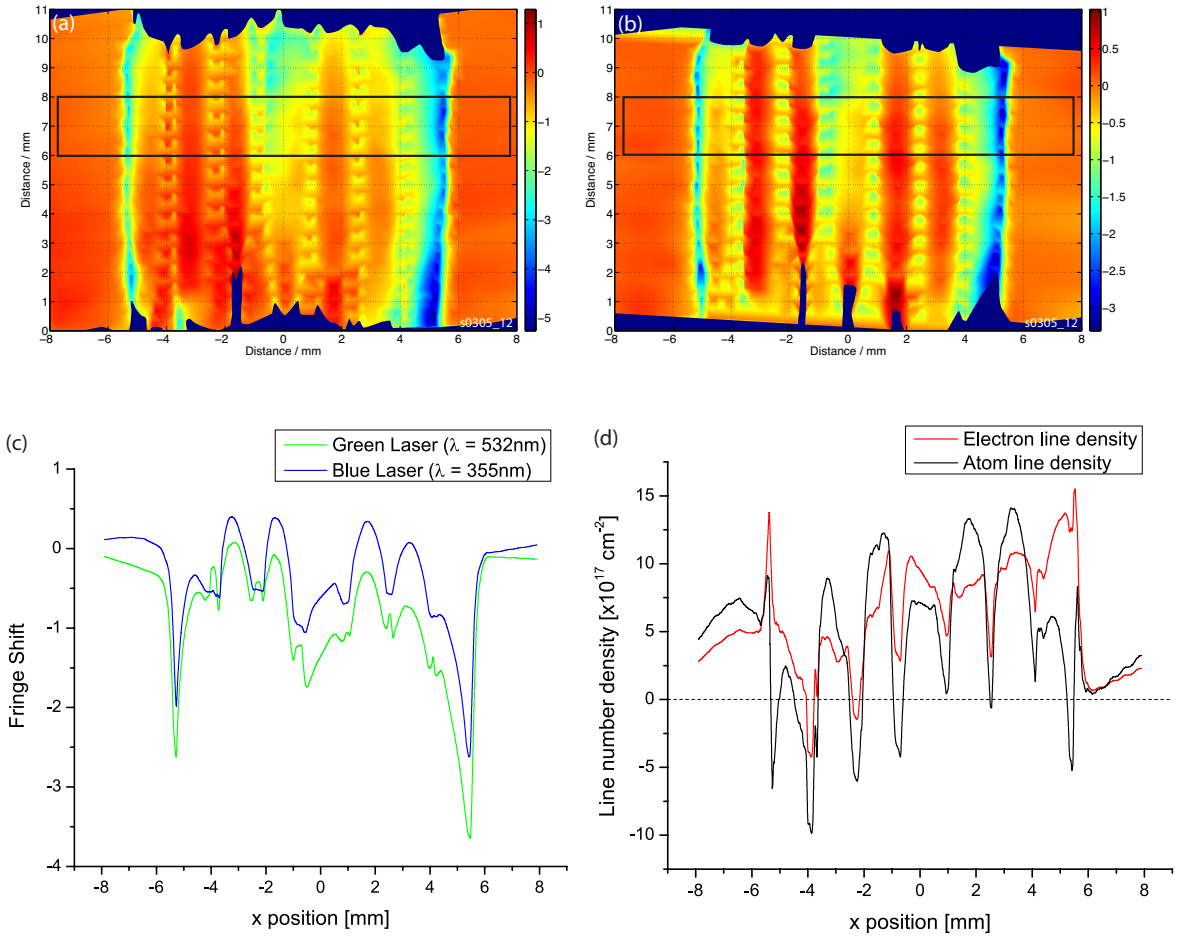

Figure 5.7: 2D fringe-shift maps of a 7×15μm linear array from a (a) green (λ=532nm) and a (b) blue (λ=355nm) laser interferometric image at 228ns. (c) Axially averaged fringe-shift line-out between the height 6-8mm (black box in (a)&(b)). (d) Electron and atom number line density obtained by simultaneously solving the green and blue fringe-shift plots in (c).

The 2D fringe-shift map clearly shows the high presence of plasma (negative fringe-shift) on the outermost edges of the first and last wire, while the rest of the wires show a modest positive fringe-shift between 0-0.5. In both 2D map images

(green and blue) we see what appears to be a stream of plasma at varying axial positions between adjacent wires. This pattern is not real, it is an effect from the interpolation method used by the MATLAB program.

The averaged fringe-shift line-outs (Figure 5.7(c)) shows a large negative peak on both sides of the preconditioned linear array. This peak reaches a value of -2.0 and -2.6 for the blue and green laser respectively on the LHS of the plot, and a value of -2.6 and -3.6 for the blue and green laser respectively on the RHS of the plot. This variation is expected as electromagnetic waves of lower wavelengths are less sensitive to free electrons in a plasma. Due to the high presence of plasma around the two edge wires, the neutral (positive) peak cannot be easily identified. However we can clearly see the peaks caused by neutral atoms for the rest of the wires in between (excluding the central wire) in both the green and blue fringe shift line-outs. The blue peaks are higher than the green since electromagnetic waves of lower wavelengths are more sensitive to bound electrons in atoms.

In the LHS region of the plot (between x=-6mm to x=0mm) we see that in between the neutral peaks at a position of x=-4 and -2mm, the value of the green fringe-shift is larger than the blue. Theoretically this is not possible and most likely this is due to the fact that the size of the fringe thickness in the interferometric image (Figure 5.6) is comparable to the fringe-shift value, generating a large error when tracing the fringe.

The green fringe-shift line-out is mainly in the negative region and the wire neutral peaks barely reaches zero. Comparing this to the 2 central wires in a cylindrical 8×15μm array (Chapter 3, Section 3.1.3, Figure 3.11(d)) we clearly see that the effect of plasma in a linear array is much larger than that of a cylindrical array. That is because a load in this arrangement has a lower inductance allowing for a greater portion of the current to flow through.

The line density plots (Figure 5.7(d)) shows a large electron density on the edges of the array as expected from a large negative fringe shift, reaching a peak of ~ 15×10^{17} cm^{-2}. A significant part of the atom line density plot between x=0mm to

x=-6mm lies in the negative region which is not real and that is due to an error in fringe-shift values as explained earlier, hence generating the wrong fringe-shift difference between the blue and green. Therefore we will ignore the LHS of this plot. Between x=0mm to x=5mm, both the electron and atom line density plot are in the positive region. The electron line density is maximum at the central region of each wire due to the lower inductance path of current at those positions. Focusing our analysis on the two adjacent wires at x=1.8 and 3.3mm, we see that around the edges the electron line density closely matches the atom line density for a skin thickness of ~ 0.2mm, suggesting an ionisation of Z=1. In between the wires the atom line density falls down to nearly zero however the electron density maintains a value which is ~ 3-4 times larger suggesting a higher degree of ionisation in between the wires. Around the atom line density peak the electron density maintains a roughly constant value which is ~ 0.6-0.7 of the atom peak value, suggesting a significant bulk of the wire has been ionised.

We see that the wires have just begun to merge at 228ns. The atom line density shows the edges of the two wires barley 'touch' at x=2.5mm. This plot was taken ~ 50ns before the switch, which means a further 50ns of expansion and merging before the current switch. We can conclude that a cylindrical array consisting of 16×15μm Al wires will merge before the current switch time.

5.2 Formation of a cylindrical 'shell'

5.2.1 Experimental setup

The hardware setup for a 2-stage wire array Z-pinch is kept the same as in previous experiments and is similar to Figure 5.1, including the inverse array properties and the length of the load (15mm). However the load section notched discs were changed to support wires in a cylindrical geometry of an 8mm diameter. We have formed a cylindrical plasma 'shell' by preconditioning a load array of 16×10μm and 16×15μm Al wires. We have seen in the previous section that wires of such arrays would merge before the current switch.

5.2.2 Initial current prepulse

At the the start of the current pulse, resistive division triggers a current prepulse into the the load section. The preconditioning effect of the prepulse has been observed for the 16×10μm array (Chapter 3, Section 3.1.3), however the prepulse data for such an array was missing in our experiment due to a faulty Rogowski groove. For this reason we have used the prepulse data of a 2×30μm array (Chapter 3, Section 3.1.2) - which contains the same mass per length as a 16×10μm array - to compare it with the 16×15μm array which contains double the mass per length. Figure 5.8 shows the current data and calculated temperature for both arrays during the prepulse phase.

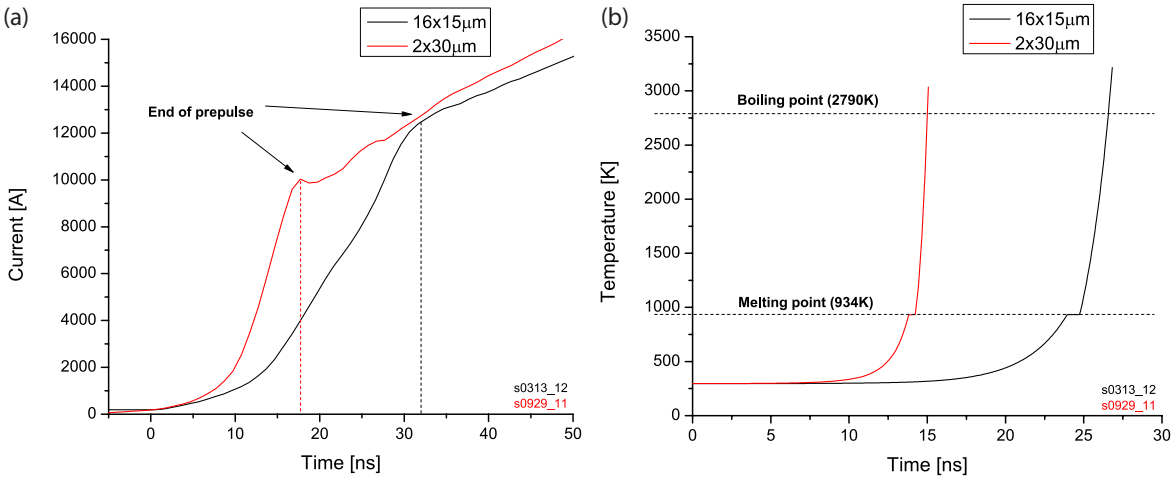

Figure 5.8: (a) Current and (b) temperature variation of a 2×30μm and 16×15μm Al wire array load at the early stage of the experiment.

From the above figure we clearly see that a prepulse current has gone through the 16×15μm array, reaching a peak value of ~ 12kA in ~ 32ns. The average wire temperatures reached beyond boiling point before the end of the current prepulse, a strong indication the wires will be in a gaseous *preconditioned* state as in previous experiments. We have seen in Chapter 4 that the 'change of state' timings did not vary with increasing mass per length of the load from 25 to 50μm wire (Section 4.2, Figure 4.3). The reason we see a large variation in Figure 5.8 is to do with the fact that one of the Marx banks fired late in the 16×15μm experiment, and therefore the whole experiment was actually driven by current from only 3 banks, hence a slower current prepulse.

5.2.3 2D density analysis of 'shell' before current switch

Interferometric images taken after the current prepulse and before the current switch from green and blue (λ = 532 & 355nm) laser in Figure 5.9 clearly shows preconditioned wires for both 16×10μm and 16×15μm array. Ignoring the electrode end-effects and focusing around the central axial region, fringe-shift increases and decrease in a 'wave-like' pattern as we move across the array, with peaks correspond to the maximum neutral line density at the original wire position. The 'wave-like' pattern and hence the absence of gaps between the wires does not necessarily mean that wires have merged. This is the overlapping effect of front and back wires not being perfectly aligned. By zooming at the outer edges of the 'shell' we see a downward shift in fringes due to the presence of plasma.

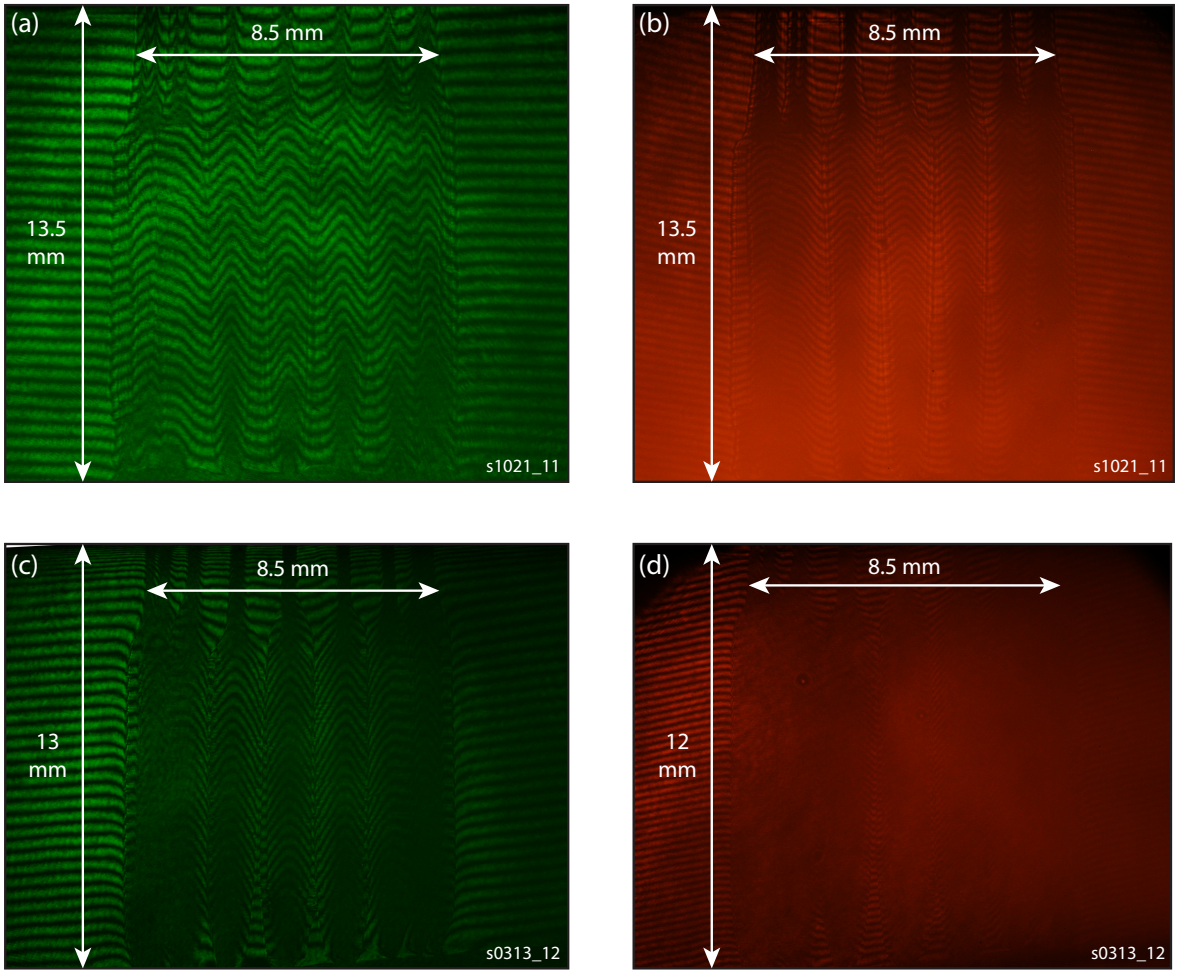

Figure 5.9: Laser interferometric images of a cylindrical Al wire array of (a,b) 16×10μm at 168ns [~100ns before the switch] and (c,d) 16×15μm at 247ns [~25ns before the switch]. Images (a & c) are taken with the green laser (λ=532nm) and images (b & d) are taken with the blue laser (λ=355nm).

Fringes can be seen all the way across the 16×10μm array in both green and blue image. The fringes in the green laser image gets fainter when the wire thickness is increased from 10 to 15μm (Figure 5.9(a)&(c)). This is expected as we have doubled the number of particles over the same image area. By adjusting the brightness and contrast of this image (Figure 5.9(c)) using Adobe Photoshop we have managed to fringe trace the central region. However the blue interferometric image for the 16×15μm array was completely dark with no visible fringes in the area were wires have expanded. The interpolated 2D fringe-shift map was generated for interferometric images with traceable fringes (i.e Figure 5.9(a), (b)&(c)). Figure 5.10 shows the 2D fringe-shift map for a 16×10μm array along with horizontal line-outs in the region specified by the black box.

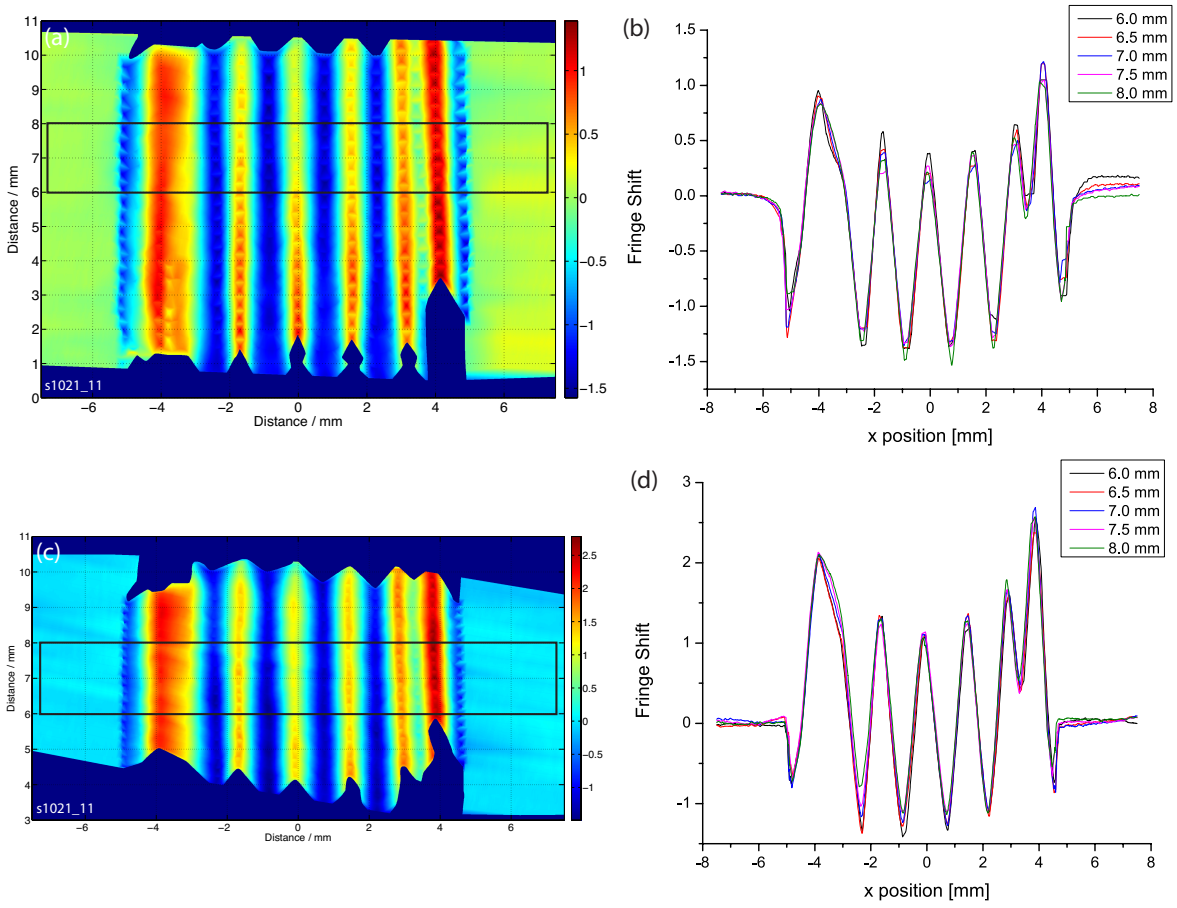

Figure 5.10: 2D fringe-shift maps for a 16×10μm Al wire array at 168ns from a (a) green λ=532nm and (c) blue λ=355nm laser along with fringe-shift line-outs (b) and (d) respectively between the axial height 6-8mm (the region inside the black box in the 2D maps).

From the 2D maps of both green and blue laser we clearly see positive fringe shifts (red) at the initial wire position caused by neutrals, while a negative shift (blue) is observed in between the preconditioned wires and at the outer edges of the array suggesting the presence of plasma. We have taken horizontal line-outs (Figure 5.10(b)&(d)) every 0.5mm between the axial height 6-8mm from the both 2D maps. The line-outs indicate that the outer plasma around each wire have most likely merged as we do not observe a zero fringe-shift in between the wires. The outer peaks are greater than the inner ones as they contain 3 preconditioned wires instead of 2.

If we compare the line-outs from the green laser (Figure 5.10(b)) to the ones presented in Chapter 3 Section 3.1.3 (Figure 3.11(h)) which has been taken from the same experiment at the same time (168ns) but from a different camera and viewing angle, we do not observe the large negative fringe-shifts around the array edges and in between the wires, and the fringe-shift peaks are roughly twice as large. The optical system and camera used for Figure 5.10 generated interferometric images with a better focus and resolution around the load section, and hence a more accurate fringe trace around the wire edges. Therefore, the most likely reason for this large difference is an error in fringe tracing of the interferometric image in Chapter 3. This is reflected by the over-estimated value of the experimentally calculated total number of particle from the plot in Figure 3.11(h).

We observe a minimal variation in fringe-shift pattern within the specified axial region. This could be seen around the peaks and troughs of the plots and it is not correlated to the change in axial height. This suggests that those variations are caused by the interpolation method used and therefore an averaged fringe-shift line-out is obtained within this axial region (6-8mm). Figure 5.11(a) shows the averaged fringe-shift line-out of both green and blue laser between the axial height 6-8mm. Those two plots were solved simultaneously to obtain the averaged electron and atom line density in this axial region (Figure 5.11(b)).

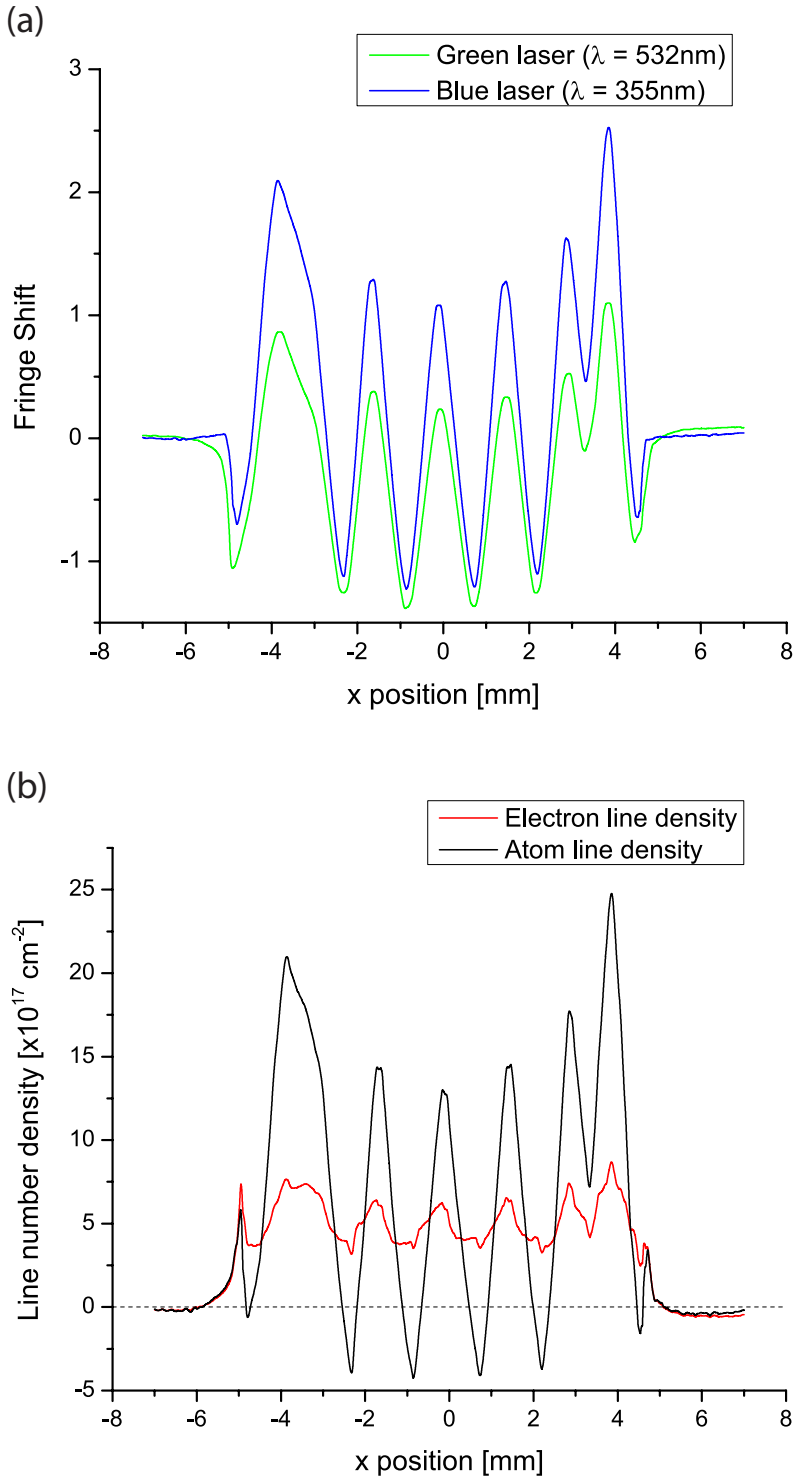

Figure 5.11: (a) Averaged fringe-shift line-out from the blue and green laser between the axial region 6-8mm from the cathode, and (b) the averaged electron and atom line density obtained by simultaneously solving the two fringe-shift plots in (a) for a 16×10μm Al wire array at 168ns.

The averaged fringe-shift plot of the blue laser sits nicely above the green plot possessing higher positive peaks caused by neutrals (at original wire positions) and a lower magnitude of negative troughs caused by plasma (in between wires), which

is expected from a lower wavelength laser. The electron line density in Figure 5.11(b) shows a clear merging of the outer plasma in each wire, reaching a maximum of ~ 8×10^{17} cm^{-2} and a minimum of ~ 3×10^{17} cm^{-2}. The electron density maximum and minimum peaks are aligned with the atom density maximum and minimum peaks. On the outer edges of the plot, the increase in electron density closely matches the increase in atom line density reaching roughly the same peaks which strongly suggests that the outer plasma is singly ionised. Looking at the atom line density, we see that some portion lies in the negative region which again is not real and we will ignore it. Just considering the positive part of the atom distribution, we see that there are gaps of ~ 0.5mm in between the edges of the preconditioned wires. The wires have expanded to ~ 1.1mm in 150ns after the prepulse, which corresponds to an average expansion velocity of 7.3μm/ns. The interferometric image in Figure 5.9 was taken ~ 100ns before the current switch time. Therefore, assuming the wires maintain the same expansion velocity, a further 0.73mm increase in diameter is expected for each wire at the current switch time, closing the gaps between them.

By integrating the electron and atom line density plot we have managed to estimate the total number of electrons and atoms per length to be 5.08×10^{17} cm^{-2} and 7.99×10^{17} cm^{-2} respectively. The latter is only 5% greater than the actual total number of atoms per length in the solid wires. The ratio of the total number of electrons to atom suggests that at this stage of the experiment ~ 60% of the load array mass is in a plasma state.

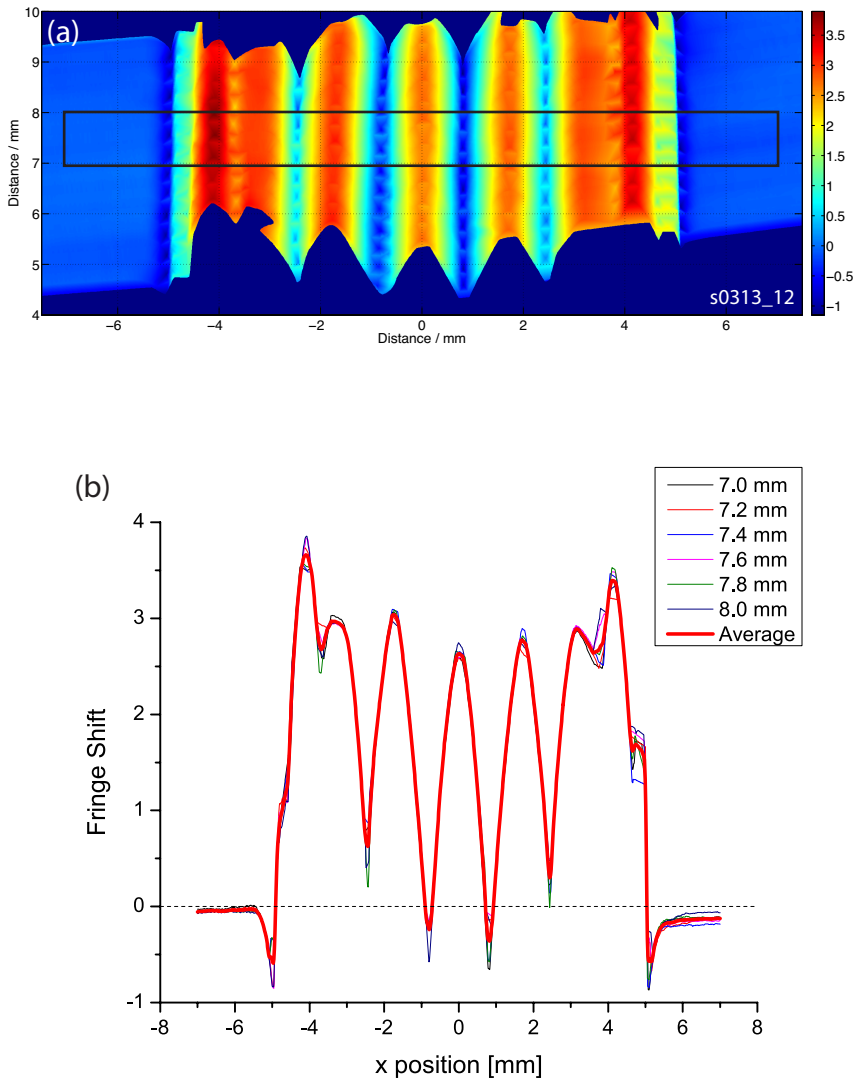

Figure 5.12: (a) 2D fringe-shift map from the green (λ=532nm) interferometric image along with (b) line-outs between the axial positions 7-8mm (as shown by the black box) for a 16×15μm wire array at 247ns.

The same pattern is observed in the 2D fringe-shift map for a 16×15μm array (Figure 5.12(a)) were positive shifts caused by neutrals are seen at the centre of each wire while plasma - negative shifts - occupy the space in between. However the positive shifts occupy a much larger space than the 16×10μm array (more red), reducing the extent of plasma in between. This is simply to do with the fact that we have doubled the total number of atoms per length in this array and it is taken at later time where the wires have expanded further into the gaps.

Figure 5.12(b) shows the axially averaged fringe-shift line-out between the height 7-8mm from the cathode. The effect of plasma is clearly seen on the outer sides of

the array with fringe-shifts reaching a minimum of ~ -0.6 corresponding to a plasma line density of ~ 2.5×10^{17} cm^{-2}. The bulk of the preconditioned wires is dominated by positive fringe-shifts reaching peaks of ~ 3 fringe-shift. Some plasma is observed in between the central wires (x=0) reaching an average of ~ -0.25. The array outer edges contain more plasma since it is the least inductive root for the current than the edges in between the wires. This has been observed in the previous density analysis of a 16×10μm array, were the electron line density is at a minimum in between the wires.

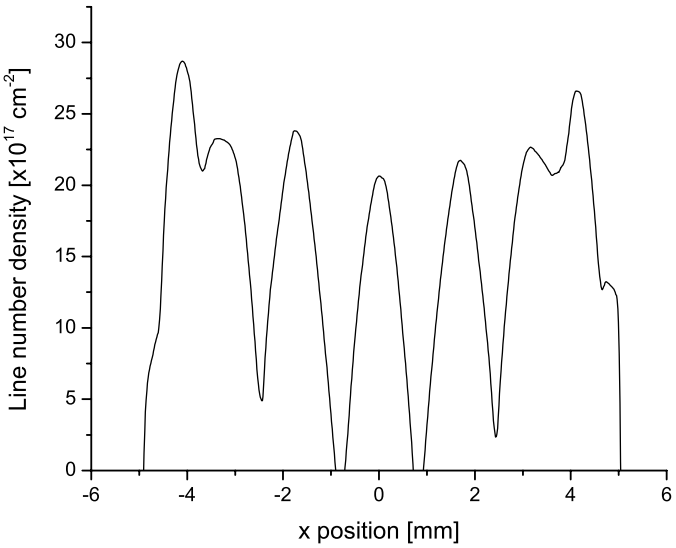

Figure 5.13: The averaged neutral line density between the axial height 7-8mm of a 16×15μm Al wire array at 247ns.

Since we were not been able to fringe trace the blue image of a 16×15μm array and hence remove the effect of plasma by simultaneously solving the two wavelengths fringe-shift data. We have assumed that all positive fringe-shifts in Figure 5.12 is caused by neutrals, and therefore multiplying this by the appropriate constants we have plotted the neutral line density for this array in Figure 5.13. On the outer sides, the neural density reaches its maximum peak of ~ 27.5×10^{17} cm^{-2} as this region contains 3 overlapping compared to the lower peaks around the centre of the array which contain 2 wires each. The value of the neutral peaks decrease gradually as we move inwards. This is caused by the fact that those peaks positions at the central region are also the position of the least inductive route for current to take and hence an increase in plasma presence, lowering the positive fringe-shift value. For this reason the calculated total number of atoms per length

by integrating the above plot produces a value which is 7% less than the real value (1.70×10^{18} cm^{-2}).

Focusing at the central peak at x=0, we see that the neutral part of the wires did not yet merge. A gap of ~ 0.2mm exists between adjacent wires. The central wire expanded to a diameter of ~ 1.4mm in 247ns, corresponding to an average expansion velocity of ~ 5.7μm/ns. We note this value is smaller than the 10μm array since this experiment was only prepulsed by current from 3 Marx banks, delivering less energy to the load array at the start of the experiment. The current switch happened 25ns after the interferometric images were taken and therefore even if the wires maintain this expansion velocity, the wires would be 0.06mm shy of merging. However this is such a small number below our error limits, and this gaps will soon close at the start of the implosion.

5.3 Implosion dynamics of 'shell' after current switch

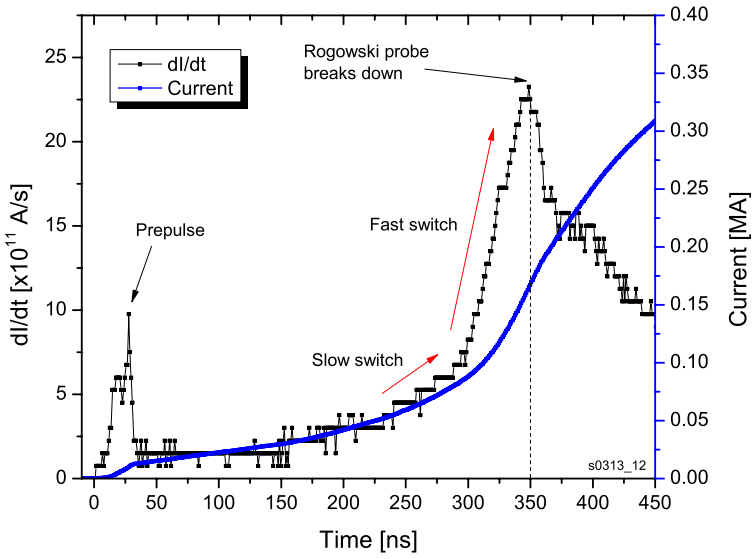

Figure 5.14: dI/dt and current variation with time from a Rogowski groove for a cylindrical array load consisting of 16×15μm Al wire.

During the preconditioning phase the inverse array continuously ablates material radially outwards. Those ablation streams of plasma creates a complicated resistive

current path which increases with time. Before the full explosion of the inverse array, the current slowly switches into the load due to this resistive current path of the inverse array. The fast current switch happens when enough material has been depleted from the inverse array to form gaps along the wires and the array fully explodes. Figure 5.14 shows those two stages of current switch (slow and fast) from a Rogowski groove for a 16×15μm Al wire array load. This fast current switch creates a high voltage at the rogowski groove of the order of ~ 1kV causing the break-down of the groove and the signal gradually decays back to zero.

The implosion dynamics during this fast switch of current into the wire array 'shell' has been captured by images from several diagnostics including an optical streak camera, an optical framing camera and a 4-frame XUV camera. Those images are presented in Figure 5.15 & 5.16 for a 16×10μm wire array.

In all images we see that the plasma implodes towards the centre after the current switch. As discussed earlier in Chapter 3, the formation of gaps along the inverse array triggers the current to flow through the ablated streams of plasma. This causes an explosion of this plasma and also creates an expanding plasma 'bubble' at the top of the inverse array. This can be seen in the image taken at 218ns in Figure 5.16. This bubble reaches the bottom of the load and triggers the current switch which progresses upwards as this bubble expands. At the early stage of the implosion, ~ 30ns after the current switch the array has barely moved inwards, and is at a position of ~ 90-85% of the initial radius. During this time the current heats and ionises the neutral bulk of the 'shell'. After this period we observe an accelerating plasma shell in both optical streak and optical framing image. This acceleration is accompanied by the development of Rayleigh-Taylor instability of a λ ~ 1.5 - 0.7μm, which can be seen in both optical framing and XUV images at 296 and 308ns respectively.

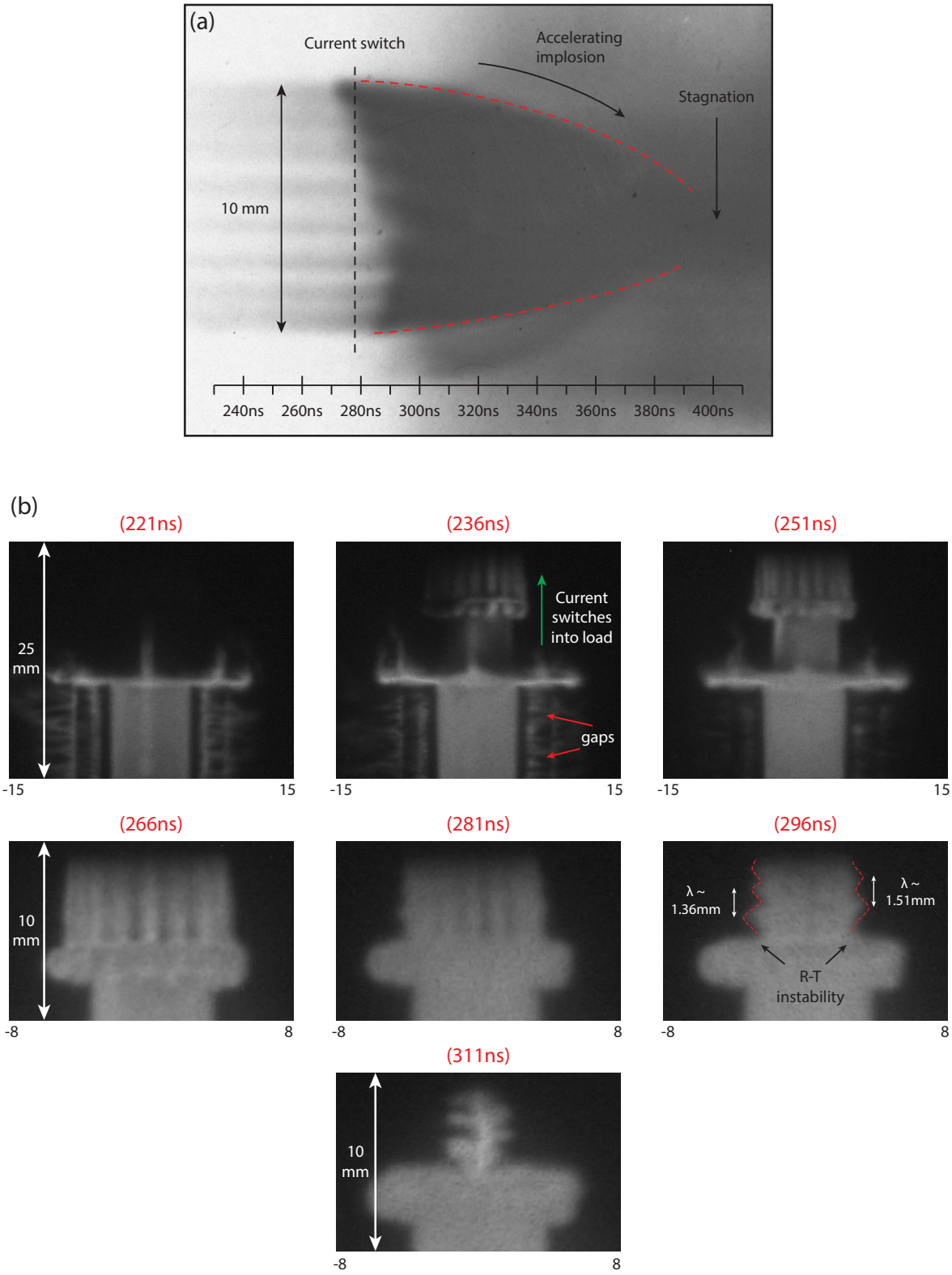

Figure 5.15: Images for a cylindrical array load consisting of 16×10μm Al wires from: (a) optical streak camera showing a radial slice at the centre of the load. (b) Optical framing camera with a 15ns inter-frame timing. All length scales are in mm. All images taken from the experiment s1021_11.

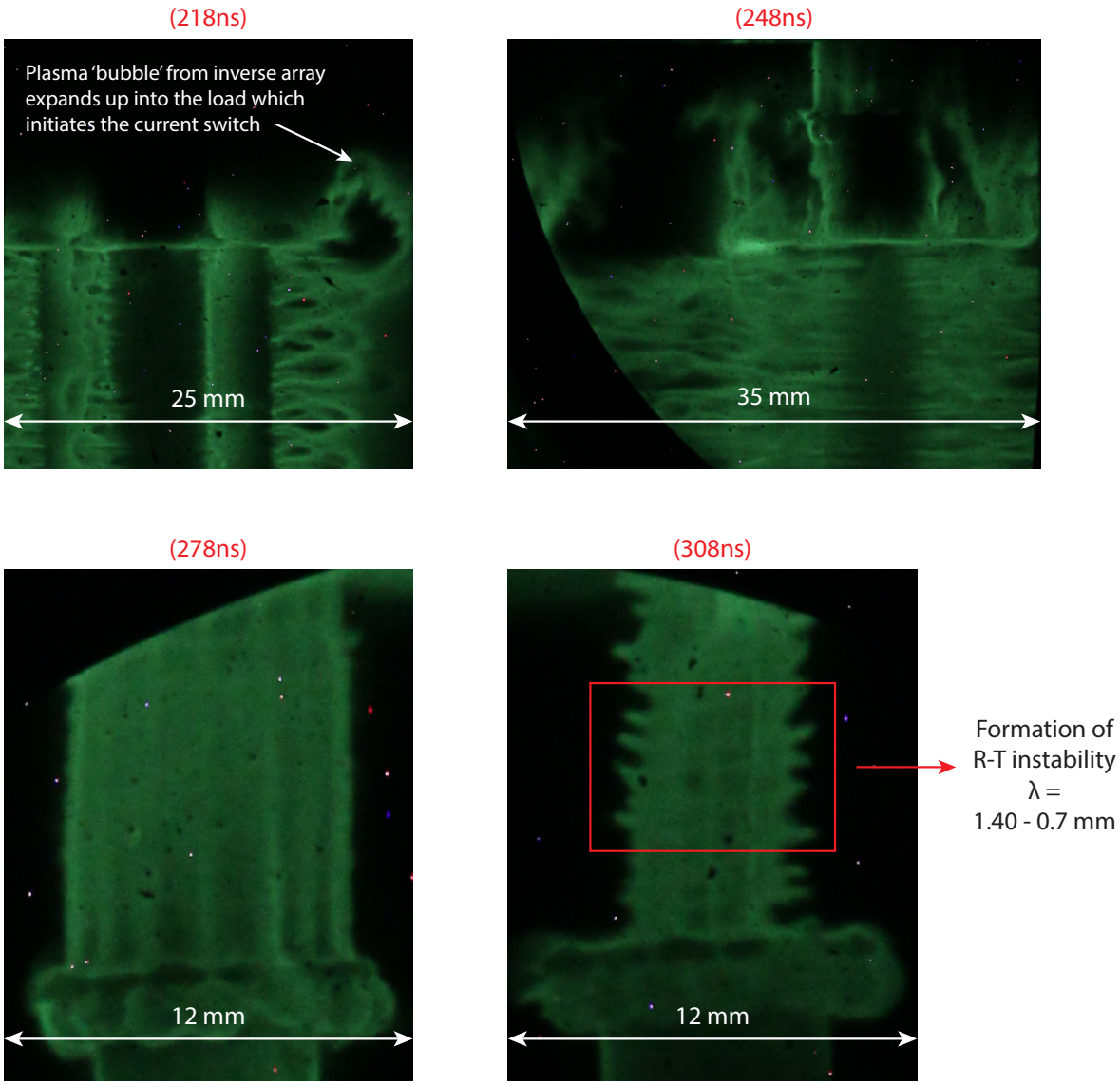

Figure 5.16: Images for a cylindrical array load consisting of 16×10μm Al wires from a 4-frame XUV camera with a 30ns inter-frame timing. All images taken from the same experiment (s1021_11).

We see that there is a timing mismatch of ~ 40ns between the current switch time from the streak and optical framing camera. Such a mismatch has been observed in previous experiments (Chapter 4 Section 4.3.2). Again most probably this is to do with the assumption that time variation along the optical streak image is linear. This timing mismatch is also reflected in the implosion time from both image where the optical streak shows an implosion time of 75-80ns while the optical streak shows an implosion time of ~ 110ns. The implosion trajectories and timings are investigated in detail in the next section.

Implosion dynamic images for a 16×15μm Al wire array is shown Figure 5.17 & 5.18. The optical streak camera was not working for this experiment. We note that the current pulse from the late Marx bank arrived at the load after the current switch time at ~ 275ns, and was in-phase with the rest of the current pulse. However it takes ~ 250ns for this pulse to reach its peak and will not have a significant increase in the total magnitude of current at the load.

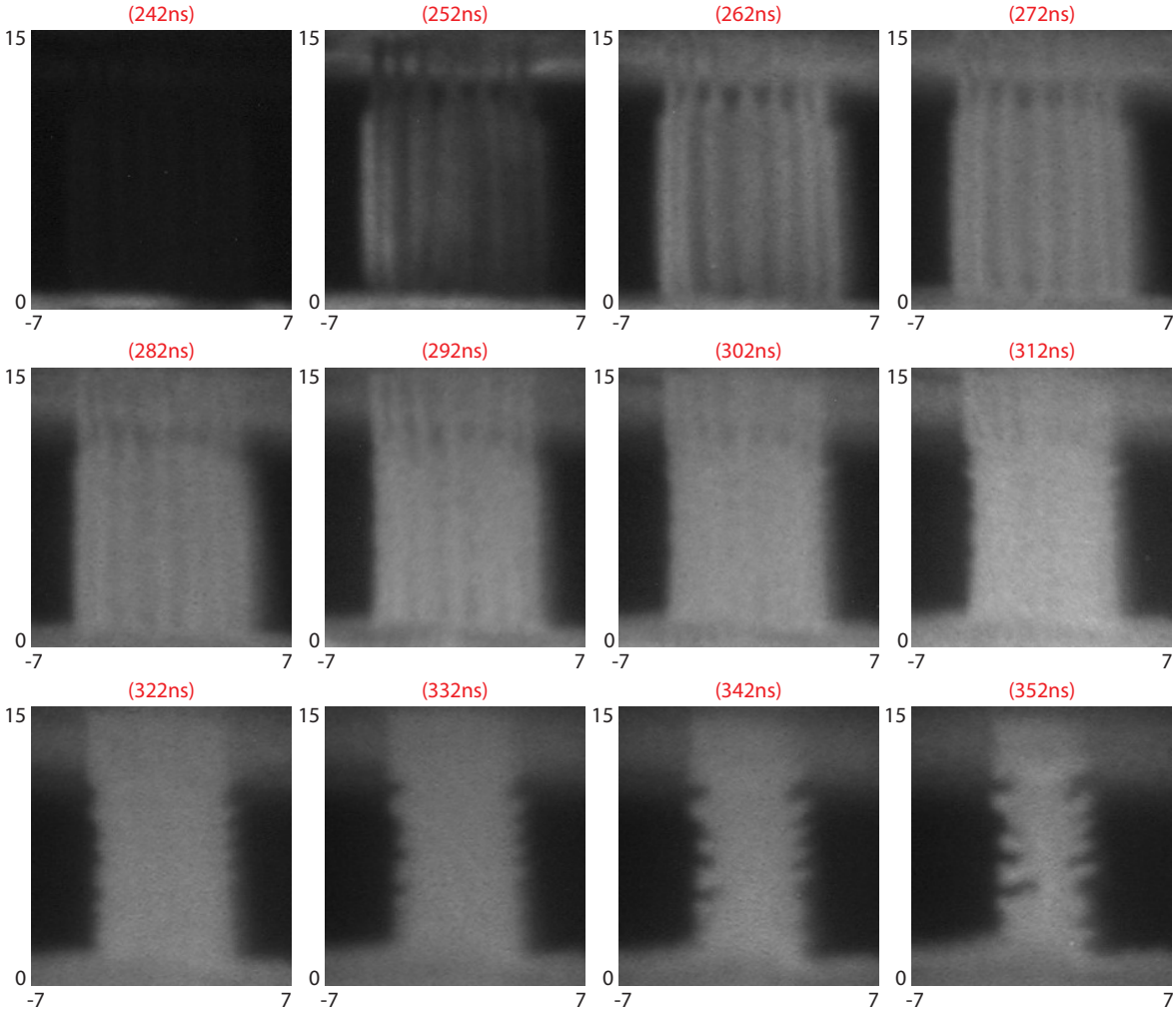

Figure 5.17: Images for a cylindrical array load consisting of 16×15μm Al wires from an optical framing camera with a 10ns inter-frame timing. All length scales are in mm and all images are taken from the same experiment (s0313_12).

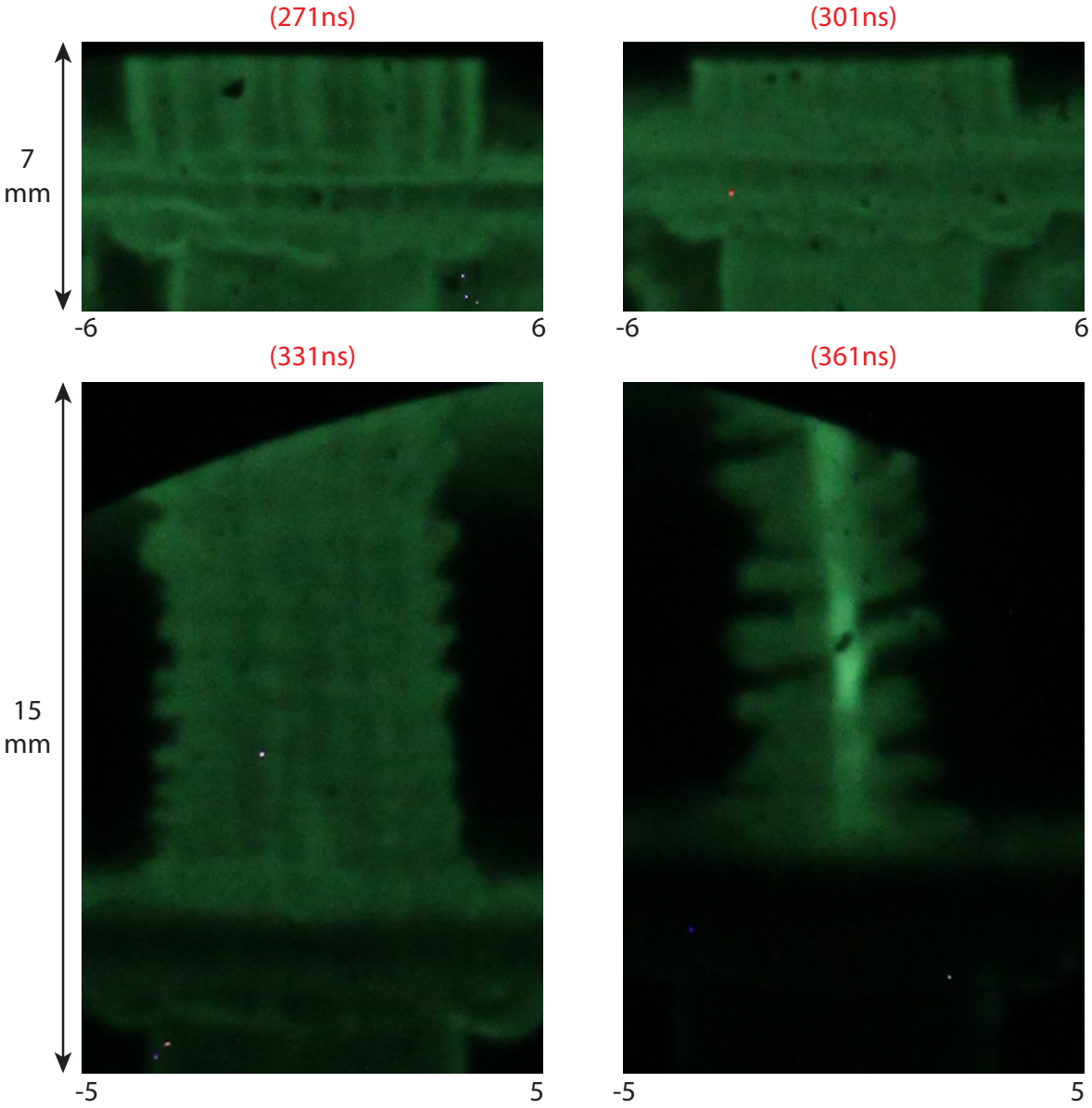

Figure 5.18: Images for a cylindrical array load consisting of 16×15μm Al wires from a 4-frame XUV camera with a 30ns inter-frame timing. All length scales are in mm. All images taken from the same experiment (s0313_12).

Both optical and XUV images clearly shows that the 'shell' formed from a 16×15μm implodes towards the axis. However the implosion appears to be much slower than the 16×10μm array load with an implosion time of ~ 110ns. The first reason is that it contains more than double the mass per length and hence a larger inertia and secondly the implosion is driven by current from 3 Marx banks. Rayleigh-Taylor instability appears as soon as the mass moves radially inwards with a characteristic wavelength λ ~ 1.1 - 1.9μm.

5.3.1 Development of Rayleigh-Taylor instability

As the implosion progresses so does the growth of R-T instability. The theory of R-T instability is explained in Chapter 1 Section 1.4. In this part of the analysis we attempt to estimate the initial perturbations caused by the prepulse current. The initial linear stage of R-T growth can be modelled by Eq(5.1) [15].

$$\xi(t) = \xi_0 \exp(G(t)) \tag{5.1}$$

Where,

$$G(t) = \int_0^t \Gamma(t')\,dt' \tag{5.2}$$

ξ is the amplitude of instability, ξ_0 is the initial perturbation amplitude and Γ is the instability growth rate. Eq(5.2) can be transformed to

$$\frac{G}{\sqrt{kR_0}} = \sqrt{1 - \frac{r}{R_0}} \times F \tag{5.3}$$

where k is the instability wave-vector ($2\pi/\lambda$), r is the radius of implosion, R_0 is the initial radius of the shell at the start of implosion, and F is the form factor which varies between 1.63 and 1.83 and depends on the temporal profile of current [31]. Eq(5.3) shows that G and hence the growth rate weakly depends on the current temporal profile while strongly depends on the radial position of the shell. In the following calculations we have chosen F = 1.7.

From both optical and XUV images of a 16×10μm array in Figure 5.15 & 5.16, the dominant instability has an average $\lambda \sim 1.4$mm. The amplitude of such instability varies slightly along the array length. From the optical framing image at 296ns, r = 2.79mm and ξ = 0.24 - 0.48mm. This corresponds to initial perturbations ξ_0 = 1.0 - 2.2μm. From the XUV image at 308ns, r = 2.45mm and ξ = 0.23 - 0.51mm, corresponding to initial perturbations ξ_0 = 0.7 - 1.5μm. The large variation in ξ_0 between the two independent calculations is most likely due to a variation in the length calibration of their corresponding images and therefore we will take the overlapping range of values of the two calculations. Hence, the initial perturbation

induced by the prepulse current into the 16×10μm wire array is of the order 1.0 - 1.5μm.

The average λ of the dominant instability was also ~ 1.4mm for the 16×15μm array (Figure 5.17 & 5.18). From the optical framing image at 322ns, r = 3.57mm and ξ ~ 0.2mm, corresponding to an initial perturbation ξ_0 = 2.7μm. While the XUV image at 331ns, with r = 3.05mm and ξ ~ 0.2mm resulted in ξ_0 = 1.3μm. To have a better estimate of ξ_0, we have plotted the experimental values of ξ taken from the last 4 images in Figure 5.17 vs the radial convergence (R_0/r), along with theoretical plots calculated for the linear stage of instability development using Eq (5.1 & 5.3) for initial perturbations ξ_0 = 1.3, 2.0 & 2.7μm (Figure 5.19). The experimental values of instability growth lies within the theoretically predicted values with an initial perturbation ξ_0 = 1.3 - 2.0μm.

In both cases the initial perturbation was quite small and undetectable by our imaging diagnostics suggesting a highly uniform plasma at start of implosion.

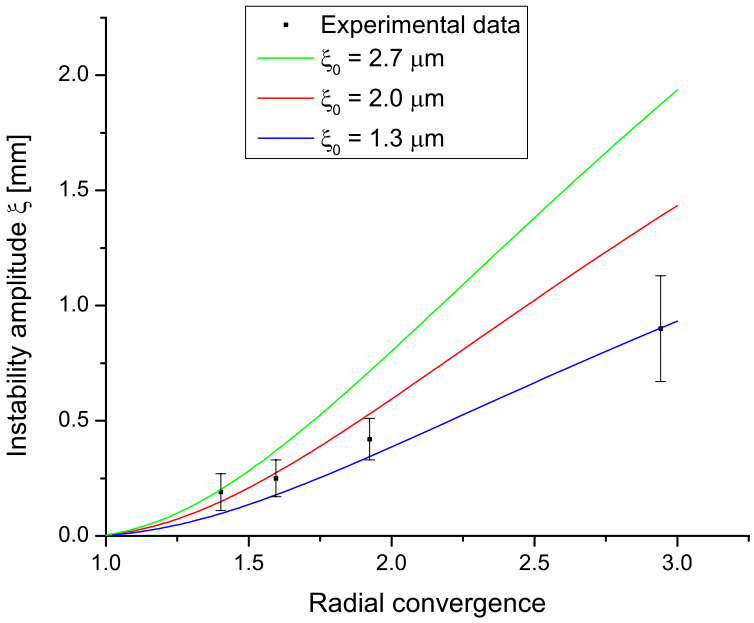

Figure 5.19: Theoretically calculated growth of R-T instability during initial linear stage vs radial convergence for an imploding shell with different initial perturbation ξ_0, along with the experimental values from an optical framing camera for a 16×15μm Al wire array load.

5.3.2 Implosion trajectory

We have produced a radius vs time plot for both 16×10μm and 16×15μm Al wire array loads from the implosion images in Figure 5.15, 5.16, 5.17 & 5.18. Those plots are shown in Figure 5.20. We clearly see the timing mismatch between the optical framing and optical streak images in Figure 5.20(a) for a 16×10μm array. The radial profile of the two XUV images (at 278 and 308ns) closely match the radial trajectory from the optical framing camera within the specified error bars. This agreement between the optical framing and XUV images is further strengthened by the implosion trajectory data of a 16×15μm load array (Figure 5.20(b)). Therefore we will ignore the optical streak data due to an error in time calibration and we will focus our analysis on trajectories from optical framing and XUV images.

The implosion of a 'shell' formed from the lighter array (16×10μm) clearly shows an accelerating plasma towards the axis. Plasma converges from R_0 ~ 5mm to r ~ 0.5mm with an implosion time of 75ns. On the other hand, the implosion of a 'shell' formed from the heavier array (16×15μm) shows a slight acceleration as the mass implodes towards the axis. The plasma converges from R_0 ~ 5mm to r ~ 0.5mm in 110ns. This is 1.5 times longer than the lighter shell, which is a direct consequence of having more mass in the load. In addition to that, the driving current was only from 3 Marx banks. The increase in error bar in both plots as the implosion progresses is a consequence of the increase in R-T instability amplitude.

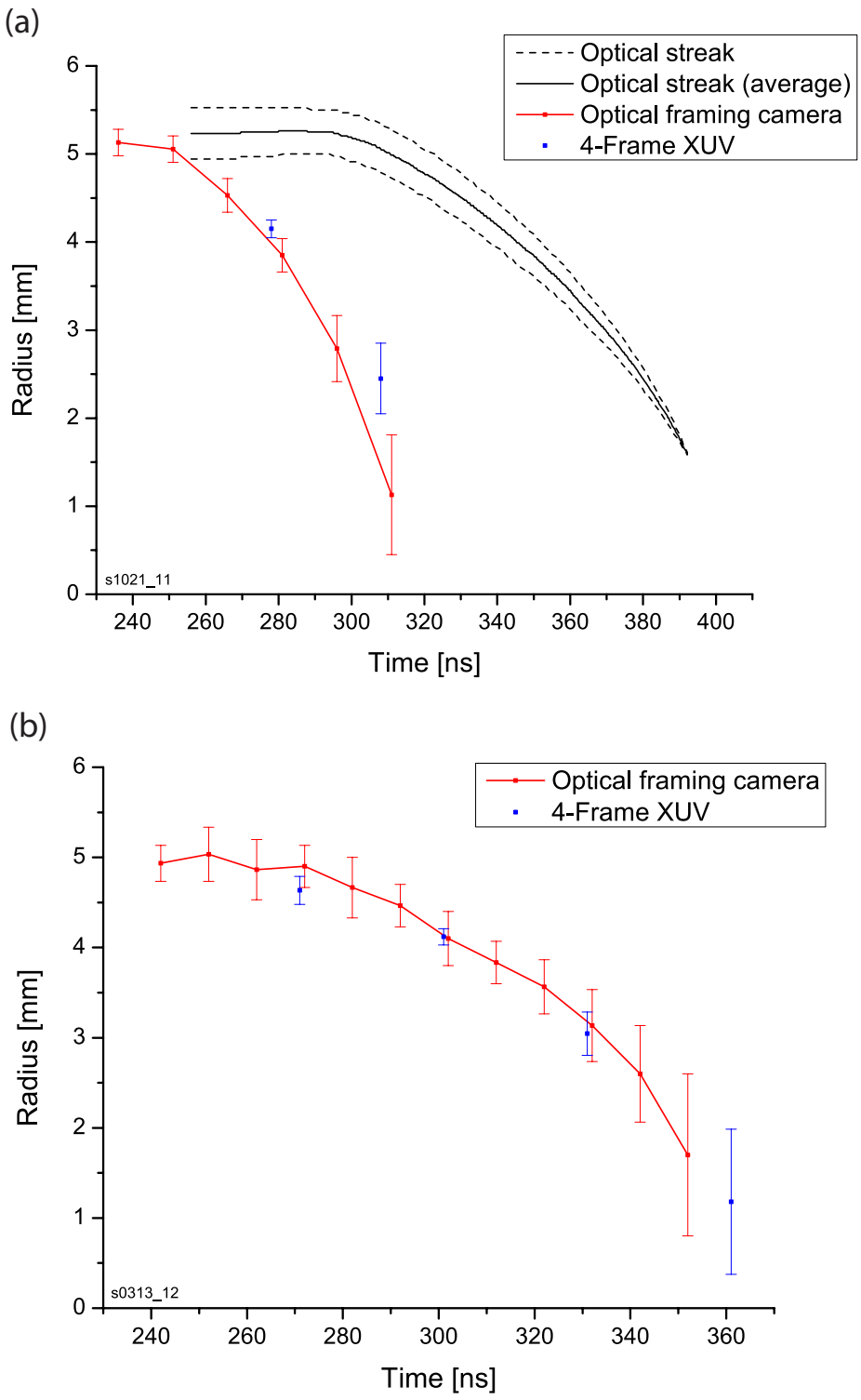

Figure 5.20: Implosion trajectory (radius vs time) plots for a 'shell' formed by preconditioning an Al wire array load of (a) 16×10μm and (b) 16×15μm.

In the simplest possible case, the implosion of a load array consisting of merged preconditioned wires can be modelled as a thin structureless annular shell imploding symmetrically on axis. From Chapter 1 Section 1.3.1, the equation of radial motion for such a system in dimensionless parameters is

$$r\ddot{r} = -\Pi I^2 \tag{5.4}$$

where,

$$\Pi = \frac{\mu_0 I_{\max}^2 \tau^2}{4\pi m_0 r_0^2} \tag{5.5}$$

r is the radial function of time t, I is the current temporal profile, $I_{\max}$ is the peak current at the point of stagnation, τ is the implosion time, m_0 is the total mass per length of the load and r_0 is the initial radius at the start of implosion.

This model can be used to estimate the current temporal profile and I_{max} from the implosion trajectories in Figure 5.20. The solver 'ode45' was used in MATLAB to solve the differential equation Eq(5.4). Figure 5.21 shows the implosion trajectory from the 'thin-shell' model for different current functions along with the experimental data from the optical framing camera in Figure 5.20.

The implosion trajectories from the 'thin-shell' model for both 16×10μm and 16×15μm array predicts that the most probable current temporal profile through the load is a function between a step function of constant current and a square-root function of time, with an Imax value varying between ~ 0.5 - 0.8 MA. We notice a minimal difference in $I_{\max}$ between the two arrays for all current functions, suggesting that the late current from one of the Marx banks in the 16×15μm experiment either managed to arrive before the start of implosion or the discharge of current and switching of the various components of the pulsed power device was not too effective or symmetrical in the 16×10μum experiment. Either way this suggests that the slow implosion of the 16×15μm array is mainly to do with an increase in mass per length.

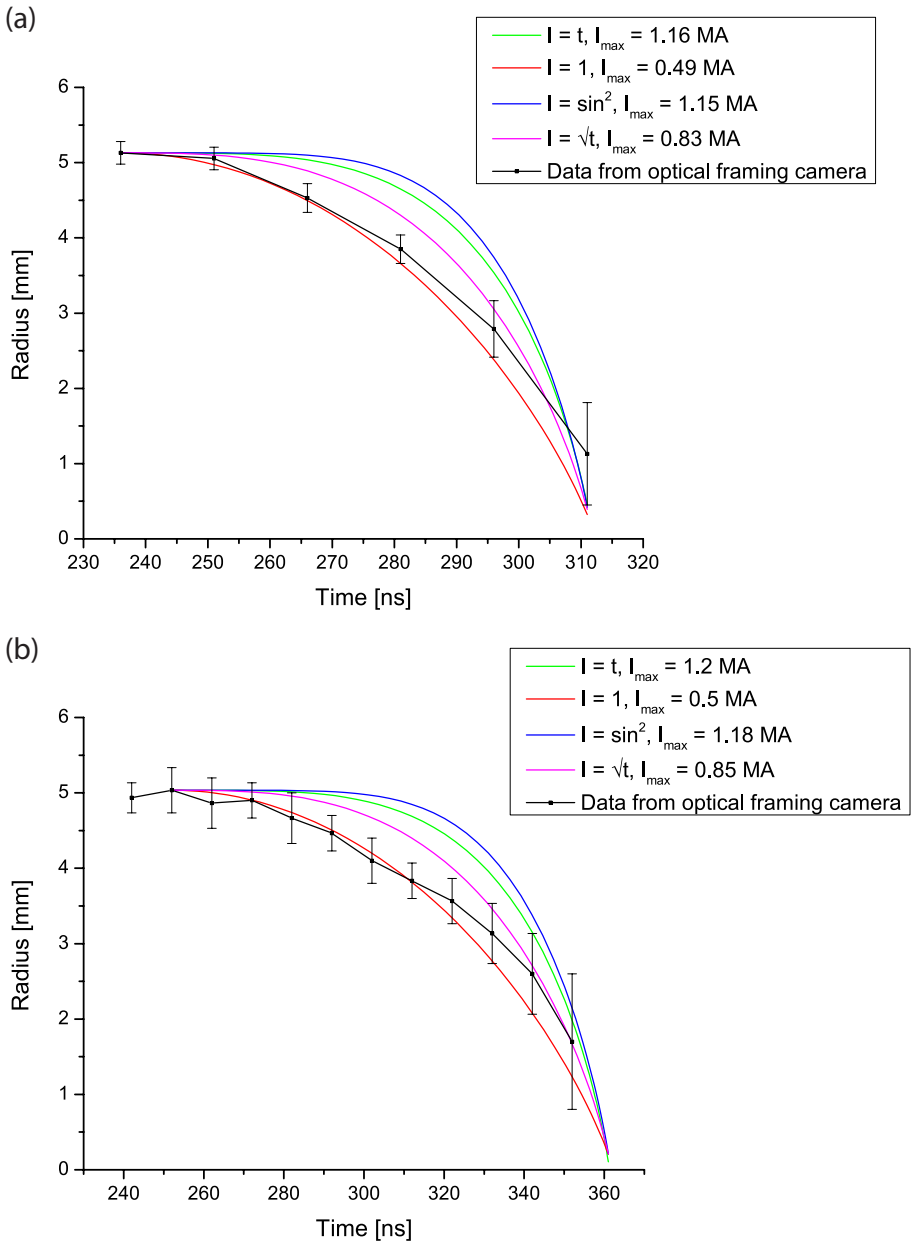

Figure 5.21: Implosion trajectory plots from the thin-shell model for different current functions along with the experimental data of the optical framing camera taken from Figure 5.20 for a (a) 16×10μm and (b) 16×15μm Al wire array load.

5.3.3 Stagnation and X-ray production

When the plasma stagnates on axis, the kinetic energy contained in the accelerating shell is thermalised and emitted as an X-ray pulse. This X-ray pulse has been observed from filtered PCD signals for the 16×10μm array. This is shown in Figure 5.22 along with the implosion trajectory from an optical framing camera (the trajectory is reproduced from the previous section Figure 5.20(a)). We see that soon after the shell stagnates at 311ns the soft X-ray pulse from the 6μm

polycarbonate PCD rises from 0.75V to a peak of ~ 10V in less than 10ns. This peak corresponds to the thermalisation of the shell's kinetic energy. After which the pulse falls before rising up again reaching a peak of ~ 8V at 330ns. The most likely source of this X-ray peak is ohmic heating and PdV compression of the stagnated plasma column. The low hard X-ray signal from the Beryllium filtered PCD suggest that most of the detected X-rays by the polycarbonate filtered PCD is actually soft X-ray.

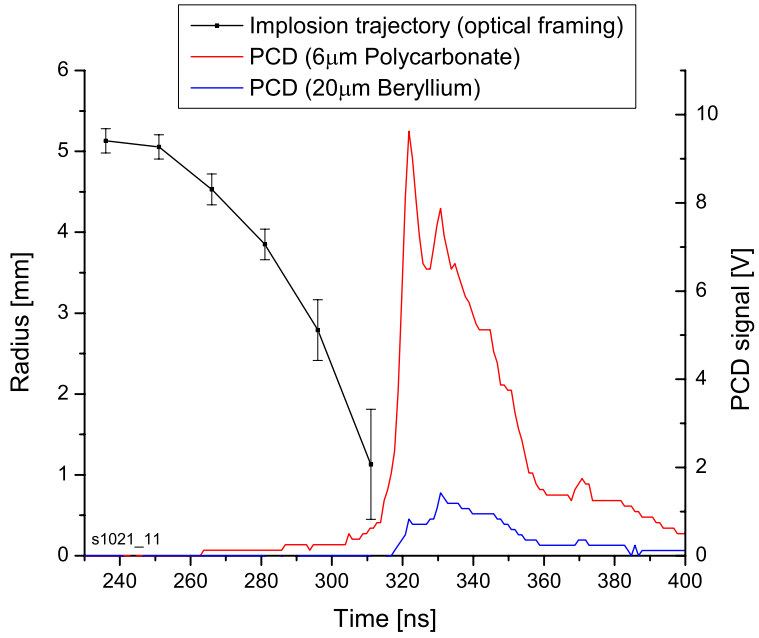

Figure 5.22: X-ray signals from a 6μm polycarbonate and 20μm Beryllium filtered PCD along with the implosion trajectory from optical framing camera for a 16×10μm Al wire array load.

The implosion and stagnation of the 16×15μm from the experiment s0313_20, where its implosion trajectory was presented in the previous section, did not generate any detectable X-rays by the filtered PCDs. However in a different experiment (s0320_12) with identical load properties, a large X-ray pulse was detected (Figure 5.23(b)) saturating the 6m polycarbonate PCD signal to 22V in 3ns. We do not have implosion trajectory data for this experiment due to a late current start time, hence all the diagnostics fired early relative to the current start. However we managed to obtained the current switch time from dI/dt Rogowski signal in Figure 5.23(a) to be around 395ns.

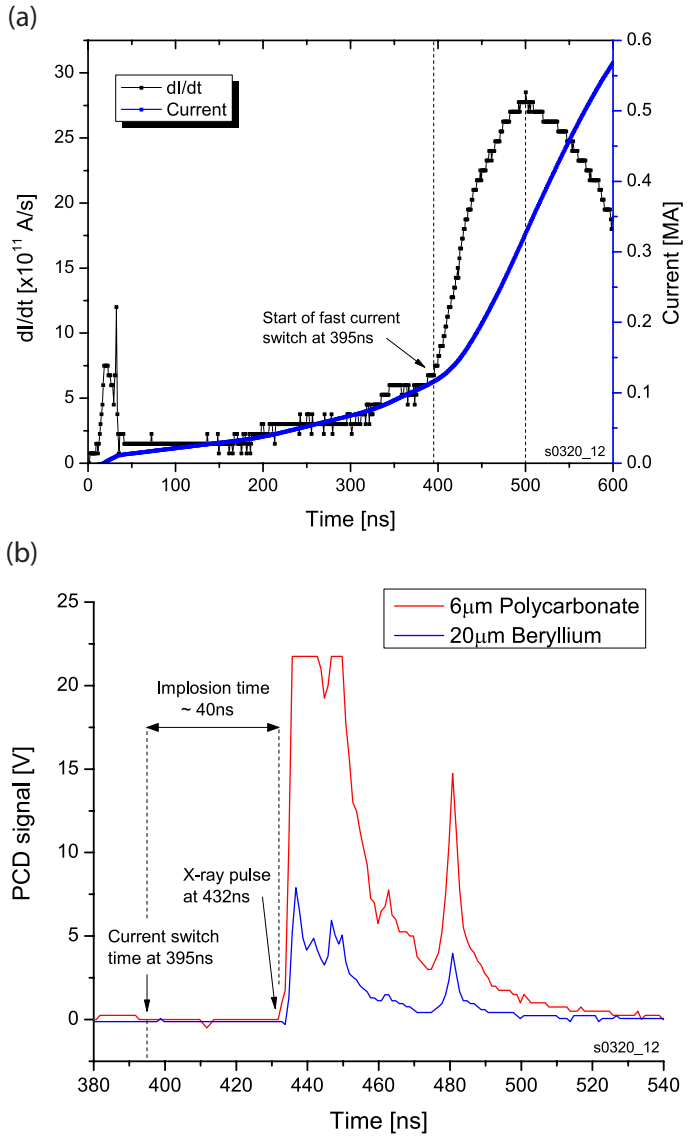

Figure 5.23: (a) dI/dt and current signal from a Rogowski groove and (b) X-ray signal from a 6μm polycarbonate and 20μm Beryllium filtered PCDs for a 16×15μm Al wire array load taken from experiment s0320_12.

If we assume that stagnation happens at the start of the X-ray pulse rise which is 432ns then the implosion time for this experiment is ~ 40ns. This is less than half the implosion time seen for the s0313_12 experiment, and is even faster than the lighter 16×10μm array. In addition, the current value from Figure 5.23(a) at the point of Rogowski break-down is roughly twice as large as the one from experiment s0313_12 (Figure 5.14).

To understand this huge difference in implosion time and hence X-ray generation between two identical loads, we looked into the time at which current was discharged from the Marx banks and into the load. In experiment s0313_12 where

we had a slow implosion and no X-ray pulse, all banks fired on time except one fired 275ns later. In experiment s0320_12 where we had a fast implosion and a large X-ray pulse, one bank fired on time while the rest 3 banks fired 190ns later. In the former experiment the switch happens at ~ 260ns. This is 10ns after the machine's current reached its peak (assuming peak time at 250ns), and therefore the implosion is driven by a decreasing current. After ~ 110ns when the implosion stagnates, the current would most probably have decreased to roughly half its peak value and hence the lack of X-ray production. In the other experiment (s0320_12), the first pulse works on ablating the inverse array for the first 190ns before the larger current pulse from the other 3 Marx banks 'kick-in'. The current switch happens at the temporal point which is 45ns before the major (late) current pulse reaches its peak value. Hence the implosion is driven by an increasing current reaching its maximum value soon after stagnation and hence the large X-ray pulse.

The X-ray pulse of a 16×15μm array in Figure 5.23(b) shows a similar double peak as seen in the 16×10μum array where the first peak at 436ns corresponds to the thermalisation of kinetic energy and the second peak at 446ns corresponds to ohmic heating and PdV compression of the stagnated plasma. The time between the two peaks (~ 10ns) is similar to the one seen for a 16×10μm array. The source of the third peak could be due to the plasma column breaking creating a large local electric field which drives an electron beam generating mainly hard X-rays.

Time integrated pinhole images were obtained for the stagnated column from a 16×15μm array through a 7μm Be filter (Figure 5.24). No image was observed through the 6μm Al filter and for this reason it is not presented. The stagnated plasma column structure is similar to standard wire array Z-pinch where the X-ray generation is not uniform throughout the axial length but rather localised within 'hot-spots' region (darker colour in image). Those regions are caused by the development of the m=0 instability after stagnation, which in turn is induced by the Rayleigh-Taylor instability during implosion. The distance between the 'hot-spots' varies within ~ 1-3mm.

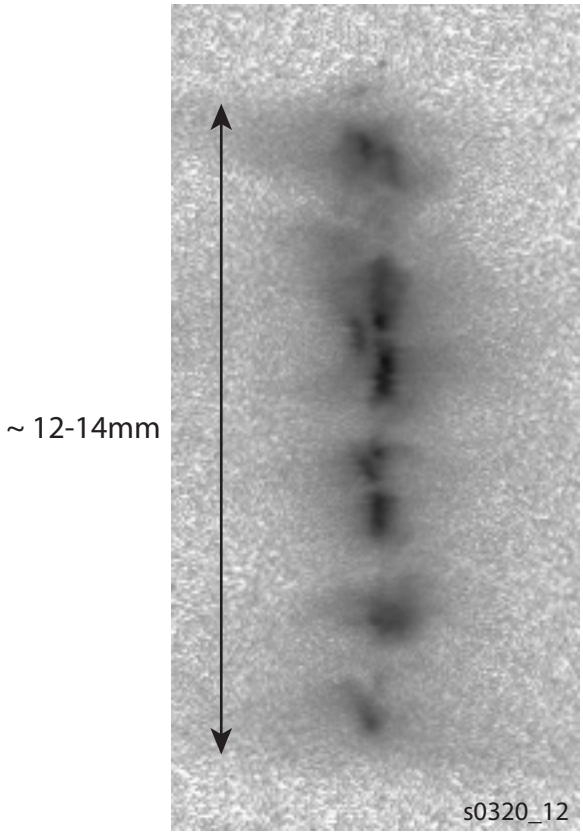

Figure 5.24: Time integrated pinhole image through a 7μm Be filter of the stagnated plasma column from a 16×15μm Al wire array.

Chapter 6

Conclusion

The main objective of this research was to investigate the creation and implosion of a cylindrical plasma shell using a two-stage wire array Z-pinch configuration. The implosion of a shell in a 0D manner could have potential applications in Z-pinch ICF such as in a dynamic hohlraum. In this two-stage configuration the load wires are pre-pulsed with a short duration current pulse of ~ 15-20ns and allowed to 'freely' thermally expand with minimal current flowing through for ~ 200-250ns. Then a fast rising current switches into the load triggered by the explosion of the inverse array. This current fully ionises the bulk of the wire mass causing an implosion of a cylindrically symmetric load.

The aim is to *precondition* (wire expansion after being pre-pulsed) a load of large number of wires with a small inter-wire separation to achieve wire merging before the main current switch into the load. Previous experiments involving a two-stage wire array configuration were only performed on 8 wire loads of Al [31]. Therefore our initial investigation was to understand how sensitive the preconditioning effect of this two-stage configuration to variation in load wire number.

Investigation of the preconditioning effect for loads of different wire numbers

We have investigated the preconditioning effect of cylindrical array loads of 2×30μm, 4×20μm, 8×15μm & 16×10μm Al wires in a two-stage wire array configuration. We have varied the wire thickness in order to keep the total mass per length of the load constant at ~ 40g/cm. The preconditioning effect was characterised by looking at wire expansion and line density plots obtained from analysis of interferometric images. A prepulse current was observed in all load

setups and the calculated temperature from this current pulse suggested that all wires have reached temperatures beyond boiling point. After the pre-pulse all wires preconditioned (thermally expand) into columns of Al gas which was evident from interferometric images. The preconditioned wires show a high degree of axial uniformity along majority of the length, with the exception of the 'end-effects' near the electrodes. Later work demonstrated that it is possible to mitigate this effect by an appropriate arrangement of the electric field at the electrodes. Thus, the analysis were focused on the properties of the preconditioned wires in the central, uniform region of the load. Line density plots have shown that thicker wires expand to larger diameters than thiner wires. The 30μm wire expanded to a diameter of 3.7±0.4mm while the 10μm wire expanded to a diameter of 1.6±0.4mm. In addition such plots showed that thicker wires had a significant amount of plasma around the wire surface (for the 30μm wire, $N_i \leq 0.18N_{tot}$), whereas this was hardly detectable in thinner wires. The expansion rate and temperatures of thicker wires were also greater, the average temperature of a 30μm wire reached 4.5eV. However this value is not large enough to overcome the first ionisation potential and therefore suggesting that the expanding gaseous wires in all the arrays investigated were mostly in a neutral state.

Current switch mechanism

The two-stage configuration is designed to rapidly switch current into the load. Obtaining a direct measurement of current in the load is crucial for analysing the implosion dynamics. Attempts to measure the current using Rogowski probes placed at one of the loads return posts and around the load itself were not successful. Therefore an experiment with a specially designed current-measuring load incorporating B-dot probes was conducted in order to obtain a direct measurement of current at the load section after the switch.

Analysis of dI/dt signals and XUV images of the load section have suggested a more dynamical current switch mechanism. As gaps form along the inverse array triggering the final explosion, both the inductance and resistance of this array increases significantly driving a great portion of the current into the load leading to the start of the current switch. As the explosion progresses a plasma 'bubble'

formed at the top electrode of this array expand upwards into the load section and closes the gap in between the load and inverse array. The current through the plasma in the gap causes it to implode after some time and only then the current fully switches into the load. The expanding plasma forms a secondary current return path and therefore the return current is divided between this plasma path and the return post. This mechanism might have a more favourable scaling with increasing generator current causing a faster implosion of plasma in the gap and hence a more rapid current switch. However one possible negative aspect is that the switching time along the axial length of the load is not uniform leading to a 'zippering' effect in ionisation and perhaps non-uniform implosion in larger current machines.

Single wire load

In standard single wire Z-pinch experiments the core-corona plasma structure dominates the behaviour of the pinch. Current flows through the low density plasma - which constitutes a small fraction of the total mass - and it becomes highly unstable. X-rays are generated from 'hot-spots' formed as a result of the development of instabilities.

Single wire loads of 25, 40 and 50μm Al wire in a two-stage wire array configuration was investigated. A prepulse current through all of them was observed and the calculated temperature reached beyond boiling point. Both the 25 and 50μm wire reached boiling point at the same time, which agrees with the theoretical analysis that the change in energy deposition rate per atom does not vary with wire thickness. However this was not in agreement with wire expansion velocity, where the 25μm expanded at an average rate of ~ 0.56±0.09 cm/μs corresponding to an average temperature of ~ 0.94±0.30 eV. While the 50μm expansion velocity was twice as much at ~ 1.03±0.18 cm/μs corresponding to an average temperature of ~ 3.17±1.11 eV (3 times the 25μm temperature). This is a strong indication that ohmic heating after the wires reach boiling point is not consistent for different wire thicknesses. The variation in expansion velocity - in addition to the initial expansion soon after the prepulse - results in different diameters of preconditioned wire just before the switch, were the 25μm wire

reached ~ 2.8mm and the 50μm wire reached ~ 4.5mm. From Abel inverted line density plots it appears that the preconditioned wires try to keep a roughly constant density profile in the same order of magnitude for all wire thicknesses. From the two wavelength analysis of fringe-shift, electron atom line density was obtained. This showed a strong presence of plasma around the surface of the thicker 50μm wire with an ionisation Z ~3. Very little plasma is observed around the 25 and 40μm preconditioned wire. Abel inversion of the atom line density from the left and right side shows a very good azimuthal symmetry in preconditioned wires.

As the current switches into this preconditioned single axial wire, it acts on all the mass converting neutrals into plasma before the start of implosion. As a result, the single preconditioned wire demonstrates a snowplough-like implosion with an implosion time ~ 25-30ns. An estimated current of ~ 0.8 - 1.0MA was obtained from snowplough implosion trajectory fits using the measured density distribution before the current switch. There was no development of R-T instability, and it generated X-ray from the whole length of the wire. In effect, the single preconditioned wire behaves like a gas-puff Z-pinch starting from a very uniform mass distribution. Development of m=1 MHD instability into an expanding helix after stagnation was observed and coincided with the X-ray peak seen in the 40μm wire implosion.

Formation and implosion of a plasma shell

The final part of this research was creating and imploding a plasma shell by preconditioning a large number of wires with a small inter-wire separation. However before we attempted to create a shell we did some preliminary experiment to explore any dynamics that could arise between preconditioned wires at close proximity. Experiments involving two preconditioned wires with a ~ 0.7mm gap in between does not show any kind of interaction between the wires due to the low level of current during this stage of the experiment. The two wires expanded independently with no significant presence of mass in the gap. Hence concluding that the wires need to physically 'touch' in order to achieve merging.

Experiments were also done on linear array loads to investigate the minimum inter-wire spacing needed to form a shell. This is because overlapping wires in a side-on image of a cylindrical array geometry makes it difficult to judge if adjacent wires have or have not merged. It was found from a 7×15μm linear array experiment that a minimum of ~ 1.6mm inter-wire spacing is needed for a 15um Al wire array to merge. Therefore to form a 'shell' from this wire thickness, an array of 16×15μm wires on an 8mm diameter load section was assembled.

Two cylindrical wire arrays were assembled to form a 'shell' from preconditioned wires: a 16×10μm and a 16×15μm array. Wires did expand sufficiently to merge just before the current switch. Two wavelength interferometry analysis have shown that ~ 60% (assuming ionisation Z = 1) of the 16×10μm wire array mass is in a plasma state at ~ 170ns. Both cylindrical wire arrays of preconditioned wires demonstrated a 0D implosion dynamics, with no prior ablation and no trailing mass was left behind the implosion. this is in contrast to the behaviour of standard wire arrays were the dynamics is dominated by the ablation of stationary core-corona structure wires for ~ 80% of implosion time. This ablation is highly modulated in the axial direction, and at the beginning of implosion the level of perturbation in the mass distribution is very significant. In the case of a preconditioned wire 'shell', development of classical R-T instability was observed, which is driven by the acceleration of the plasma shell. An estimate of the level of initial perturbation was obtained by applying the theory of linear R-T instability growth in a converging shell on the experimentally measured wavelength and amplitude of instability. This corresponded to a very small level of effective initial perturbation at ~ 1 - 2μm.

Possible application of results obtained and future work

Single preconditioned wires could be used as targets for laser-plasma interaction experiments. This target is quite interesting since its density lies between a solid target and a gas jet target both of which have been extensively researched. This new target density could be controlled by varying the timing delay after the prepulse current. These targets could be used for ion acceleration experiments (Al, with low level of impurities).

Another interesting possibility is to use this preconditioned wire target for HEDP (High Energy Density Physics) shock experiments. Energy deposition by a laser could drive strong shocks / blast waves in condition when radiative cooling is significant. A single shock or colliding shocks (generated by two laser beams) can be formed and investigated. In addition, it would be possible to add a magnetic field to the system to study laser driven shocks in magnetised plasma.

The fact that preconditioned wires possess a very low level of initial perturbations is very promising to scale the 'shell' formation approach of a two-stage wire array experiments in larger current Z-pinch facilities such as the Z facility at Sandia National Laboratory. In addition, this approach to form shell-like loads allow us to investigate several techniques previously proposed for mitigating R-T instability growth in fast Z-pinch implosions, such as the use of nested plasma shells and axially 'hour-glass' shaped mass distribution. Those techniques were not directly applicable to standard wire arrays due to the wire ablation phase dominating the total implosion time and re-distributing the mass causing a snowplough implosion and not a shell-like implosion.

Bibliography

1. Basko, M.M., *Inertial confinement fusion: steady progress towards ignition and high gain (summary talk).* Nuclear Fusion, 2005. **45**(10): p. S38-S47.
2. Lindl, J., *Development of the Indirect-Drive Approach to Inertial Confinement Fusion and the Target Physics Basis for Ignition and Gain.* Physics of Plasmas, 1995. **2**(11): p. 3933-4024.
3. Lindl, J.D., et al., *The physics basis for ignition using indirect-drive targets on the National Ignition Facility.* Physics of Plasmas, 2004. **11**(2): p. 339-491.
4. Dittrich, T.R., et al., *Review of indirect-drive ignition design options for the National Ignition Facility.* Physics of Plasmas, 1999. **6**(5): p. 2164-2170.
5. Keane, C.J. *Capsule Implosions.* [cited 2013; Available from: https://lasers.llnl.gov/for_users/experimental_capabilities/capsule_implosions.php.
6. Hammer, J.H., et al., *High yield inertial confinement fusion target design for a z-pinch-driven hohlraum.* Physics of Plasmas, 1999. **6**(5): p. 2129-2136.
7. Cuneo, M.E., et al., *Double Z-pinch hohlraum drive with excellent temperature balance for symmetric inertial confinement fusion capsule implosions.* Physical Review Letters, 2002. **88**(21).
8. Bailey, J.E., et al., *Dynamic hohlraum radiation hydrodynamics.* Physics of Plasmas, 2006. **13**(5).
9. Bailey, J.E., et al., *X-ray imaging measurements of capsule implosions driven by a Z-pinch dynamic hohlraum.* Physical Review Letters, 2002. **89**(9).
10. Slutz, S.A., et al., *Dynamic hohlraum driven inertial fusion capsules.* Physics of Plasmas, 2003. **10**(5): p. 1875-1882.
11. Cuneo, M.E., et al., *Compact single and nested tungsten-wire-array dynamics at 14-19 MA and applications to inertial confinement fusion.* Physics of Plasmas, 2006. **13**(5).
12. Arnold, P.A., et al., *Status of the NIF Power Conditioning System.* 2007 Ieee Pulsed Power Conference, Vols 1-4, 2007: p. 1457-1461.

13. Pereira, N.R., *X-Rays from Z-Pinches on Relativistic Electron-Beam Generators.* Journal of Applied Physics, 1988. **64**(3): p. R1-R27.

14. Haines, M.G., *A review of the dense Z-pinch.* Plasma Physics and Controlled Fusion, 2011. **53**(9).

15. Ryutov, D.D., M.S. Derzon, and M.K. Matzen, *The physics of fast Z pinches.* Reviews of Modern Physics, 2000. **72**(1): p. 167-223.

16. Deeney, C., et al., *Enhancement of X-ray power from a Z pinch using nested-wire arrays.* Physical Review Letters, 1998. **81**(22): p. 4883-4886.

17. Sanford, T.W.L., et al., *Improved symmetry greatly increases X-ray power from wire-array Z-pinches.* Physical Review Letters, 1996. **77**(25): p. 5063-5066.

18. Deeney, C., et al., *Power enhancement by increasing the initial array radius and wire number of tungsten Z pinches.* Physical Review E, 1997. **56**(5): p. 5945-5958.

19. Lebedev, S.V., et al., *Effect of core-corona plasma structure on seeding of instabilities in wire array Z pinches.* Physical Review Letters, 2000. **85**(1): p. 98-101.

20. Kalantar, D.H. and D.A. Hammer, *Observation of a Stable Dense Core within an Unstable Coronal Plasma in Wire-Initiated Dense Z-Pinch Experiments.* Physical Review Letters, 1993. **71**(23): p. 3806-3809.

21. Deeney, C., et al., *Streaked laser shadowgraphy of tungsten wire array implosions on the Saturn generator.* Review of Scientific Instruments, 1997. **68**(1): p. 653-655.

22. Lebedev, S.V., et al., *The dynamics of wire array Z-pinch implosions.* Physics of Plasmas, 1999. **6**(5): p. 2016-2022.

23. Lebedev, S.V., et al., *Effect of discrete wires on the implosion dynamics of wire array Z pinches.* Physics of Plasmas, 2001. **8**(8): p. 3734-3747.

24. Douglass, J.D., et al., *Structure of the dense cores and ablation plasmas in the initiation phase of tungsten wire-array Z pinches.* Physics of Plasmas, 2007. **14**(1).

25. Chittenden, J.P. and C.A. Jennings, *Development of instabilities in wire-array Z pinches.* Physical Review Letters, 2008. **101**(5).

26. Aivazov, I.K., et al., *Formation of a Plasma Precursor Due to the Collapse of Multiwire Liners.* Jetp Letters, 1987. **45**(1): p. 28-31.

27. Bott, S.C., et al., *Dynamics of cylindrically converging precursor plasma flow in wire-array Z-pinch experiments.* Physical Review E, 2006. **74**(4).

28. Sinars, D.B., et al., *Measurements of the mass distribution and instability growth for wire-array Z-pinch implosions driven by 14-20 MA.* Physics of Plasmas, 2005. **12**(5).

29. Lebedev, S.V., et al., *Snowplow-like behavior in the implosion phase of wire array Z pinches.* Physics of Plasmas, 2002. **9**(5): p. 2293-2301.

30. Chittenden, J.P., et al., *X-ray generation mechanisms in three-dimensional simulations of wire array Z-pinches.* Plasma Physics and Controlled Fusion, 2004. **46**: p. B457-B476.

31. Harvey-Thompson, A.J., et al., *Suppression of the Ablation Phase in Wire Array Z Pinches Using a Tailored Current Prepulse.* Physical Review Letters, 2011. **106**(20): p. 205002.

32. Harvey-Thompson, A.J., *An Experimental Investigation of Inverse Wire Array Z-Pinches*, 2010, Imperial College: United Kingdom.

33. Velikovich, A.L., I.V. Sokolov, and A.A. Esaulov, *Perfectly conducting incompressible fluid model of a wire array implosion.* Physics of Plasmas, 2002. **9**(4): p. 1366-1380.

34. Mitchell, I.H., et al., *A high impedance mega-ampere generator for fiber z-pinch experiments.* Review of Scientific Instruments, 1996. **67**(4): p. 1533-1541.

35. Hall, G.N., et al., *Modifying Wire-Array Z-Pinch Ablation Structure and Implosion Dynamics Using Coiled Wires.* Ieee Transactions on Plasma Science, 2009. **37**(4): p. 520-529.

36. Suzuki-Vidal, F., et al., *Effect of Wire Diameter and Addition of an Axial Magnetic Field on the Dynamics of Radial Wire Array Z-Pinches.* Ieee Transactions on Plasma Science, 2010. **38**(4): p. 581-588.

37. Greenly, J., et al., *The Role of Flux Advection in the Development of the Ablation Streams and Precursors of Wire Array Z-pinches.* Dense Z-Pinches, 2009. **1088**: p. 53-56.

38. Bland, S.N., et al., *Extreme ultraviolet imaging of wire array z-pinch experiments.* Review of Scientific Instruments, 2004. **75**(10): p. 3941-3943.

39. Bland, S.N., et al., *Diagnostics for studying the dynamics of wire array Z pinches.* Review of Scientific Instruments, 2006. **77**(10).

40. Spielman, R.B., *Diamond Photoconducting Detectors as High-Power Z-Pinch Diagnostics (Invited).* Review of Scientific Instruments, 1995. **66**(1): p. 867-870.

41. Muraoka, K., *Laser-Aided Diagnostics of Plasma and Gases*. Plasma Physics2000: Institute of Physics Publishing. 200.

42. Hutchinson, I.H., *Principles of Plasma Diagnostics*. 2nd ed2002: Cambridge University Press.

43. Weber, B.V. and S.F. Fulghum, *A high sensitivity two-color interferometer for pulsed power plasmas.* Review of Scientific Instruments, 1997. **68**(2): p. 1227-1232.

44. Chase, M.W., *JANAF thermochemical tables*, 1986.

45. Harvey-Thompson, A.J., et al., *Quantitative analysis of plasma ablation using inverse wire array Z pinches.* Physics of Plasmas, 2009. **16**(2).

46. Bland, S.N., et al., *Effect of radial-electric-field polarity on wire-array Z-pinch dynamics.* Physical Review Letters, 2005. **95**(13).

47. Sarkisov, G.S., et al., *Interferometric measurements of dynamic polarizabilities for metal atoms using electrically exploding wires in vacuum.* Physical Review A, 2006. **73**(4).

48. Pikuz, S.A., et al., *Multiphase foamlike structure of exploding wire cores.* Physical Review Letters, 1999. **83**(21): p. 4313-4316.

49. Zel'Dovich, Y.B. and Y.P. Raizer, *Physics of Shock Waves and High Temperature Hydrodynamic Phenomena*1967.

50. Chittenden, J.P., et al., *Plasma formation in metallic wire Z pinches.* Physical Review E, 2000. **61**(4): p. 4370-4380.

51. Lorenz, A., et al., *Influence of a prepulse current on a fiber Z pinch.* Physical Review Letters, 1998. **81**(2): p. 361-364.

52. Pereira, N.R., N. Rostoker, and J.S. Pearlman, *Z-Pinch Instability with Distributed Current.* Journal of Applied Physics, 1984. **55**(3): p. 704-707.